Università degli Studi di Ferrara

DOTTORATO DI RICERCA IN
SCIENZE CHIMICHE

Curriculum: Fotochimica e Fotocatalisi

CICLO XXI

COORDINATORE Prof. G. Gilli

Photoelectrochemical and photophysical characterization of new molecular photosensitizers and electron transfer mediators for Dye-Sensitized Solar Cells.

Settore Scientifico Disciplinare CHIM/03

Dottorando
Dott. Cazzanti Silvia

Tutore
Prof. Bignozzi C. Alberto

Anni 2006/2008

A Marco

La vita dei morti si trova nella memoria dei vivi.

Cicerone

Index

Chapter 3: Experimental techniques and procedures.

Chapter 4: Electron transfer mediators for DSSCs.

Abbreviations:

ACN: acetonitrile

bpy: 2,2'-bipyridine

bpy-(COOEt)$_2$: 2,2'-bipyridine-di-4,4'- ethyl ester

bpy-(COOnBut)$_2$: 2,2'-bipyridine-di-4,4'- n-butyl ester

bpy-(COOTBut)$_2$: 2,2'-bipyridine-di-4,4'-tert-butyl ester

BQ: bisquinoline

CB: conduction band

CT: Charge Transfer

DBA: 4,4'-ditertbutylamide- 2,2-bipyridine

DEA: 4,4'-diethylamide- 2,2-bipyridine

DEEST: 4,4'-diethylester- 2,2-bipyridine

DM-s1: [Ru(pyrrbpy)$_2$(dcbH)$^{2+}$]

DM-s2: [Ru(pyrr$_2$bpy)$_2$(dcbH)$^{2+}$]

DM-s3: [Ru(pyrrldbpy)$_2$(dcbH)$^{2+}$]

DM-s4: [Ru(pyrrld$_2$bpy)$_2$(dcbH)$^{2+}$]

DM-d1: [Ru(pyrrbpy)$_2$(dcbH)(NCS)$_2$]

DM-d2: [Ru(pyrr$_2$bpy)$_2$(dcbH)(NCS)$_2$]

DM-d3: [Ru(pyrrldbpy)$_2$(dcbH)(NCS)$_2$]

DM-d4: [Ru(pyrrld$_2$bpy)$_2$(dcbH)(NCS)$_2$]

dcbH: 4,4'-dicarboxylic acid- 2,2-bipyridine

dnbpy: 4,4'-dinonyl- 2,2-bipyridine

DMB: 4,4'-dimethyl- 2,2-bipyridine

DSSC: Dye Sensitized Solar Cell

DTB: 4,4'-ditertbutyl- 2,2-bipyridine

DTBEST: 4,4'-ditertbuyl ester- 2,2-bipyridine

EDOP: ethylendioxypyrrole

EDOT: ethylendioxythiophene

EtOH: ethanol

Fc: ferrocene

FTO: fluorine-doped tin oxide

HOMO: Highest Occupied Molecular Orbital

IPCE: Incident Photon to Current Conversion Efficiency

ITO: Indium-doped tin oxide

LHE: Light Harvesting Efficiency

LUMO: Lowest Unoccupied Molecular Orbital

MeTbPQ: 4-methyl-4'-tert-butyl-2,2'-pyridil quinoline

MLCT: Metal to Ligand Charge Transfer

MPN: methoxypropionitrile

N3: Ru(dcbH)$_2$(NCS)$_2$

N-719: Ru(dcbH-TBA$_2$)$_2$(NCS)$_2$

PEDOP: poliethylendioxypyrrole

PEDOT: ethylendioxythiophene

pyrrbpy: 4-pyrrole- 2,2-bipyridine

pyrr$_2$bpy: 4,4'-dipyrrol- 2,2-bipyridine

pyrrldbpy: 4-pyrrolidine- 2,2-bipyridine

pyrrld$_2$bpy: 4,4'-dipyrrolidine- 2,2-bipyridine

PQ: 2,2'-pyridil-quinoline

PTZ: phenothiazine.

Tbpy: 4-tert-Butylpyridine.

TCO: thin conductive oxide

VB: valence band

Z907: Ru(dcbH)(dnbpy)(NCS)$_2$

Introduction

World demand for energy is projected to more than double by 2050 and to more than triple by the end of the century. Finding sufficient supplies of clean energy for the future is one of society's most important challenges. Sunlight provides by far the largest of all carbon-neutral energy sources. More energy from sunlight strikes the Earth in one hour (4.3×10^{20}) than all the energy consumed on the planet in a year (4.1×10^{20} J). Yet solar electricity provides only approximately 1 millionth of the total electricity supply, and renewable biomass provides less than 0.1% of the total energy consumed. The huge gap between our present use of solar energy and its enormous undeveloped potential defines a grand challenge in energy research.

Solar energy conversion systems fall in three categories according to their primary energy product: solar electricity, solar fuels and solar thermal systems. Inorganic chemistry has played a fundamental role in the design of materials and molecular systems for solar energy conversion to electricity .

The challenge in converting sunlight to electricity via photovoltaic cells is dramatically reducing the cost/watt of delivered solar electricity. New materials to efficiently adsorb sunlight and new approaches based on nanomaterials can revolutionize the technology used to produce solar electricity. The technological development of single-crystal solar cells demonstrates the practicality of photovoltaics, while novel approaches exploiting thin films, organic semiconductors, dye sensitisation offer new opportunities for cheaper, long lasting systems.

For millennia, cheap solar fuel production from biomass has been the primary energy source on the planet, however the use of existing types of plants requires large land areas to meet a significant portion of primary energy demand. Inorganic chemistry has been involved in the design of solar fuels based on artificial, molecular-level energy conversion machines exploiting the principles of natural photosynthesis. Artificial assemblies of organic and inorganic materials replacing natural plants or algae, can now use sunlight to directly produce hydrogen by splitting water. The current laboratory

systems are however unstable over long periods, and too inefficient for practical applications. Basic research is needed therefore to bridge the gap between the frontier and practical technology.

Chapter 1

Solar energy conversion: from amorphous silicon to Dye-Sensitized Solar Cells

1.1 Photovoltaic history.

1.2 Operation of traditional photovoltaic devices.

1.3 Thin film solar cells.

1.4 Multijunction and tandem cells.

1.5 Solar concentrators.

1.6 Photoelectrochemical solar cells.

1.1 Photovoltaic history

Solar power can be converted directly into electrical power in photovoltaic (PV) cells. The sun has a surface temperature of about 6,000°C, and its hot gases at this temperature emit light that has a spectrum ranging from the ultraviolet, through the visible, into the infrared. Sunlight contains photons with energies that reflect the sun's surface temperature; in energy units of electron volts (eV), the solar photons range in energy (hν) from about 3.5 eV (ultraviolet region) to 0.5 eV (infrared region). The energy of the visible region ranges from 3.0 eV (violet) to 1.8 eV (red); the peak power of the sun occurs in the yellow region of the visible region, at about 2.5 eV. At high noon on a cloudless day, the surface of the Earth receives 1,000 watts of solar power per square meter (1 kW/m2).

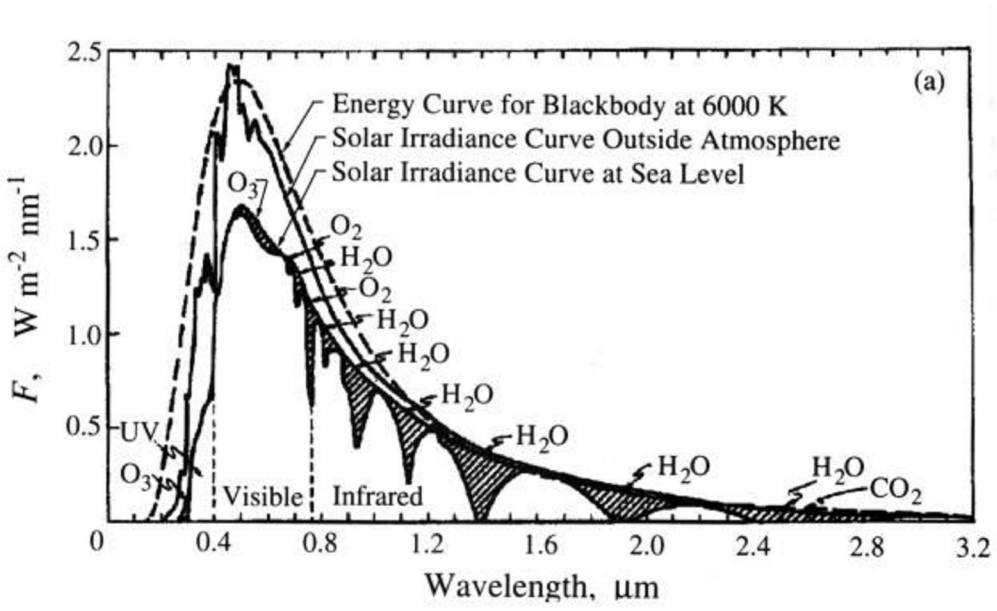

Figure 1. Energy distribution of solar irradiance

Photovoltaic cells generally consist of a light absorber that will only absorb solar photons above a certain minimum photon energy. This minimum threshold energy is called the "energy gap" or "band gap" (Eg); photons with energies below the band gap pass through the absorber, while photons with energies above the band gap are absorbed. The light

absorber in PV cells can be either inorganic semiconductors, organic molecular structures, or a combination of both.

In inorganic semiconductor materials, such as Si, electrons (e^-) have energies that fall within certain energy ranges, called bands. The energy ranges, or bands, have energy gaps between them. The band containing electrons with the highest energies is called the valence band. The next band of possible electron energies is called the conduction band; the lowest electron energy in the conduction band is separated from the highest energy in the valence band by the band gap. When all the electrons in the absorber are in their lowest energy state, they fill up the valence band, and the conduction band is empty of electrons. This is the usual situation in the dark. When photons are absorbed, they transfer their energy to electrons in the filled valence band and promote these electrons to higher energy states in the empty conduction band. There are no energy states between the valence and conduction bands, which is why this separation is called a band gap and why only photons with energies above the band gap can cause the transfer of electrons from the lower-energy-state valence band into the higher-energy-state conduction band. When photons transfer electrons across the band gap, they create negative charges in the conduction band and leave behind positive charges in the valence band; these positive charges are called holes (h^+). Thus, absorbed photons in semiconductors create pairs of negative electrons and positive holes. In a PV cell, the electrons and holes formed upon absorption of light separate and move to opposite sides of the cell structure, where they are collected and pass through wires connected to the cell to produce a current and a voltage , thus generating electrical power Figure 2.

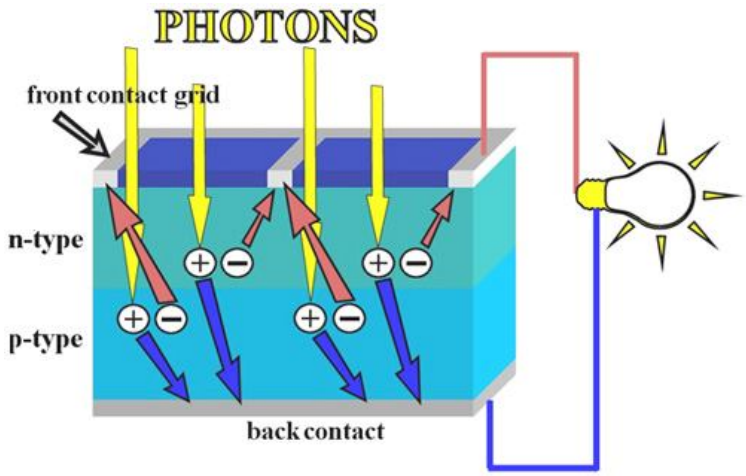

Figure 2. Photoinduced charge separation in a p-n junction.

A French physicist, Edmund Becquerel[1], discovered the photovoltaic (PV) effect in 1839, when he observed that a voltage and a current were produced when a silver chloride electrode immersed in an electrolytic solution and connected to a counter metal electrode was illuminated with white light. However, the birth of the modern era of PV solar cells occurred in 1954, when D. Chapin, C. Fuller, and G. Pearson at Bell Labs demonstrated solar cells based on p-n junctions in single crystal Si with efficiencies of 5–6% .

From the mid 1950s to the early 1970s, PV research and development (R&D) was directed primarily toward space applications and satellite power. Then, in 1973, a greatly increased level of R&D on solar cells was initiated following the oil embargo in that year, which caused widespread concern regarding energy supply. Total global PV (or solar) cell production increased from less than 10 MWp/yr in 1980 to about 1,200 MWp/yr in 2004; the current total global PV installed capacity is about 3 GWp. The "peak watt" (Wp) rating is the power (in watts) produced by a solar module illuminated under the following standard conditions: 1,000 W/m^2 intensity, 25°C ambient temperature, and a spectrum that relates to sunlight that has passed through the atmosphere when the sun is at a 42° elevation from the horizon (defined as air mass [or AM] 1.5; i.e., when the path through the atmosphere is 1.5 times that when the sun is at high noon).

In organic molecular structures, the energy of the photons also must first exceed a certain threshold to be absorbed. This absorption creates an energetic state of the molecular system, called excited state. These excited molecular states can also generate separated electrons and holes.

Furthermore, certain organic polymers and other molecular structures can form organic semiconductors that provide the basis for organic PV devices. One difference between inorganic and organic PV cells is that in organic cells, the electrons and holes are initially bound to each other in pairs called excitons; these excitons must be broken apart in order to separate the electrons and holes to generate electricity. In inorganic PV cells, the electrons and holes created by the absorption of light are not bound together and are free to move independently in the semiconductor.

PV cells can be divided into three categories: (1) inorganic cells, based on solid-state inorganic semiconductors; (2) organic cells, based on organic semiconductors; and (3) photoelectrochemical (PEC) cells, based on interfaces between semiconductors and

[1] Becquerel, E. *Comptes Rendus*, **1839**, 9, 561 [First paper reporting the observation of photovoltaic effect].

molecules. Figure 3 shows the structure of an inorganic solar cell based on a sandwich structure of two types of semiconductor material: one type has mobile free negative electrons (called an n-type semiconductor), and the second type has mobile free positive holes (called a p-type semiconductor). The sandwich, called p-n junction, allows the photogenerated electrons and holes to be separated and transferred to external wires for electrical power production. All PV cells depend upon the absorption of light, the subsequent formation and spatial separation of electrons and holes, and the collection of the electrons and holes at different energies (called electrical potential). The efficiency of electron and hole formation, separation and collection determines the photocurrent, and the energy difference between the electrons and holes in their final state before leaving the cell determine the photovoltage.

The cell delivers maximum power P_{max} when operating at a point on the characteristic where the product IV is maximum. This is shown graphically in Figure 4 where the position of the maximum power point represents the largest area of the rectangle shown. The efficiency (η) of a solar cell is defined as the power P_{max} supplied by the cell at the maximum power point under standard test conditions, divided by the power of the radiation incident upon it. Most frequent conditions are: irradiance 100 mW/cm^2 , standard reference spectrum, and temperature 25 ^{0}C. The use of this standard irradiance value is particularly convenient since the cell efficiency in percent is then numerically equal to the power output from the cell in mW/cm^2.

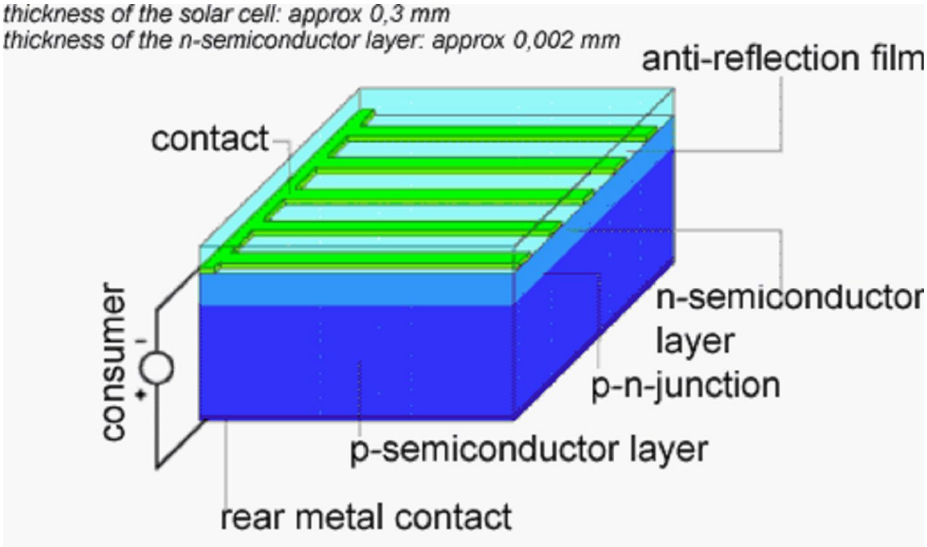

Figure 3. Schematic structure of a sandwich PV cell.

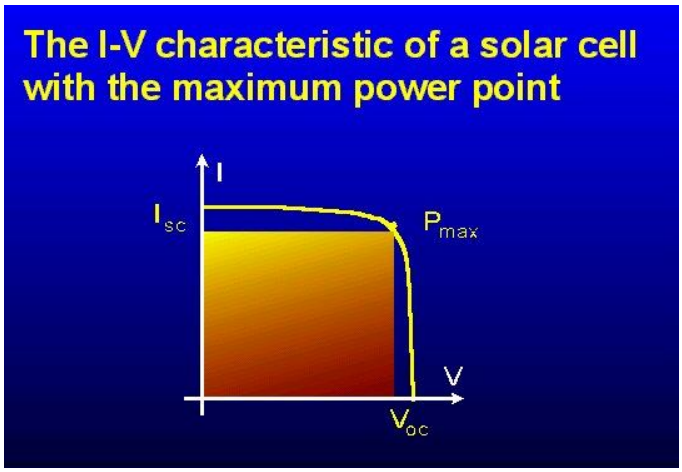

Figure 4. IV curve of a solar cell and maximum power delivered.

1.2 Operation of traditional photovoltaic devices

Silicon is a group (IV) atom. This means that each Si atom has 4 valence electrons in its outer shell. Silicon atoms can covalently bond to other silicon atoms to form a solid. There are two basic types of solid silicon, amorphous (having no long range order) and crystalline (where the atoms are arranged in an ordered three dimensional array). There are various other terms for the crystalline structure of silicon; poly-crystalline, micro-crystalline, nano-crystalline etc, and these refer to the size of the crystal "grains" which make up the solid. Solar cells can be, and are made from each of these types of silicon, the most common being poly-crystalline.

At room temperature, pure silicon is a poor electrical conductor. In quantum mechanics, this is explained by the fact that the Fermi level lies in the forbidden band-gap. To make silicon a better conductor, it is "doped" with very small amounts of atoms from either group III or group (V) of the periodic table. These "dopant" atoms take the place of the silicon atoms in the crystal lattice, and bond with their neighbouring Si atoms in almost the same way as other Si atoms do. However, because group III atoms have only 3 valence electrons, and group V atoms have 5 valence electrons, there is either one too few, or one too many electrons to satisfy the four covalent bonds around each atom. Since these extra electrons, or lack of electrons (known as "holes") are not involved in the covalent bonds of the crystal lattice, they are free to move around within the solid. Silicon which is doped with group III atoms

(aluminium, gallium) is known as p-type silicon because the majority charge carriers (holes) carry a positive charge, whilst silicon doped with group V atoms (phosphorous, arsenic) is known as n-type silicon because the majority charge carriers (electrons) are negative. It should be noted that both n-type and p-type silicon are electrically neutral, i.e. they have the same numbers of positive and negative charges, it is just that in n-type silicon, some of the negative charges are free to move around, while the converse is true for p-type silicon.

By far the most common material for solar cells (and all other semiconductor devices) is crystalline silicon. Crystalline silicon solar cells come in three primary categories:

Single crystal or monocrystalline wafers made using the Czochralski process. Most commercial monocrystalline cells have efficiencies on the order of 16–17%.

Poly or multi crystalline made from cast ingots - large crucibles of molten silicon carefully cooled and solidified. These cells are cheaper than single crystal cells but are less efficient (typically ~15–16%). However, they can easily be formed into square shapes that cover a greater fraction of a panel than monocrystalline cells, and this compensates for their lower efficiencies.

Amorphous silicon. From its discovery in the early 1970s, hydrogenated amorphous silicon (a-Si:H) has stimulated a large worldwide effort to develop various semiconductor device applications. The main advantage of a-Si:H for PV is the low materials and manufacturing costs. The films can be deposited on ordinary window glass, as well as on flexible substrates (stainless steel or polyimide), to make PV products such as flexible roofing shingles, semitransparent modules for windows or skylights, and portable power modules. The basic cell structure is a *p-in* structure, with an undoped (intrinsic) a-Si:H layer between two very thin doped layers. This structure produces an electric field throughout the cell to separate photogenerated electrons and holes and produce electricity. The main disadvantage of a-Si:H is the modest efficiency that has been achieved to date. Stable, small-area cell efficiencies reach ≅ 10%. The high absorption coefficient of a-Si:H stems from its lack of crystalline order. However, this same disorder limits cell efficiencies and results in a self-limiting degradation known as the Staebler-Wronski effect, or “light-induced instability.” No fundamental solution to this problem has yet been found, so solar cells are made with thin undoped layers to minimize this degradation in efficiency (about 15–25% decrease from the initial efficiency).

Figure 5**,** illustrates the various commercial large-area module efficiencies and the best laboratory efficiencies obtained for various materials and technologies.

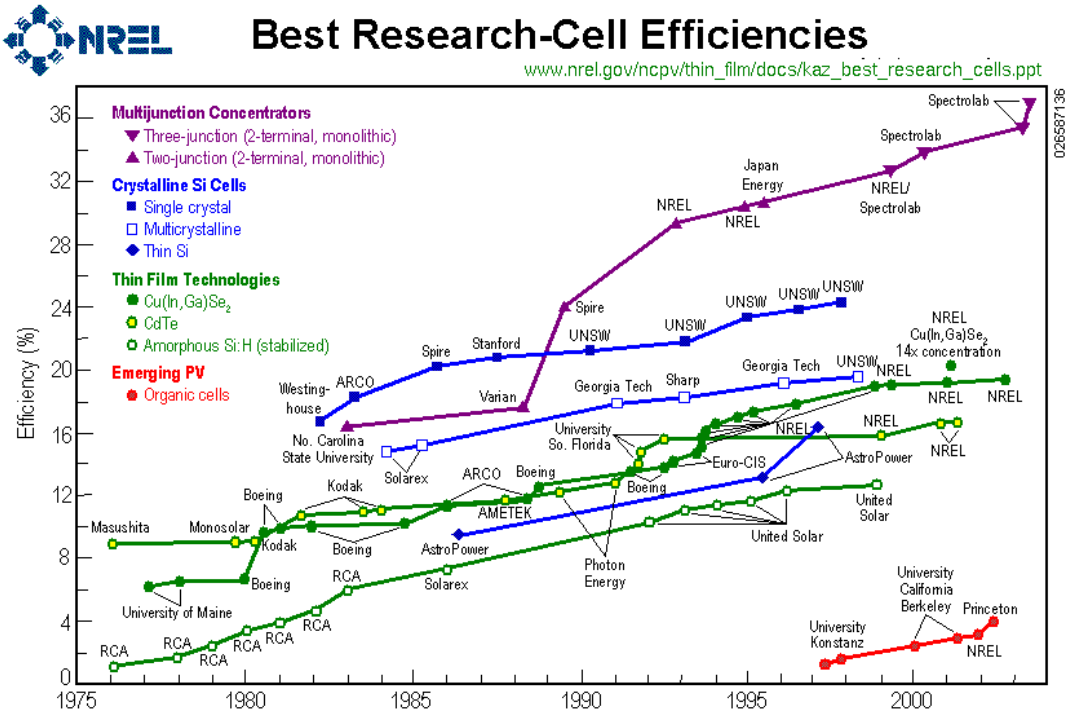

Figure 5. Best laboratory efficiencies obtained for various solar devices.

1.3 Thin film solar cells

Although conventional solar cells based on silicon are produced from abundant raw materials, the high-temperature fabrication routes to single-crystal and polycrystalline silicon are very energy intensive and expensive. The search for alternative solar cells has therefore focused on thin films composed of amorphous silicon and on compound semiconductor heterojunction cells based on semiconductors (e.g., cadmium telluride and copper indium diselenide) that can be by less energy-intensive and expensive routes. A key problem in optimizing the cost/efficiency ratio of such devices is that relatively pure materials are needed to ensure that the photo-excited carriers are efficiently collected in conventional planar solar cell device. Substantial research efforts have produced CdTe and $CuInSe_2$ solar cells with efficiencies approaching 20%. Industrial efforts to manufacture cells made of these materials in high volumes are beginning to demonstrate success. However, this process has been slower

than expected because much of the basic science of these solar cells is not understood. These polycrystalline solar cells are affected by many things, including the grain structure obtained for growth on foreign substrates, the effects of intentional and unintentional impurities on doping and performance, and the nature of the active junction and ohmic contacts formed by poorly understood processes.

The thin-film cadmium telluride/cadmium sulphide solar cell has for several years been considered to be a promising alternative to the more widely used silicon devices. It has several features which make it especially attractive: the cell is produced from polycrystalline materials and glass, which is a potentially much cheaper construction than bulk silicon. CdTe has a bandgap which is very close to the theoretically-calculated optimum value for solar cells under unconcentrated AM 1.5 sunlight. CdTe has a high absorption coefficient, so that approximately 99% of the incident light is absorbed by a layer thickness of only 1 μm (compared with around 10μm for Si), cutting down the quantity of semiconductor required.

A concern often expressed about CdS/CdTe solar cells is the effect on health and the environment of the cadmium used. However, the thinness of the films means that the amount of active material used is relatively small; it has been estimated that even if CdTe solar cells were to provide more than 10% of the world's energy requirements, this would still only account for less than a tenth of the world's cadmium usage. To put the risk into perspective, B.P. Solar modules have been reported to have passed the appropriate U.S. Environmental Protection Agency tests, whereas fluorescent tubes (containing mercury) and computer screens (containing lead) do not.

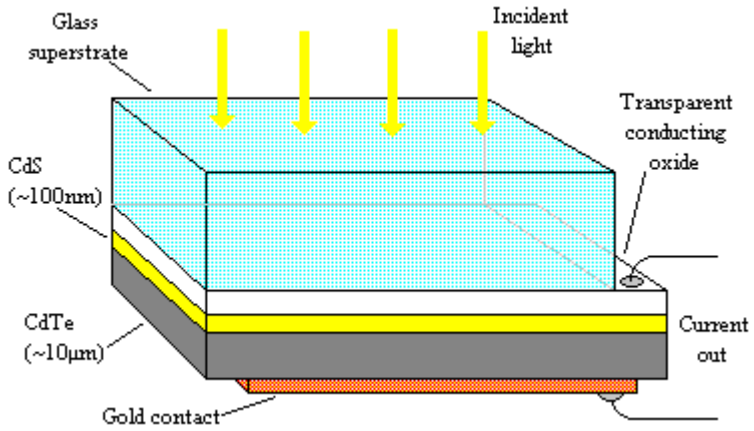

Figure 6. Schematic structure of a sandwich CdS(n)-CdTe(p) solar cell.

The CdTe/CdS solar cell is based around the heterojunction formed between n-type CdS and p-type CdTe.

1.4 Multijunction and tandem cells

Despite all the progress achieved in the fabrication of PV cells there is an intrinsic source of efficiency reduction coming from the lost of sub-bandgap energy photons, which are not adsorbed into the cell. One of the approaches to this problem is the construction of multijunction cells, which consist of devices involving more than one solar cell, in such way that the higher energy radiation is adsorbed by a larger bandgap solar cell, and the residual low-energy solar radiation is adsorbed by a smaller bandgap solar cell[2,3] .

The absorption of different wavelength radiation by different devices can be achieved by an optical beam splitter, by mechanically stacking two or more solar cells, with reduced bandgap as we go down in the stack, or by a monolithical multijunction structure . For mechanically stacked solar cells it can be used a GaAs solar cell (Eb = 1.4 eV) and a GaSb solar cell (Eb = 0.7 eV).

The structure of a monolithic multijunction solar cell is shown in Figure 7,

[2] Bube, R. H. *Photovoltaic Materials*; Imperial College Press: London, 1998. [Textbook covering the properties of materials for photovoltaic applications.]

[3] Olson, J. M.; Kurtz, S. R.; Kibbler, A. E.; Faine, P. *Appl.Phys.Lett.* **1990**, *56*, 623. [Paper concerning construction and properties of highly efficient multijunction solar cells.]

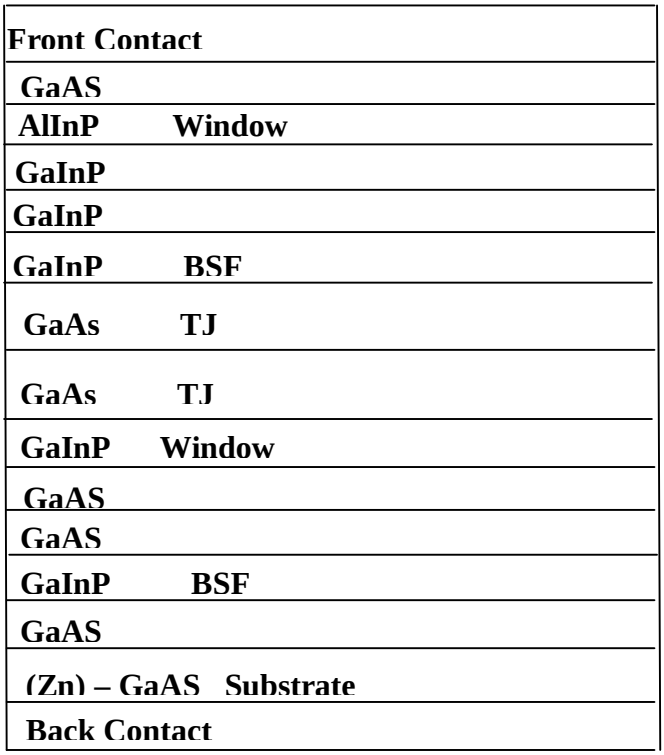

Figure 7. Layer structure of a multijunction. It shows two similar structures from top, with window and back surface (BSF) layers, and joined together by two layers of GaAs (TJ, tandem junction).

where we can appreciate the repetition of the structure for the two different cells, where the GaInP-based cell must have a larger gap than the GaAs-based one. A substrate of GaAs makes lattice matching compatible.

Triple and quadruple-junction have a theoretical efficiency of 30% and 40% due to its broader spectral response[4]. The external quantum efficiency for a triple junction is shown in Figure 8. The lower lines represent the individual cell efficiencies which are chosen for a different range of the spectrum, and we can see how the total efficiency of the junction (the highest curve) is largely increased when they are added up together.

[4] Dimiroth, F. In *Proceedings of the 17th PV European Conference*: WIP-Munich, 2001; p 2150. [Examples and properties of multijunction solar cells are described.]

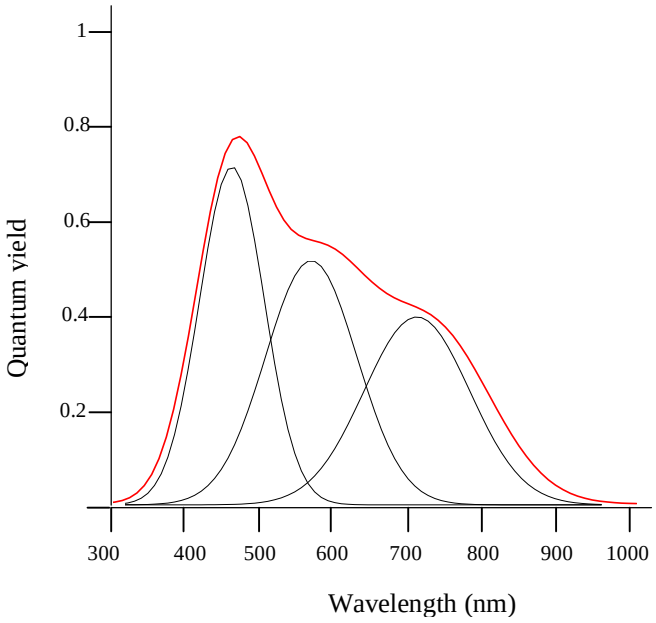

Figure 8. External quantum efficiency for a triple junction solar cell.

1.5 Solar concentrators

The key elements of a concentrator PV system are low-cost concentrating optics, low-cost mounting and tracking systems, and high-efficiency (and relatively low-cost) solar cells (Figure 9).

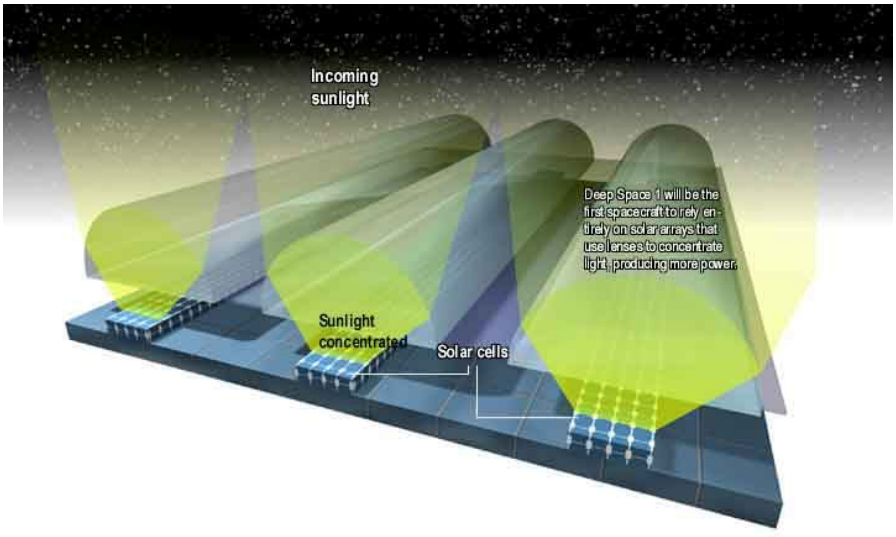

Figure 9. Schematic representation of a solar concentrator.

The large-scale manufacturability of all components has already been demonstrated, including 27%-efficient silicon cells (up to 400 suns concentration) and 28%-efficient GaAs cells.

Concentrator systems using point-focus Fresnel lenses (up to 400 suns) have been routinely fabricated. Module efficiencies of up to 20% have been demonstrated by commercially made 25%-efficient silicon solar cells. Recent progress in multijunction, III-V-based solar cells for space applications has led to looking at their terrestrial potential in concentrating applications.

1.6 Photoelectrochemical solar cells

Since their appearance in the early 1990s by the work of Gratzel[5], photoelectrochemical solar cells based on the principle of sensitization of wide band-gap mesoporous semiconductors, have attracted the interest of the scientific community due to their outstanding performances which started the envision of a promising alternative to conventional junction-based photovoltaic devices. For the first time a solar energy device operating on a molecular level showed the stability and the efficiency required for potential practical applications.

The principle of dye sensitization of semiconductors can be traced back to the end of 1960s[6] , however the efficiencies obtained with single crystal substrates were too low due to the poor light absorption of the adsorbed monolayer of dye molecules. The breakthrough in the field was brought by the introduction of mesoscopic films made of sintered nanoparticles of a semiconductor metal oxide with a large surface area which allowed the adsorption, at monolayer coverage, of a much larger number of sensitizer molecules leading to absorbance values, of thin films of a few microns, well above unity[7]. The research field grown around dye-sensitized solar cells (DSC) is strongly multidisciplinary, involving several areas such as

[5] O'Regan, B.; Graetzel, M. *Nature* **1991**, *335*, 737.[The developement and characterization of highly efficient photoelectrochemical cells is reported.]

[6] Gerischer, H.; Tributsch, H. *Ber.Bunsenges.Phys.Chem.* **1968**, *72*, 437 [The principles of sensitization of semiconductors are discussed.]

[7] DeSilvestro, J.; Graetzel, M.; Kavan, L.; Moser, J.; Augustynski, J. *J.Am.Chem.Soc.* **1985**, 2988. [The developement and characterization of mesoporous thin films is reported.]

nanotechnology, materials science, molecular engineering photochermistry and electrochemistry among the foremost.

Chapter 2

Dye Sensitized Solar Cells: principles and mechanisms

2.1 Dye Sensitized Solar cells.

2.2 Semiconductor materials.

- 2.2.1 Semiconductors properties.
- 2.2.2 Properties of the electrolyte – semiconductor interface.
- 2.2.3 Mesoporous oxide film.
- 2.2.4 Metal oxides as blocking layers to prevent the back reactions.

2.3 Electron transfer processes.

- 2.3.1 Marcus theory in homogeneous and heterogeneous electron transfer reactions.
- 2.3.2 Photoinduced charge separation at the dye – semiconductor interface.

2.4 Sensitization of wide band gap semiconductors.

- 2.4.1 Inorganic molecular sensitizers.
- 2.4.2 Natural sensitizers.

2.5 Electron transfer mediators.

- 2.5.1 I^-/I_3^- as ideal electron transfer mediator for DSSCs.
- 2.5.2 New electron transfer mediators based on Co(II) or Cu(I) compounds as alternatives to I^-/ I_3^- as redox couple in DSSC.
- 2.5.3 Towards solid state devices.

2.1 Dye Sensitized Solar cells

Dye sensitized solar cells (DSSCs) are photoelectrochemical solar devices, currently subject of intense research in the framework of renewable energies as low-cost photovoltaic devices. DSSCs are based upon the sensitization of mesoporous, nanocrystalline metal oxide films to visible light by the adsorption of molecular dyes.

The working principle of a dye-sensitized solar cell is schematized in Figure 9[8] . The device is comprised of two faced electrodes, a photoanode and a counter electrode, with an electrolyte in between. Both electrodes are usually made from a sheet of common float glass coated on one side with a thin transparent conductive layer of fluorine-doped tin dioxide (FTO) or indium-doped tin oxide (ITO). Surface electrical resistivities of a few Ω-square can be easily obtained while preserving a good optical transmission over the whole visible and near infrared spectrum. In the photoanode, the transparent conductive electrode is covered with a thin film (7-10 μm) of a mesoporous semiconductor oxide obtained via a sol-gel procedure. This oxide layer can be deposited, starting from a colloidal suspension, by means of a variety of methods including spraying, screen printing, dip coating, spin coating or the simple doctor blade technique[9]. After deposition, the layer is sintered in an oven at a temperature of 450°C, a treatment which has the scope of creating a network of interconnected particles through which electrons can percolate.

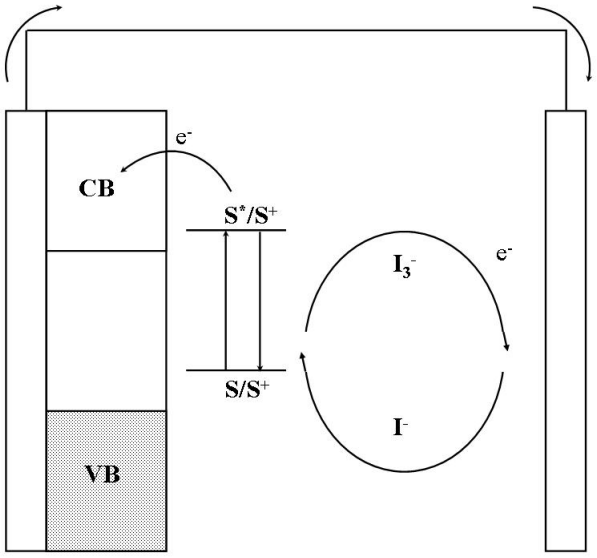

Fig. 9 Schematic working principle of a dye sensitized solar cell.

[8] Graetzel, M. *Inorg.Chem.* **2005**, *44*, 6841.
[9] Heglein, A. *Chem.Rev*. **1989**, *89*, 1861.

Molecular sensitization is obtained when a photoexcited molecule, called sensitizer, in its electronically excited state is capable of promoting an heterogeneous charge transfer process with the semiconductor metal oxide. When the excited state energy level of the sensitizer is higher with respect to the bottom of the conduction band, an electron can be injected with no thermal activation barrier in the semiconductor, leaving the sensitizer in its one electron oxidized form (Figure 10.a). When the excited state is lower in energy with respect to the top of the valence band, an electron transfer (formally a hole transfer) between the semiconductor and the sensitizer can take place leaving the molecule in its one electron reduced form (Figure 10.b)[10].

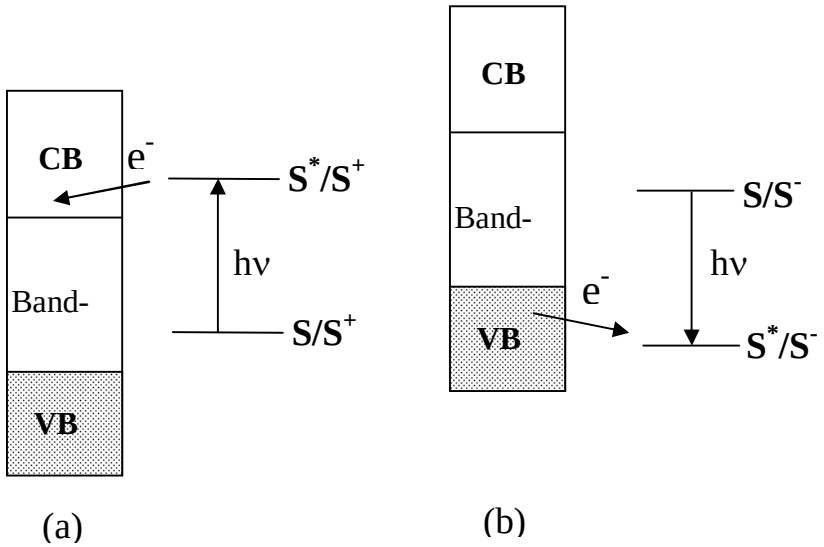

Figure 10. Charge injection sensitization: a) electron injection b) hole injection.

The sensitizer is usually firmly attached to the surface of the semiconductor by virtue of suitable anchoring groups in order to ensure a better donor-acceptor interaction between dye molecules and semiconductor substrate, increasing the electron transfer efficiency.

Dye coverage of semiconductor nanoparticles is generally obtained from alcoholic solutions of the sensitizer in which the sintered film is left immersed for a few hours. Sensitizers are usually designed to have functional groups such as –COOH, $-PO_3H_2$[11], $-B(OH)_2$[12] for stable adsorption onto the semiconductor substrate. The dye covered film is in

[10] Memming, R. *Progr.Surf.Science* **1984**, *17*, 7
[11] Hervé Zabri, Fabrice Odobel, S. Altobello, S. Caramori, C. A. Bignozzi; *Journal oh Photochemistry and photobiology A: Chemistry* 166 (**2004**) 99-106.
[12] S. Altobello, C. A. Bignozzi, S. Caramori, G. Larramona, S. Quici, G. Marzanni, R. Lakhmiri; *Journal of Photochemistry and Photobiology A: Chemistry* 166 (**2004**) 91-98.

intimate contact with an electrolytic solution containing a redox couple dissolved in a suitable solvent. The electron donor member of the redox couple must reduce quickly and quantitatively the oxidized sensitizer.

The counter electrode is a conductive glass covered with a few clusters of metallic platinum which has a catalytic effect in the reduction process of the electronic mediator acceptor member.

The complete photoelectrochemical cycle of the device can be outlined as follows: the adsorbed sensitizer molecules (S) are brought into their excited state (S^*) by photon absorption and inject one electron in the empty conduction band of the semiconductor in a time scale of femtoseconds. Injected electrons percolate through the nanoparticle network and are collected by the conductive layer of the photoanode electrode, while the oxidized sensitizer (S^+) in its ground state is rapidly reduced by I^- ions in solution. Photoinjected electrons flow in the external circuit where useful electric work is produced and are available at the counter electrode for the reduction of the electron mediator acceptor I_3^-. The entire cycle consists in the quantum conversion of photons to electrons.

$S + h\nu \rightarrow S^*$	photoexcitation
$S^* + TiO_2 \rightarrow S^+ + (e^-, TiO_2)$	electron injection
$2S^+ + 3I^- \rightarrow 2S + I_3^-$	sensitizer regeneration
$I_3^- + 2e^- \rightarrow 3I^-$	electron donor regeneration

Photoinjected electrons should escape from any recombination process in order to have a unit charge collection efficiency at the photoelectrode back contact. The two major waste processes in a DSC are due to i) back electron transfer, at the semiconductor-electrolyte interface, between electrons in the conduction band and the oxidized dye molecules, and ii) reduction of I_3^- at the semiconductor nanoparticles surface:

$S^+ + (e^-, TiO_2) \rightarrow S$	back electron transfer;
$I_3^- + 2(e^-, TiO_2) \rightarrow 3I^-$	electron capture from mediator.

Efficiencies of DSSCs of up to 10.4%[13] have been reported for devices employing nanocrystalline TiO_2 films. The performance of dye-sensitized solar cells can be understood in regard of the kinetic competition of the various redox processes involved in the conversion of light into electricity (Figure 11). Ultrafast electron injection has been observed in the femtosecond-picosecond (10^{-15}-10^{-12} s) time domain[14]. Regeneration of the oxidized dye is typically characterized by rate constants of 10^{7}-10^{9} s^{-1}. This is more than 100 times faster than recombination of injected electrons with the oxidized redox species and orders of magnitude faster than back transfer to the dye cation in the absence of a redox mediator. As electron transport in the semiconductor electrode is generally one order of magnitude faster than recombination, the charge collection efficiency is near unit for optimized cells. Because of the prevailing role of electron transfer dynamics in DSSCs, the various processes have been widely studied in the last decade. While photo-electrochemical techniques have proved to be most adequate for the study of electron transport, time-resolved optical spectroscopy remains the leading tool for the study of interfacial electron transfer. Dye regeneration and back transfer reactions have been intensively studied by nanosecond laser spectroscopy. Because of its astonishing rate, the forward electron transfer reaction remained unresolved for several years: the advent of femto-second laser spectroscopy opened the door to enter the domain of ultrafast chemical processes[15].

The functioning of DSSCs is the interlacing of several subsystems which should work in tandem: the dye sensitizer, i.e. the dye adsorbed on the semiconductor surface able to absorb the visible and near-IR photons and to pump electrons into the conducting band of semiconductor, the electron mediator for the “hole" conduction and the counter electrode.

Principles of functioning and main components of dye sensitized solar cells, as the electron transfer processes, the properties of the semiconductor materials, the sensitization of the semiconductor and the kinetic requirements of the electron transfer mediators, will be described in the next paragraphs of this chapter.

[13] M. K. Nazeeruddin, P. Pechy, T. Renouard, S. M. Zakeeruddin, R. Humphry-Baker, P. Comte, P. Liska, L. Cevey, E. Costa, V. Shklover, L. Spiccia, G. B. Deacon, C. A. Bignozzi, M. Graetzel, *J.Am.Chem.Soc* **2001**, *123*, 1613.
[14] Graetzel, M.; Moser, J. E. In *Electron Transfer in Chemistry*; Balzani, V., Ed.; Wiley-VCH: Weinheim, 2001; Vol. 5, p 589.
[15] Neil A. Anderson and Tianquan Lian; *Coordination Chemistry Review*, Vol. 248, Issues 13-14, July **2004**, 1231-1246.

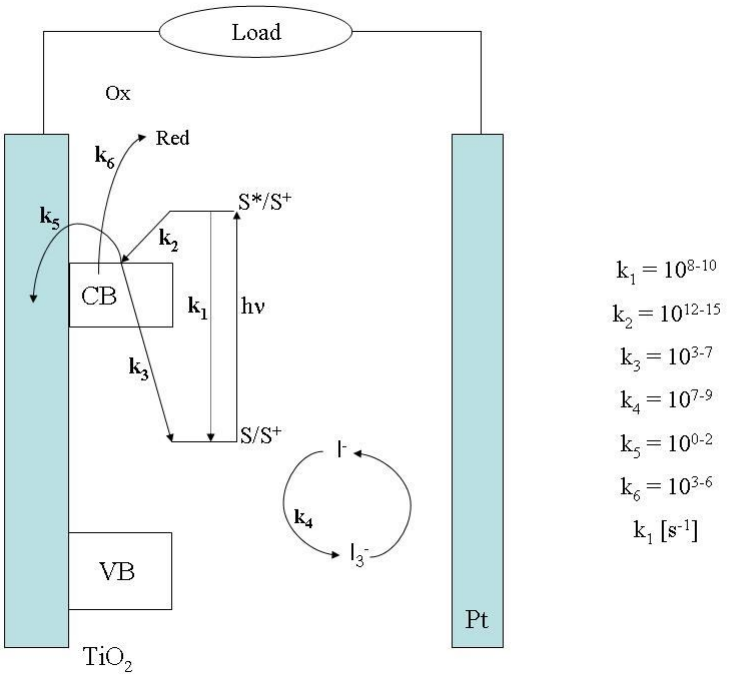

Figure 11. Electron transfer processes involved in a DSSC.

2.2 Semiconductor materials

2.2.1 Semiconductors properties

A semiconductor is a material having a conductivity intermediate between that of metal and insulators, usually solids classed as semiconductors have conductivities from about 10^{-9} to 10^{3} Ohm^{-1} cm^{-1} [16].

The properties of semiconductor electrodes and their differences from those of metallic electrodes can be understood by examining the electronic structure of these materials[17]. The solid might be regarded as a giant molecule, with the assembly of valence electrons ranging over the whole solid: one approach to the problem of treating electronic levels in solids is to start with the levels for the isolated atoms and to consider what happens as an assembly of isolated atoms is brought together to form a crystal. Due to the essentially infinite number of atoms that must be considered, the electronic structure of solids is

[16] Hannay, N. B. *Semiconductors*, Reinhold Publishing Corporation, New York, 1959.
[17] Hannay, N. B. *Semiconductors*, Reinhold Publishing Corporation, New York, 1959.

typically discussed in terms of energy bands which are made up of atomic orbitals of the individual atoms: as a result of the large numbers of interacting orbitals the spacing of electronic energies within a band, arising from a given quantum state, becomes so small that the band can be effectively considered a continuum of energy levels, however the energy gap between the groups of levels corresponding to different atomic quantum states is preserved. Thus we see that the allowed electronic energies fall into energy bands of closely spaced levels, with forbidden gaps between these bands. As with molecular orbitals, often the energy levels of interest are the highest occupied (called the valence band, VB) and the highest unoccuppied (called the conduction band CB) bands. The energy gap (the band gap) between these bands (i.e., the difference in energy between the upper edge of the valence band and the lower edge of the conduction band) determines the properties of the material.

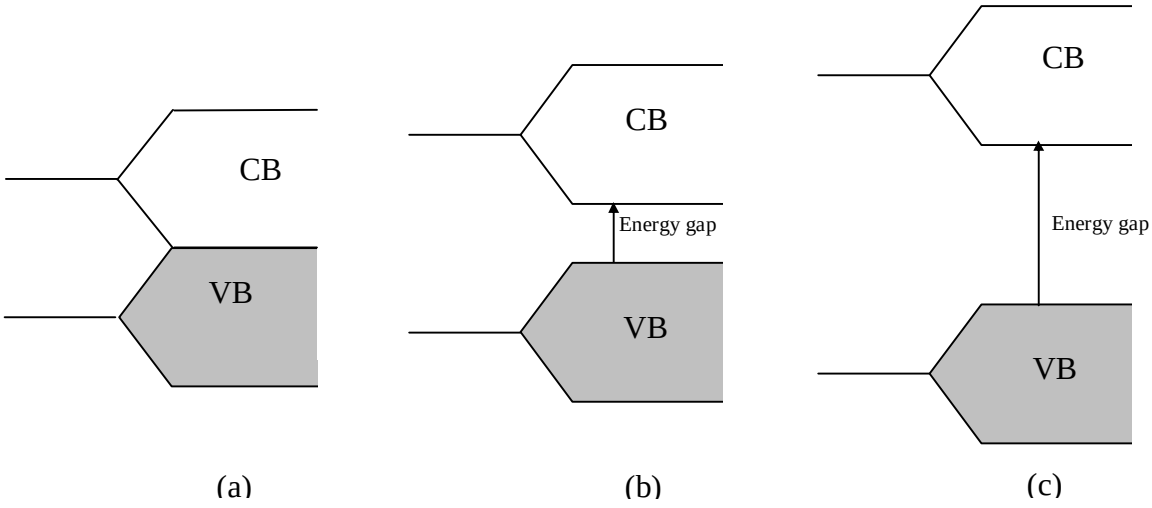

Figure 12 : Representation of conduction band (CB) anf valence band (VB) in therms of band theory for a metal (a) a semiconductor (b) and an insulator (c).

In insulators the valence band is full, the conduction band is empty and no net motion of charge results from the application of an electric field. In a metal the uppermost energy band containing electrons is only partially filled, or a filled band overlaps an empty band. These electrons are free to move in a field and, since they are present in large numbers, they result in very high conductivities ($10^4 – 10^6$ Ohm^{-1} cm^{-1}). In semiconductors the situation is similar to that in insulators, except that the band gap is smaller and electrons can be thermally or optically promoted to the conduction band, resulting in an electrical conductivity which is

smaller than that of metals because of the smaller number of charge carriers. The promotion of electrons from the VB to the CB leaves a positively charged vacancy in the VB, which is referred to as a hole. These holes can be moved through space by the transfer of one electron to the vacancy, therefore holes are considered to be mobile. However there is another method to generate charge carriers within a semiconductor, referred to as doping. Doping involves the addition of a different element to the semiconductor: the simplest example of this involves the introduction of a group V element (e.g. P) or of a group (III) element (e.g. B) to a group IV element like Si. Doping Silicon with Phosphorus introduces occupied energy levels into the band gap which are close in energy to the lower edge of the CB allowing facile promotion of electron into the CB (Fig. 13.a). The addition of an electron deficient element to the semiconductor lattice results in the formation of vacant energy levels close to the upper edge of the valence band, which allows facile promotion of electrons from the VB (Fig. 13.b).

Doped semiconductors, referred as extrinsic semiconductors, in which the majority charge carriers are electrons are referred as *n-type* semiconductors, while those in which holes are the dominant charge carriers are indicated as *p-type* semiconductors.

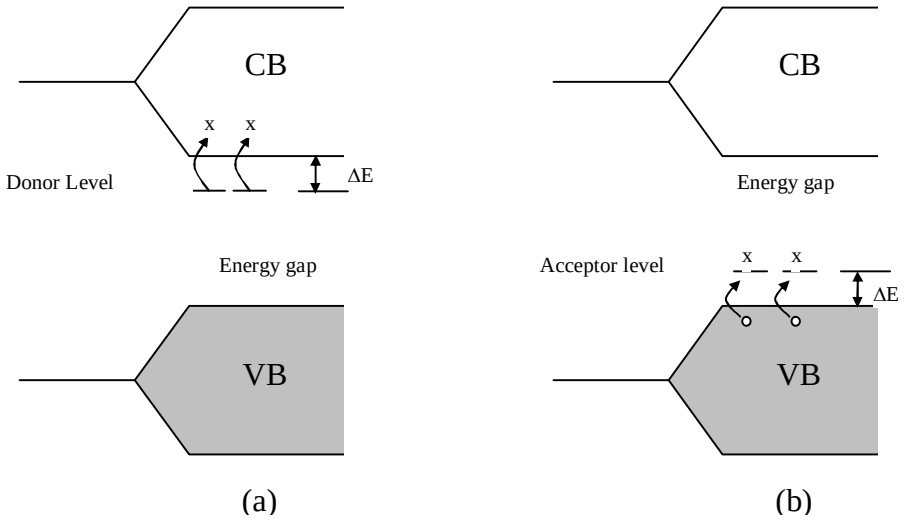

Figure 13 : Diagram of the energy levels of an n-type semiconductor (a) and of a p-type semiconductor (b)

Another important concept in the discussion of solid state materials is the Fermi Level. The Fermi – Dirac distribution is given by:

$$f(E) = \frac{1}{1 + e^{\frac{(E - E_F)}{kT}}} \tag{2.1}$$

where $f(E)$ is the probability that a state of energy E is occupied, E_F is a parameter called the Fermi energy, k is the Boltzmann's constant and T is the absolute temperature. It can be easily seen from (2.1) that E_F is the energy for which $f(E) = \frac{1}{2}$, in other words it is a virtual energy level which has the 50 % of probability to be occupied by the electrons.

We have considered the system from a statistical point of view, however it is possible to derive thermodynamic quantities from the statistics. The entropy of the system expressed in terms of statistics is given by:

$$S = k \ln W \tag{2.2}$$

Where W is the thermodynamic probability of the state of the system, which is determined by the number of ways of distributing the particles in the available states. For a Fermi-Dirac system, the change in enthropy resulting from the addition of one particle to a state of energy E is:

$$dS = k \ln\left(\frac{f-1}{f}\right) \tag{2.3}$$

From (2.1) we obtain:

$$dS = \frac{E_F - E}{T} \tag{2.4}$$

On the other hand, the total differential for the entropy change for the addition of dN particles at energy E may be written as:

$$dS = \left(\frac{\partial S}{\partial N}\right)_{E,V} dN + \left(\frac{\partial S}{\partial E}\right)_{N,V} dE \tag{2.5}$$

where N is the total number of particles. Comparing (2.4) and (2.5) and noting that energies in equation (2.4) are "one electron energies", i.e. they represent the change in energy resulting from the addition of one electron to the system, we see that:

$$\left(\frac{\partial S}{\partial N}\right)_{E,V} = \frac{E_F}{T} \tag{2.6}$$

By definition the electrochemical potential $\overline{\mu}$ is

$$\mu = \left(\frac{\partial G}{\partial N}\right)_{p,T} = -T\left(\frac{\partial S}{\partial N}\right)_{E,V} \tag{2.7}$$

Thus comparing (2.6) and (2.7) we demonstrate that the Fermi energy is just the electrochemical potential, or partial molar free energy per electron. This result is physically understandable considering two systems in equilibrium : thermodynamically we expect them to exchange particles (electrons in this case) until their electrochemical potentials are equal. From the point of view of Fermi statistics, the transfer of particles from one system to another, which fills states of lower energy in one system emptying higher lying filled states in the other system will proceed until the distributions over energy in the two systems match, i.e., the Fermi levels are equal.

For an intrinsic semiconductor the Fermi level lies at the midpoint of the band gap (Figure 14). Doping changes the distributions of electrons within the solid and consequently changes the Fermi energy: for an n-type semiconductor the Fermi level lies just below the conduction band, whereas for a p-type semiconductor it lies just above the valence band (Figure 15). In addition, as with metal electrodes, the Fermi energy of semiconductor electrodes varies with the applied potential, for example applying a positive potential will lower the Fermi level.

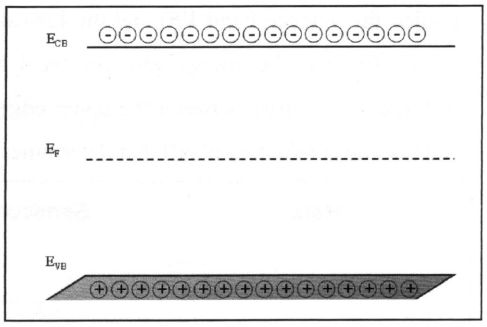

Figure 14 Fermi level in an intrinsic semiconductor

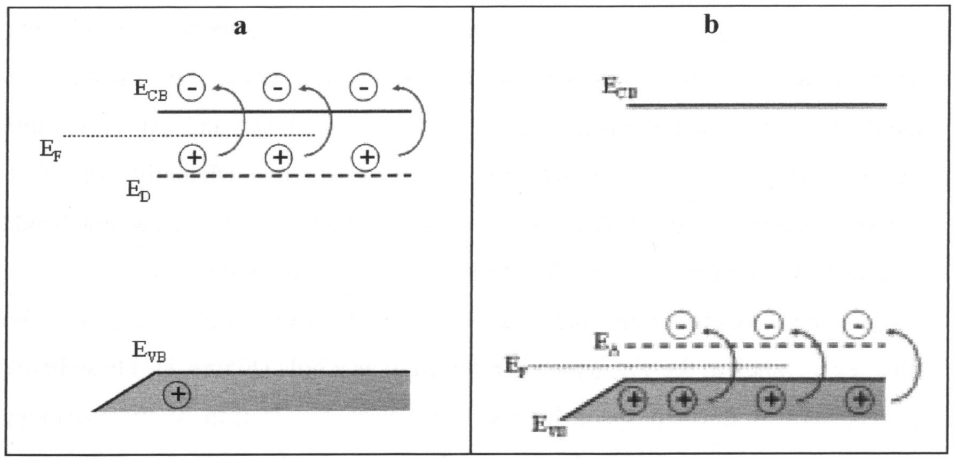

Figure 15 Fermi level in an n-type semiconductor (a) and in a p-type semiconductor (b).

2.2.2 Properties of the electrolyte – semiconductor interface

The interface between a semiconductor electrode and an electrolyte solution is also of great interest for our systems and needs to be described. As in the previous considerations, in order for the two phases to be in equilibrium, their electrochemical potential must be the same. The electrochemical potential of the solution is determined by the redox potential of the electrolyte, while the electrochemical potential of the semiconductor is determined by its Fermi level. If the redox potential of the solution and the Fermi level of the semiconductor do not lie at the same energy, a movement of charge between the semiconductor and the solution is required in order to equilibrate the two phases. The excess of charge that is now located on the semiconductor, due to the relatively low density of charge carriers, extends into the electrode for a significant distance (10-100 nm) forming the so called *space charge region.*

For an n-type semiconductor at open circuit the Fermi level is typically higher than the redox potential of the electrolyte, hence electrons will be transferred from the electrode to the solution. Therefore there is a positive charge associated with the space charge region which is reflected in an upward bending of the band edges (Figure 16.a). Since the majority of charge carriers are removed from this region, this is also called *depletion layer*. On the contrary, a p-type semiconductor has a Fermi level that is generally lower than the redox potential of the electrolyte, so that an electron flow from the solution to the electrode occurs. This generates a negatively charged space charge which causes a downward bending of the bands. Since the

majority of carriers (holes) are removed from this region the term depletion layer is used also in this case (Figure 16.b).

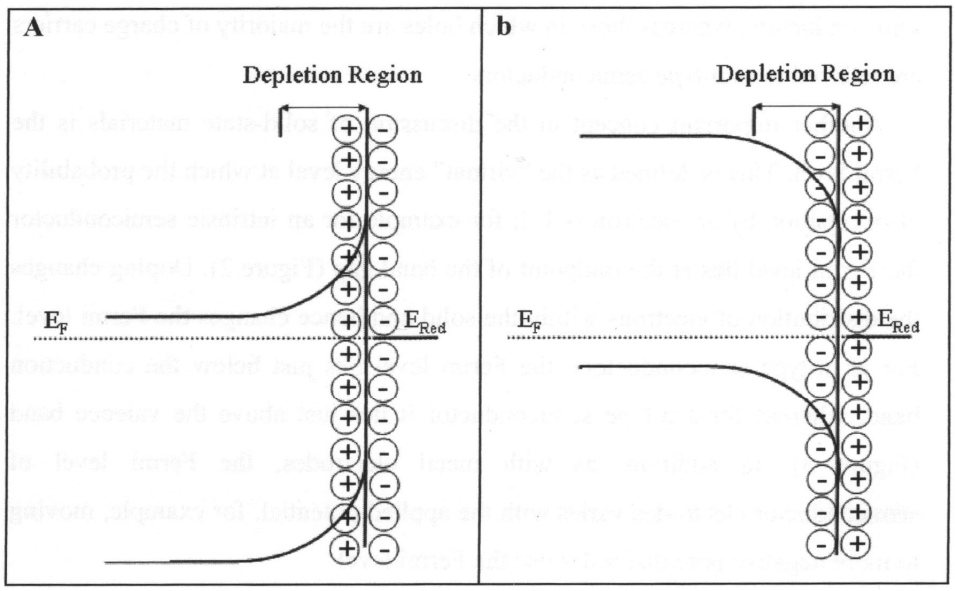

Figure 16 Band bending for an n-type semiconductor **(a)** and a p-type semiconductor **(b)** in equilibrium with an electrolyte.

The formation of a space charge region and the consequent band bending is an important feature when one considers the photovoltaic effect. If the semiconductor electrode is exposed to radiations of sufficient energy, electrons can be promoted to the conduction band. If this process occurs in the interior of the semiconductor, recombination of the promoted electron and the resulting hole typically occurs, together with the production of heat. However, if it occurs in the space charge region, the electrical field existing here will favour the spatial charge separation. For example for an n-type semiconductor, the band edges curve upwards, electron moves to the interior of the semiconductor, while the hole moves towards the interface. The hole is usually an high energy specie able to extract an electron from a redox couple present in solution; that is the n-type semiconductor electrode acts as a photoanode.

In contrast to the convential systems, where the semiconductors assumes both the task of light absorption and charge carrier transport, the two functions are separated in the dye sensitized solar cells (DSSC). Light is absorbed by a sensitizer anchored to the surface of a wide band gap semiconductor. Charge separation takes place in the dye via photoinduced

electron injection from the dye into the conduction band of the solid. Carriers are transported through the conduction band of the semiconductor to the charge collector, while the original state of the dye is restored by an electron donor, usually the I^-/I_3^- couple, dissolved in a low volatility organic solvent. The use of sensitizers based on transition metal complexes having a broad absorption band in conjunction with oxide films of nanocrystalline morphology permits an high light harvesting efficiency, allowing to achieve near quantitative conversions of incident photons into electric current over a wide spectral range.

2.2.3 Mesoporous oxide films

The material of choice for DSSCs applications is TiO_2 (anatase), although alternative wide band gap oxides such as ZnO and Nb_2O_5 have also given promising results[18,19]. TiO_2 is a wide band gap semiconductor with a gap of 3-3.2 eV, therefore is transparent to the visible region of light. There are three common crystal structures of TiO_2: rutile, anatase and brookite. Rutile crystallizes in the tetragonal system, in which six oxygen atoms form a distorted octahedral around the titanium with four shorter and two longer Ti-O bonds. Anatase has a slightly different octahedral structure. Rutile to anatase transformation occurs in the temperature range of 700-1000 °C depending on crystal size and impurities. The main difference between the two allotropic forms is the band gap which is of about 3 eV for Rutile and of 3.2 eV for Anatase[20,21]. The valence band is composed of oxygen 2p orbitals hybridized with titanium 3d orbitals, whereas the conduction band is composed primarly of titanium 3d orbitals[22,23]. Titanium dioxide is chemically inert, non toxic and biocompatible. It is easy to produce in large scale at low cost. Due to the high surface affinity toward carboxylates, salicylates, phosphonates and boronates it can be sensitized by a large variety of dyes, some of them allowing an incident photon/electron conversion efficiency close to unity. TiO_2 mesoporus films are commonly produced via a sol-gel type process involving an hydrothermal step (see experimental section). Figure 17 illustrates the morphology of a nanocrystalline TiO_2 layer deposited on a TCO glass and sintered at 450 C° for 30'.

[18] Tennakone, K.; Kumara, G. R. R. A.; Kottegoda, I. R. M.; Perera, V. P. S. *Chem.Comm.* **1999**, *15*, 15.
[19] Sayama, K.; Suguhara, H.; Arakawa, H. *Chem.Mater.* **1998**, *10*, 3825.
[20] Grant, F. A. *Rev.Mod.Phys.* **1958**, *31*, 646
[21] Bickley, R. I. *Chem.Phys.Solids Surf.* **1978**, *7*, 118.
[22] Glassford, K. M.; Chelikowski, J. R. *Phys.Rev.B* **1992**, 3874.
[23] Silvi, B.; Forati, N.; Nada, R.; Catlow, C. R. A. *J.Phys.Chem.Solids* **1991**, *52*, 1005.

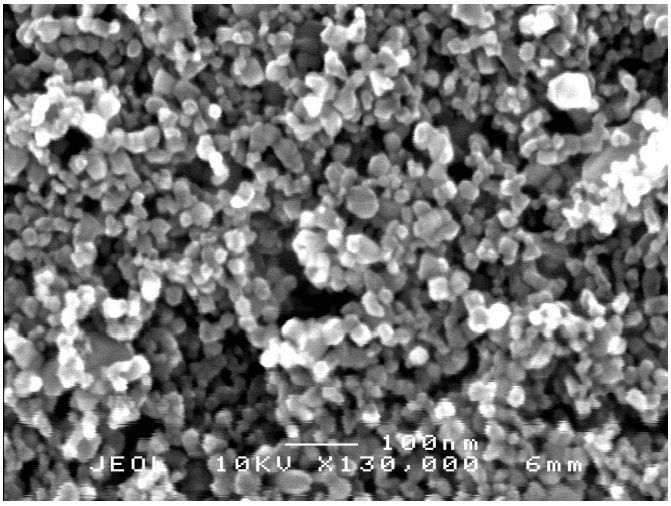

Figure 17 SEM image of the surface of a mesoporous film prepared from the hydrothermal TiO_2 colloid.

Nanocrystalline morphology of TiO_2 is a fundamental requirement in determining the solar conversion efficiency. The use of a porous nanostructured film of very high surface roughness directly affects the light harvesting efficiency. When light penetrates the photosensitized semiconductor "sponge" it crosses hundreds of adsorbed dye monolayers.

Thereby photons whose energy is close to the absorption maximum of the dye are almost completely absorbed[24]. Thus the mesoporous morphology of the film, consisting of nanocrystalline oxide particles with a diameter of 10-20 nm[25] sintered together to allow electronic conduction plays a crucial role in the harvesting of sunlight. Depending on film thickness, their real surface area can easily be made 100-1000 times larger than the apparent one.

2.2.4 Metal oxides as blocking layer to prevent the back reactions.

The most efficient DSSCs to date are based on Ru(II) containing metallorganic dyes adsorbed on nanocrystalline TiO_2, the best of which have been reported to convert solar energy to electrical energy with an efficiency around 10-11%[26] (see also reference 13). The nanocrystalline morphology of the semiconductor metal oxide is not the only requirement a photoanode have to fulfill to ensure a good electrons collection; a key aspect of optimizing the

[24] O'Regan, B.; Graetzel, M. *Nature* **1991**, *353*, 737.
[25] Barbè, C. J.; Arendse, F.; Comte, P.; jirousek, M.; Lenzmann, F.; Shklover, V.; Graetzel, M. *J.Am.Chem.Soc* **1997**, *80*, 3157.
[26] M. K. Nazeeruddin, A. Kay, I. Rodicio, R. Humphry-Baker, E. Miller, P. Liska, N. Vlachopoulos and M. Graetzel; *J. Am. Chem. Soc*. 115 (**1993**), 6382.

electrons collection is the ratio between the rates of injection and recombination electron transfer reactions.

In order to obtain a better clarification on electron transfer mechanisms from photoexcited dye to the conduction band of the semiconductor a lot of studies have been performed on electronic density spatial distribution of Ru(II) polipyridyl compounds[27,28]. The high energy conversion efficiency of the widely used N3 sensitizer and other related Ru(II) polipyridyl complexes derives from the spatial separation of the donor LUMO orbital, which is closed to the TiO_2 surface, and the acceptor HOMO, resulting in injection which is much faster then recombination. (Forward and back electron transfer reactions at the semiconductor – electrolyte interface have been studied by electrochemical methods[29] or by spectroscopical techniques which involve the optical excitation of the sensitizer[30]. These kind of measurements will be widely discussed in the results section).

Although these initrinsic properties of Ru(II) based dyes, several efforts have been performed for a long time in order to replace these rare and expensive Ru(II) complexes with the cheaper and environmentally friendly natural dyes[31].

However in natural dyes this charge density separation is not present and recombination reaction of the photoinjected electron with oxidized dye becomes a significant contribution to the loss of efficiency of these devices. In these case, the use of compact layer between conductive glass and TiO_2 or between TiO_2 and the sensitizer is very useful to minimize the effect of the back recombination reaction on the overall photoconversion efficiency.

Blocking layer of TiO_2 as underlayer were used in order to block the recombination reaction with the back contact. Its function was previously studied by Cameron et al.[32] that verified that the introduction of compact TiO_2 in polipyridyl Ru(II) based sensitized solar cells has only marginal effects on conversion efficiencies. More evidences of the effect of this compact layer on the back recombination reaction have been seen using the natural dyes as

[27] S. Fantacci, F. De Angelis, A. Selloni; *J. Am. Chem. Soc*. **2003**, 125, 4381.
[28] F. De Angelis, S. Fantacci, M. Graetzel et al.; *J. Am. Chem. Soc*. **2005**, 127, 16835.
[29] L. M. Peter, N. W. Duffy, R. L. Wang, K. G. U. Wijayantha, *Journal of Electroanalytical Chemistry*, 524-525 (**2002**) 127-136.
[30] Saif A. Haque, Yasuhiro Tachibana, Richard L. Willis, Jacques E. Moser, Michael Graetzel, David R. Klug and James Durrant; *J. Phys. Chem. **B***, **2000**, 104, 538-547.
[31] N. J. Cherepy, G. P. Smestad, M. Graetzel and J. Z. Zhang; *J. Phys. Chem. **B*** **1997**, 101, 9342-9351-
[32] Petra J. Cameron, Laurence M. Peter and Sarminala Hore; *J. Phys. Chem. **B*** **2005**, 109, 930-936.

sensitizers. Graetzel et al.[33] verified that the introduction of a compact layer induces an increase of the overall effiency from 1% to 1.6% under simulated full sun illumination and more than doubled at lower intensities. This is a strong evidence that the more widely employed Ru(II) based sensitizers act as to "insulate" the anode against recombination losses and that many planar organic dyes employed in DSSCs could greatly benefit from the use of a TiO_2 blocking layer.

Moreover the introduction of metal oxides, such as Al_2O_3, as overlayer between the dye and TiO_2 film was studied in order to block the back recombination not only from the back contact but also from the conduction band of TiO_2[34,35]. Al_2O_3 is a semiconductor oxide with a band gap of 9 eV and a conduction band level at -4.45 v vs SCE. Its function is to induce a retardation of interfacial recombination dynamics leading to an improvement in device performances.

Several studies have also previously reported that treatment of nanocrystalline TiO_2 with $TiCl_4$ solutions results in a significant improvement in device performance[36]. This treatment typically results in a significant increase in J_{sc}. The improvement in device performance has been variously attributed to increased film thickness, increased dye absorption and necking growth during post annealing leading to improved electron transport[37]. It appears possible that the enhancement in J_{sc} widely observed with the use of this film treatment may derive, at least in part, from a retardation of interfacial recombination process due to the formation by this treatment of an interfacial blocking layer.

All these treatments of photoanode are most effective for improving the efficiency of relatively inefficient devices, with minimal effect on efficient devices in which electron transport through the TiO_2 film is already optimized, thereby preventing significant recombination losses at short circuit conditions[38].

---

[33] Anthony Burke, Seigo Ito, Henry Snaith, Udo Bach, Joe Kwiatkowski, and Michael Graetzel, *Nano Lett.*, Vol. 8, No. 4, **2008.**

[34] Emilio Palomares, John N. Clifford, Saif A. Haque, Thierry Lutz and James R. Durrant, *CHEM. COMMUN.*, 2002, 1464–1465.

[35] Emilio Palomares, John N. Clifford, Saif A. Haque, Thierry Lutz and James R. Durrant, *J. Am. Chem. Soc.* **2003**, 125, 475-482

[36] Zhang, D.; Ito, S.; Wada, Y.; Kitamura, T.; Yanagida, S.; *Chem.Lett.* **2001**, 1042-1043.

[37] Kambe, S.; Nakade, S.; Wada, Y.; Kitamura, T.; Yanagida, S.; *J. Mater. Chem*, **2002**, 723-728.

[38] Park, N. G.; Schlichthoerl, G.; Van De Lagemaat, J.; Cheong, H. M.; Mascarenhas, A.; Frank, A. J.; *J. Phys. Chem. B* **1999**, 103, 3308-3314.

As it will be shown in the results section, these different treatments of the photoanode will be performed (to optimize the performances of the studied dye sensitized solar cells) depending on the sensitizer or the electron transfer mediator that will be tested.

2.3 Electron transfer processes

2.3.1 Marcus Theory in homogeneous and heterogeneous electron transfer reaction.

The electron transfer reaction can be schematized as:

$$*A + B \longrightarrow A^+ + B^-$$

where an excited donor (*A) transfers an electron to an acceptor B becoming an oxidized species B^+ at the ground state.

The general equation expressing the rate constant of a reaction is the Eyring equation:

$$k_{et} = k\nu\exp\left(\frac{-\Delta G^*}{KT}\right) \qquad (2.8)$$

where ΔG^* is the activation energy of the process, K and T are the Boltzmann constant and the absolute temperature respectively, ν is the nuclear frequency factor and k is the transmission coefficient, a parameter which expresses the probability of the system to evolve from the reactant configuration to the product one once it has been reached the crossing of the potential energy curves along the reaction coordinate (Figure 18).

In case of electron transfer reaction it has been proposed a modification of (2.8) due to R. Marcus[39,40,41]:

$$k_{et} = k\nu\exp\left(\frac{-(\Delta G^0 + \lambda)^2}{4\lambda KT}\right) \qquad (2.9)$$

[39] R. A. Marcus, *Discuss.Faraday.Soc.* **1960**, *29*, 21.
[40] R. A. Marcus, *Annu.Rev.Phys.Chem.* **1964**, *15*, 155.
[41] T. J. Meyer, H. Taube, *Comprehensive Coordination Chemistry*, *Vol. 1*, Oxford,U.K., **1987**.

where the activation energy ΔG* is expressed as

$$\Delta G^{*} = \left(\frac{(\Delta G^{0} + \lambda)^{2}}{4\lambda} \right) \tag{2.10}$$

ΔG° is the free energy variation which accompanies the process, while λ is the total reorganizational energy and represents the vertical energy necessary to transform the nuclear configurations of the reactant and of the solvent to those of the product state (Figure 18). It is the sum of inner λ_i and outer λ_o components: λ_i is due to the vibrational rearrangement consequent to the electron transfer, while λ_o is comprehensive of the reorganization of the solvation sphere (repolarization).

Electron transfer reactions have been also treated from the quantum mechanical point of view in formal analogy to radiationless transitions, considering the weakly interacting states of a supermolecule AB: the probability (rate constant) of the electron transfer is given by a "golden rule" expression of the type[42]:

$$k_{et} = \frac{4\pi^{2}}{h} \left(H_{AB}^{el} \right)^{2} FCWD \tag{2.11}$$

Where H^{el}_{AB} is the electronic coupling factor between the two electronic states involved in the process and FCWD is the Franck-Condon factor (nuclear factor) weighted for the Boltzmann population of the energy levels. It can be shown that in the high temperature limit (when hν<kT for the relevant nuclear vibrational frequencies, an approximation not too inaccurate for many cases at room temperature) the nuclear factor takes the form:

$$FCWD = (1/4\pi\lambda kBT)^{1/2} \exp[-(\Delta G^{0} + \lambda)^{2}/4\lambda kBT] \tag{2.12}$$

The exponential term of Eq. (2.12) is the same as that predicted by the classical Marcus model, based on parabolic (free) energy curves for reactants and products such as those of Figure 18, where the activation free energy is that required to go from the equilibrium

[42] J. H. Alstrum Acevedo, M. K. Brennaman, T. J. Meyer, *Inorg.Chem.* **2005**, *44*, 6802.

geometry of the reactants to the crossing point of the curves. Both the classical and quantum results in equations (2.9) and (2.12) contain an important prediction, namely, that three typical kinetic regimes exist, depending on the driving force of the electron transfer reaction: (i) a "normal" regime for small driving forces ($-\lambda < \Delta G^0 < 0$) where the process is thermally activated and is favored by an increase in driving force; (ii) an "activationless" regime ($-\lambda = \Delta G^0$) where no gain in rate can be obtained by changing the driving force; (iii) an "inverted" regime for strongly exergonic reactions ($-\lambda > \Delta G^0$) where the process slows down with increasing driving force. Increasing λ slows down the process in the normal regime, but accelerates it in the inverted regime. The three kinetic regimes are schematically shown, in terms of classical Marcus' parabolas, in Figure 19.

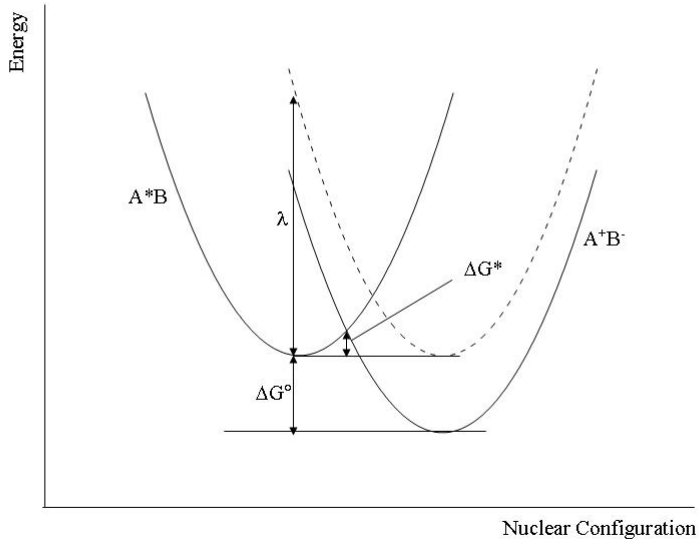

Figure 18. Free energy curves and kinetic parameters for an electron transfer process.

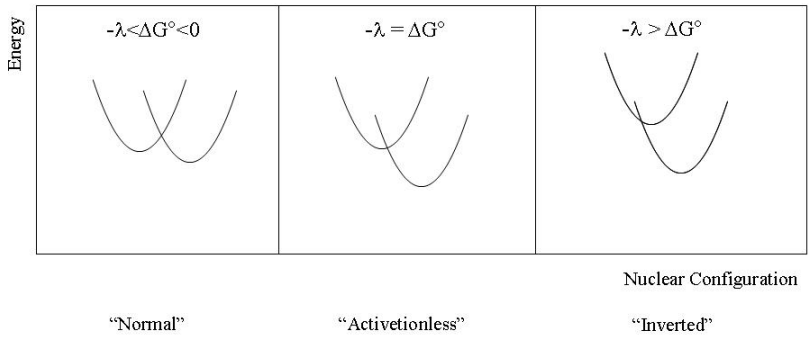

Figure 19. Free energy curves for reactant and product states of an electron transfer process in the energy ranges of the Marcus model.

The inverted region was initially predicted by Marcus and the decrease in the electron transfer rate constant with -ΔG° has been observed experimentally many times[43]. This is an important and remarkable result both for natural and artificial photosynthesis and energy conversion: it predicts that, following electron transfer quenching of the excited A*-B, the back electron transfer in the inverted region for the charge separated state A^+-B^- becomes slower as the energy stored increases.

The Marcus theory can be applied also to heterogeneous electron transfer, namely electrode reactions, in close analogy to homogeneous reactions[44]. The two main assumptions at the basis of this model are the following: 1) the electron transfer reaction, whether homogeneous or heterogeneous, is a radiationless transition occurring between isoenergetic states (the electron must move from an initial state on the electrode or in the reductant to a receiving state in the species O or on the electrode of the same energy) 2) reactants and products maintain their configurations during the actual act of charge transfer because the nuclear momenta and positions do not change on the time scale of electronic transitions: thus the reactant and the product share a common nuclear configuration at the moment of the transfer. These assumptions lead to an expression relating the heterogeneous electron transfer (reduction) rate constant, k_{et}, to the activation energy, $\Delta G^{\ddagger}$, of the type:

$$k_f = K\nu\kappa_{el}\exp(-\Delta G^{\mu}/RT) \qquad (2.13)$$

where K is a precursor equilibrium constant representing the ratio of the reactant concentration in a reactive position (precursor state) to the concentration in the bulk solution; for an heterogeneous electron transfer the precursor state can be considered to be a reactant molecule situated near the electrode at a distance where electron transfer is possible, thus, for a reduction reaction, $K = C_{o,surf}/C_{o,bulk}$ where $C_{o,surf}$ is the surface concentration of electron acceptor in mol/cm^2, ν is the nuclear frequency factor (s^{-1}) which represents the frequency of attempts on the energy barrier and k_{el} is the electronic transmission coefficient

[43] C. A. Bignozzi, S. Schoonover, F. Scandola, *Molecular Level Artificial Photosynthetic Materials, Vol. 44*, J.Wiley & Sons, New York, **1997**.
[44] A. J. Bard, L. R. Faulkner, *Electrochemical Methods: Fundamentals and Applications*, J.Wiley & Sons, INC., **2001**.

(related to the probability of electron tunnelling). The dimension of k_f appearing in eq. (2.13) is, as required, cm/s.

The act of electron transfer is usually considered as a tunnelling of the electron between states in the electrode and those in the reactant. Tunneling effects are included in the transmission coefficient κ_{el} which falls off exponentially with the distance according to :

$$\kappa_{el} = \kappa_{el}^{0} \exp(-\beta x) \tag{2.14}$$

where *x* is the distance over which the tunnelling occurs and β is a factor depending on the height of the energy barrier and on the nature of the intervening medium. κ_{el} depends on the electronic coupling between the reactant and the electrode: a strong coupling results in a splitting of the curves (Fig. 20.a) at the crossing, which results in an higher probability for the system to evolve from the reagent to the product configuration once it has reached the transition state. A situation where the system stays on the lower curve passing from reagent to product is called adiabatic (κ_{el}=1). If the splitting is small compared to kT, the system tends to reside on the original reactant configuration and is said to be non adiabatic ($\kappa_{el} < 1$).

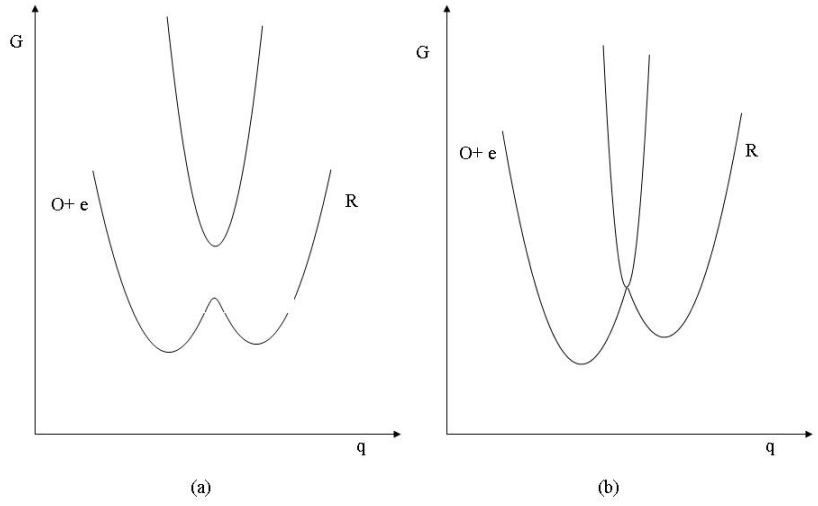

Figure 20. Splitting of energy curves for a reduction reaction. In (a) the strong coupling leads to a considerable splitting and to a continuous curve connecting the reactant and the products configurations, favouring the evolution of the system towards the product state. In (b) the small splitting favour the tendency of the system to remain in the reactant curve (O + e).

2.3.2 Photoinduced charge separation at the dye - semiconductor interface

The electron transfer from a sensitizer to the conduction band of a semiconductor give rise to an anodic current given from the equation (2.15):

$$i_{cb} = n_m F \int k_{et}(E) N_{CB} D_{red}(E) dE \qquad (2.15)$$

where n_m is the number of molecules present on the electrodic surface, F is the Faraday constant, k(E) is the electron transfer constant, N_{CB} is the number of empty states in the conduction band and finally D(E) is the dye's gaussian distribution of energy levels due to fluctuations of outer sphere reorganizational energy.

A factor of particular relevance in determining the magnitude of the anodic current is the electron transfer constant k_{et}. In case of sensitizers based on coordination compounds usually the absorption of a photon populates a singlet Metal-to-Ligand Charge Transfer state $(MLCT)^1$ from which charge injection to the CB or relaxation to the triplet $MLCT^3$ state can occur. $MLCT^3$ is also capable of charge injection to the semiconductor (Fig.21), however this process is in kinetic competition with other photophysical deactivation pathways, i.e. radiative and non radiative deactivation to the ground state. If the reagents and products curves cross each other in a point in which $\Delta G^0 = -\lambda$ the electron transfer will be determined only by the magnitute of the electronic coupling. It can be shown that if the electronic factor H_{el} is large the electron transfer is determined only by the nuclear frequency factor (adiabatic limit) according to equation (2.16):

$$k_{et} = \frac{KT}{h} \qquad (2.16)$$

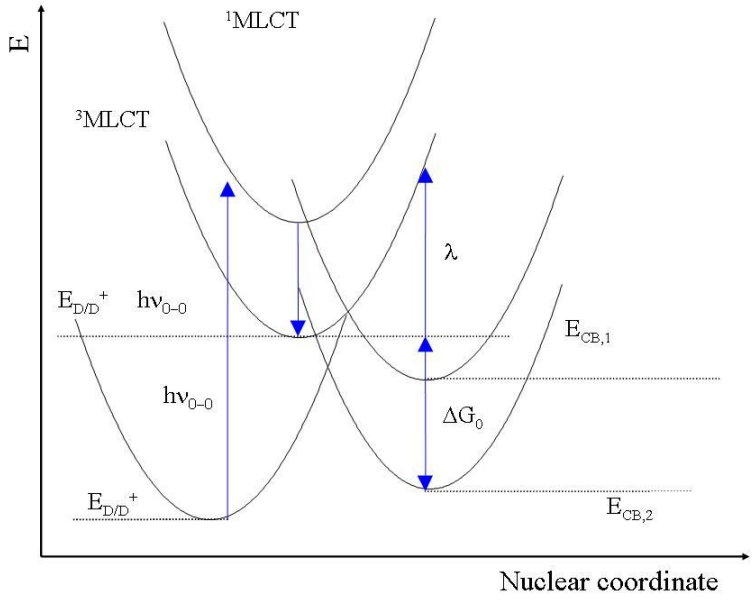

Figure 21 Electron transfer to from MLCT states of an excited sensitizer to the semiconductor.

In many cases the electron transfer is activationless because there is a continuum of electronic states in the conduction band accessible to the injected electron, which, combined with the different vibrational levels of the other reaction product, i.e. the oxidized dye, yields a moltitude of possible reaction pathways, so at least one channel is like to be without activation barrier and will be the preferred one for the reaction.

Some rate constants for electron transfer from excited dyes into TiO_2 have been determined by time resolved laser photolysis experiments. These rates vary over 8 orders of magnitude depending on the type of the dye employed. The fastest injection times are observed for dyes with a suitable anchoring group, such as carboxylate, phosphonate or cathecol moieties, through which the dye is firmly grafted on the surface of titania. The role of these groups is to provide a good overlap between the sensitizer's excited states and the acceptor levels, i.e. the 3d band of the semiconductor.

The carboxylate groups serve to attach the Ru complex to the surface of the oxide and to establish a good electronic coupling between the π^* orbital of the ligand, which is the lowest LUMO of the complex and the 3d orbital manifold of the TiO_2. Since the electronic transition is of MLCT character, optical excitation transfers the electron to a site from which electron injection to the semiconductor can readily occur. With molecule like these charge injections in the femto-second time domain have been reported (see reference 14) . On the

other hand the recombination between the injected electron and the oxidized dye is at least six orders of magnitude slower. The main reason for such behaviour arises from the fact that this process is usually characterized by a large driving force, frequently around 1.5 eV, and by a small reorganizational energy, of the order of few fractions of eV. This confines the recombination in the inverted Marcus region, reducing its rate by several orders of magnitude. In addition the electronic recapture involves a predominantly Ru centered d orbital whose electronic overlap with the TiO_2 conduction band is small. The spatial contraction of the wavefunction upon oxidation of Ru(II) to Ru(III) furtherly weakens the electronic coupling.

The presence of an electric field at the dye/semiconductor interface is also of relevance in determining the charge separation at the basis of the photovoltaic effect. While no band bending is supposed to be formed, due to the small size of the particles, a surface field is spontaneously created by proton transfer from the acid functions anchoring the dye, producing a surface dipole layer. If the semiconductor is placed in contact with a protic solvent the latter can also act as a proton donor. In aprotic media, like those commonly employed for DSSCs, Li^+ and Mg^{2+} are potential determining ions for TiO_2 and may be used to charge the surface positively. The local potential gradient from the sensitizer to the positively charged semiconductor drives the injected electron in the desired direction. The same field inhibits to some extent the electrons from exiting the solid after the injection has taken place

2.4 Sensitization of wide band-gap semiconductors.

2.4.1 Inorganic molecular sensitizers.

The main requirements a dye molecule should fulfill in order to be considered as a good candidate for spectral sensitization of semiconductors can be summarized by the following points:

a) Strong absorption across the entire visible spectrum (broad range of wavelength and high molar extinction coefficient);
b) Strong binding to the semiconductor surface (chemical group that can attach to the TiO_2 paste);
c) Energy levels at the proper positions (LUMO high enough in energy for efficient charge injection and HOMO low enough for efficient regeneration);

d) Rapid electron transfer to the TiO_2 in comparison to decay to the ground state of the dye;
e) Stability over many years of exposure to sunlight;
f) Low cost
g) Simple and reproducible synthesis and purification;
h) small reorganization energy for excited and ground state electron transfer to minimize energy losses.

The best solar to electric power conversion efficiency has been achieved (as previously mentioned) with polypyridyl complexes of Ru(II) bearing carboxylated ligands (see references 13 and 25). These species give rise to intense visible metal-to-ligand charge transfer (MLCT) bands. Among this family of compounds, outstanding results have been achieved with thiocyanate derivatives.

The energies of the MLCT states of these species can be varied systematically by changing the substituents at the chromophoric ligands (electron-withdrawing substituents tend to decrease the energy of the π^* orbitals of the polypyridine ligand, while the opposite effect is observed with electron donating substituents) as well as by changing the non-chromophoric ligands. For bis-chelate complexes of the type *cis*-$[Ru^{II}(bpy)_2(X)_2]$, MLCT absorption bands shift to higher energy changing X from π donating ligands to π accepting ligands. The main effect, in this case, is a direct perturbation of the electronic density at the metal center.

In particular, the performances of the NCS complex (named N3) in photoelectrochemical solar cells were found to be outstanding[45] . The complex showed a photoaction spectrum dominating almost the entire visible region, with IPCE of the order of 90% between 500-600 nm. Short-circuit photocurrents exceeding 17 mA/cm^2 in simulated A.M. 1.5 sunlight and open-circuit photovoltages of the order of 0.7 V, were obtained by using the couple I^-_3/I^- as redox electrolyte. For the first time a photoelectrochemical device was found to give an overall conversion efficiency of 10%. These performances are in part expected for the high reducing ability of the ^{3}MLCT state (ca. - 1 eV vs SCE) and the positive ground-state oxidation potential (+ 0. 85 eV vs SCE).

[45] P. Wang, C. Klein, R. Humphry-Baker, S. H. Zakeeruddin, M. Graetzel, *J.Am.Chem.Soc* **2005**, *127*, 808.

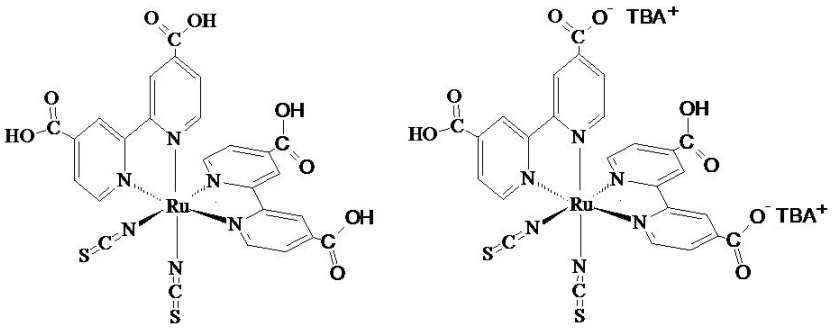

(a) **(b)**

Figure 22. Molecular structure of N3 (a) and N719 (b) sensitizers.

The development of general synthetic procedures for the preparation of molecular sensitizers is of major importance for practical applications as well as for fundamental studies, and several efforts have been made to accomplish this task. An example is offered by the step by step synthesis of tris-heteroleptic Ru(II) of the type $[Ru(dcbH)(dnbpy)(SCN)_2]$, (or Z-907) where the ligands ($dcbH_2$ = 4,4' dicarboxy-2,2'-bipyridine and dnbpy = 4,4'-dinonyl-2,2'-bipyridine) are introduced sequentially[46,47].

In Z907 (Figure 23) the substitution of one $dcbH_2$ ligand in the N3 molecule with a bpy substituted in the 4,4' positions with an amphiphilic group, leads to the following advantages: a) a higher pK_a value of the -COOH functions which results in a stronger binding to TiO_2, b) a reduced electrostatic repulsion between dye molecules due to the lower charge, which increases dye adsorption, c) a lower dye desorption in the presence of water thanks to hydrophobic interactions with the amphiphilic chains, d) a reversible oxidation of the metal with the relevant consequence of a better stability.

[46] S. M. Zakeeruddin, Md. K. Nazeeruddin, R. Humphry-Baker and M. Graetzel; *Inorg. Chem.* **1998**, 37, 5251-5259

[47] Peng Wang, Shaik M. Zakeeruddin, Jacques E. Moser, Mohammad K. Nazeeruddin, Takashi Sekiguchi and Michael Graetzel; *Nature materials*, Vol.2, June **2003**.

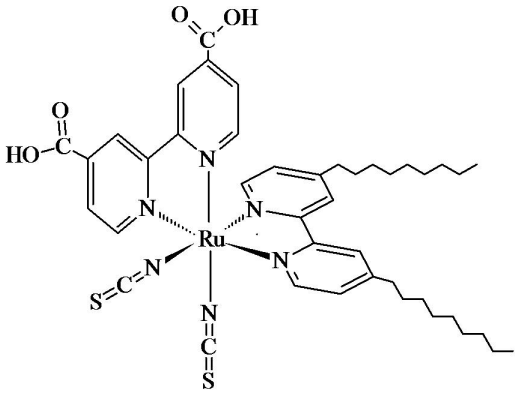

Figure 23. Molecular structure of Z907 sensitizer.

Trisbipyridyl Ru(II) complexes have also been used as sensitizers. In particular $Ru(dcbH)_3^{2+}$ and $Ru(dcbH)_2(dnbpy)$ which have a redox potential higher then N3 or Z907.

These sensitizers were designed to provide an adequate driving force for efficient Fe(II) oxidation by the Ru(III) centers in DSSCs where trisbipyridyl iron complexes were used as co-mediators. The introduction of the alkyl group in $Ru(dcbH)_2(dnbpy)$ has the function to limit the charge recombination with the oxidized mediator via the blocking effect of the long alkyl chains (Figure 24). More details of this field will be explained in the further sections (2.5.2).

In collaboration with Prof. (Dr) Philippe Gros, of Université Henri Poincaré of Nancy, other polipyridyl Ru(II) complexes have been studied; in particular the spectroscopical and spectroelectrochemical properties of Ru(II) polipyridiyl complexes bearing pyrrole and pyrrolidine moieties in 4,4' position to the bipyridine ring have been studied in order to evaluate their ability to work as sensitizers in photoelectrochemical solar cells with standard liquid electrolyte[48]. An important advantage of this kind of compounds is the availability of the pyrrole group for further polymerization and access to solid state device[49]. This kind of compounds, named as DM-s1 $[Ru(pyrrbpy)_2(dcbH)^{2+}]$, DM-s2 $[Ru(pyrr_2bpy)_2(dcbH)^{2+}]$, DM-s3 $[Ru(pyrrldbpy)_2(dcbH)^{2+}]$ and DM-s4 $[Ru(pyrrld_2bpy)_2(dcbH)^{2+}]$ are shown in Figures 25 and 26.

[48] David Martineau, Marc Beley, Philippe c. Gros, Silvia Cazzanti, Stefano Caramori and Carlo A. Bignozzi; *Inorg. Chem.* **2007**, 46, 2272-2277

[49] S. Caramori, S. Cazzanti, L. Marchini, R. Argazzi, C. A. Bignozzi, D. Martineau, P. C. Gros, M. Beley; *Inorganica Chimica Acta* 361 (**2008**) 627-634.

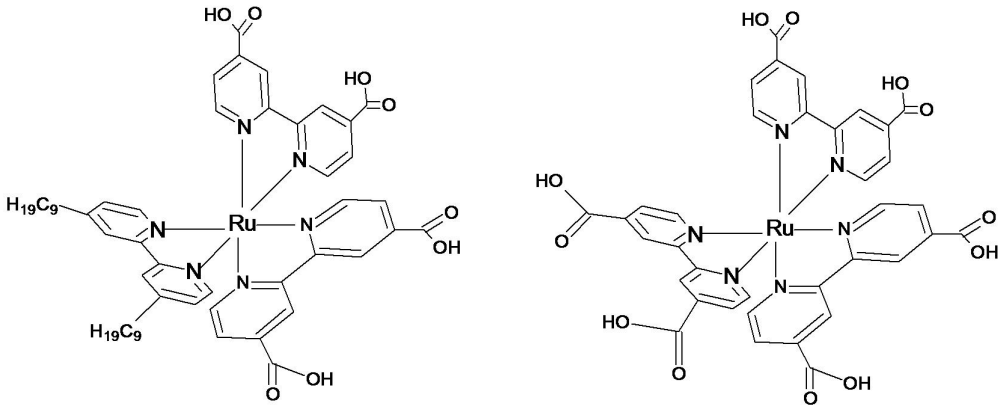

(a) (b)

Figure 24. Molecular structure $Ru(dcbH)_2(dnbpy)$ (a) and $Ru(dcbH)_3^{2+}$ (b) of sensitizers.

The electronic effect of the pyrrole and pyrrolidine containing ligands, due to the propensity of such electron-donor substituents to destabilize the HOMO metal orbital (π t_{2g}) more than the LUMO (π^*) orbital of the ligand, induces a lower gap between the 2 orbital energy level with respect of a standard $Ru(bpy)_3$, leading to a red shift of the metal-to-ligand charge transfer absorption. In this way it's possible to obtain a sensitizer both with an extended absorption domain and with a very positive ground state redox potential in order to have an efficient regeneration.

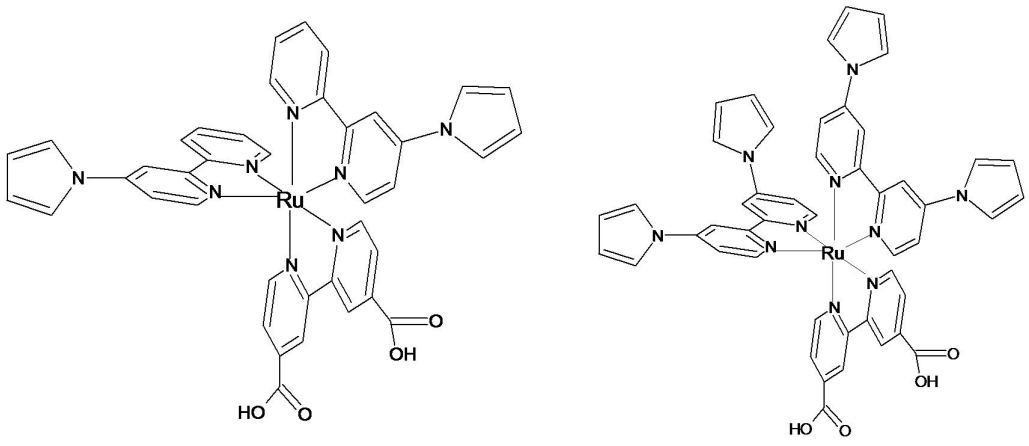

(a) (b)

Figure 25. Molecular structure of DM-s1 (a) and DM-s2 (b) sensitizers.

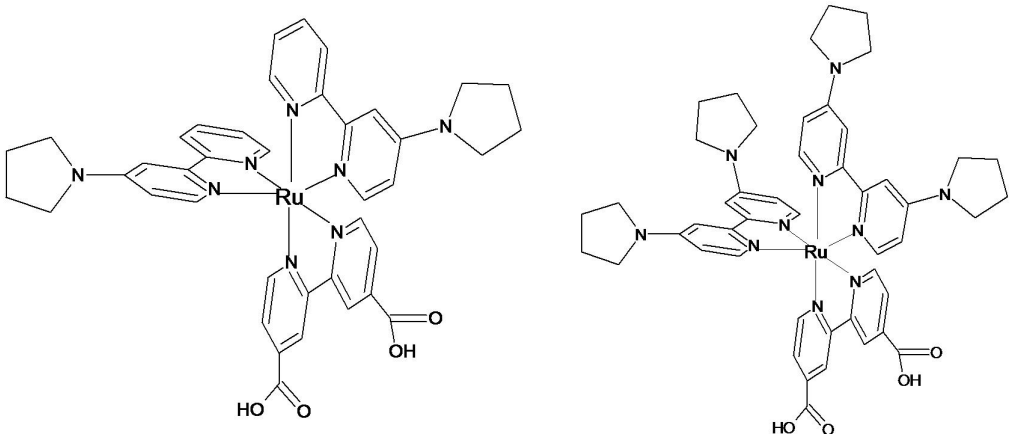

(a) (b)

Figure 26. Molecular structure of DM-s3 (a) and DM-s4 (b) sensitizers.

We also decided to investigate the effect of such ligands on the properties of trisheteroleptic Ru(L)(dcbpy)$(NCS)_2$ complexes, where L is a bipyridine ligand bearing a pyrrole or pyrrolidine function on 4,4' position (Figures 27 and 28).

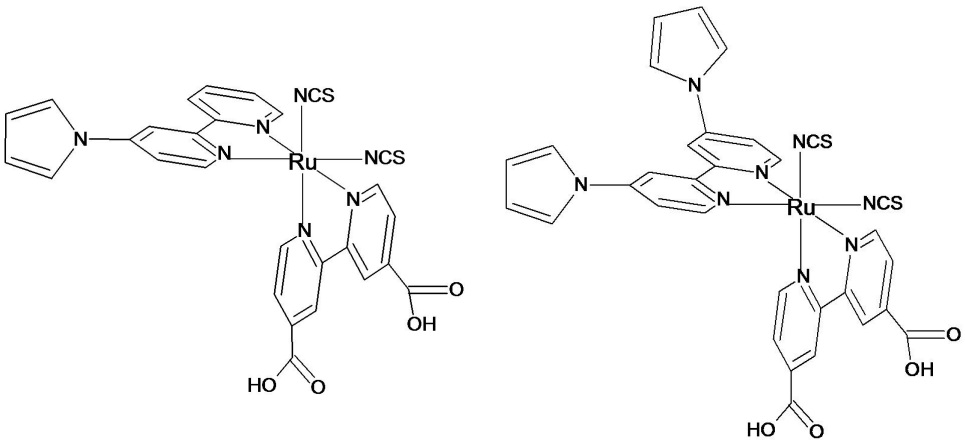

(a) (b)

Figure 27. Molecular structure of DM-d1 [Ru(pyrrbpy)(dcbH)$(NCS)_2$], (a) and DM-d2 [Ru($pyrr_2$bpy)(dcbH)$(NCS)_2$], (b) sensitizers.

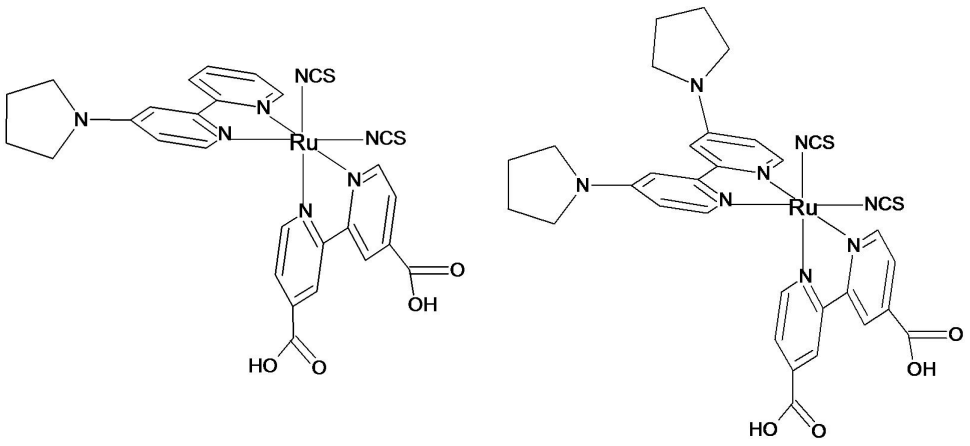

(a) (b)

Figure 28. Molecular structure of DM-d3 [Ru(pyrrldbpy)(dcbH)$(NCS)_2$], (a) and DM-d4 [Ru(pyrrld$_2$bpy)(dcbH)$(NCS)_2$], (b) of sensitizers.

Another trisheteroleptic dyes was synthesized by Philippe Gros and co-workers in order to evaluate the effect of charge delocalization on light absorption of the dye and the effect of the steric hindrance on the electron transfer reaction with the redox couple used as mediator (Figure 29)[50].

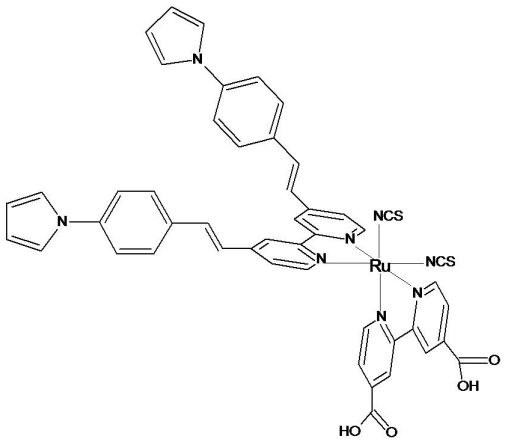

Figure 29. Molecular structure of Ag-78 sensitizer.

Bisterpyridyl Ru(II) complexes bearing thiophenic units in 10 position to the terpyridyl ring were also examined as sensitizers (Figure 30).

[50] A. Grabulosa, D. Martineau, M. Beley, P. C. Gros, S. Cazzanti, S. Caramori and C. A. Bignozzi, Dalton Transactions, (2008) DOI 10.1039/b000000x.

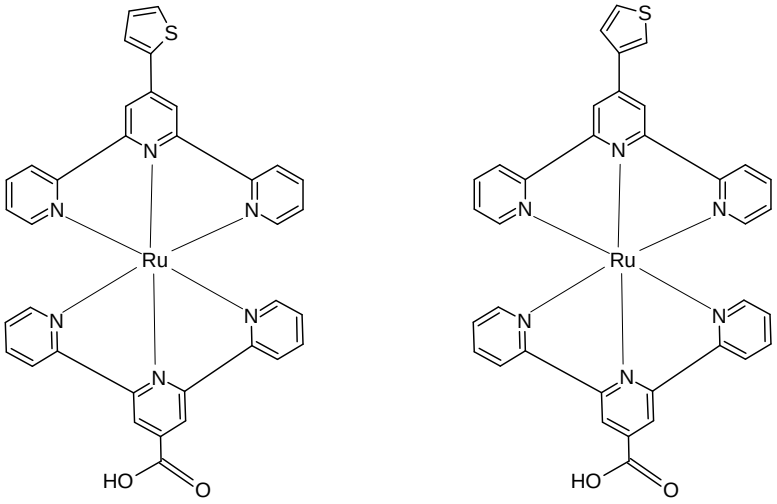

(a) (b)

Figure 30. Molecular structure of Fr-3 (a) and Fr-4 (b) sensitizers.

2.4.2 Natural dyes

In order to replace the rare and expensive Ru(II) compounds many kinds of organic synthetic dyes have been actively studied and tested as low-cost materials: chlorophyll derivatives[51], porphyrins[52], phtalocyanines[53], carboxylated derivatives of anthracene[54], coupled semiconductors with lower energy band-gaps, among others

In nature, some fruits, flowers and so on show various colour and contain several pigments that can be easily extracted and then employed in DSSCs. Therefore, unlike artificial dyes, the natural ones are available, easy to prepare, low in cost, non toxic, environmentally friendly and fully biodegradable. In most case, their photoactivity belongs to the anthocyanins family. The anthocyanins are water soluble flavonoids responsible for the red and blue colours of many fruits and leaves and may serve as photoprotective agents, antioxidants and osmotic regulatory. Moreover their absorption spectra have favourable overlap with the solar spectrum. Recently, Hara et al. make a remarkable advance in the use

[51] A. Kay, M. Graetzel, *J.Phys.Chem.* **1993**, *97*, 6272.
[52] F. Odobel, E. Blart, M. Lagree, M. Villieras, H. Boujtita, N. El Murr, S. Caramori, C. A. Bignozzi, *J.Mater.Chem.* **2003**, *13*, 502.
[53] M. K. Nazeeruddin, R. Humphry-Baker, M. Graetzel, D. Wohrle, G. Schnurpfeil, Schneider.A., N. Hirth, J. Trombach, *Porphyrins Phthalocyanines 3* **1999**, 230.
[54] P. V. Kamat, W. E. Ford, *Chem.Phys.Lett.* **1987**, *135*, 421.

of organic dyes for DSSCs[55]. Other groups have obtained good solar electric power conversion efficiencies, testing natural dyes as cheap and environmentally friendly alternatives to artificial sensitizers for DSSCs[56].

In collaboration with Dr. Giuseppe Calogero, of CNR of Messina, we have studied several natural extracts as molecular sensitizers for DSSC. These extracts contain several pigments and other additives, such as citric acid, and they have been directly employed for TiO_2 sensatization without any further purification.

The natural dyes we have employed for this purpose are extracted from red oranges, eggplants, red radicchio, Sicilian red wines, as Nero d'Avola and Giacchè, blueberry, mulberry and red turnip.

Most of them contain pigments that belongs to the anthocyanins family. Their general molecular structure is shown in Fig.31.

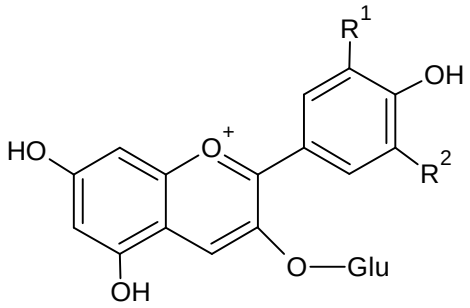

Figure 31 Chemical structure of anthocyanines.

Table I. Main pigments, that belong to the anthocyanins family, present in the natural extracts of eggplants, red radicchio, red wines and red orange juice.

	R^1	R^2
Cyanidine-3-glucoside	OH	H
Delphinidine-3-glucoside	OH	OH
Malvidine-3-glucoside	OCH_3	OCH_3

Red orange juice contains a high concentration of cyanidine 3-glucoside pigment, of citric acid and other antioxidants,such as delphinidine 3-glucoside, flavones (hesperedin and

[55] K. Hara, M. Kurashige, Y. Dan Ho, C. Kasada, A. Shippo, S. Suga, K. Sayama, H. Arakawa; *N. J. Chem.* 27 (**2003**) 783.
[56] Q. Dai, J. Rabani; *N. J. Chem*. 26 (**2002**) 421.

narirutin) and hidroxynamminic acids. The extracts from eggplants peels, rich in anthocyanins, contains nasunin, a mixture of cis-trans isomers of delphinidine 3-(p-coumaroylrutinoside)-5-glucoside.

The presence of other additives in the extracted, such as hidroxynamminic acids and citric acid, which act as co-adsorbers is responsible for a better sensitization of these solution on to titanium dioxide film. In fact these compounds, filling the free space between the dye molecules, partially block the physical contact between iodine solution and titanium dioxide semiconductor film surface reducing recombination reactions and inhibiting dye aggregation. Moreover, the presence of 2/3 hydroxyl groups in cyanidine and delphinidine pigments favoures the chelating effect towards titanium, inducing the attachment of Ti(IV) to the hydroxyphenol moiety where the LUMO electron density is located. Hence this leads to an efficient electron injection from the dye to the semiconductor film.

Delphinidine is the main pigment of the red radicchio too, while, in the extracts of the red wines, the most responsible pigment for their red-violet colour is the malvidine. The main drawback of this component is the presence of methylic groups on the phenolic ring. For this reason the phenolic groups is not able to chelate the titanium and most of the sensitization occurs from delphinidine which is the lowest components of these natural compounds.

The extracts of red turnips contain pigments that belong to the betalain family. They have been previously studied from Zhang et al. but efficiencies of the devices obtained using these natural pigments are very low[57]. Like anthocyanins, the betalains have favourable light absorbing and antioxidant properties , are capable of complexing metal ions, and exist in nature in association with various copigments which modify their light absorption properties. Betalains possess the requisite functional group (-COOH) to bind to TiO_2. While the absorption of anthocyanins to titanium dioxide depends on the presence of –OH groups, in betalains the attachment on to TiO_2 film is from carboxylic functions and this should lead to a stronger electronic coupling and rapid forward and reverse electron transfer reactions. The betalain pigment (Fig.32) comprise the red purple betacyanins, betanine and betanidine, and the yellow betaxanthine.

[57] D. Zhang, S. M. Lanier, J. A. Downing, J. L. Avent, J. Lum, J. L. McHale*; J.Photochem. Photobio*. A **2008**, 195, 72-80.

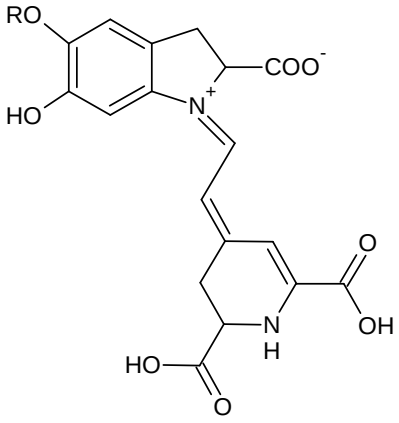

Figure 32 Chemical structure of betalains.

Table II. Substituents R in betanine and betanidine species.

	R
Betanine	β-D-glucose
Betanidine	H

The structure of indixanthine is shown in figure 33; it shows an absorption band at 480 nm.

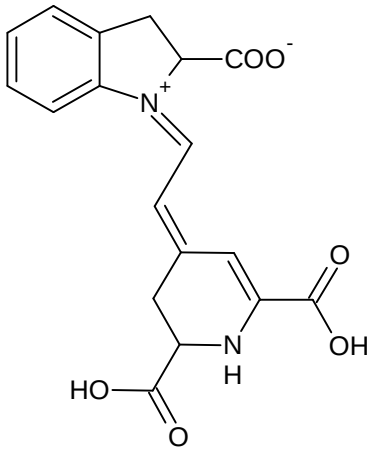

Figure 33 Chemical structure of indicaxanthin.

2.5 Electron transfer mediators

2.5.1 I^-/I_3^- as ideal electron transfer mediator for DSSCs

Following the initial charge separation, electrons and holes are confined in two different chemical phases: electrons in the nanocrystalline semiconductor and holes (oxidized redox species) in the electrolyte solution that permeates the solid phase. In the absence of a redox couple able to regenerate the photoxidized dye, interfacial recombination may result as a major energy loss mechanism. So far the iodide/iodine electrolytes have been the most efficient and commonly used redox mediators, due to the fact that I^- allows for a fast regeneration of the oxidized dye, intercepting it on a nanosecond time scale[58,59], whereas the reduction of I_2 and I_3^- is a complex multi-step reaction which involves the breaking of chemical bonds. Some authors[60,61] have studied it in great detail and suggested a first dissociation of I_3^- in I^- and I_2, a subsequent reduction of I_2 to I_2^- followed by the rate limiting dismutation of two I_2^- to give I^- and I_3^-. The same authors suggested that the reduction of I_2 occurs only with adsorbed I_2 molecules and the overall process is further slowed down by its relatively low concentration compared to I_3^- in solution.

In summary, the electronic recapture involving I_3^- is kinetically so slow on both TiO_2 and SnO_2 surfaces that, under short circuit conditions, most of electrons survive the transit through the mesoporous film and the SnO_2 surface and appear in the external circuit. Thus the I^-/I_3^- couple appears to have ideal kinetic properties which lead to an "asymmetric behaviour" at the basis of the efficient functioning of the DSSC: the forward electron donation by I^- is a facile monoelectronic process which ensures an efficient dye recovery (k_4 in Fig.11), while the reduction I_3^- appears to be largely inefficient allowing for a minimization of the interfacial back recombination (k_6 in Fig.11).

In other respects the I^-/I_3^- redox couple is less than ideal for a number of reasons: I_2 in equilibrium with I_3^- is volatile, complicating long term cell sealing; I_3^- is darkly colored and limits the light harvesting efficiency of the dye, DSSC cathodes require platinum coatings to effectively catalyze the I_3^- reduction. Most importantly, I^-/I_3^- is corrosive and will corrode

[58] T. A. Heimer, E. J. Heiweil, C. A. Bignozzi, G. J. Meyer, *J.Phys.Chem.A.* **2000**, *104*, 4256.
[59] I. Montanari, J. Nelson, J. R. Durrant, *J.Phys.Chem.B.* **2002**, *106*, 12203.
[60] G. Schlichthorl, S. Y. Huang, J. Sprague, A. J. Frank, *J.Phys.Chem.B.* **1997**, *101*, 8141.
[61] S. Y. Huang, G. Schlichthorl, A. J. Nozik, M. Graetzel, A. J. Frank, *J.Phys.Chem.B.* **1997**, *101*, 2576.

most metals, posing a serious problem for the scaling up of the solar cells to large areas. Indeed, the sheet resistance of the conductive glass is relatively high, leading to a serious ohmic loss in cells of area exceeding few square cm. A way to solve this problem is based on the deposition of metallic grids, acting as electron collectors, on the transparent oxide: a solution that cannot be reliably applied in DSCs as long as the iodide/iodine couple is used. Besides these practical problems the search for new electron transfer mediators potentially capable of replacing the iodide/iodine couple is attractive because the discovery of new efficient electron mediators may open the way to new strategies for changing, optimizing and improving DSSC design and performances. This type of research is challenging for a number of reasons related to the fact that an efficient electron mediator must simultaneously fulfill at least three relatively strict requirements: it has to intercept efficiently the oxidized form of the dye, recombine slowly with photoinjected electrons on both TiO_2 and SnO_2 substrates and allow for an efficient mass transport in solution and into the TiO_2 mesopores. As explained above, a sluggish electron recapture onto semiconductor oxide surfaces is believed to be crucial for the correct operation of the mediator.

2.5.2 New electron transfer mediators based on Co(II) or Cu(I) complexes as alternatives to I^-/I_3^- as redox couple in DSSC

The electrochemical properties of coordination compounds can be tuned through a rational choice of the metal and an appropriate design of the coordination sphere. These features might guarantee the necessary flexibility to project an electron transfer mediator capable of meeting the kinetic requirements at the basis of the functioning of the DSC. In principle, to minimize recombination kinetically slow couples have to be privileged. The relatively high concentration of electrolyte employed in photoelectrochemical cells (0.1 - 0.5 M in redox active species) requires the use of substantial amounts of electron mediators: as a consequence the choice and the design of the redox couple has to be done with consideration towards inexpensive and available metals like the elements of the first transition row and easily synthesizable ligands. To date, the most successful attempts have been based on octahedral cobalt(II)[62] complexes. The Co(II)/(III) couple is usually characterized by an high

[62] H. Nusbaumer, J. E. Moser, S. M. Zakeeruddin, M. K. Nazeeruddin and M. Graetzel; *J. Phys. Chem.* ***B*** **2001**, 105, 10461.

inner sphere reorganization energy associated to the electron transfer, essentially due to the involvement of a metal centred e_g redox orbital with antibonding characteristics.

It was found that particular cobalt polipyridine complexes formed from structurally simple ligands did function as efficient electron-transfer mediators in DSSCs[63]

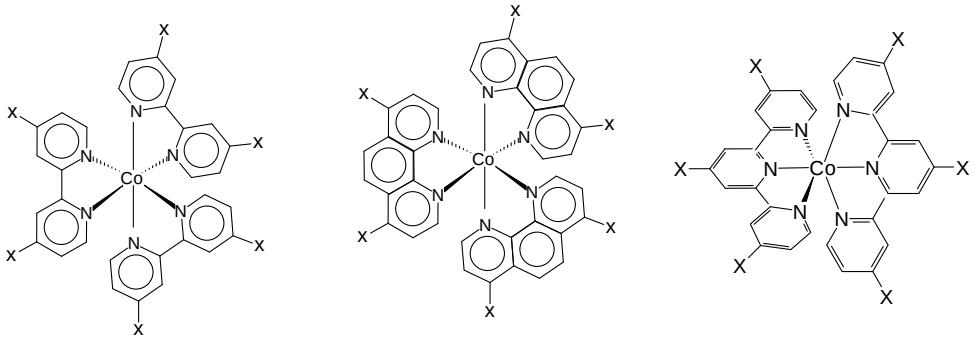

(a) (b) (c)

Figure 34. Structure of polypyridilic Co(II) complexes: (a) X = *tert*-butyl (DTB), Methyl (DMB), H (bpy). (b) X =H (phen). (c) X = *tert*-butyl (tTbterpy), Ethyl (tEterpy).

The cobalt complexes reported in Fig. 34 exhibit similar UV-Vis absorption spectra. Each of the Co(II) complexes has a weak absorption band centered at ca. 440-450 nm. The onset of the ligand-based π-π^* transition occurs in the UV above 350-380 nm for each of the ligands. The most intense visible absorption is for $Co(tTbterpy)_3^{2+}$ with $\varepsilon_{450}=1.4\ 10^3\ M^{-1}\ cm^{-1}$.

The remaining complexes all exhibit $\varepsilon_{440\text{-}450}$ values that are approximately an order of magnitude smaller. For the sake of comparison, the $\varepsilon_{440\text{-}450}$ value for I^-_3 is ca. $2\ \ 10^3\ M^{-1}\ cm^{-1}$; therefore, except $Co(tTbterpy)_3^{2+}$ that has a comparable absorbance, considerably less visible light is absorbed by all of the remaining cobalt complexes at similar concentrations.

Electrochemical characterization of these complexes revealed an unexpected electrode surface dependence to the electron-transfer kinetics. In the case of 4-4' substituted polypyridine Co(II) complexes, gold electrodes exhibit the most reversible and ideally shaped CVs. Glassy carbon and platinum electrodes also produce quasi-reversible voltammograms, although less reversible than gold. In general, the shapes of the quasi-reversible waves indicate that, in cases where the heterogeneous electron transfer is slow, the transfer coefficient, α, is considerably greater than 0.5. In other words, for equivalent overpotentials

[63] S. A. Sapp, C. M. Elliott, C. Contado, S. Caramori, C. A. Bignozzi, *J. Am. Chem. Soc.* **2002**, *124*, 11215.

the heterogeneous reduction of the Co(III) complex is considerably faster than the corresponding oxidation of the Co(II) species.

Recombination of injected electrons with the oxidized mediator can also be one of the primary loss mechanism in DSSC. The problem could be particularly serious in the case of Co(II)/(III) electron transfer mediators in which the outer sphere mono-electronic Co(III) reduction at the photoanode could be considerably more efficient than the multi-step I_3^- reduction. Through transient spectroscopy it's possible to compare the back electron transfer reaction between the substrate and the two different oxidized electron transfer mediators (I_3^- and $Co(DTB)^{3+}$) and it was verified that the CB electron interception in the case of triodide has a lower efficiency than Cobalt complex[64].

In the effort of improving the performance of such mediators the possibility of using kinetically fast couples in conjunction with the best Co(II) mediators has been explored[65]. Kinetically fast couples efficiently reduce the oxidized dye, but due to the fast recombination with injected electrons are totally unsuccessful as mediators in DSSC. However, when mixed with an excess of cobalt mediator, if their redox potential is appropriate (i.e. more positive than the Co(III)/(II) couple), a cascade of electron transfer events allows to confine the hole on Co(III) (Fig.35) which, by virtue of its very slow heterogeneous electron transfer on semiconductor oxides gives rise to a very inefficient electron recapture. As a consequence, the large majority of Co(III) created in the second electron transfer step is free to diffuse to the counter electrode of the cell, whereupon is reduced. The use of a long alkyl chain dyes like Z907, for example, is beneficial to the system allowing to further reduce back recombination enhancing the electron collection efficiency.

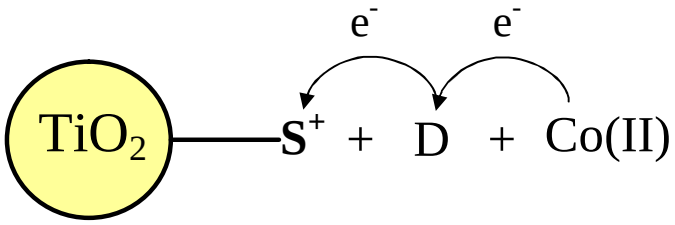

Figure 35 Sequence of electron transfer events involving the oxidized dye(S^+) the co-mediator(D) and the cobalt complex (Co(II)).

[64] For further details about electron transfer reactions of Co(II) complexes in DSSC see PhD thesis Hervè Nusbaumer, EPFL, 2004.METTERE TITOLO

[65] S. Cazzanti, S. Caramori, R. Argazzi, C. M. Elliott, C. A. Bignozzi, *J.Am.Chem.Soc.* **2006**, *128*, 9996.

Phenothiazine (PTZ) and ferrocene (Fc), both of which have a small reorganization energy associated to the electron transfer, are the first co-mediators that have been considered. Each has a potential which falls between 0.22 and 0.75 V vs SCE, respectively, the potential of the $Co(DTB)_3^{3+/2+}$ and of the dye $[Ru(DCB)(dnbpy)(NCS)_2]^{+/0}$. Because of the facile electron transfer the photoxidized dye would be predominantly reduced by the co-mediator. Its oxidized form (PTZ^+ and Fc^+) can be then rapidly intercepted by Co(II), preventing the direct charge recombination between the oxidized co-mediator and the electrons in the TiO_2.

An analogous behaviour extends to other species having small reorganization energies and appropriate potentials such as the iron(II) complexes $Fe(DMB)_3^{2+}$ and $Fe(DTB)_3^{2+}$ ($E_{1/2} \approx$ 0.95 V Vs SCE). When used in the presence of an excess of $Co(DTB)_3^{2+}$ and in conjunction with suitable sentizers like the heteroleptic dye $Ru(dnbpy)(DCB)_2^{2+}$ ($E_{1/2}$ = 1.25 V Vs SCE) the iron(II) co-mediators (Fig. 36) clearly enhance the performance of the $Co(DTB)_3^{2+}$ and outperform the I^-/I_3^- redox couple, at least in terms of monochromatic photon to current conversion efficiency, with maximum values close to 85%.

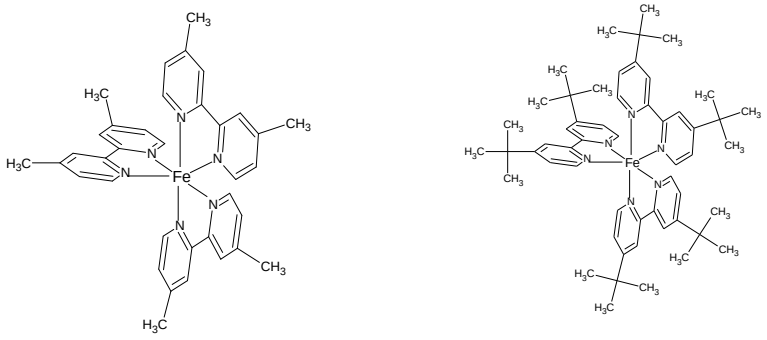

(a) (b)

Figure 36. Molecular structures of (a) $Fe(DMB)_3^{2+}$ where DMB is 4,4'-dimethyl-2,2'bipyridine and (b) $Fe(DTB)_3^{2+}$ where DtB is 4,4'-ditertbutyl-2,2'bipyridine.

Along with Cobalt complexes some interesting results have been obtained with copper (I) coordination compounds. According to the Franck Condon principle electron transfer does not occur until the reactant is vibrationally excited to match the geometry of the product complex: usually this can be accomplished by a simple adjustments of bond lengths, but for copper complexes such process requires a large energy because Cu(I) and Cu(II) have different preferred coordination geometries (tetrahedral and tetragonal, respectively)[66,67]. In

[66] D. B. Rorabacher, *Chem. Rev*. **2004**, *104*, 651.
[67] B. J. Hathaway, *Coord.Chem.Rev*. **1981**, *35*, 211.

nature electron transport systems based on blue copper proteins present optimized copper sites for a fast electron transfer, showing a distorted tetrahedral coordination geometry, intermediate between Cu(I) and Cu(II) geometries[68,69]. Blue copper model complexes[70] with a distorted tetrahedral geometry have been recently employed as efficient electron transfer mediators for DSSC. The assembly of solar cells based on copper complexes required TiO_2 optimization and multilayered photoanodes with a compact TiO_2 underlayer, necessary to suppress the back recombination from the exposed FTO contact.

Thus the use of copper complexes with a distorted tetragonal geometry, in which the structural change between Cu(I) and Cu(II) complexes is minimized, show promise for developing alternative low cost mediators for photoelectrochemical cells.

The electrochemical properties of another series of Cu(I) complexes, based on substituted bipyridine and quinoline derivatives, have been investigated[71] (Fig.37). To stabilize the Cu(I) oxidation state of Cu(I) polypyridine complexes, electron withdrawing substitutents like esters have been considered. The same effect was obtained also with pyridil-quinoline and biquinoline complexes, thanks to the increased π accepting properties of the quinoline condensed aromatic ring.

[68] E. T. Adman, *Adv.Protein Chem.* **1991**, *42*, 141.
[69] E. I. Solomon, M. D. Lowery, *Science* **1993**, *259*, 1575.
[70] S. Hattori, Y. Wada, S. Yanagida, S. Fukuzumi, *J.Am.Chem.Soc.* **2005**, *127*, 9648.
[71] M. Brugnati, S. Caramori, S. Cazzanti, L. Marchini, R. Argazzi, C. A. Bignozzi, *International Journal of Photoenergy* **2007**, *ID 80756*, 1.

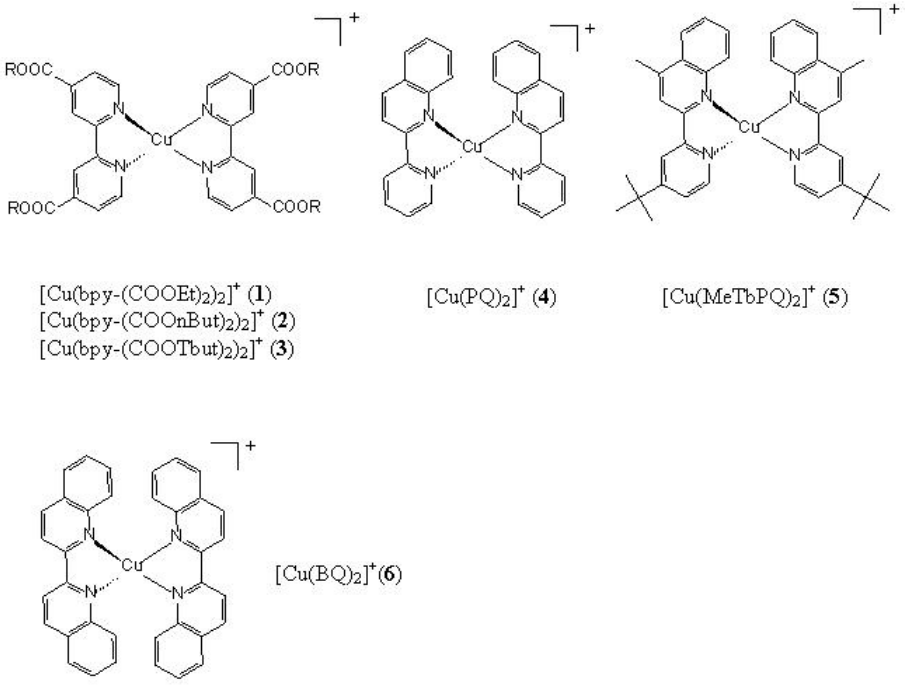

Figure 37. Structure of Cu(I) complexes employed as electron transfer mediators in photoelectrochemical cells.

Oxidation of a tetrahedral Cu(I) complex to Cu(II) involves the removal of an electron from a metal centred T_2 orbital with a prevailing antibonding character.

2.5.3 Towards solid state solar cells

In the most efficient dye-sensitized solar cell a porous nanocrystalline TiO_2 is in contact with a liquid electrolyte and, as already seen, the key processes take place at the interface between the nanostructured film and the liquid electrolyte. However the electrolyte may degrade over a period of time due to intrinsic chemical instability of the redox species, solvent evaporation or leaking caused by sealing imperfections. The search for suitable solid materials that can replace the liquid electrolyte is therefore an interesting and active area of research. In a solid state DSSC the solid hole conducting material captures the holes (the positive charges left on the dye as a result of the photo-induced charge injection in the n-type material) and closes the circuit with the counter electrode. Solid hole conductors include conducting polymers, organic hole conductors and inorganic semiconductors.

Conductive polymers based on polythiophenes and polypyrroles could be interesting candidates for replacing the liquid electrolyte in DSSC, due to their low cost, thermal stability

and good conductivity[72]. Thanks to these properties, these systems have already found application in the OLED technology as charge transporting matrices. PEDOP (poly-ethylene-dioxy-pyrrole) can be deposited on a sensitized TiO_2 photoanode via a photoassisted electropolymerization (see reference 50) initiated by the purpose built ruthenium complex $[Ru(dcbH)(pyrr\text{-}bpy)_2]^{2+}$ (see reference 49) (Fig.38): the oxidized dye, $[Ru^{III}(dcbH)(pyrr\text{-}bpy)_2]^{3+}$, created after the charge injection into TiO_2, is a sufficiently strong oxidizer, with a potential of 1.19 V/SCE, to oxidize EDOP monomers and induce their cationic polymerization, leading to the growth of polymeric chains chemically attached to the dye with a possible advantage in term of electronic coupling and charge transfer rate between electron donor (PEDOP) and acceptor (oxidized dye).

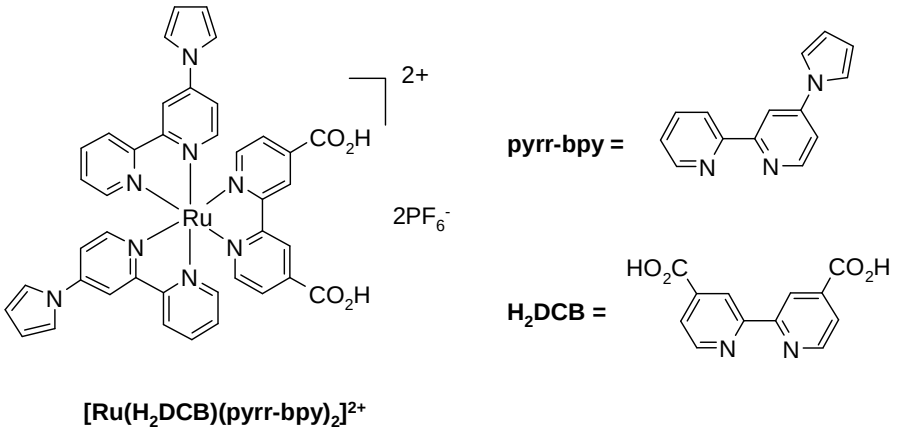

Figure 38 Ru(II) complex uses for in situ photo-assisted PEDOP growth.

[72] K. R. Murakoshi, R. Y. Kogure, Y. Wada, S. Yanagida, *Sol.Energy Mater.Sol.Cells* **1998**, *55*, 113.

Chapter 3

Experimental techniques and procedures.

3.1 Electrochemical methods.

Various electrochemical techniques have been employed to extract useful informations from the molecules object of this study. Usually electrochemical methods are of fundamental importance in evaluating the potential of a redox couple, the kinetics of the heterogeneous electron transfer and the reversibility of the electrodic processes. Useful information about the diffusion coefficient of an electroactive specie can also be obtained from a variety of controlled potential experiments. Figure 39 is a picture of the basic experimental system. A *potentiostat* has control of the voltage across the working electrode-counter electrode pair, and adjusts this voltage to maintain the potential difference between the working and the reference electrodes (through a high impedence feed back loop) in accord with the program defined by a function generator.

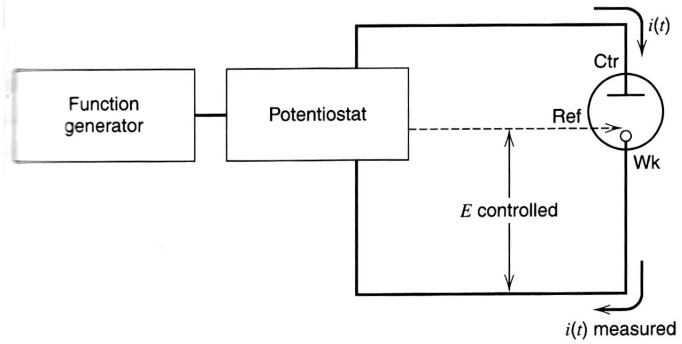

Figure 39 Experimental arrangement for controlled potential experiments.

3.1.1 Chronoamperometry

The usual observable in controlled potential experiments are currents as functions of time and potential. If the potential is stepped to the mass transfer controlled region, the concentration of the electroactive specie is nearly zero at the electrode surface and the current is totally controlled by the mass transfer. Regardless if the kinetics of the electrodic process are basically facile or sluggish, they can be activated by a sufficiently high potential (unless the solvent or the supporting electrolyte are oxidized or reduced first). This condition will hold at any more extreme potential.

Considering a planar electrode (e.g. a Pt disk) and an unstirred solution it can be shown that the current - time response is given by:

$$i_d = \frac{nFAD^{\frac{1}{2}}C^*}{\pi^{1/2}t^{1/2}} \qquad (3.1)$$

which is known as the Cottrell equation [73]. Its validity was verified in detail by Kolthoff and Laitinen[74,75], who measured and controlled all parameters (number of exchanged electrons, electrodic area, diffusion coefficient and bulk concentration of the electroactive specie). Thus the diffusional current is linear with respect to the inverse of $t^{1/2}$. From the slope it is possible, for example, to calculate D, knowing all the other experimental parameters. In practical measurements under Cottrell conditions one must be aware of different instrumental and experimental limitations: equation (3.1) predicts large currents at short times, but the actual maximum current may depend on the current-voltage output of the potentiostat. In addition during the initial part of the current transient, the recording device may be overdriven and some time may be required for recovery. A non faradic current which decays with a constant time given by R_uC_d , where R_u is the cell uncompensated resistance and C_d is the double layer capacitance, also flows during a potential step. So for a period of about 5 time constants an appreciable contribution of the charging current to the total measured current exists. Figure 40 is an example of the waveform used for a potential step experiment and of the resulting current-time response.

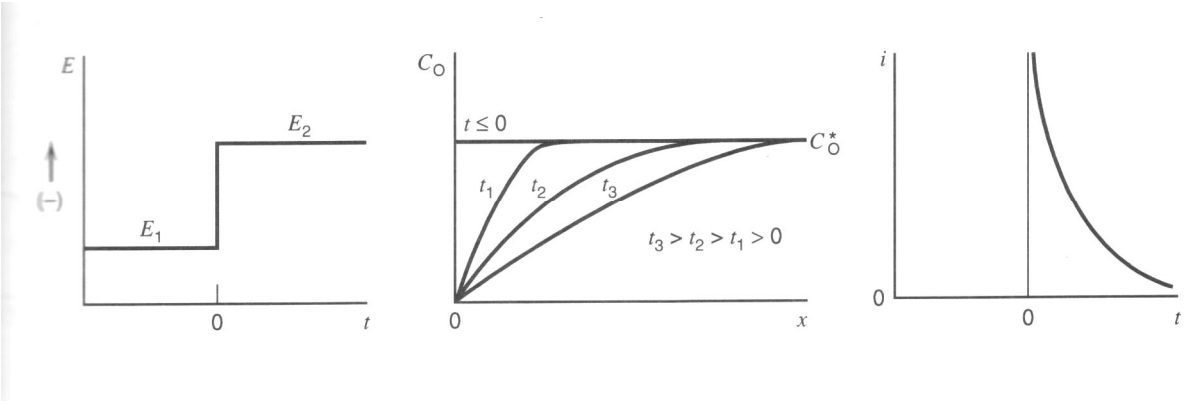

(a) (b) (c)

Figure 40 (a) waveform for a step experiment in which the electroactive specie is electroinactive at E_1 but is reduced at the diffusion limited rate at E_2. (b) Concentration profiles for various times of the experiment. (c) Current flow vs.time.

[73] F. G. Cottrell *Z. Physik. Chem* **1902**, *42*, 385
[74] Laitinen, H. A.; Kolthoff, I. M. *J.Am.Chem.Soc* **1939**, *61*, 3344.
[75] Laitinen, H. A.; Kolthoff, I. M. *Trans.Electrochem.Soc.* **1942**, *82*, 289.

3.1.2 Steady state voltammetry

In conception sampled current voltammogramms involve the recording of an i(τ)-E curve by application of a series of steps to different final potentials E. The current is then sampled at a fixed time τ after the step, then i(τ) is plotted vs E. Usually the initial potential is chosen to be to a constant value where no faradic process occur. For example, as depicted in figure 41 at potential 1 there is no faradic current, while at potential 2 and 3 the faradic process occurs but not so effectively that the surface concentration of the electroactive specie is zero. At potentials 4 and 5 we obtain the same current determined by the mass transport of the redox specie from the bulk of the solution to the electrodic surface. Actually in the common practice one does not even need to apply steps. It is satisfactory to change the potential linearly with time and to record the current continuously, as long as the rate of change is small compared to the rate of adjustment of the steady state.

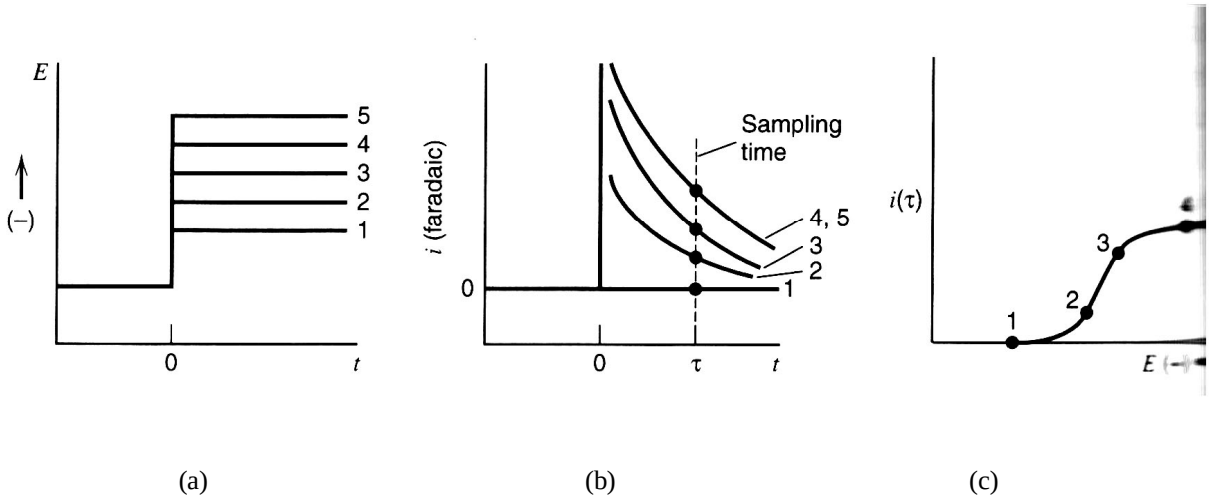

(a) (b) (c)

Figure 41. Sampled current voltammetry: (a) Step waveforms applied in a series of experiments. (b) current time curves observed in response to the steps. (c) Sampled current voltammogramm.

The shape of the voltammogram obtained for a reversible system in sampled current voltammetry is described by the following equations:

$$E = E^{0'} + \frac{RT}{nF}\ln\frac{D_R^{1/2}}{D_O^{1/2}} + \frac{RT}{nF}\ln\frac{i_d - i}{i} \qquad (3.2)$$

When $i = i_d/2$ the current ratio becomes unity so that the third term vanishes. The potential for which it is so is $E_{1/2}$ and it is called the *half wave potential*.

$$E_{1/2} = E^{0'} + \frac{RT}{nF} \ln \frac{D_R^{1/2}}{D_O^{1/2}} \tag{3.3}$$

Usually (3.2) is often written as:

$$E = E_{1/2} + \frac{RT}{nF} \ln \frac{i_d - i}{i} \tag{3.4}$$

As shown in figure 42 these relations predict a wave that rises from baseline to the diffusion controlled limit in a fairly narrow potential region (about 200 mV) centred on $E_{1/2}$. Since the ratio of diffusion coefficients in (3.3) is nearly unit in almost any case, $E_{1/2}$ is usually a very good approximation to $E^{0'}$ for a reversible couple.

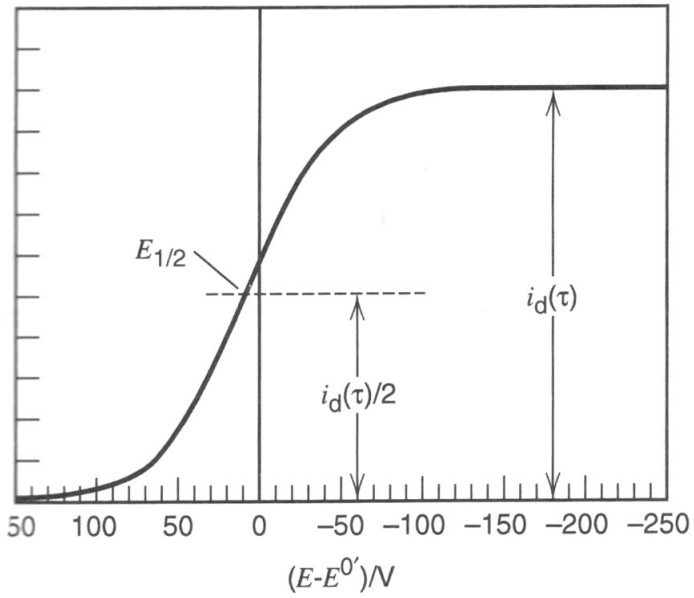

Figure 42. Characteristics of a reversible wave in sampled current voltammetry.

For a reversible system the wave slope from (3.4) should be about 60/n mV. Larger slopes are generally found for systems that do not have both nernstian heterogeneous kinetics and overall chemical reversibility; thus the slope can be used to diagnose reversibility. In addition, for a simple one step O + n(e) → R reaction, from the steady state voltammogram, one can obtain current-overpotentials values useful for determining the exchange current

density, according to the low field approximation of the Butler and Volmer equation[76]. It is in fact possible to show that the current is linearly related to overpotential in a narrow potential region in the immediate proximity of the equilibrium potential. In contrast with reversible cases just examined, in quasi-reversible cases the electron transfer kinetics of the system are not so fast to instantaneously adjust to the new electrodic potential, in other words the concentration of the oxidized and reduced species at the electrodic surface cannot be satisfactory described by the Nernst equation at that determined potential. Kinetic parameters like the electron transfer rate constants and the transfer coefficients influence the response to potential steps and can often be evaluated from those responses. Usually working curves[77] or computer programs are used to simulate these curves and to obtain the parameters of interest.

3.1.3 Cyclic voltammetry

Cyclic voltammetry has become a very popular technique for initial electrochemical studies of new systems and has proven very useful for obtaining informations about fairly complicated electrodic reactions. A typical linear sweep voltammetry for a system like anthracene is shown in figure 43. If the scan is begun at a potential well positive of $E^{0'}$ only capacitive current flows until in the vicinity of the $E^{0'}$ the reduction begins and the faradic current starts to flow. As the electrode potential continues to grow more negative the current increases until the surface concentration of the electroactive specie drops nearly to zero, the mass transfer of anthracene to the surface reaches a maximum rate and then it declines as the depletion effect sets in. The observation is therefore a peaked current – potential curve like that depicted.

[76] A. J. Bard; L. R. Faulkner *Electrochemical Methods, Fundamentals and Applications*; 2nd ed.; John Wiley and Sons, INC: New York, 2001, pages 114-115.
[77] A. J. Bard; L. R. Faulkner *Electrochemical Methods, Fundamentals and Applications*; 2nd ed.; John Wiley and Sons, INC: New York, 2001, pages 193-197.

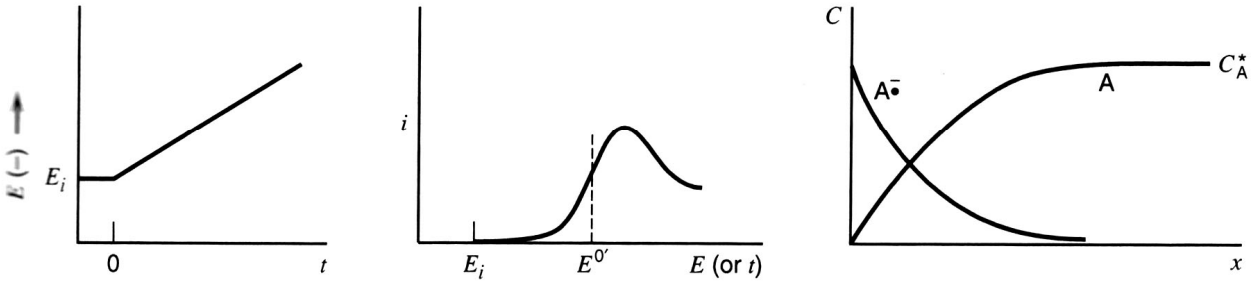

(a) (b) (c)

Figure 43 (a) Linear potential sweep starting at E_i. (b) Resulting i-E curve. (c) Concentration profiles of the oxidized and reduced species.

If at some point we reverse the potential scan, we approach and then pass $E^{0'}$ sweeping in a positive direction and consequently the radical anion that has been generated during the forward scan, present in large concentration in the vicinity of the electrode becomes reoxidized and an anodic current flows. This reversal current has a shape much like that of the forward peak for essentially the same reasons (Figure 44).

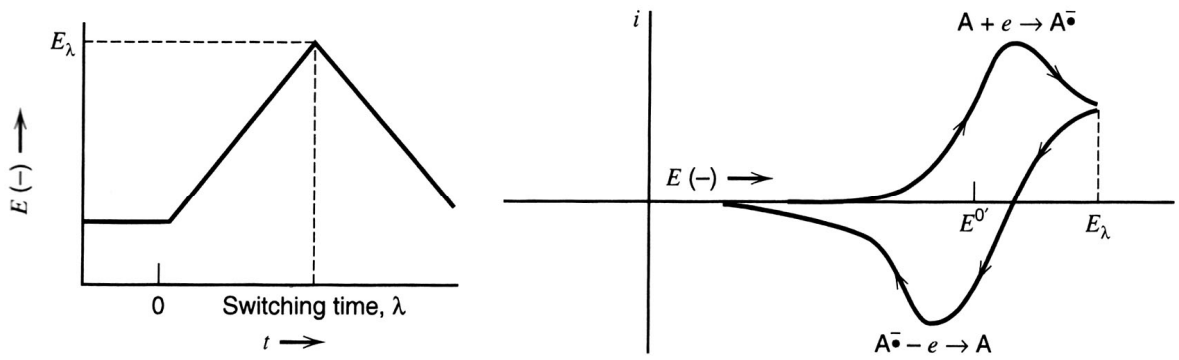

(a) (b)

Figure 44. (a) Cyclic potential sweep. (b) resulting cyclic voltammogram

Parameters of interest obtainable from cyclic voltammogramms are obviously the half wave potential, which is related to $E^{0'}$ by a relationship previously described (3.3) and can be easily calculated form the average of anodic and cathodic peak potentials, the peak separation and the peak current. In case of an ideally Nernstian electrochemical process the peak separation should be of the order of 60/n mV, in addition the half wave potential and the peak separation should be independent from the scan rate. Deviations from this behaviour are

usually determined by sluggish electron transfer kinetics of the system under study or to other kinetic complications. In case of a diffusion-limited electrodic process the peak current should be linearly related to the square root of the scan speed according to equation (3.5):

$$I_p = (2.69\ 10^5)\ n^{3/2}\ AD^{1/2}Cv^{1/2} \qquad (3.5)$$

For a Nernstian wave with a stable product the ratio between the anodic and cathodic peak should be unitary, regardless of the scan rate and diffusion coefficient. Deviations from unity are indicative of coupled homogeneous chemical reactions or complications in the electrodic process. If the electrochemical response is given by a specie adsorbed on the surface of the electrode the peak current is proportional to the scan speed, providing a powerful tool to discriminate between electrochemical processes originated by species diffusing to the electrodic surface from the solution or, on the contrary, directly adsorbed on the electrode. In case of quasi reversible couples the peak separation is a function of v, k_0 and α. It has been developed a method (often called the *method of Nicholson*)[78] useful for estimating the electron transfer constant k_0 based on the determination of the peak separations at various scan speeds, from which it is possible, with the aid of proper working curves and tables, to calculate the heterogeneous rate constant . Even if this method is simple and widely used it must be pointed out that in some cases uncompensated resistance can give effects on peak separation that are similar to those due to kinetic limitations of the system. The effect of uncompensated resistance is particularly critical when the current is large and when k_0 approaches the reversible limit, so that ΔE_p differs only slightly from the reversible value.

3.1.4 Differential pulse voltammetry

Differential pulse voltammetry is mainly used to reach better sensitivities than potential sweep and normal pulse techniques. The main advantage of DPV is the large

[78] Nicholson, S. R. *Anal.Chem.* **1965**, *37*, 1351.

supression of the non faradic current. Figure 45 depicts the potential program usually employed for differential pulse experiments.

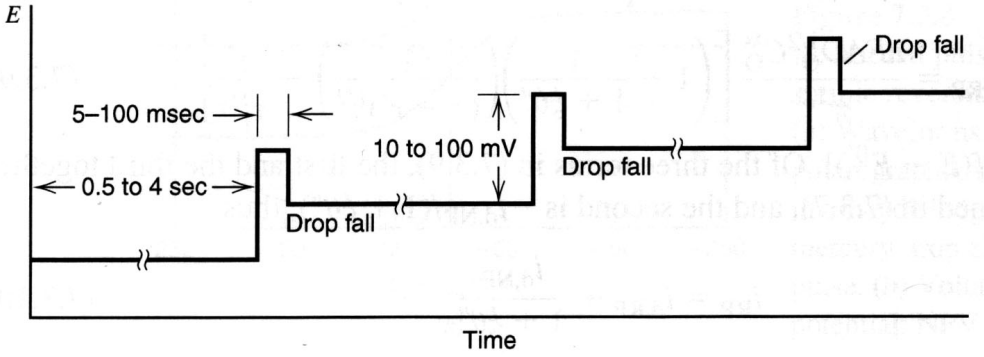

Figure 45. Potential program for a differential pulse polarographic experiment.

The figure refers to a specific case of differential pulse polarography, but the waveform and the measurement strategy are general for the method in its broader sense. It is applicable to every solid state electrode. The base potential is changed steadily in small increments to a final value. Potential pulses of small height (10-100 mV) are superimposed to the base potential. Two current samples are taken during each pulse lifetime, one at τ' immediatly before the pulse and the second at τ late in the pulse, just before it ends. The record of the experiment is a plot of the current difference ($\delta i = i(\tau) - i(\tau')$) versus the base potential. The differential measurement gives a peaked output (Figure 46). The reason is easily understood qualitatively: when the base potential is too small to activate the electron transfer no faradic current flows before the pulse and the change in potential manifested in the pulse is too small to stimulate the faradic process, thus $\delta i = i(\tau) - i(\tau')$ is virtually 0, at least for the faradic component. Late in the experiment when the base potential is in the diffusion-limited-current region the electroactive specie reacts at the maximum rate possible and the pulse cannot increase the current further; hence δi is again small. Only in the region near $E^{0'}$ there is an appreciable faradic current observed, infact only in potential regions where a small potential difference can make a sizeable difference in current flow does the differential pulse technique show a response.

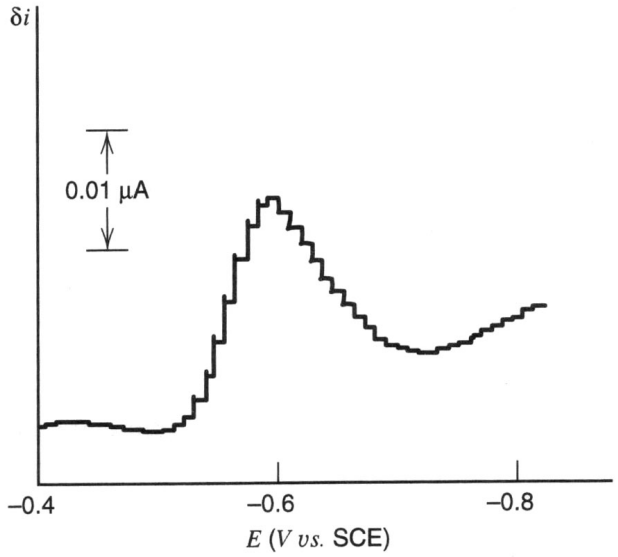

Figure 46. Differential Pulse Voltammetry for 10^{-6} M Cd^{2+} in 0.01 M HCl.

For a reversible case it can be shown[79] that:

$$E_{MAX} = E_{1/2} - \Delta E /2 \qquad (3.6)$$

Where E_{MAX} is the peak potential and ΔE is the pulse height. Since ΔE is small, the potential of maximum current lies close to $E_{1/2}$.

3.2 Solar Cell Assembly

3.2.1 Mesoporous oxide paste preparation.

The colloidal TiO_2 paste involves the controlled hydrolysis of Ti(IV) isopropoxide followed by peptization in acidic water to produce a sol, a colloidal liquid. Autoclaving these sols (heating at 200-250 C° for 12 h) allows the controlled growth of the primary particles and improves their crystallinity. During the hydrothermal growth smaller particles dissolve and fuse together to form larger particles by a process known as *Ostwald ripening*. The resulting TiO_2 particles consist of Anatase or of a mixture of Anatase and Rutile. The Sol-Gel process is ideal for the preparation of mesoporous semiconductor oxides: it is simple and

[79] A.J.Bard; L.R.Faulkner *Electrochemical Methods, Fundamentals and Applications*; 2 nd ed.; John Wiley and Sons, INC: New York, 2001, pages 289-290.

requires common laboratory instrumentations, the starting materials are not needed at a particularly high purity level and are commonly available at low cost.

A typical preparation involves the slow addition of 50 ml of Ti(IV) Tetraisopropoxide to 300 ml of deionized water acidified with 2.1 ml of concentrated HNO_3. The formation of a white TiO_2 precipitate is immediatly observed. The resulting mixture is heated at 80 C° for 8 hours during which the peptization of the precipitate and the formation of a colloidal suspension occurs. The suspension is allowed to concentrate to about 100 ml corresponding to a TiO_2 concentration of about 150 g/l. The average diameter of colloidal nanoparticles is estimated to be 5-8 nm. The colloidal sol is autoclaved at 220 C° for 12 h. During this process the hydrothermal growth of the nanoparticles occurs and a white colloidal paste is obtained. 3-3.5 g of Carbowax, a polymer that acts both as a tensioactive and as a binder, are then added to the paste and the mixture is stirred at room temperature for 6-8 hours, after that the colloid is ready for deposition on the TCO substrate.

3.2.2 Photoanodes preparation.

The transparent conductive oxide (TCO) of choice for realizing DSSCs is an highly fluorine doped SnO_2 film (FTO-Fluorine–Tin-Oxide) deposited on glass. The average surface conductivity of the conductive glasses used in this work is about 10 Ω/sq. SnO_2:F allows an effective light transmission while providing good conductivity for current collection, in addition it establishes a good mechanical and electrical contact with the dye sensitized oxide in order to obtain a satisfactory electronic percolation from the semiconductor to the electron collector. The conductive glass is covered on two parallel edges with 3M adhesive tape (ca 20 μ thick) to control the thickness of the TiO_2 film. The colloid is applied to one edge of the conducting glass and distributed with a glass rod sliding over the tape-covered edges. After air drying, the electrodes are heated in an oven at 450°C for 30 min in the presence of air. The resulting film thickness is of the order of 6-7 μm. A solution c.a 10^{-4} M of a proper sensitizer dissolved in an appropriate solvent is used to carry out sensitization of the photoanodes. Usually the dye adsorption is conducted at reflux for 3-5 hours. Experimental details about the dye adsorption conditions are reported in Chapters 4, 5 and 6.

3.2.3 Counter electrodes.

Different kinds of counter electrodes were used: platinum coated counter electrodes, gold coated electrodes and carbon coated electrodes. Platinum metal clusters were deposited on FTO electrodes by spraying a $5*10^{-3}$ M solution of hexachloroplatinic acid in isopropanol. The procedure is repeated 5-7 times until an homogeneous distribution of hexachloroplatinic acid clusters on the surface is observed. The resulting surfaces are then dried in air for 5 minutes and cured at 380 C° in an oven for 15 minutes, during which the pyrolisis of the hexachloroplatinic acid occurs and metallic Pt clusters are formed. This procedure creates transparent counter electrodes. Reflective Pt coated glasses were obtained by Pt sputtering. Gold covered electrodes were obtained by thermal evaporation. Usually, due to the poor stability of the Au deposit on FTO, a chromium underlayer few nanometers thick was previously deposited by thermal evaporation or controlled electrolysis on the conductive glasses, and subsequently the deposition of a gold layer 20-30 nm thick on chromium was performed. Carbon coated electrodes were obtained by spraying the surfaces 5 –6 times with Areodag G (Achelson) graphite spray. The carbon deposit produced in this way was very fragile, and fragmentation of the coated surface was commonly observed after a single use of this kind of counter electrode.

3.2.4 Cell Assembly.

Two kinds of cells were prepared: open cells and closed cells. Open cells are made by simply pressing together the photoanode and the counter electrode and blocking the glasses together with small metal clamps. The electrolyte was allowed to fill the gap between the sensitized semiconductor and the counter electrode by capillarity. In many cases a suitable parafilm® spacer inserted between the electrodes allows to confine the electrolytic solution inside the cell for longer times, leading to a more stable cell configuration required for prolonged experiments. This kind of cells are also called “thick” cells because there is a thicker layer of electrolyte between the photoanode and the cathode. Closed cells are cells sealed by melting a thermoplastic polymer (Surlyn®, 400 nm thick) inserted between the

anode and the counter electrode that, on cooling, firmly binds the two electrodes to each other. The electrolyte was injected through a small hole with a pump that created vacuum in the cell. The hole was then sealed with ephoxy resin. The closed cell configuration is required for stability tests of DSSCs when it is necessary to confine the electrolytic solution inside the cell for very long periods, even months. Solar cells without spacer are built by directly pressing the TiO_2 photoanode over the counterelectrode; the mediator solution is later introduced by capillarity inside the cell, obtaining a liquid layer of substantially reduced thickness compared to the previous case. This cell configuration is less stable than the former. In both cases metallic clamps are used to hold firmly the two electrodes together.

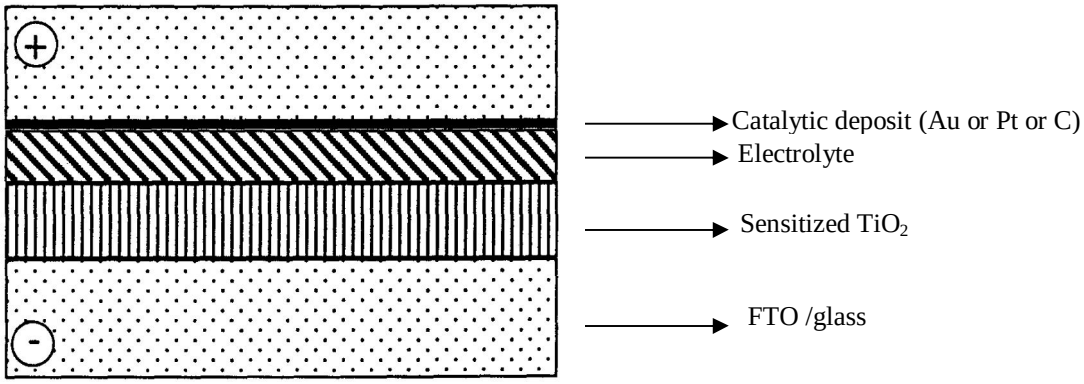

Figure 47 Schematic view of a sandwich Dye Sensitized Solar Cell.

The electrolyte preparation will be described in detail in Chapter 4.

3.3 DSSCs Characterization

The performance of the cell can be quantified on a macroscopic level with parameters such as Incident Photon to Current Efficiency (IPCE), open circuit photovoltage (V_{oc}), and the overall efficiency of the photovoltaic cell, η_{cell}.

The parameter that directly measures how efficiently incident photons are converted to electrons is the IPCE. The wavelength dependent IPCE term can be expressed as a product of the quantum yield for charge injection (Φ), the efficiency of collecting electrons in the external circuit (η) and the fraction of radiant power absorbed by the material or light harvesting efficiency (LHE), as represented by Equation 3.7:

$$IPCE = (\Phi_{inj})(\eta)(LHE) \quad (3.7)$$

While Φ and η can be rationalized on the basis of kinetic parameters, LHE depends on the active surface area of the semiconductor and the cross section for light absorption of the molecular sensitizer. In practice the IPCE measurements are performed with monochromatic light and $IPCE_{(\lambda)}$ values are calculated according to Equation 3.8.

$$IPCE_{(\lambda)} = 1.24 \cdot 10^3\ (eV \cdot nm) \cdot I_{sc}\ (\mu A \cdot cm^{-2}) / \lambda(nm)\ I\ (mW \cdot cm^{-2}) \quad (3.8)$$

In Equation 3.8, I_{sc} is the photocurrent density produced by the cell, λ the excitation wavelength and I the incident photon flux.

The light harvesting efficiency, or absorption factor, is related to the dye molar extinction coefficient ($\varepsilon(\lambda), L \cdot mol^{-1} \cdot cm^{-1}$) and to the surface coverage ($\Gamma, mol \cdot cm^{-2}$) by Equation 3.9.

$$LHE_{(\lambda)} = 1 - 10^{-[1000\varepsilon(\lambda)\Gamma]} \quad (3.9)$$

An absorption factor above unity is ideal for a solar energy device as almost all the incident radiant power is collected.

In the absence of photodecomposition reactions, the quantum yield for electron injection from the excited sensitizer to the semiconductor is given by Equation 3.10.

$$\phi_{inj} = \frac{k_{inj}}{\sum k_d + k_{inj}} \quad (3.10)$$

where k_{inj} is the rate constant for electron injection and $\sum k_d$ is the sum of all rate constants for the excited state deactivation processes. Charge injection from the excited dye will be activated if the donor energy is positive with respect to the conduction band edge (E_{CB}). Electron injection will be, on the contrary, activationless if the donor level has energy equal to or more negative than the conduction band edge. This condition is met when $E_{(S+/S^*)} + \lambda > E_{cb,}$ where $E_{(S+/S^*)}$ represents the excited state oxidation potential of the sensitizer

(which is related to the ground state oxidation potential and to the spectroscopic energy by: $E_{(S+/S^*)} = E_{(S+/S)} - E_{oo}$) and λ represents the reorganization energy accompanying the charge injection process.

The fraction of injected charges which percolate through the TiO_2 membrane and reach the back contact of the photoanode is represented by the factor η. It has been shown that the electron diffusion length (L_n), which is a key parameter for charge collection, given by $L_n = \sqrt{D_0 \tau_0}$ (D_0 and τ_0 are the diffusion coefficient and lifetime of electrons in conduction bands), is of the order of 20-100 μm for the liquid electrolyte based DSSCs, allowing thus to use relatively thick photoanodes for optimizing the light harvesting efficiency of the solar device. It is accepted that electron diffusion occurs with an ambipolar mechanism, which involves simultaneous motion of electrons and electrolyte cations. Although the diffusion coefficient of cations in the nanoporous network are normally small, high concentrations of cations, intercalated between the semiconductor nanoparticles, support a fast transport of the electrons as minority carriers, as shown by electron-density-dependent diffusion coefficients when high-ion-concentration electrolytes are used.

Moreover J-V curves under white light are useful to determine the quality of the cell as source of power and necessary to determine the global photovoltaic performance of the system. The general current-voltage characteristic of a solar cell may be approximated by the diode equation[80] :

$$I = I_{ph} - I_S\left(\left(e^{\frac{V_a}{V_t}} - 1\right) - \frac{V_a}{R_{sh}}\right) \qquad (3.11)$$

Where I is the current, I_s is the saturation current of the diode , I_{ph} is the photocurrent which is assumed to be independent by the applied voltage V_a. R_{sh} is the shunt resistance of the circuit and is introduced to take into account the internal resistance and energy dissipation mechanisms of the cell.

V_t is the thermal voltage given by $V_t = \frac{nkT}{e}$.

Equation 3.11 can be obtained from the circuit represented in figure 48 which shows the equivalent circuit of the cell. Obviously it is only a simplified model of the DSSC which is

[80] Nusbaumer, H. In *Alternative Redox Systems for Dye Sensitized Solar Cell*; EPFL: Lausanne, 2004; pp 42-46.

actually thought to correspond to a multidiode model to take into account the different mechanisms of charge transport within the cell.

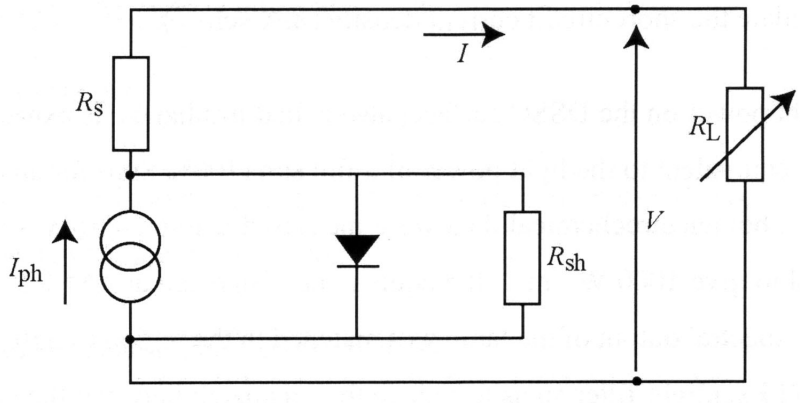

Figure 48. The DSSC under irradiation can be expressed as a non perfect current generator mounted in parallel to a non perfect diode.

Figure 49 shows a typical i-V response of a solar cell with the power curve in the lower part. There will be a couple of current and voltage values whose product gives the maximum power output of the cell. The dots represent the maximum power output.

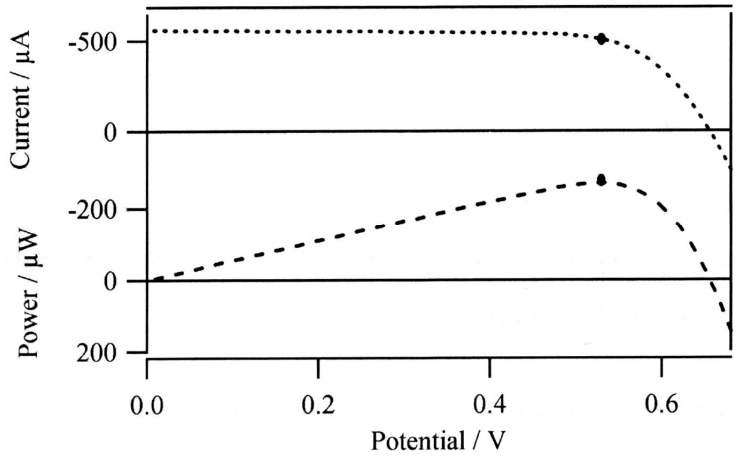

Figure 49 i-V curve showing the variations in photocurrent and power as a function of the potential.

The short circuit current I_{sc} is the cell photocurent measured at zero voltage, when the series resistance R_s is minimal. Therefore V_a =0 and $I_{sc}=I_{ph}$. J_{sc} is simply the short circuit current divided by the active area of the cell. The open circuit photovoltage V_{OC} is the cell potential measured when the current within the cell is equal to zero. V_{OC} can be obtained from (3.11) by setting I =0 and $V_a=V_{OC}$. Under these conditions:

$$V_{OC} \cong V_t \ln\left(\frac{I_{ph}}{I_S}\right) \tag{3.12}$$

Obviuosly both I_{sc} and V_{OC} are functions, through I_{ph}, of the irradiance.

Experimentally i-V curves are collected by imposition of an external potential in opposition to the cell, sweeping it from zero to the V_{OC} value of the cell under illumination, and recording the current as a function of the external potential. When the applied potential is zero, the cell is in short circuit conditions, while when the external potential matches the open circuit potential the current drops to zero.

The fill factor (FF) measures the cell's quality as a power source and is therefore the ratio between the maximum power and the external short circuit current and open circuit voltage.

$$FF = \frac{I_M V_M}{I_{SC} V_{OC}} \tag{3.13}$$

This parameter indicates the deflection of the curve from a square like curve, and is always minor than unity.

The efficiency η describes the performance of the solar cell and is defined as the ratio of the maximum electric power generated by the cell to the incident radiation power on the solar cell surface:

$$\eta = \frac{I_{SC} V_{OC} FF}{P_{in}} \tag{3.14}$$

As the efficiency is a function of I_{SC},V_{OC} and FF, improvement of the photovoltaic yield is achieved by optimization of these three parameters.

3.4 Laser Flash Photolysis.

Electron transfer dynamics at the Semiconductor/Dye/electrolyte interface were studied mainly by time resolved absorbance measurement. Following the excitation pulse, a population of excited dye molecules able to inject charge into the semiconductor is created. The electron injection is much faster (fs-ps) than the time resolution of the technique employed (ns) , so that a population of oxidized dye molecules is instantaneously created. The

decay of the oxidized dye absorption recorded in various conditions gives information about the efficiency of charge transfer from the electron mediator and about the dynamics of electron recapture. Laser Flash Photolysis (LFP) was also used to determine the excited state lifetime in solution of several sensitizers studied in this thesis work.

3.4.1 Experimental apparatus.

The transient absorption apparatus is schematized in figure 50:

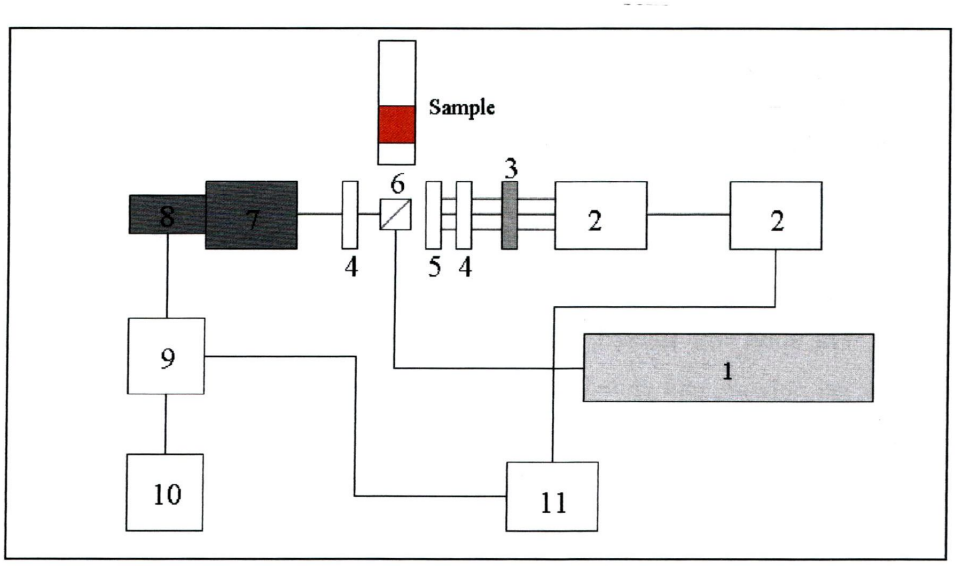

Figure 50. Laser Flash Photolysis apparatus: 1) Surelyte II Nd:YAG Laser 2)Xe Lamp-Trigger 3) Shutter 4) Filter 5) Diaphragm 6) Sample 7) Monochromator 8) Photomultiplier 9) Oscilloscope 10) Computer 11) Switch.

The excitation source is a solid state Nd-Yag laser equipped with Q-switch and frequency multipliers in order to obtain 532, 355 and 266 nm excitation wavelengths with a pulse amplitude at half width of about 7 ns. A continuous 150 Xe lamp generates the analysis light which is oriented at 90° with respect to the excitation beam. A computer controlled external trigger sinchronizes all the components of the apparatus. Time resolved absorption studies were carried out using the 532 nm excitation, attenuating the pulse energy by means of a $KMnO_4$ filter to the value of 0.25 mJ/pulse. The sample, a solid sensitized TiO_2 film sintered on a microscope slide was oriented at 45° with respect to the excitation pulse. An interferential filter placed in front of the monochromator provided the elimination of the intense 532 nm light scattering. The oxidized dye recovery was observed at different wavelengths according to the different sensitizer specie. Satisfactory signal to noise ratio

were usually obtained by averaging 20/30 shots. In these conditions the transient absorption decays approached quite satisfactory a mono-exponential behaviour, in particular in presence of electron mediators. At higher pulse intensities a multiexponential behaviour gradually appeared, probably due to an increase in recombination rate determined by a larger electronic concentration in the semiconductor and by intraband states population.

3.4.2 Transient Absorption.

Before the laser pulse (time zero) only dye molecules at the ground state, whose concentration and extinction coeffcient are respectively $[A_0]$ and ε_A, are present in the sample. After excitation a population of oxidized dye is created, with a certain concentration $[A]^+_t$ and extinction coefficient $\varepsilon_A{}^+$. For these reasons the absorption of the analysis light at a particular wavelength λ will be different before and after the laser pulse. The laser induced absorption variation is subjected to a temporal evolution according to the time evolution of oxidized sensitizer population. The oscilloscope detects a time dependent tension which is proportional to the light intensity transmitted through the sample.

Before the excitation the optical density of the sample is given by:

$$\log \frac{I_0}{I_t} = \varepsilon_A [A_0] l = OD \tag{3.15}$$

where I_0 and I_t are the light intensities transmitted at time 0 and t and l is optical path.

After excitation:

$$\log \frac{I_0}{I_t^+} = \varepsilon_A [A]_t l + \varepsilon_{A^+} [A]_t{}^+ l = OD^+ \tag{3.16}$$

where $[A]_t = [A]_0 - [A]_t^+$

The resulting difference in optical density, detected by the oscilloscope will be given by:

$$\Delta OD = \log \frac{I_0}{I_t} - \log \frac{I_0}{I_t^+} = (\varepsilon_A{}^+ - \varepsilon_A)[A]_t^+ \tag{3.17}$$

Usually the absorption coefficient of the oxidized dye (Ru(III)) is smaller than the absorption coefficient of Ru(II) (at least in large part of the visible region) thus ΔOD assumes negative values (bleaching). The considerations reported here are obviously of general validity and can be extended to every case in which the generation and the evolution of a

population of chemical species with different absorption properties with respect to their initial state is monitored spectroscopically. In many cases the excited state absorption can be stronger than the ground state, in this case ΔOD will be positive.

3.4.3 Transient Emission.

The same apparatus depicted in figure 50 also works for collecting transient emission. Obviously the lamp and the other equipment for absorption is not necessary and not used. Emission from the excited sample is collected at 90°. Assuming an instantaneous formation of the excited state, the laser flash produces a concentration of an excited chemical specie $[A]_0^*$ which deactivates by emitting radiation of certain frequencies. The intensity of emitted light is proportional to the excited state concentration. In the simplest case the emission of radiation is described by a first order process.

$A^* \longrightarrow A + h\nu$

$$-\frac{d[A]^*}{dt} = \frac{1}{\tau}[A]^* \tag{3.18}$$

Whose integration gives

$$[A]^* = [A]_0^* \exp(-t/\tau) \tag{3.19}$$

Also

$$I(\lambda) = I_0(\lambda)e^{\frac{-t}{\tau}} \tag{3.20}$$

Thus the emission profile is mono-exponential and its time constant, obtained by linearization of (3.20) or direct fitting of the decay gives directly the lifetime of the excited specie.

Chapter 4

Electron Transfer mediators for DSSC.

4.1 Electron Transfer Mediators based on polipyridyl Co(II) complexes.

4.1.1 Electrochemistry and Photoelectrochemistry of Co(II) complexes.

4.1.2 Electron transfer mediators mixtures: introduction of a kinetically fast redox couple in conjunction with $Co(DTB)_3^{2+}$.

4.1.3 Mass transport limitations using Co(II) compounds as mediators.

4.1.4 Effect of an Al_2O_3 overlayer on Co(II) complexes mediated DSSCs.

4.2 Electron Transfer Mediators based on Cu(I) metal complexes.

4.2.1 Experimental section.

4.2.1.1 Materials.
4.2.1.2 Analytical measurements.
4.2.1.3 Photoanodes preparation.
4.2.1.4 Counter electrodes preparation.
4.2.1.5 Solar cell assembly.
4.2.1.6 Thin layer electrochemical cell.

4.2.2 Synthesis of ligands and related Cu(I) complexes.

4.2.2.1 Ligands preparation.
4.2.2.2 Cu(I) complexes synthesis.

4.2.3 Electrochemical characterization.

4.2.4 Photoelectrochemical characterization in Z-907 Sensitized Solar Cells.

4.2.5 Electrochemical behaviour of $Cu(MeTbPQ)_2^+$ and $Cu(bpy\text{-}(COOEt)_2)_2$ on TiO_2 surface.

4.2.6 Photoelectrochemical characterization under monochromatic conditions of Z-907 SSC using $Cu(MeTbPQ)_2^+$ and $Cu(bpy\text{-}(COOEt)_2)_2$ as electron transfer mediators.

4.2.7 Evaluation of the heterogeneous electron transfer processes at gold counter electrode of $Cu(MeTbPQ)_2^+$ and $Cu(bpy\text{-}(COOEt)_2)_2$.

4.2.8 Conclusion.

4.1 Electron transfer mediators based on polipyridyl Co(II) complexes.

4.1.1 Electrochemistry and Photoelectrochemistry of Co(II) complexes.

DSSCs convert sunlight to electricity by a different mechanism than conventional p-n junction solar cell. Light is absorbed directly at the solid/liquid interface by a monolayer of adsorbed dye and initial charge separation occurs without the need of exciton transport [81,82].

Following the initial charge separation, electrons and holes are confined in two different chemical phases: electrons in the nanocrystalline semiconductor and holes (oxidized redox species) in the electrolyte solution that permeates the solid phase. According to the widely accepted kinetic model, electron transport to the charge collector occurs by diffusion in an electric field-free regime (ref. 81). No electric field is created, essentially due to the fact that the sintered TiO_2 nanoparticles are too small and too lightly doped to support a significant space charge, and also due to a screening effect by the surrounding electrolytic solution. It is a chemical potential gradient that drives the electrons to the back contact, while the opposite electrical potential gradient, developed between the photoinjected electrons and the positive charges (either oxidized dye or oxidized electrolyte species) is screened by the electrolyte (according to some authors, without this effect, in the absence of band bending, most of photoinjected electrons would never be able to escape form their image charge and recombine before reaching the electron collector)[83]. Anyway, to contribute to the photocurrent the photoinjected electrons must diffuse through hundreds of nanoparticles in close proximity to the oxidized redox species (electron acceptors) in solution and, in the absence of an electrostatic barrier, interfacial recombination may result as a major energy loss mechanism.

As alternative to the commonly used Iodide/Iodine redox couple, whose drawbacks have been previously mentioned (chapter 2.5.1), it was found that particular cobalt polipyridine complexes formed from structurally simple ligands did function as efficient electron-transfer mediators in DSSCs[84]. The main focus of the investigation was thus to

[81] B. A. Gregg, *Coord.Chem.Rev.* **2004**, *248*, 1215
[82] B. A. Gregg, F. Pichot, S. Ferrere, C. R. Fields, *J.Phys.Chem.B* **2001**, *105*, 1422.
[83] F. Pichot, B. A. Gregg, *J.Phys.Chem.B.* **2000**, *104*, 6.
[84] S. A. Sapp, C. M. Elliott, C. Contado, S. Caramori, C. A. Bignozzi, *Journal of the American Chemical Society* **2002**, *124*, 11215.

identify which structural and thermodynamic motifs generate the best mediators allowing for the assembly of cells with the closest match to the performance of the I/I_3^- mediator.

The cobalt complexes reported in figure 51 can be easily produced by mixing 1 equivalent of $[Co(H_2O)_6]^{2+}$ with 3 equivalents of a bidentate ligand or 2 equivalents of a tridentate ligand under magnetic stirring in refluxing methanol for 2 h. Addition of ethyl ether results in the precipitation and isolation the product which is then usually used without any further purification.

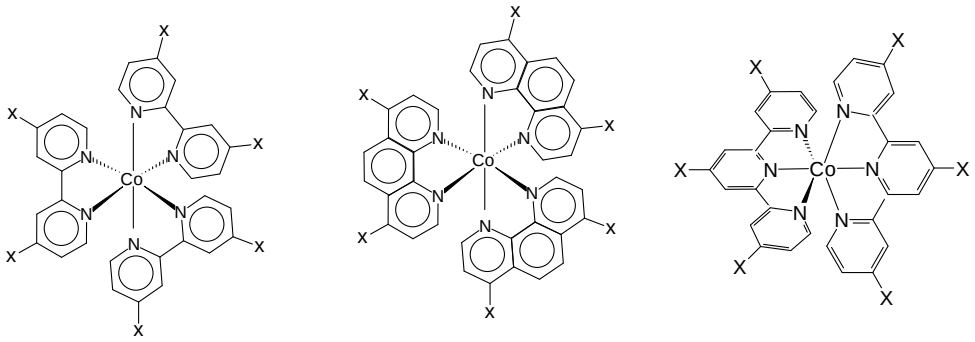

(a) (b) (c)

Figure 51. Structure of polypyridilic Co(II) complexes: (a) X = Tert-butyl (DTB), Methyl (DMB), H (bpy). (b) X =H (phen). (c) X = Tert-butyl (tTbterpy), Ethyl (tEterpy).

All of the complexes under consideration exhibit similar UV-Vis absorption spectra. Each of the Co(II) complexes has a weak absorption band centred at ca. 440-450 nm. The onset of the ligand-based π-π^* transition occurs in the UV above 350-380 nm for each of the ligands. The most intense visible absorption is for $Co(tTbterpy)_3^{2+}$ with ε_{450}=1.4 10^3 M^{-1} cm^{-1}. The remaining complexes all exhibit $\varepsilon_{440\text{-}450}$ values that are approximately an order of magnitude smaller. For the sake of comparison, the $\varepsilon_{440\text{-}450}$ value for I^-_3 is ca. 2 10^3 M^{-1} cm^{-1}; therefore, except $Co(tTbterpy)_3^{2+}$ that has a comparable absorbance, considerably less visible light is absorbed by all of the remaining cobalt complexes at similar concentrations.

Electrochemical characterization of these complexes revealed an unexpected electrode surface dependence to the electron-transfer kinetics. In the case of 4-4' substituted polipyridine Co(II) complexes, gold electrodes exhibit the most reversible and ideally shaped CVs. Glassy carbon and platinum electrodes also produce quasi-reversible voltammograms, although less reversible than gold. In general, the shapes of the quasi-reversible waves indicate that, in cases where the heterogeneous electron transfer is slow, the transfer

coefficient, α, is considerably greater than 0.5. In other words, for equivalent overpotentials the heterogeneous reduction of the Co(III) complex is considerably faster than the corresponding oxidation of the Co(II) species.

The voltammetric results also suggest that, while platinum is the cathode of choice for the I^-/I_3^- redox mediator, it should *not* be the optimal choice for cobalt complex-based mediators. Likewise, while carbon is a poor cathode with the I^-/I_3^- redox mediator system, it should be acceptable for any of the cobalt systems considered here. It must be noted that, among the series of figure 51, one of the most promising cobalt complexes ($Co(DTB)_3^{2+}$) is nearly *electrochemically inactive* on FTO and ITO electrodes, meaning that the unwanted Co(III) to Co(II) reduction at the photoanode requires high overpotentials to be effective. The dramatic dependence of the $Co(DTB)_3^{2+/3+}$ heterogeneous electron transfer rate on the chemical nature of the electrode surface is most probably consequence of specific interactions between the surface and the electroactive species which modify the electronic coupling and/or the activation barrier for the heterogeneous electron-transfer reaction. The electrochemical behaviour on metal oxide surfaces is in this case similar to the one of the I^-/I_3^- couple for which the electron transfer from the FTO substrate to I_3^- is a very slow multi-step process[85].

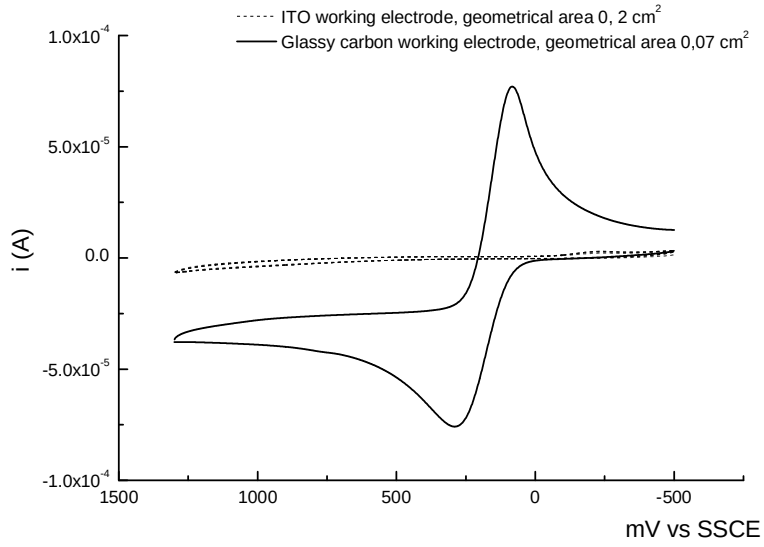

Figure 52. Cyclic voltammetry of approximately 1×10^{-3} M $Co(DTB)_3^{2+}$ recorded in ACN/$TBAPF_6$ 0.1 M on GC (solid line), and on ITO (dotted line).

[85] P. J. Cameron, L. M. Peter, *J.Phys.Chem.B* **2003**, *107*, 14394.

The performances of the photoelectrochemical cells are strongly dependent on the composition of the electrolyte solution (Figure 53). A maximum conversion efficiency of ca. 80%, in correspondence to the metal-to-ligand charge transfer absorption maximum of N3 was obtained in the presence of 0.25 M LiI/0.025 M I_2, whereas, with the cobalt based mediators, the best performances (ca. 50-55 % of IPCE) were observed when solutions of $Co(DTB)_3^{2+/3+}$ and $Co(tTBterpy)_2^{2+/3+}$ were used. In the other investigated cases, $Co(phen)_3^{2+/3+}$ $Co(tEterpy)_2^{2+/3+}$ and $Co(DMB)_3^{2+/3+}$ mediators exhibited much lower conversions, with maximum IPCE values in the range of 10-20%.

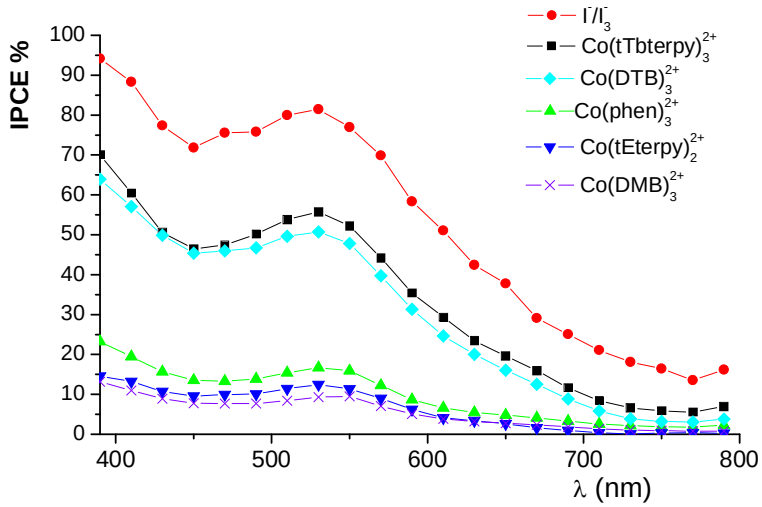

Figure 53. Photoaction spectra of N3 bound to nanocrystalline TiO_2 films in the presence of different electron mediators in MPN solutions: 0.25 M LiI/25 mM I_2 (red circles), 0.25 M $Co(tTBterpy)_2^{2+}$/25 mM $NOBF_4$ (black squares), 0.25 M $Co(DTB)_3^{2+}$/25 mM $NOBF_4$ (light blue squares), 0.25 M $Co(phen)_3^{2+}$/ 25 mM NOBF4 (green triangles), 0.25 M $Co(tEterpy)_2^{2+}$/25 mM $NOBF_4$(blue triangles), saturated (<0.15 M) $Co(DMB)_3^{2+}$/15 mM $NOBF_4$ (purple crosses). 0.25 M $LiClO_4$ was added to all solutions containing a cobalt mediator.

Generally, cobalt complexes of unsubstituted and methylsubstituted bipyridine or terpyridine ligands are poor electron transfer mediators in the type of DSSCs considered herein. In contrast, if the ligand contains a tertiary butyl substituent in the para position, the resulting cobalt based cells yield quite good IPCE. The observed substituent effect cannot be related to an electronic perturbation of the Co(II) redox orbitals and to a consequent modification of the electrochemical properties of the coordination compound, since the electron-donating effect of all simple alkyl substitutents (e.g., methyl, ethyl, *tert*-butyl, etc.)

is essentially the same[86] and all of the complexes of a given ligand-type (i.e., bipyridine, phenanthroline, or terpyridine) were expected and found to have very similar $E_{1/2}$ (100-200 mV vs SCE) values for the relevant Co(II/III) couple.

Nanosecond time resolved experiments allowed for the rationalization of the lower efficiency of the cobalt based couples with respect to iodide/iodine and for the clarification of their structure-dependent performance. Figure 54.a shows the decay of the photogenerated N3 dye cation, observed at 480 nm in the presence of $Co(DTB)_3^{2+}$ 0.1 M and TBAI 0.1 M: in both cases a $\tau_{2/3}$ of about 0.35 μs indicates that dye regeneration by iodide and by Co(II) occurs at a very similar rate. Upon Li^+ addition (Figure 54.b) an increased reduction rate by iodide is observed ($\tau_{2/3}$ = 0.12 μs), whereas regeneration of the oxidized dye by Co(II) is substantially unchanged. Indeed, TiO_2 surface adsorption/intercalation by Li^+ creates a positive polarization which attracts a surface excess of iodide in close proximity of the dye sites, allowing for a faster interception of the oxidized sensitizer. The same effect is obviously absent in the case of positively charged Co(II) complexes which do not experience any attraction with a positively polarized photoelectrode: the slower oxidized sensitizer reduction observed in the case of Co(II) electron mediators is thus believed to be one of the main reasons that limit Co(II) mediator performances with respect to Iodide[87].

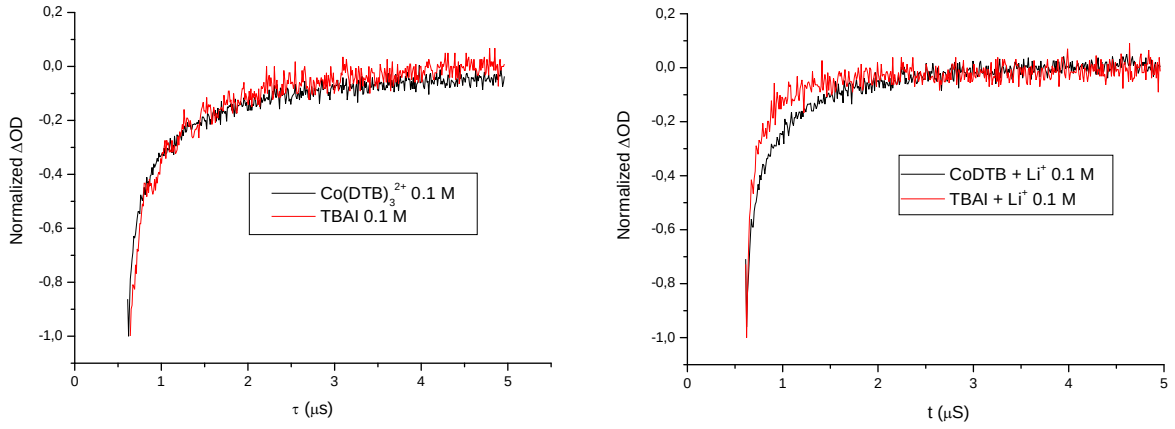

(a) (b)

Figure 54. 480 nm $Ru(III)(H_2DCB)_2(NCS)_2^+$ recovery in the presence of: (a) Tetrabutyl-ammonium iodide (red) and $Co(DTB)_3^{2+}$ (black) 0.1 M; (b) Tetrabuty-ammonium iodide (red) and $Co(DTB)_3^{2+}$ (black) 0.1 M + $LiClO_4$ 0.1 M. Pulse energy ≈ 1mJ/cm^2.

[86] L. G. Wade, *Organic Chemistry*, Prentice Hall, Englewood Cliffs, New Jersey, **1991**.
[87] A complete dissertation on electrochemical and photoelectrochemical behaviour of Co(II) polipyridyl complexes is present in PhD Thesis of Stefano Caramori, Chemistry Department of Ferrara University, 2005.

Cobalt mediator performance was found to be strongly dependent upon the presence of high charge density cations, with the best results in terms of both J_{sc} and V_{oc} obtained in the presence of relatively high concentration of Li^+ or Mg^{2+} (0.3-0.5 M). Since Li^+ is not instrumental in accelerating dye regeneration, the explanation must lye in the control of the parasitic back recombination.

4.1.2 Electron transfer mediators mixtures: introduction of a kinetically fast redox couple in conjunction with $Co(DTB)_3^{2+}$.

The results that have been obtained indicate that, although for now less efficient than the iodide/iodine couple, cobalt complexes formed with relatively simple and commercially available alkylsubstituted polypyridines are promising electron transfer mediators for DSSCs. Their kinetic limitations reside essentially in a slower oxidized dye regeneration and in a faster recombination with photoinjected electrons: however, while the back recombination can be passivated by choosing an appropriate electrolytic composition (i.e. Li^+, Mg^{2+} ions, Tert-butyl-pyridine) and by the introduction of bulky substitutents in the coordination sphere of the dye and/or of the mediator, the slow electron donation is an intrinsic characteristic of polypyridine cobalt complexes.

In the effort of improving the performance of such mediators the possibility of using kinetically fast couples in conjunction with the best Co(II) mediators has been explored[88]. Kinetically fast couples efficiently reduce the oxidized dye, but due to the fast recombination with injected electrons are totally unsuccessful as mediators in DSSC. However, when mixed with an excess of cobalt mediator, if their redox potential is appropriate (i.e. more positive than the Co(III)/(II) couple), a cascade of electron transfer events allows to confine the hole on Co(III) which, by virtue of its very slow heterogeneous electron transfer on semiconductor oxides gives rise to a very inefficient electron recapture. As a consequence, the large majority of Co(III) created in the second electron transfer step is free to diffuse to the counter electrode of the cell, whereupon is reduced. The use of a long alkyl chain dyes like Z907, for example, is beneficial to the system allowing to further reduce back recombination enhancing the electron collection efficiency.

[88] S. Cazzanti, S. Caramori, R. Argazzi, C. M. Elliott, C. A. Bignozzi, *J.Am.Chem.Soc*. **2006**, *128,* 9996.

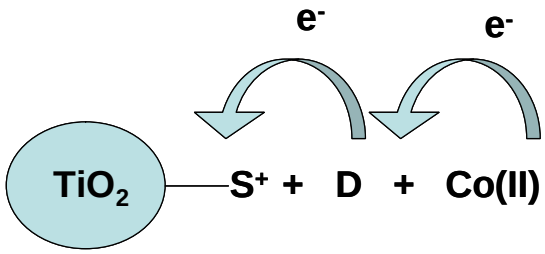

Figure 55. Sequence of electron transfer events involving the oxidized dye(S^+) the co-mediator(D) and the cobalt complex (Co(II)).

Phenothiazine (PTZ) and ferrocene (Fc), both of which have a small reorganization energy associated to the electron transfer, are the first co-mediators that have been considered. Each has a potential which falls between 0.22 and 0.75 V vs SCE, respectively, the potential of the $Co(DTB)_3^{3+/2+}$ and of the dye $[Ru(DCB)(dnbpy)(NCS)_2]^{+/0}$. Because of the facile electron transfer the photooxidized dye would be predominantly reduced by the co-mediator. Its oxidized form (PTZ^+ and Fc^+) can be then rapidly intercepted by Co(II), preventing the direct charge recombination between the oxidized co-mediator and the electrons in the TiO_2. Nanosecond transient absorption measurements confirmed a faster dye regeneration by both PTZ and Fc relative to $Co(DTB)_3^{2+}$, despite their higher redox potential (Figure 56).

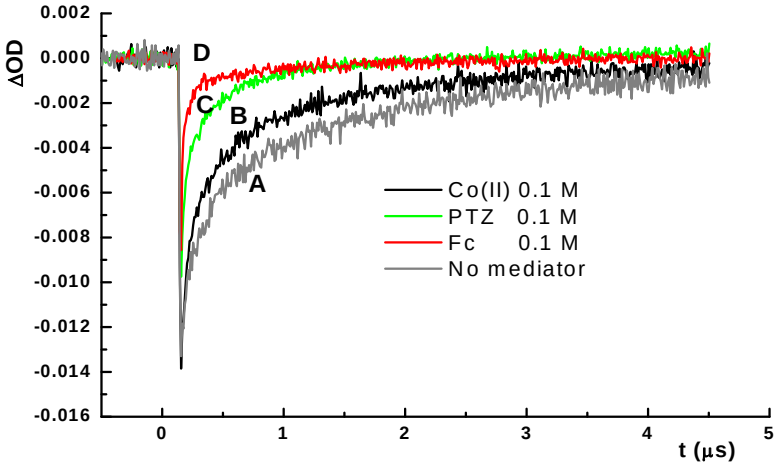

Figure 56. Decay kinetic of photooxidized Z907 adsorbed on TiO_2 in the presence of various electron mediators : (A) no mediator; (B) 0.1 M $Co(DTB)_3^{2+}$; (C) 0.1 M PTZ; (D) 0.1 M Fc. Differential absorbance changes measured at 480 nm. Pulse energy: 5 mJ/cm^2.

The best results were observed using a co-mediator/Co(II) ratio of 1:2 with 0.15 M $Co(DTB)_3^{2+}$ in acetonitrile. Addition of 0.5 M Li^+ and 0.1 M Tbpy generally improved the open circuit photovoltage. In the presence of the PTZ/Co(II) mixture cell IPCE % reached

more than 80 % (Inset Figure 57), a value well comparable to the best I^-/I_3^- cells. Under white light irradiation the J_{sc} was also comparable, with the advantage of a better fill factor and higher V_{oc} for the cobalt based cell (Figure 57).

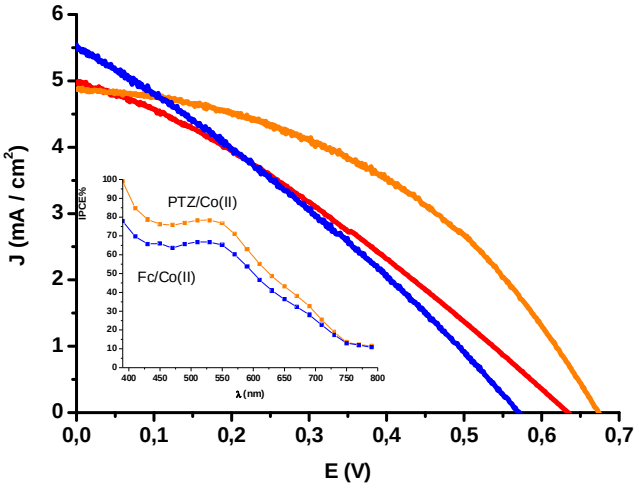

Figure 57. J-V curves obtained in the presence of Co(II)/PTZ (orange), I^-/I_3^- (red) and Co(II)/Fc in methoxypropionitrile. Inset: photoaction spectra . Incident irradiance ≈ 0.1 W/cm^2 .

In general the Co(II)/Fc mixture gave poorer overall photovoltaic performances than the equivalent Co(II)/PTZ system, notably a poorer V_{oc} and fill factor. Since ferrocene was found to be faster in dye regeneration, an explanation can lye in a less efficient interception of Fc^+ by Co(II) centres, resulting in a larger steady state concentration of Fe(III) which undergoes recombination on the TiO_2 surface. Indeed, Chronocoulometry and cyclic voltammety experiments at FTO electrodes allowed to verify that PTZ^+ was from 1.5 to 2 times more effective than Fc^+ in the oxidation of Co(II), thus having a smaller probability of recombining with photoinjected electrons.

An analogous behaviour extends to other species having small reorganization energies and appropriate potentials such as the iron(II) complexes $Fe(DMB)_3^{2+}$ and $Fe(DTB)_3^{2+}$ ($E_{1/2}$ ≈ 0.95 V Vs SCE). When used in the presence of an excess of $Co(DTB)_3^{2+}$ and in conjunction with suitable sentizers like the heteroleptic dye $Ru(dnbpy)(DCB)_2^{2+}$ ($E_{1/2}$ = 1.25 V Vs SCE) (Figure 58) the iron(II) co-mediators clearly enhance the performance of the $Co(DTB)_3^{2+}$ and outperform the I^-/I_3^- redox couple, at least in terms of monochromatic photon to current conversion efficiency, with maximum values close to 85%.

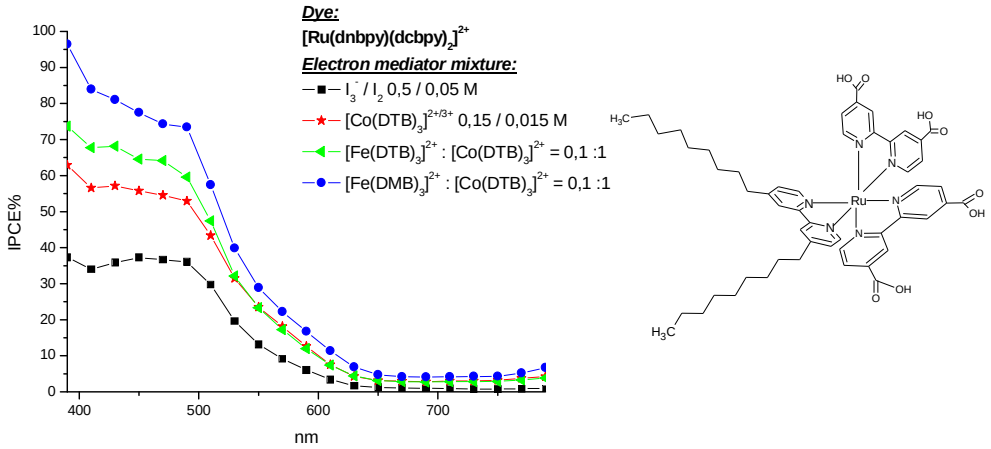

Figure 58. IPCE spectra of Ru(dnbpy)$(H_2DCB)_2^{2+}$ obtained in the presence different electron transfer mediators.

Interestingly, the polypyridine Fe(II)/Co(II) mediator mixtures were rather insensitive to variations of the Fe(II) to Co(II) concentration ratio. Very similar performances were obtained over a Fe(II)/Co(II) ratio ranging from 0.1 to 0.5, with the optimum at 0.1. For higher Fe(II)/Co(II) ratios the cell performance dropped, ostensibly due to the formation of an excess of Fe(III) which was no longer effectively intercepted by Co(II) and recombined on the TiO_2 surface. In the case of electron mediator mixtures characterized by the presence of a kinetically fast couple, the decrease in ς potential and the blocking effect obtained by using heteroleptic dyes with hindering chains is more than ever important for controlling electron recapture: meaningfully, the performances of the Fe(II)/Co(II) mixtures used in conjunction with the homoleptic $Ru(DCB)_3^{2+}$ were rather poor, not exceeding a maximum IPCE% of 30 %, whereas the iodide/iodine couple produced almost identical conversions (ca. 40%) to those reported with the heteroleptic Ru(dnbpy)$(DCB)_2^{2+}$.

4.1.3 Mass transport limitations using Co(II) complexes as redox mediators.

The transport of the electroactive ions is expected to play a significant role in determining DSSC efficiency: this is particularly true under strong illumination when a large number of photooxidized dye molecules are simultaneously generated at the photoanode ad an efficient turnover of electron donating species is required to sustain the photocurrent. Iodide/tririodide species are relatively simple and small ions that can diffuse efficiently in solution and within the TiO_2 mesopores, whereas larger complex ions like the polypyridine

Co(II)/(III) can experience mass transport limitations due to their larger hydrodynamic radius and their positive charge which leads to electrostatic attraction towards the TiO_2 surface and reduces ion mobility. Chronoamperometry experiments at a platinum electrode under Cottrell conditions[89] in acetonitrile/$LiClO_4$ allowed to calculate a diffusion coefficient for $Co(DTB)_3^{2+}$ equal to 9.8 10^{-6} cm^2 s^{-1}. More recently, rotating disk experiments substantially confirmed the former value, yielding in similar conditions a value of 6.7 10^{-6} cm^2s^{-1} . To make a comparison, iodide was found to have a substantially larger diffusion coefficient, of the order of 1.6 10^{-5} cm^2/s^{-1}. It must be noted that the diffusion coefficients have been obtained in different conditions (i.e. diluted Co(II) solutions) from those actually met in the concentrated electrolyte employed for the DSSC. Under working conditions a large increase (11x) in solvent (acetonitrile) viscosity was found for the cobalt based mediators, whereas iodide/iodine solutions accounted only for a 5x increase. Considering this effect, the bulk diffusion of I^- and I_3^- can be evaluated as about 6 times faster than $Co(DTB)_3^{2+/3+}$. Futhermore, into the pores of the TiO_2 the slow diffusion of the cobalt mediator can be exacerbated by channel constrictivity effects on the large cations and by electrostatic interactions with the surface.

Indeed, when using Co(II)/(III) couples mass transport limitations are evident from the lack of linearity of the photocurrent vs incident power plots (Figure 59): in the presence of a spacer the photocurrent density produced by the cobalt mediated cell is very close to the iodide/iodine system at low irradiation intensities (0.018 and 0.033 W/cm^2), but clearly approaches a plateau at incident light intensities superior to 0.07 W/cm^2. On the other hand, the J_{sc} delivered by the iodide/iodine mediated cells continues to increase in almost linear fashion with the incident power.

[89] A. J. Bard, L. R. Faulkner, *Electrochemical Methods: Fundamentals and Applications*, J.Wiley & Sons, INC., **2001**.

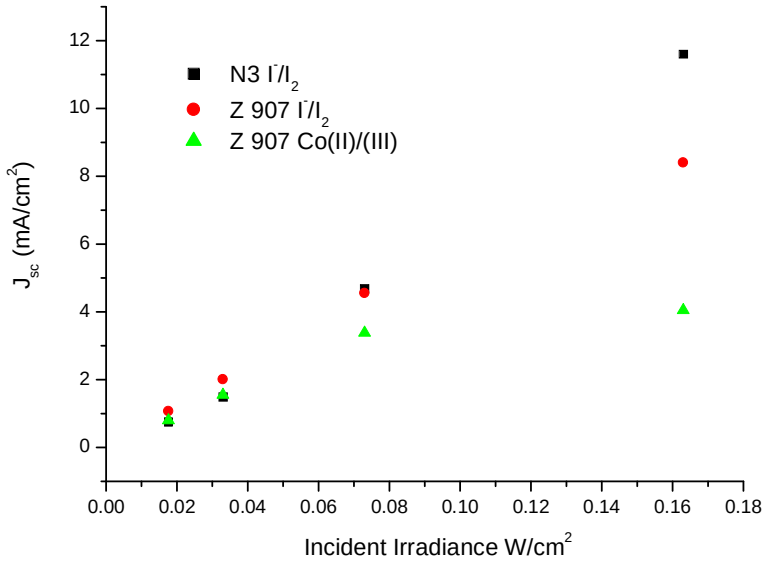

Figure 59. Jsc Vs incident irradiance plot : LiI/I_2 0.3/0.03 M + 0.1 M Tbpy in acetonitrile in conjunction with N3 (black sqares) : LiI/I_2 0.3/0.03 M 0.1 M Tbpy in acetonitrile in conjunction with Z907 (red circles); $Co(II)(DTB)_3^{2+}$ 0.15 M + 0.5 M Li^+ + 0.1 M Tbpy in acetonitrile in conjunction with Z907 (green triangles). 120 μm spacer.

The limiting role of the diffusion in case of Co(II) electrolytes could be further investigated by recording photocurrent transients under strong illumination (ca. 0.1 W/cm^2) (Figure 60).

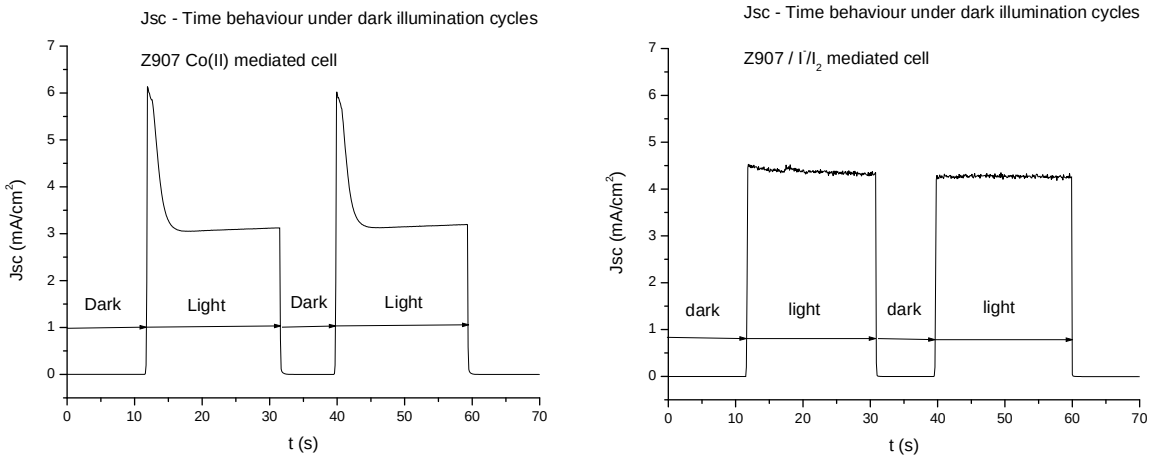

(a) (b)

Figure 60. Photocurrent transients recorded on: (a) $Co(DTB)_3^{2+}$ mediated DSSC. Electrolyte composition: Co(II) = 0.15 M, Li^+ = 0.5 M, Tbpy = 0.1 M (b) LiI/I_2 0.3/0.03 M + 0.1 M Tbpy in acetonitrile.

The time resolved experiment clearly shows an instantaneous rise of the photocurrent as soon as the cell is exposed to light, the appearance of a peak of about 6 mA/cm^2 followed

by a relaxation to a steady regime within about 10 seconds. A constant photocurrent density of nearly 3 mA/cm^2 is then maintained as long as the cell is left under illumination.

The appearance of a photocurrent peak followed by a decay to a steady value could be explained either by electron recombination after the initial charge injection, or by a slow $Co(DTB)_3^{2+}$ diffusion unable to sustain the amount of photocurrent initially produced. If the transients were determined by the former process a much faster drop to a steady value would be observed since charge recombination usually occurs in the microsecond/millisecond time domain. Furthermore, time resolved spectroscopy allowed to verify that with an appropriate dye and electrolytic composition charge recombination is not a limiting process with respect to the iodide/iodine couple. As a consequence the observed behaviour could be quite confidently assigned to a mass transport limitation of the cell. Indeed, the same phenomenon is not observed with iodide/triiodide mediated cells which show under identical irradiation a more ideal rectangular shape of the photocurrent transients (figure 60.b) The limiting role of cobalt diffusion can be confirmed by comparing photocurrent transients obtained from cells equipped with an electrolyte-confining spacer (120 µm) to those recorded with cells assembled by pressing the TiO_2 photoanode and the counter electrode in a direct contact (Figures 61.a and 61.b)

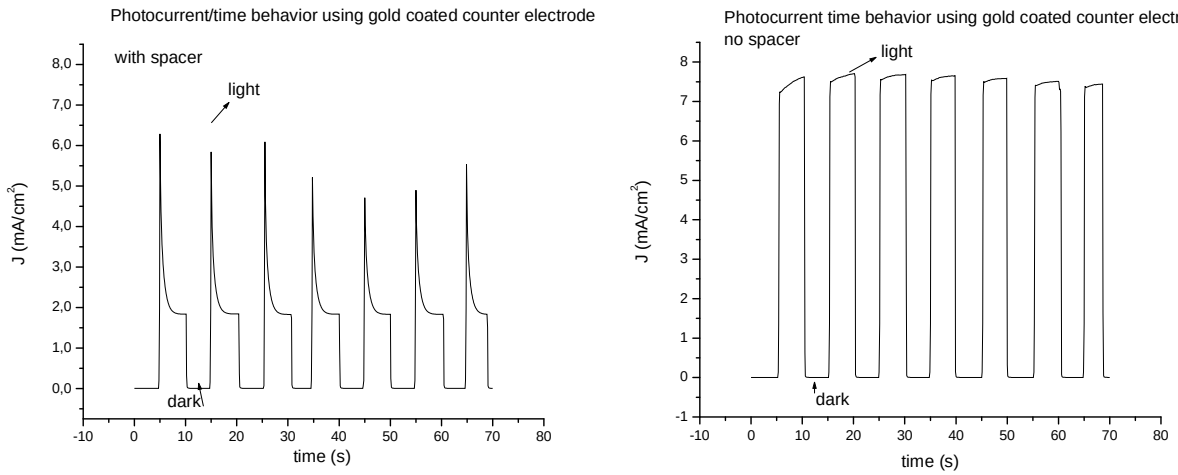

(a) (b)

Figure 61. Photocurrent transients obtained with : (a) spacer equipped cells; (b) without spacer. Electrolyte composition: 0.15 M $Co(II)(DTB)_3^{2+}$ + 0.5 Li^+ + 0.1 M Tbpy in acetonitrile.

In the presence of the spacer (Figure 61.a) an initially high photocurrent value (≈ 6 mA/cm^2) is achieved, but, due to the larger spacing between the two electrodes, the

diffusion of the electron mediator is not fast enough to supply new reduced mediator to the TiO_2/dye interface, from which, under irradiation, is constantly depleted. Thus, a steady photocurrent value, significantly lower than the initial spike is attained after a few seconds. In figure 61.b the reduced diffusional path for the electron mediator allows for a more effective mass transport which accounts for the generation of a stable photocurrent without the observation of photoanodic relaxation processes.

Cell and TiO_2 engineering are therefore required to avoid or reduce the mass transport limitations in DSSCs based on coordination compounds as redox mediators: minimizing the spacing between the electrodes, choosing low viscosity solvents, changing the morphology of the TiO_2 substrate (i.e. ordered nanostructures with large pore size, TiO_2 nanotubes and nanorods) are expected and required to enhance mediator transport and cell efficiency.

4.1.4 Affect of an Al_2O_3 overlayer on Co(II) mediated DSSCs.

In chapter 4.1.1 several Co(II) trisbipyridyl complexes have been studied as electron transfer mediators in solar cells in which N3 has been used as sensitizer and Co(DTB) resulted to be the best electron transfer mediator both for the photocurrent and the overall photoconversion efficiency.

Successively it has been demonstrated that Co(DTB) gave best performances when used as electron transfer mediator in DSSC in which z-907 was employed as sensitizer[90]. The steric hindrance due to the presence of the alchilic chains in Z-907 slows down the back electron transfer processes between the oxidized mediator and the back contact.

On the basis of this result, we decided to start again the study of Co(II) complexes in devices where z-907 was the sensitizer. In particular the analysis was directed to Co(4,4'-diethylamide-2,2-bipyridine)$_3$ [Co(DEA)], Co(4,4'-ditertbutylamide-2,2-bipyridine)$_3$ [Co(DBA)], Co(4,4'-diterbutyl-2,2-bipyridine)$_3$ [Co(DTB)], Co(4,4'-diethylester- 2,2-bipyridine) [Co(DEEST)] and Co(4,4'-diterbutylester- 2,2-bipyridine) [Co(DTBEST)]. Figure 62 depicts the molecular structure of these compounds. The complexes were synthesized following previous published procedures (see reference 85). The electrochemical behaviour of these compounds has been previously studied; in general Co(II) complexes with bipyridine

[90] S. Cazzanti, S. Caramori, R. Argazzi, C. M. Elliott, C. A. Bignozzi, *J.Am.Chem.Soc.* **2006**, *128,* 9996.

leading in 4,4' positions strongly electron withdrawing substituents (as amide or ester) have a significantly more positive ground state redox potential. In table III the electrochemical behaviour of the Co(II) complexes on glassy carbon is reported.

Table III. Electrochemical behaviour of Co(II) complexes on GC/PT/SCE, at 100 mV/s in $LiClO_4$ 0.1 M in acetonitrile.

Co(II) complex	E_{pa} (mV)	E_{pc} (mV)	$E_{1/2}$ (mV)	ΔE (mV)
$Co(DTB)_3$	242	3	122	239
$Co(DEA)_3$			400	
$Co(DBA)_3$	468	385	426	83
$Co(DEEST)_3$	517	417	467	100
$Co(DTBEST)_3$	548	411	479	137

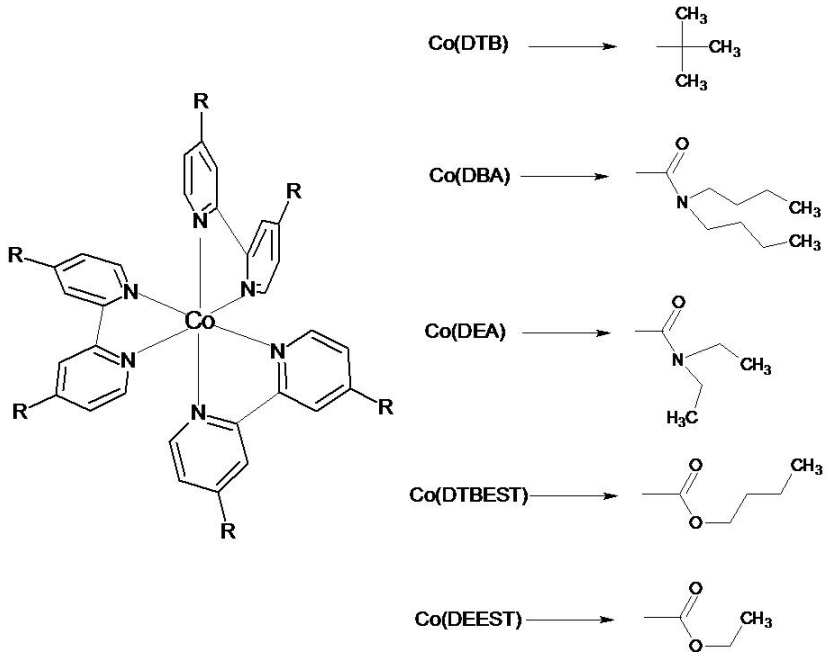

Figure 62. Molecular structure of Co(II) complexes.

What one expect from the electrochemistry is an enhancement of the open circuit potential from Co(DTB) to Co(DTBEST). Figure 63 shows the J-V curves recorded in solar simulated conditions related to Z-907 using the different Co(II) complexes as electron transfer mediator[91].

[91] J-V curves were performed on Z-907 sensitized solar cells, without spacer, by irradiation of a Xenon lamp set up at 0.1 W/cm^2 and filtered with a cut off at 400 nm. The electrolyte solutions contain Co(II) complex 0.15 M,

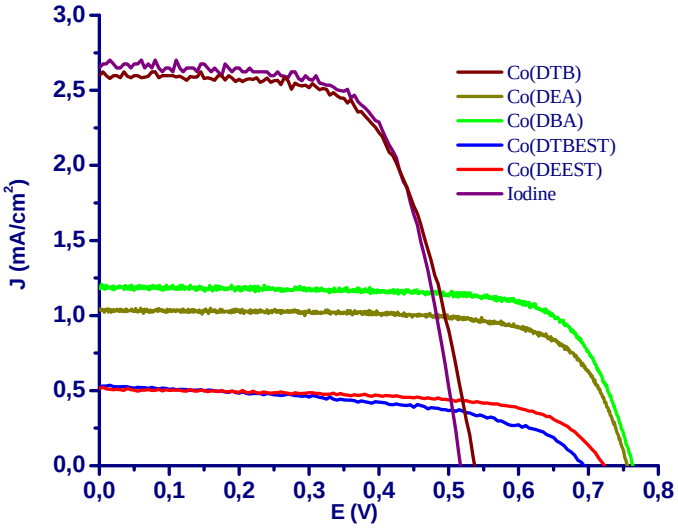

Figure 63. Current potential curves in solar simulated conditions (0.1 W/ cm2 using a Xe lamp filtered with a 400 nm cut off) of Z-907 SSC with several Co(II) complexes as electron transfer mediator.

Table IV. Photoelectrochemical parameters of Z-907 SSCs extrapolated from J-V curves shown in Figure 63.

E. T. Mediator	$E_{1/2}$ (mV)*	J_{sc} (mA/cm^2)	V_{oc} (mV)	FF%	η%
LiI/I_2	200	2.65	515	0.63	0.916
$Co(DTB)_3^{2+/3+}$	122	2.60	535	0.64	0.891
$Co(DEA)_3^{2+/3+}$	400	1.05	756	0.71	0.563
$Co(DBA)_3^{2+/3+}$	426	1.19	764	0.74	0.67
$Co(DEEST)_3^{2+/3+}$	467	0.515	725	0.63	0.234
$Co(DTBEST)_3^{2+/3+}$	479	0.528	695	0.52	0.193

* The redox potential are measured with a Pt/GC/SCE standard electrochemical cell using $LiClO_4$ 0.1 M in acetonitrile as support electrolyte.

As shown in figure 63, the increase of the redox potential of Co(II) complex is paralleled by an increase of the V_{oc} but at the same time a decrease of the J_{sc} is observed due to the lower driving force for the dye regeneration. It should be noted that, although Co(DTBEST) and Co(DEEST) have a ground state redox potential higher than Co(DEA) and Co(DBA), the V_{oc}'s are lower. This fact is most probably related to a faster back recombination which involve the mediator specie. Comparing in fact the dark current

Co(III) complex 0.015 M (by oxidation with a stoichiometric amount of $NOBF_4$), LiOTf 0.5 M and tButylpyridine 0.1 M in γ-Butirrolactone.

measurements, performed on the same cells, it's clear that $Co(DEEST)^{3+}$ and $Co(DTBEST)^{3+}$ recombine with the substrate faster than $Co(DBA)^{3+}$ and $Co(DEA)^{3+}$.

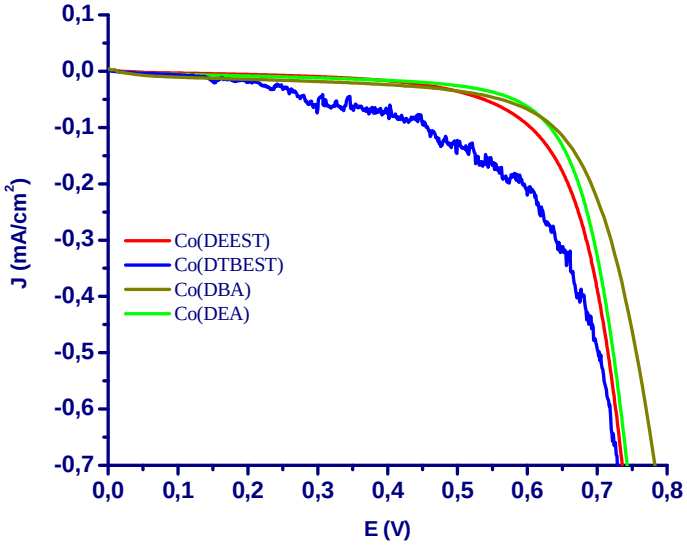

Figure 64. Dark current measurements.

In an attempt to improve both the open circuit photovoltage and the photocurrent densities, we have introduced an alumina overlayer on the photoanode. Allumina overlayers were built, following a previous published procedure[92], directly on TiO_2 film before of the sensitization procedure.

The obtained electrodes, sensitized with Z-907, were used as photoanodes in solar cells in order to test the effect of alumina overlayer with the different Co(II) complexes. While in the case of Co(DTB), as electron transfer mediator, no significant improvement of the photoconversion efficiency was obtained, a remarkably effect was observed with the other Co(II) complexes. Figure 64, 65 and 66 show in fact that using Co(DBA) and Co(DTBEST) as electron transfer mediators, an enhancement of the current from 0.83 mA/cm^2 to 1.27 mA/cm^2 for the former and from 0.79 mA/cm^2 to 0.98 mA/cm^2 for the latter was obtained meaning that the allumina overlayer is effective in slowing down the back electron transfer reactions to Co(III) complexes. For Co(DTB) the alumina overlayer has no influence probably for the high screening effect produced by tert butyl groups. With this complex it is possible to

[92] Emilio Palomares, John N. Clifford, Saif A. Haque, Thierry Lutz and James R. Durrant, *J. Am. Chem. Soc.* **2003**, 125, 475-482

obtain an overall efficiency of 1.09% which is comparable to that observed with I_2/I_3^- (0.91%) (Table V).

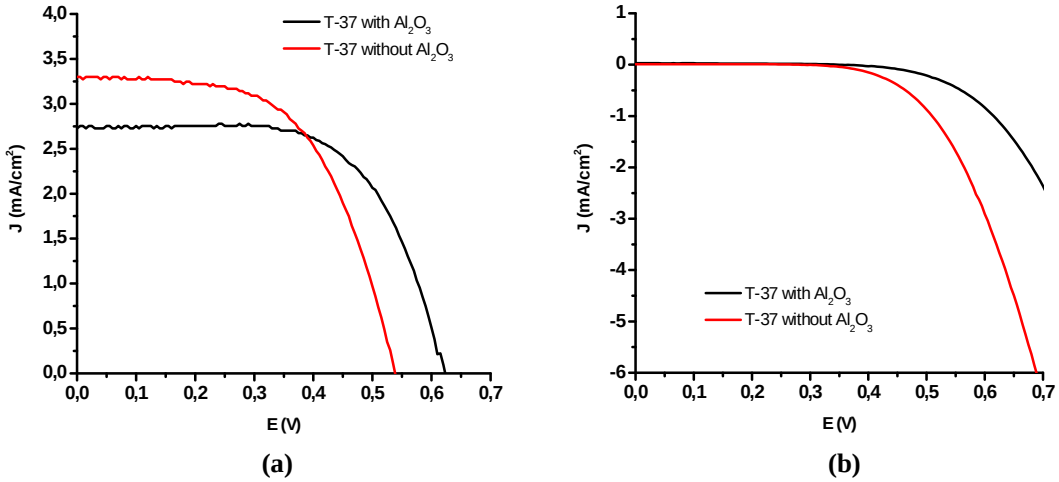

Figure 64. (a) J-V curves of Z-907 sensitized solar cells using Co(DTB) 0.15 M as electron transfer mediator with an Allumina overlayer (black line) or without (red line). (b) Dark current measurements performed on these soar cells.

Table V. . Photoelectrochemical parameters of Z-907 SSCs extrapolated from J-V curves shown in Figure 64.

	Jsc (mA cm^{-2})	Voc (mV)	FF	η %
TiO2(T-37) w/o Al2O3	3.30	540	0.58	1.03
TiO2(T-37) w Al2O3	2.74	625	0.64	1.09

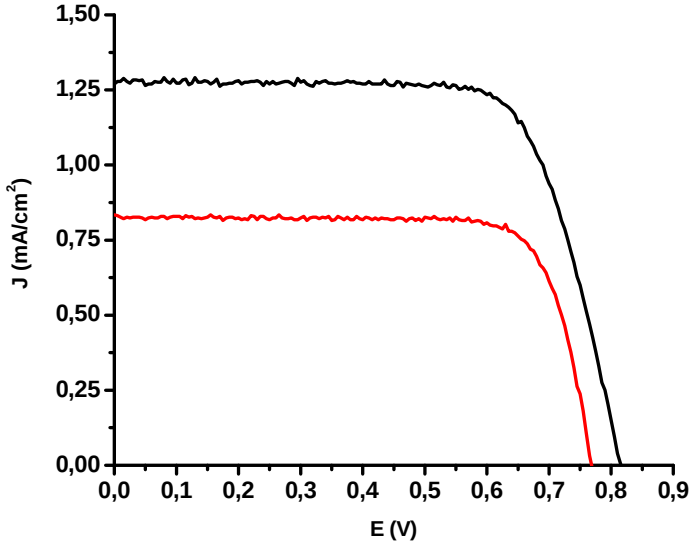

Figure 65. J-V curves of Z-907 sensitized solar cells using Co(DBA) 0.15 M as electron transfer mediator with an Allumina overlayer (black line) or without (red line).

Table VI. . Photoelectrochemical parameters of Z-907 SSCs extrapolated from J-V curves shown in Figure 65.

	Jsc (mA cm-2)	Voc (mV)	FF	h %
TiO2(T-37) w/o Al2O3	0.834	770	0.79	0.505
TiO2(T-37) w Al2O3	1.27	815	0.73	0.758

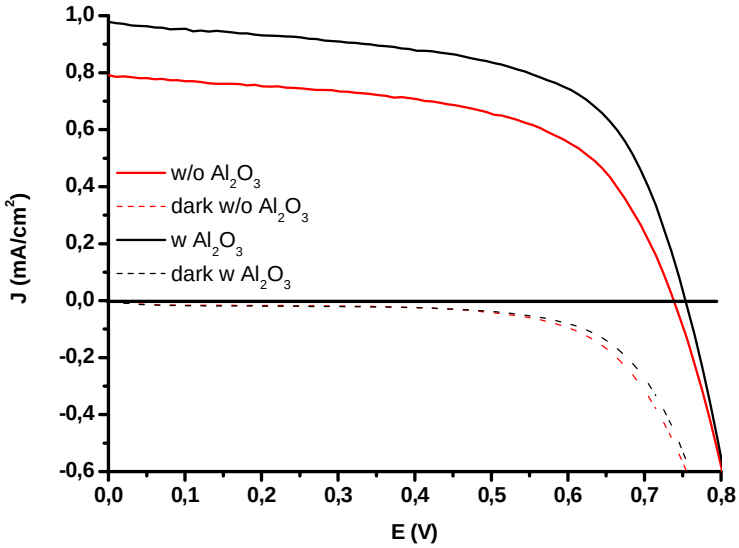

Figure 66. (a) J-V curves of Z-907 sensitized solar cells using Co(DTBEST) 0.15 M as electron transfer mediator with an Allumina overlayer (black line) or without (red line). Dark current measurements performed on these soar cells.

Table VII. Photoelectrochemical parameters of Z-907 SSCs extrapolated from J-V curves shown in Figure 66.

	Jsc (mA cm-2)	Voc (mV)	FF	h %
TiO2(T-37) w/o Al2O3	0.791	735	0.58	0.341
TiO2(T-37) w Al2O3	0.978	755	0.6	0.447

4.2 Electron Transfer Mediators based on Cu(I) Metal Complexes.

The study of new electron mediators potentially capable of replacing the iodide/iodine couple is attractive for at least two reasons : first, the investigation of new redox systems may improve our knowledge of the basic charge separation events and their dependence from the inherent structural and electrochemical properties of new mediators, second, the discovery of new efficient non corrosive electron mediators may boost DSSC diffusion as a convenient renewable energy source.

Cu(I)/(II) coordination compounds might also result attractive due to the relevant nuclear rearrangement that should occur when tetrahedral Cu(I) complexes are oxidized to octahedral or trigonal-bi-pyramidal[93,94] Cu(II) species and vice-versa.

In this study we report the preparation and the photoelectrochemical characterization of a series of Cu(I) complexes, based on substituted bipyridine and quinoline derivatives, used as electron transfer mediators in sandwich type DSSCs. To stabilize the Cu(I) oxidation state of Cu(I) polypyridine complexes, electron withdrawing substituents like esters have been considered. The same effect was obtained also with pyridil-quinoline and biquinoline complexes, thanks to the increased π accepting properties of the quinoline condensed aromatic rings.

4.2.1 Experimental Section.

4.2.1.1 Materials : 2-nitrobenzaldehyde, 2-acetyl-pyridine, 4-tert-butyl-pyridine, 2-nitro-acetophenone, biquinoline, trimethylsilyl cyanide, dimethyl-carbamyl-chloride, iodomethane, hydrogen peroxide, magnesium sulphate, magnesium shavings, tin granules, copper powder, $Cu(ClO_4)_2$ x 6 H_2O, iron (II) ammonium sulphate, NH_4Cl, Na_2CO_3, $SOCl_2$, normal-butanol were purchased from Aldrich and used without further purifications. Analytical grade tert-butanol (Fluka) was dried over molecular sieves (3Å) before use. Other analytical grade solvents, concentrated ammonium hydroxide and glacial acetic acid were from Fluka, Carlo Erba and Fisher and used as received, unless otherwise stated.

4,4' dimethyl-2,2' bipyridine was prepared by catalytic dehydrogenation of freshly distilled 4-picoline (Aldrich) in presence of 10 % Pd(C) (Fluka)[95]. 2,2'-bipyridine-4,4'-di-carboxylic acid (H_2DCB) was prepared by oxidation of 4,4'-dimethyl-2,2' -bipyridine with chromic acid according to a previously reported procedure[96]. 2,2'-bypiridine-di-4,4'-ethyl ester (bpy-$(COOEt)_2$) (**1**) was prepared following literature methods[97]. 2,2'-pyridil-quinoline (PQ) (**4**) was synthesized following a previously reported Friedlander condensation[98]. Titanium

[93] Itoh, S.; Kishikawa, N.; Suzuki, T.; Takagi, H. D. *Dalton Transactions* **2005**, *6*, 1066-1068
[94] Hattori, S.; Wada, Y.; Yanagida, S.; Fukuzumi, S. *J.Am.Chem.Soc.* **2005**, *127*, 9648-9654.
[95] Sprintschnik, G.; Sprintschnik, H. W.; Kirsch, P.; Whitten, D. G. *J.Am.Chem.Soc.* **1977**, *99*, 4947.
[96] Oki, R. A.; Morgan, R. J. *Synthetic Communications* **1995**, *25*, 4093-4097.
[97] Gillaizeau-Gautier, I.; Odobel, F.; Alebbi, M.; Argazzi, R.; Costa, E.; Bignozzi, C. A.; Qu, P.; Meyer, G. J. *Inorg.Chem.* **2001**, *40*, 6073-6079.
[98] Harris, C. M. *Aust.J.Chem.* **1972**, *25*, 1631.

isopropoxide ($Ti(^{i}PrO)_4$) 98%, $TiCl_4$ 98% and absolute ethanol were obtained from Fluka and used as received. The ruthenium sensitizer [$Ru(dnbpy)(H_2DCB)(NCS)_2$] (Z 907), where (dnbpy) is the 4,4'dinonyl-2,2'-bipyridine, was prepared according to literature procedures[99].
Conductive FTO glasses, ca. 8 Ohm/□, were from Pilkington (U.K.). Prior to electrochemical measurements conductive glass pieces (ca. 0.5 cm^2) were carefully cleaned by subsequent repeated soakings and sonications in saturated KOH/isopropanol, deionized water and acetonitrile.
Spectroscopic grade acetonitrile (ACN) (Fluka) was used for photoelectrochemical and electrochemical measurements. $LiClO_4$ (Aldrich) was generally employed as a supporting electrolyte.

4.2.1.2 Analytical Measurements: ^{1}H NMR and ^{13}C spectra were recorded either on a Varian Gemini 300 MHz spectrometer or on a Bruker 200 MHz spectrometer.
ESI mass spectra were collected with a Waters Micromass ZMD-2000 spectrometer.
Elemental Analysis was carried out with a Carlo Erba CE 110 Elemental Analyzer.

Photoaction spectra were obtained with a custom made apparatus comprising a water cooled Xe lamp (Osram XBO, 150 W) coupled to an Applied Photophysics monochromator, adopting a 10 nm spectral bandwidth. Illuminated cell area was 0.5 cm^2. Photocurrents, sampled at 20 nm intervals, were recorded under short circuit conditions using an Agilent 34401A digital multimeter. Incident irradiances were measured by means of a Centronic OSD100-7Q calibrated silicon photodiode and the IPCE (Incident Photon-to-electron Conversion Efficiency) was calculated according to the formula:

$$\text{IPCE \%} = 1240\ \frac{J}{\lambda W}$$

Where J is the photocurrent density expressed in $\mu A/cm^2$, λ is the wavelength of incident monochromatic light and W is the radiant power in W/m^2.

J-V curves obtained under 510 nm monochromatic light were collected with an Amel model 562 Potentiostat, using the same apparatus described above, by varying the applied potential between 0 and -550 mV adopting a two electrode configuration.

Electrochemical measurements (CV and LSV) were carried out in a three electrode arrangement with an Ecochemie Autolab PGSTAT 30 electrochemical workstation.

[99] Wang, P.; Zakeeruddin, S. M.; Moser, J.-E.; Nazeeruddin, M. K.; Sekiguchi, T.; Graetzel, M. *Nature Materials* **2003**, *2*, 402-407.

4.2.1.3 Photoanodes preparation: in order to avoid incidental electronic recombination from the FTO back contact, a compact TiO_2 underlayer was created prior to porous TiO_2 deposition: typically ≈ 200 µl of freshly prepared precursor solution (0.2 M $Ti(ip)_4$ in absolute ethanol) , was spin coated onto cleaned FTO substrates (2 x 2.5 cm) at 2000 rpm for about 30 seconds. The resulting layer was baked at 450 °C for 30 minutes, resulting in a transparent compact 2 cm^2 TiO_2 film.

Mesoporous TiO_2 films were obtained by casting over the compact TiO_2 underlayer a colloidal TiO_2 paste[100] using the well known adhesive tape casting method. The resulting film (2 x 0.5 cm^2) was sintered in an oven at 450 C° for 40-45 minutes. The final step involved the application of an aqueous 2 M $TiCl_4$ solution onto the mesoporous TiO_2 substrate, as it has been generally recognized that such treatment improves the photoelectrochemical properties of the DSSC[101].

Sensitization was carried out by immersion of the TiO_2 photoelectrodes in a ca. 10^{-5} M sensitizer solution in absolute ethanol. This procedure was carried out in the dark either at refluxing temperature for 3-4 hours or at room temperature for approximately 12 hours. After this time, dye adsorption on TiO_2 was complete, leading to red coloured photoelectrodes characterized by a maximum absorbance > 1 in the 500-550 nm region.

4.2.1.4 Counter electrodes preparation: gold or silver coated counter electrodes (ca. 100 nm) were obtained by thermal vapour deposition of gold onto well cleaned FTO glass pieces (2.5 x 2 cm) using a custom built thermal evaporator (ISTA, Faenza, Italy). The average pressure in the evaporation chamber was of the order of 9 X 10^{-6} torr. Pt coated counter electrodes were prepared by repeated spraying of a 5 X 10^{-3} M H_2PtCl_6 solution in isopropanol onto cleaned FTO glass pieces (2.5 x 2 cm). Pyrolysis of the resulting substrates at 380 C° for 15 minutes led to the formation of stable dark Pt clusters on the FTO surface.

4.2.1.5 Solar Cell assembly: sandwich type photoelectrochemical cells were assembled by clamping the photoactive electrode over the gold coated counter electrode. A parafilm® gasket (ca. 120 µm thick) was used to avoid the direct contact between the two electrodes and to confine the electrolytic solution inside the cell. The relay consisted of a 0.15 M solution of the desired Cu(I) complex in acetonitrile. A portion of it, typically 1/10, was oxidized to Cu

[100] Zabri, H.; Gillaizeau, I.; Bignozzi, C. A.; Caramori, S.; Charlot, M.-F.; Cano-Boquera, J. C.; Odobel, F. *Inorg.Chem.* **2003**, *42*, 6656-6666.
[101] Nazeeruddin, M. K.; Kay, A.; Rodicio, I.; Humphry-Baker, R.; Mueller, E.; Liska, P.; Vlachopoulos, N.; Graetzel, M. *J.Am.Chem.Soc.* **1993**, *115*, 6382-6390.

(II) by addition of a stoichiometric amount of $NOBF_4$. Li^+ 0.5 M was added to all copper based electrolytic mixtures. The performances of the new mediators were compared to a classical LiI/I_2 0.5/0.05 M electrolyte. In case of iodide/iodine mixtures a Pt sputtered counter electrode was used.

4.2.1.6 Thin Layer Electrochemical Cell : to gain some kinetic information about the electrochemical behaviour of selected copper complexes a cofacial three electrode thin layer electrochemical cell was assembled. The surface of an FTO glass was mechanically (by scoring the FTO surface with a carborundum tip) or electrochemically etched in order to obtain an insulating gap between the two halves of the same electrode, among which a resistance > 50 MΩ was measured. One half was coated with gold and served as the working electrode (WE, 1 cm^2 geometrical area), the other was coated with silver and served as the quasi-reference electrode (QRE). The WE+QRE electrode was cofacially assembled with a gold coated counter electrode (CE), using a parafilm® frame (ca.120 µm) as a spacer. Each electrode was appropriately connected to the potentiostat leads via copper stripes protected and sealed with Surlyn®, in order to avoid accidental contacts between them and the electrolyte. Few drops of electrolyte consisting of 0.1 M $LiClO_4$ and 5 x 10^{-4} M Cu (I)/Cu (II) in ACN were injected in the cell and the measurements performed.

4.2.2 Synthesis of ligands and related Cu(I) complexes.

4.2.2.1 Ligands preparation : bipyridine and quinoline derivatives used for this study are shown in Figure 67.

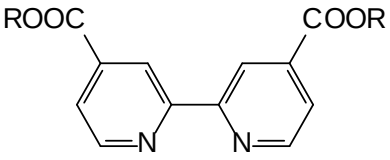

R = Ethyl (**1**),
n-butyl (**2**)
tert-butyl (**3**)

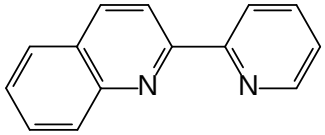

4

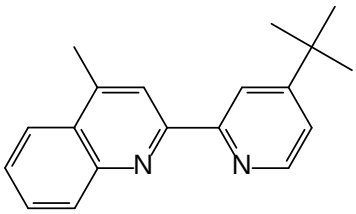

5

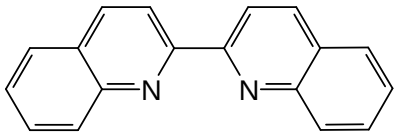

6

Figure 67. Structures of the ligands employed for the preparation of Cu(I) complexes: 2,2'- bypiridine di-4,4'-ethyl ester (bpy-$(COOEt)_2$) (**1**), 2,2'-bypiridine-di-4,4'-n-butyl ester (bpy-$(COOnBut)_2$ (**2**) , 2,2'-bypiridine-di-4,4'-Tert-butyl ester (bpy-$(COOTbut)_2$) (**3**), 2,2'-pyiridyl-quinoline (PQ) (**4**), 4-methyl,4'-Tert-butyl-2,2'pyridil-quinoline (MeTbPQ) (**5**), 2,2'biquinoline (BQ) (**6**).

2,2'-bypiridine-di-4,4'-n-butyl ester (bpy-$(COOnBut)_2$) (**2) :** A solution of 2,2'-bipyridyl-4,4'-dicarboxylic acid (850 mg; 3.48 mmol), concentrated sulfuric acid (1ml) and normal-butanol (40ml), was heated at reflux for 3 days. After this time the reaction mixture was cooled to room temperature and concentrated to few milliliters under reduced pressure. The liquid residue was neutralized by addition of aqueous Na_2CO_3 and a yellowish solid separated. Subsequent chromatographic separation of the precipitate (Silica Gel 60/ethyl acetate) afforded the pure product as white waxy solid.

^{1}H NMR (200MHz, $CDCl_3$, δ ppm): 9.00 (s,2H); 8.85 (dd,2H); 7.90 (dd,2H); 4.40 (t,4H); 1.70 (m, 4H); 1.50 (m, 4H); 1.00 (t, 6H).

2,2'-bypiridine-di-4,4'-tert-butyl ester (bpy-$(COOTbut)_2$) (**3**) : 1 g of H_2DCB was suspended in 100 ml of $SOCl_2$ and refluxed under nitrogen for several hours to obtain the corresponding di-acylchloride. The reaction was deemed complete when the solid was totally dissolved, leading to a perfectly transparent pale yellow solution. The excess $SOCl_2$ was removed by rotary evaporation and the solid residue was immediately reacted with an excess of sodium tert-butoxide (obtained by reaction of metallic Na with anhydrous tert-butanol) in tert-butanol. The resulting yellowish slurry was stirred for a few hours under gentle heating,

treated with an excess of aqueous $NaHCO_3$ and repeatedly extracted with CH_2Cl_2. The organic phase was collected, dried over Na_2SO_4 and rotary evaporated to dryness, affording the desired compound as a white waxy solid.

^{1}H NMR (300MHz, $CDCl_3$, δ ppm) : 8.8 (m,4H); 7.85 (m,2H); 1.6 (s,18H).

^{13}C NMR (300MHz, $CDCl_3$, δ ppm) : 164.21; 156.53; 149.94; 140.53; 123.14; 120.55; 28.09.

4-*tert*-butyl-pyridil-N-oxide: 14,64 ml of 4 Tert-butyl pyridine were dissolved in 66.7 ml of glacial acetic acid. 10.3 ml of 30 % v/v H_2O_2 were then added and the resulting mixture was refluxed for 24 hours. Solvents were removed by rotary evaporation and a yellow viscous oil was obtained. The residue was diluted with water and neutralized with 20 w/v NaOH. The aqueous solution was extracted with dichloromethane (2 x 40 ml). The organic layer was collected and dried over Na_2SO_4. After evaporation of the solvent under reduced pressure a pale yellow oil was obtained. The liquid solidified after 2 days at 4 C°. The purity of the product was confirmed by TLC (silica gel, AcOEt-MeOH 9-1, NH_3) and NMR.

^{1}H NMR (300 MHz $CDCl_3$ δ ppm) : 8.1 (d, 2H); 7.2 (d, 2H) 1.2 (s, 9H).

4-*tert*-butyl-2-cyano-pyridine: to a solution made of 6 g (0.0398 mol) of 4-tert-butyl-pyridyl-N-oxide and of 5 g (0.0504 mol) of trimethyl-silyl-cyanide in anhydrous dichloromethane were added, over a 30 minutes period, 4.64 ml of dimethyl-carbamyl-chloride, dissolved in 10 ml of anhydrous CH_2Cl_2. The resulting reaction mixture was left under stirring at room temperature for 36 hours, during which the colour of the solution turned from pale yellow to brownish. A 10 % Na_2CO_3 solution was slowly added by means of an addition funnel. The two phases were allowed to separate and the organic layer was collected. The aqueous phase was extracted twice with 25 ml of CH_2Cl_2. The combined organic extracts were dried over sodium sulphate and the solvent evaporated under reduced pressure. A yellow oil was obtained.

^{1}H NMR (300 MHz $CDCl_3$ δ ppm) : 8.6 (d,1H); 7.7 (d,1H); 7.5 (dd, 1H); 1.3 (s, 9H)

4-*tert*-butyl-2-acetyl-pyridine: to the Grignard reagent CH_3MgI, obtained by reaction of 2.67 g of Mg shavings with 6.89 ml of CH_3I in anhydrous diethyl ether, 6.85 g of 4-Tert-butyl-2-cyano pyridine, dissolved in 70 ml of anhydrous diethyl ether, were added. The resulting mixture was left under stirring at room temperature for 3 hours, after which the reaction was quenched with saturated aqueous NH_4Cl. The two phases separated and the organic layer was collected. The aqueous layer was further extracted with ethyl acetate (2 x 30 ml) and the resulting combined organic extracts were subsequently washed with water (3

x 30 ml), with 10 ml of a concentrated NaCl solution and dried over magnesium sulphate. The solvents were removed under reduced pressure and the residue (a viscous oil) was purified by column chromatography (silica gel 60, CH_2Cl_2). 2 g of pure product were obtained.

^{1}H NMR (300 MHz $CDCl_3$ δ ppm) : 8.6 (d ,1H); 8.1 (d ,1H); 7.5 (dd,1H); 2.73 (s,3H); 1.35 (s, 9H).

2-amino-acetophenone: 2 g of 2-nitro-acetophenone were suspended in 30 ml of water, 4.26 g of tin granules and 10,3 ml of concentrated HCl were then added and the resulting mixture was refluxed for 2 hours. After this time the reaction mixture was cooled at room temperature, filtered from undissolved tin granules and neutralized with 33% NaOH. Precipitated $Sn(OH)_2$ was removed by filtration. The aqueous filtrate was collected and extracted with diethylether (3 x 30 ml). The combined organic extracts were collected, washed with water (2 x 30 ml) and dried over sodium sulphate. The solvent was removed under reduced pressure and a yellow oil corresponding to the desired product was finally obtained.

IR in KBr pellet : 3463, 3341 cm^{-1} (NH_2) ; 1644cm^{-1} (C=O)

4-methyl,4'-tert-butyl-2,2'pyridil-quinoline (MeTbPQ) (**5**): 0.683 g of 2-acetyl-4-tertbutyl-pyridine and 0.52 g of 2-amino-acetophenone were dissolved in 20 ml of ethanol. 7 ml of 1 M KOH were added and the resulting mixture was refluxed 12 hours. The reaction mixture was poured in 100 ml of water (the formation of colloidal precipitate was observed), the pH was adjusted to neutrality with HCl and the solvents were removed under reduced pressure. The residue was dissolved in CH_2Cl_2, while the insoluble salt (KCl) was removed by filtration. The product was purified by column chromatography (silica gel 60, AcOEt/CH_2Cl_2 1/9). 0.5 g of a yellowish oil corresponding to the desired product (**5**) were obtained. The oil solidified at 4 C° after several days to give a pale yellow solid.

^{1}H NMR (300 MHz, $CDCl_3$ δ ppm) : 8.65 (d, 2H); 8.4 (s, 1H); 8.2 (d, 1H); 8 (d, 1H), 7.7 (m, 1H); 7.55 (m, 1H); 7.18 (dd,1H); 2.8 (s,3H); 1.2 s (9H). ESI-MS: 277 ($M+H^+$)

4.2.2.2 Cu(I) complexes : the structures of the complexes used in this study are reported in Fig.68.

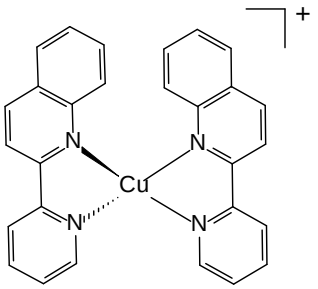

[Cu(bpy-(COOEt)$_2$)$_2$]$^+$ (7)
[Cu(bpy-(COOnBut)$_2$)$_2$]$^+$ (8)
[Cu(bpy-(COOTbut)$_2$)$_2$]$^+$ (9)

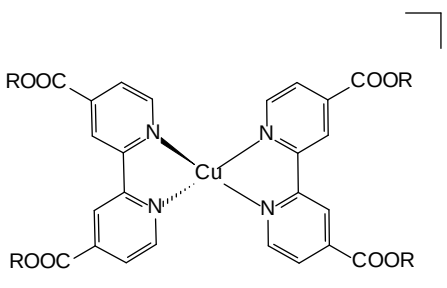

[Cu(PQ)$_2$]$^+$ (10)

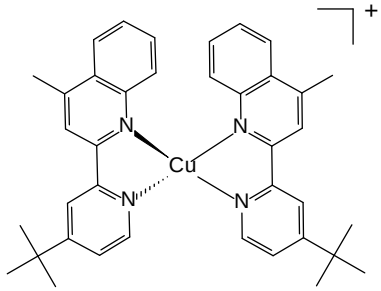

[Cu(MeTbPQ)$_2$]$^+$ (11)

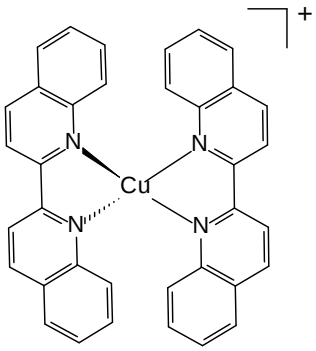

[Cu(BQ)$_2$]$^+$(12)

Figure 68. Structure of Cu(I) complexes employed as electron transfer mediators in photoelectrochemical cells.

[Cu(ACN)$_4$]ClO$_4$: [Cu(ACN)$_4$]ClO$_4$ was prepared by reacting [Cu(H$_2$O)$_6$](ClO$_4$)$_2$ with an excess of Cu^0 powder in acetonitrile (ACN), under stirring, at room temperature. In few hours the colour of the solution gradually turned from blue to colourless, testifying the disappearance of the Cu(II) starting material. The Cu(0) excess was removed by filtration and the transparent colourless solution was rotary evaporated to dryness to give a white solid[102].

General preparation of Cu(I) mediators: in order to remove eventual Cu(II) impurities one equivalent of [Cu(ACN)$_4$]ClO$_4$, dissolved in ACN, was equilibrated in presence of an excess of metallic copper powder for about 30'. Cu(0) was eliminated by filtration and the resulting solution was slowly added, under stirring, to two equivalents of the desired ligand dissolved in acetonitrile. The colour change from colourless to red-brown or purple,

[102] [Cu(I)(ACN)$_4$]$^+$ dismutes in presence of water traces to give back Cu(0) and Cu(II). As a consequence, even in the solid state, after few weeks, a chromatic variation from white to pale blue, due to the formation of Cu(II) impurities, could be observed.

depending on the ligand, was instantaneous. Nevertheless, the resulting solution was allowed to sit under stirring at room temperature for about 4 hours before isolation of the desired product. Typically, the solution was evaporated to dryness, the solid residue was redissolved in the minimum amount of ACN and precipitated by addition of an excess of diethylether. The solid was collected by suction filtration, washed with ether and dried at room temperature.

$[Cu(bpy\text{-}(COOEt)_2)_2]ClO_4$(7), brown solid:

^{1}H NMR (200MHz, CD_3OD, δ ppm): 9.1 (s,2H); 8.7 (s,2H); 8.2 (s,2H); 4.5 (q,4H); 1.45 (t, 6H);

Anal.Calcd.for $C_{32}H_{32}O_{12}N_4ClCu$: C, 50.33; H, 4.22; N, 7.33. Found : C, 48.38; H, 3.67; N 7.

$[Cu(bpy\text{-}(COOnBut)_2)_2]ClO_4$ (8), brown solid:

^{1}H NMR (200MHz, CD_3OD, δ ppm): 9.4-8 (broad,12H); 4.45 (m, broad, 8H); 1.8 (m,broad,8H); 1.5 (m,broad,8H); 1.0 (t,12H).

Anal.Calcd.for $C_{40}H_{48}O_{12}N_4ClCu$: C,54.86; H, 5.52; N, 6.40. Found: C, 54.59; H, 5.57; N, 6.48.

$[Cu(bpy\text{-}(COOTbut)_2)_2]ClO_4$ (9), brown solid:

ESI-MS: 775 (M^+)

$[Cu(PQ)_2]ClO_4$ (10), red-brown solid:

^{1}H NMR (200MHz, CD_3OD, δ ppm): 8.8 (m, 6H); 8.6 (d,2H); 8.3 (t,2H); 8.1 (d,2H); 7.8-7.6 (m,6H); 7.45 (t,2H).

Anal.Calcd.for $C_{28}H_{20}N_4O_4ClCu$: C,58.44; H, 3.5; N, 9.74. Found: C, 58.01; H, 3.43; N, 9.61.

$[Cu(MeTbPQ)_2]ClO_4$ (11), red-brown solid:

^{1}H NMR (200MHz, CD_3OD, δ ppm): 8.8 (s,2H); 8.7 (s,2H); 8.45 (d,2H); 8.2 (d,2H); 7.8 (d,2H); 7.7 (d,2H); 7.6 (t,2H); 7.45 (t,2H); 2.9 (s,6H); 1.55 (s,18H).

Anal.Calcd.for $C_{38}H_{40}N_4O_4ClCu$: C,63.77; H, 5.65; N, 7.82. Found: C, 59.87; H, 5.35; N, 7.31.

$[Cu(BQ)_2]ClO_4$ (12), purple solid :

^{1}H NMR (200MHz, CD_3OD, δ ppm): 7.45 (d,4H); 7.35 (d,4H); 6.55 (d,4H); 6.2 (d,4H); 6.05 (m,4H); 5.85 (m,4H).

4.2.3 Electrochemical Characterization.

The basic electrochemical properties of the Cu(I) complexes reported in this work, investigated by cyclic voltammetry on glassy carbon electrodes, are summarized in Table VI.

Table VIII. Electrochemical properties of Cu(I) mediators in ACN/$LiClO_4$ 0.1 M, 100 mV/s.

Complex	$E_{1/2}$ (mV Vs SCE)	Anodic Peak (mV Vs SCE)	Cathodic Peak (mV Vs SCE)	Peak separation (mV)
(7)	445	576	214	362
(8)	350	516	187	329
(9)	350	998	-302	1300
(10)	350	410	292	120
(11)	280	342	226	120
(12)	688	750	627	123

Oxidation of a tetrahedral Cu(I) complex to Cu(II) involves the removal of an electron from a metal centred T_2 orbital with a prevailing antibonding character. The preliminary electrochemical study showed that almost all of the Cu(I) complexes have a sufficiently negative oxidation potential to guarantee an ample driving force for reduction of most part of oxidized sensitizers. The sole exception is constituted by $[Cu(BQ)_2]^+$ (**12**) which, due to the strong stabilization of metal centred orbitals induced by the augmented back bonding to four quinoline rings, exhibit an $E_{1/2}$ only 100 mV negative of the dye Z 907.

In general Cu(I) complexes give rise to slow electron transfer processes, due to the high nuclear rearrangement that accompanies the electron transfer, as shown by the peak separations which, in all cases, exceed the 60 mV expected for an ideally reversible monoelectronic process. It is however clear from the data reported in Table VI that pyridil-quinoline based complexes exhibit a markedly different electrochemical behaviour with respect to the bipyridine based ones. Indeed, the former showed well defined diffusion limited peaks, with a peak separation (without compensation of cell resistance) of the order of 100 mV, while the latter showed generally broad poorly resolved peaks with separations higher than 300 mV. Exceptionally slow is the quasi-reversible process associated to the oxidation of (**9**) with a peak separation of the order of 1.3 V, maybe caused by the presence of

bulky Tertbutyl-ester groups which contribute to decouple the metal centre from the electrode. As a first approximation, neglecting specific interactions with the electrodic surface (which are however possible), such, quite unexpected, difference is ostensibly related to the geometry change that accompanies the oxidation of Cu(I) to Cu(II) : in case of Cu (I) pyridil-quinoline complexes, a smaller inner sphere reorganization energy probably contributes to limit the activation barrier for the electron transfer. In general it could not be observed a dramatic dependence of the electrochemical behaviour of the reported Cu(I) complexes from the electrode material, i.e. similar peak shapes and separations were observed also on gold and platinum substrates. While carbon might reveal itself as an interesting and cheap cathode material, for a first preliminary study we used gold coated counter electrodes, due to our possibility of obtaining stable and homogeneous gold layers of known thickness. On the other hand, at present, we do not possess the technology and the knowledge to create analogous stable carbon deposits with the same characteristics.

4.2.4 Photoelectrochemical Characterization in Z-907 Sensitized Solar Cells.

The photoaction spectra obtained with the mediators (**7**)-(**12**) are shown in figure 69.

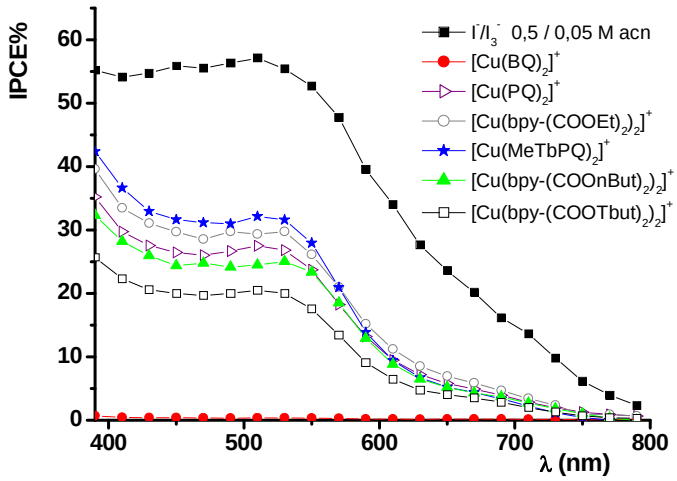

Figure 69. Photoaction spectra obtained in presence of Cu(I)/Cu(II) electron mediators using regenerative sandwich cells equipped with gold counter electrodes. (**11**) Stars; (**7**) open circles; (**10**) open triangles; (**8**) solid triangles; (**9**) open squares; (**12**) solid circles. Data compared to the I^-/I_3^- couple (black squares). Li^+ 0.5 M was added to all Copper based electrolytes.

As can be observed from Figure 69, the best performances were obtained with mediators (**11**) and (**7**), generating an almost identical maximum IPCE % of the order of

35%, about one half of that obtained with classical I^-/I_3^- couple. Copper based couples (**8**), (**9**) and (**10**) led to lower performances with maximum IPCE varying between 30 % (**10**) to about 20 % (**9**). While the low conversion efficiencies obtained with $[Cu(BQ)_2]^+$ (**12**) can be quite easily explained by the exceedingly positive oxidation potential which does not allow for an efficient dye regeneration, due to the low driving force for this process, the understanding of the different performances obtained with the other redox couples could be quite challenging. Since the same ruthenium sensitizer was used with all the different redox couples and the light harvesting efficiency (LHE) was always close to unity, the different IPCEs can only be explained in terms of different electron collection efficiencies (η). At the anodic compartment of the cell, losses due to electronic recombination with the oxidized sensitizer and with acceptor states of the electrolyte (namely Cu(II) centres) limit the number of electrons that are able to flow out of the cell as a photocurrent. Additionally, an inefficient Cu(I) regeneration at the counter electrode may lead to an increase of the steady concentration of Cu(II), ultimately increasing the probability of photoinjected electron recapture.

First we observe that, within the pyridil-quinoline based Cu(I) series, the alkyl-substituted $[Cu(MeTbPQ)_2]^+$ complex allowed to obtain a maximum IPCE about 20% higher with respect to the unsubstituted $[Cu(PQ)_2]^+$ mediator, indicating a possible beneficial effect of the alkyl chains on the mediator properties. Besides shifting the metal centred oxidation towards more negative values (280 mV for (**11**), 350 mV for (**10**)), slightly increasing the driving force for dye regeneration, the presence of bulky Tert-butyl chains might partially block the back recombination, decreasing the electronic coupling between Cu(II) acceptors and electronically occupied TiO_2 donor states. Considering the substituted bipyridine series, we clearly see that the performances decrease in the order (**7**) > (**8**)> (**9**), suggesting that, in this case, the increase in steric hindrance of the ligands does not improve the overall mediator efficiency, on the contrary, it has a detrimental effect. This finding could be surprising at first: however the electrochemical study showed that 4,4' di-substituted bipyridine complexes are intrinsically characterized by very slow electron transfer kinetics and bulky substituents might not be able to control recombination any further. On the other hand, their presence might introduce an additional, unnecessary, barrier which may affect negatively both the regeneration of the oxidized dye and the electrochemical response of the counter electrode.

In any case, all of the investigated Cu(I)/(II) couples are far from approaching the I^-/I_3^- performances, at least in terms of IPCE%, and a more detailed study of the two best

performing mediators, namely $[Cu(MeTbPQ)_2]^+$ (**11**) and $[Cu(bpy\text{-}(COOEt)_2)_2]^+$ (**7**) might allow us to gain some useful insights about their behaviour in an operating DSSC.

4.2.5 Electrochemical behaviour of $Cu(MeTbPQ)_2^+$ and $Cu(bpy\text{-}(COOEt)_2)_2$ on TiO_2 surface.

The evaluation of the electrochemical response of Cu(I)/(II) at a bare TiO_2 surface can provide us, at least qualitatively, with an indication of the importance of charge recombination events involving the copper based couples. In addition, since part of the recombination occurs at the exposed FTO surface, the effect of the presence of a compact TiO_2 blocking underlayer can be evidenced. Figure 70 reports the J-V curves recorded on FTO/TiO_2 electrodes in presence of the same concentration of Cu(I)/(II) and I^-/I_2 . Immediately prior to the measurement the oxidized mediator was electro-generated in the desired ratio in a conventional three compartments electrolytic cell by applying a constant +1V vs SCE potential, using a large area FTO working electrode.

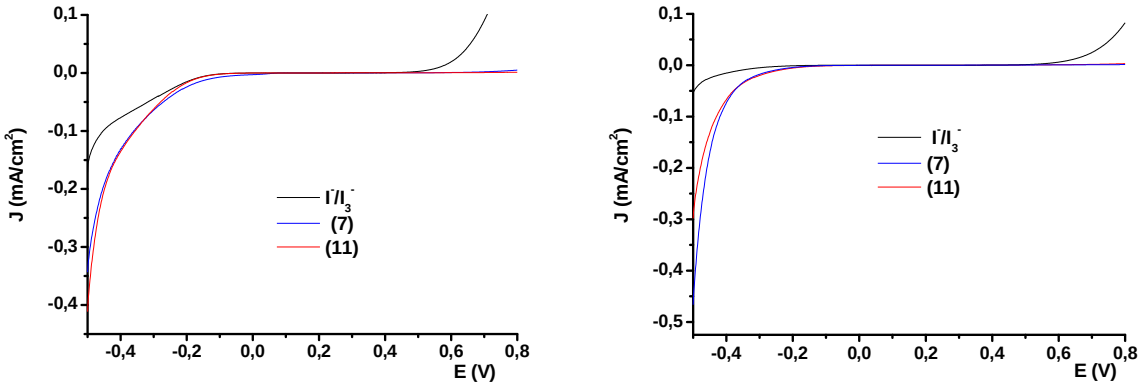

(a) (b)

Figure 70. J-V curves obtained on TiO_2 substrates in presence of 9 $x10^{-4}/10^{-4}$ M reduced/oxidized mediators in ACN/$LiClO_4$ 0.1 M. (**A**) mesoporous TiO_2; (**B**) mesoporous TiO_2 + compact TiO_2 underlayer. Scan speed 50 mV/s. Potentials are referred to SCE. The current density was calculated using the geometrical area (0.5 cm^2) of the electrode.

This experiment is basically equivalent to measuring the dark current of the cell using an uncoloured photoanode, in a three electrode arrangement. Considering Figure 70 (a), it is evident that in the potential interval between 0 and 0.5 V vs SCE only a negligible current flowed through the cell. In case of the iodide/iodine couple (black line) an anodic current,

due to I^- oxidation, quickly arose as the potential approached 0.6 V Vs SCE, while no faradic process associated to Cu(I) oxidation was observable. When the potential was scanned towards negative values a cathodic current started to flow, due to reduction of the oxidized mediator. However, at comparable potentials, the magnitude of the current obtained in case of I^-/I_3^- was about twice smaller than that observed in case of the Cu(I)/(II) complexes, suggesting a more efficient electron capture by Cu(II) centres with respect to I_3^-. It must be noted that (**7**) and (**11**) behaved almost identically with respect to current threshold and intensity. The presence of a compact blocking layer (Figure 70 (b)) had a positive effect, leading to a negative 100 mV shift of the cathodic current threshold and to an overall reduction of its magnitude. For example, in case of Cu(I) mediators, which, again, maintained an almost identical behaviour, to a current density of about 150 $\mu A/cm^2$ at -0.4 V Vs SCE (Figure 70 (a)), it corresponded, at the same potential, a value of less than 70 $\mu A/cm^2$ (Figure 70 (b)). Much smaller was, also in this case, the current associated to the bi-electronic I_3^- reduction. From these data, one might conclude that the lower efficiency of Cu(I)(/II) complexes is related to a more efficient recombination with electron-accepting species of the electrolyte, which leads to an higher dark current. Such conclusion would not have been entirely correct. Indeed, it must be considered that the presence of a dye like Z 907, with long alkyl chains designed to block recombination[103,104], might significantly modify the J-V characteristics of the real operating device.

4.2.6 Photoelectrochemical characterization under monochromatic conditions of Z-907 SSC using $Cu(MeTbPQ)_2^+$ and $Cu(bpy\text{-}(COOEt)_2)_2$ as electron transfer mediators.

Accordingly, the J-V curves of sandwich DSSCs were recorded under monochromatic light (510 nm, absorption maximum of Z 907 loaded on TiO_2) at low power intensity. We chose to investigate the photoelectrochemical behaviour of our redox systems under these conditions to avoid the set in of mass transport limitations that could conceal effects determined by their intrinsically different kinetic properties. Results are reported in Figure 71 (**A**)-(**B**)-(**C**).

[103] Wang, P.; Zakeeruddin, S. M.; Comte, P.; Charvet, R.; Humphry-Baker, R.; Graetzel, M. *J.Phys.Chem.B* **2003**, *107*, 14336-14341.
[104] Klein, C.; Nazeeruddin, M. K.; Di Censo, D.; Liska, P.; Graetzel, M. *Inorg.Chem.* **2004**, *43*, 4216-4226.

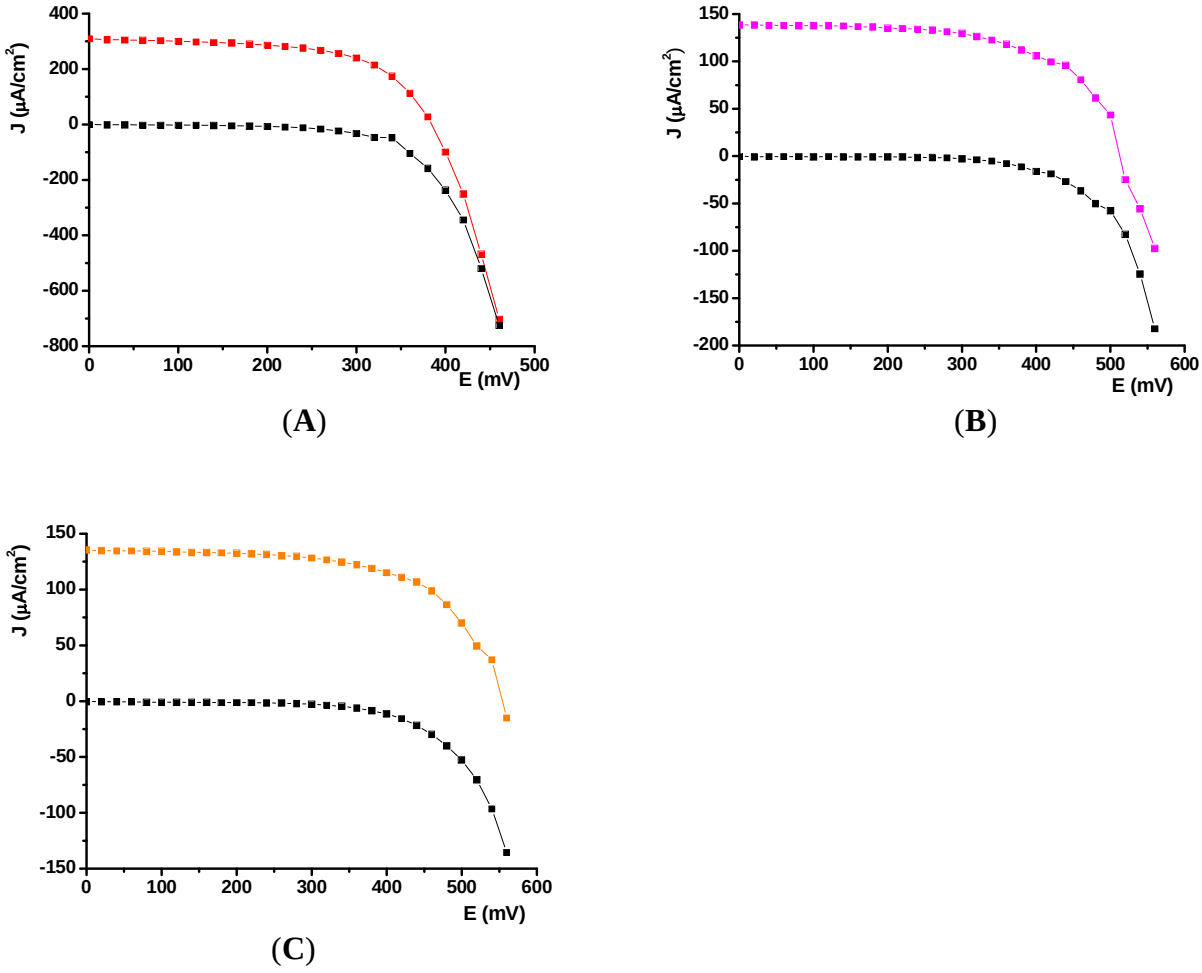

Figure 71. J-V characteristics of sandwich type DSSCs recorded under 510 nm monochromatic light irradiation. (**A**) LiI/I_2; (**B**) $[Cu(bpy\text{-}(COOEt)_2)_2]^{+/2+}$ (**7**) + 0.5 M Li^+; (**C**) $[Cu(MeTbPQ)_2]^{+/2+}$ (**11**) + 0.5 M Li^+. In all figures the black line is the cell dark current.

It is evident form the comparison of the curves in Figure 71 that the iodide/iodine couple produced the highest photocurrent, about twice that generated in presence of the copper complexes (**7**) and (**11**) which, under this point of view, showed very similar (if not identical) performances. The Voc of the I^-/I_3^- mediated cell (400 mV) was however ca. 150 mV lower than the open circuit photovoltage, of about 550 mV, obtained using copper mediators. The fill factor was slightly better in case of (**11**), with a value of 0.63, while in case of I^-/I_3^- and (**7**) very similar values of respectively 0.59 and 0.57 were obtained. The blocking effect of the dye, based on the steric hindrance of the nonyl chains, is expected to be more relevant in case of bulky mediators, like Cu(I)/(II)complexes, and the lower dark

current that was effectively obtained in such cases confirmed our expectations. The copper mediator's higher V_{oc}, lower dark current and satisfactory fill factors provide a strong indication that, on a suitably designed photoanode, recombination involving Cu(II) centres is not a critical performance limiting factor with respect to I^-/I_3^-. On the other hand, the lower Jsc generated by copper complexes might suggest a slow dye regeneration, which could be reasonably anticipated, given the slow kinetics that should be associated to the Cu(I)/(II) redox chemistry.

From the photoelectrochemical study it is evident how the two structurally different complexes (**7**) and (**11**), characterized by a distinct electrochemical behaviour (see Table VI) produce quite similar results when employed in a DSSC.

4.2.7 Evaluation of the heterogeneous electron transfer processes at gold counter electrode of $Cu(MeTbPQ)_2^+$ and $Cu(bpy\text{-}(COOEt)_2)_2$.

In order to complete the electrochemical picture of these new species, the cathodic heterogeneous electron transfer processes at gold counter electrodes were investigated. In order to do so, the Cu(I)/(II) electrochemical response was examined on the same substrates (gold coated FTO) used to build the regenerative solar cells. In order to gain kinetic information, a thin layer configuration, inspired by the work of Cameron et al.[105] was adopted. Due to the close spacing between working and counter electrodes, and to the fact that the electroactive species were continuously regenerated at the counter electrode of the cell, a kinetic controlled regime was quickly established for scan speeds higher than 300 mV/s, as demonstrated by the sigmoidal shape of the redox waves (Figure.72) and by the substantial independency of the peak current from the scan speed. Assuming a single step outer sphere electrochemical reaction, from the analysis of the cathodic branch of the voltammogram, by use of the high field approximation of the Butler and Volmer Equation, corrected for mass transport effects, one should obtain the equilibrium exchange current (which is a direct estimate of the heterogeneous electron transfer rate constant) and the transfer coefficient from, respectively, the intercept and the slope of the linear trait of the ln i Vs overpotential (η) curve (Figure 73) .

[105] Cameron, P. J.; Peter, L. M.; Zakeeruddin, S. M.; Graetzel, M. *Coordination Chemistry Reviews* **2004**, *248*, 1447-1453.

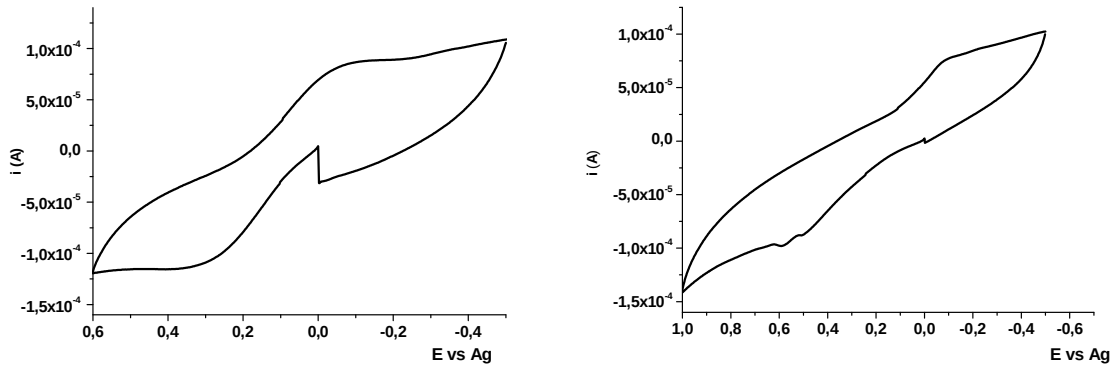

Figure 72. Cyclic voltammograms obtained in a thin layer electrochemical cell in presence of 5 x 10^{-4} M Cu(I)/(II) in ACN/$LiClO_4$ 0.1 M. Au/Au/Ag, scan speed 700 mV/s. (**A**) $[Cu(MeTbPQ)]^{+/2+}$ (11); (**B**) $[Cu(bpy\text{-}(COOEt)_2)_2]^{+/2+}$.

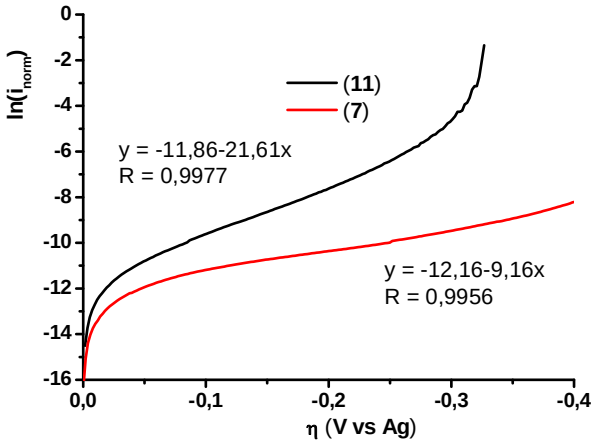

Figure 73. Logarithmic analysis of the cathodic branch of the cyclic volatammograms reported in Figure 6 . Black line (**11**); red line (**7**). The Exchange current was evaluated from the linear fit of of the ln (current)-overpotential curve. As expected, the analysis of the anodic branch led, within a good approximation, to the same result. The exchange current given in the text is the averaged value.

While the exchange currents of both complexes were found to be in the same order of magnitude, comprised between 10^{-5} and 10^{-6} A, the exchange current associated to (**11**) was about 1.5 times larger than that generated by (**7**) (7.40 ± 0.39 µA for (**11**), 4.80 ± 0.60 µA for (**7**)). The transfer coefficient of (**11**) was also higher, (ca 0.5 for (**11**), ca. 0.3 for (**7**)) as can be visibly appreciated from the steeper slope of its ln i-η curve (Figure 73, black line). These results lead us to conclude that $[Cu(MeTbPQ)_2]^{+/2+}$ couple has better (*but not dramatically better*) redox characteristics and a more satisfactory electrochemical response at the counter electrode of the cell, being potentially capable of sustaining higher current

densities. This fact may partly explain the higher fill factor obtained in case of (**11**): indeed, to a more facile heterogeneous electron transfer kinetic at the cathodic compartment it corresponds a decrease of the overall series resistance of the cell, finally leading to an improvement of the fill factor.

4.2.8 Conclusions

A series of Cu(I)/Cu(II) redox couples based on substituted bipyridines and pyridil-quinoline complexes was evaluated as electron transfer mediators in regenerative photoelectrochemical cells. The photo-electrochemical study evidenced maximum conversion efficiencies of the order of 35-40 %, still to low to be considered of practical interest for replacing the classical I^-/I_3^- couple. The reasons of such low efficiencies could be explained by a slow dye reduction, leading to modest Jsc, rather than by an efficient photoinjected electron / Cu(II) recombination, since both the Voc and the fill factor obtained with copper mediated cell were higher than the corresponding I^-/I_3^- based DSSC. The presence of a suitably designed dye is however believed to be crucial for suppressing the parasitic electronic recapture by Cu(II) acceptors. Future spectroscopic investigations of charge separation events involving these new mediators are expected to provide additional precise information about the electron transfer processes involving Cu(I)/(II) species. The understanding of the relationship between mediator structure, redox properties, and interfacial electron transfer kinetics may allow us to rationally design new more efficient relays in the near future.

Chapter 5

Natural dyes as sensitizers for DSSCs.

5.1 Methods and experimental procedures.

5.1.1 Materials.

5.1.2 DSSCs fabrication.

5.1.2.1 TiO_2 electrode preparation.

5.1.2.2 Relay solution preparation.

5.1.2.3 Counter electrodes preparation.

5.1.2.4 Photoelectrochemical cell assembly.

5.1.3 Photoelectrochemistry.

5.1.4 Transient spectroscopy.

5.2 Photophysical characterization in solution and on TiO_2 film of the natural extracts of eggplants, red radicchio, red wines such as Nero d'Avola and Giacché.

5.2.1 Stationary absorption spectroscopy.

5.2.2 Transient absorption spectroscopy.

5.3 Photoelectrochemical characterization of natural extracts sensitized solar cells.

5.3.1 Sensitization of TiO_2 through absorption from an alcoholic dye solution.

5.3.2 Sensitization of TiO_2 through absorption from an acidic aqueous dye solution.

5.4 Evaluation of the regeneration kinetics of the photoxidized dye by the electron transfer mediator through transient absorption spectroscopy.

5.5 Study of photoelectrochemical behaviour of DSS**C** containing raw red turnip extracts.

5.5.1 Methods and experimental procedures

5.5.2 Results and discussion.

5.1 Methods and experimental procedures.

5.1.1 Materials.

Acetonitrile, anhydrous ethanol and all other solvents (spectro grade and synthesis) are used as received. 4,4'-di-*tert*-butil-2,2'-bipyridine (Aldrich); $[Co(H_2O)_6](OTf)_2$, $LiSO_3CF_3$ (Aldrich), LiI and I_2 (Aldrich). All other materials are reagents grade and are used as receveid.

Synthesis of $[Co(DTB)_3](OTf)_2$: 4,4'di-*tert*-butyl-2,2'-bypiridine (3 equivalents) was dissolved under vigorous stirring in methanol at room temperature; when dissolution was completed, 1 equivalent of $[Co(H_2O)_6](OTf)_2$ was added. The solution turned immediately brown and the stirring was continued for 4 hours. The solvent was removed by rotary evaporation, the brown solid residue was re-dissolved in a minimum amount of acetonitrile and precipitated with diethyl ether. The solid was collected by suction filtration, washed twice with diethyl ether and allowed to dry at room temperature. In order to charachterize the complex by H-NMR spectroscopy, the Co(II) complex was oxidized to the diamagnetic Co(III) form by addition of a slight excess of the strong oxidizer $NOBF_4$ to an acetonitrile solution of the reduced form. The oxidation was completed almost instantaneously.

^{1}H-NMR of $[Co^{(III)}(DTB)_3](OTf)_2$ 300 MHz, δ ppm CD_3OD: 9,0 (d, 6H); 7,85 (m, 6H); 7,3 (d, 6H); 1,5 (s, 54H).

Natural extracts solutions: the natural extracts from eggplants peels, red radicchio leaves and red wines grapes have been furnished by Dc. Giuseppe Calogero, of CNR of Messina, Italy, directly in pH = 1 hydrochloric acid solution.

5.1.2 DSSCs fabrication

5.1.2.1 TiO_2 electrode preparation: TiO_2 nanoparticles were prepared by hydrolysis of Ti(IV) isopropoxide as describedbefore [106]. The nanocristalline TiO_2 thin films were deposited onto transparent conductive glass (FTO) by doctor blading. These films were fired at 450°C for 40 minutes. The still hot

[106] Nazeeruddin, M. K.: Kay, A.; Rodicio, I.; Humphry-Baker, R.; Mueller, E.; Liska, P.; Vlachpoulos, N.; Graetzel, M. *J. Am. Chem. Soc.* **1993**, 115, 6382.

electrodes were immersed in the dye solution and kept at room temperature (≈ 25°C) for 12 hours after which the absorption is deemed complete. The efficiency of absorption was evaluated by UV-Vis spectroscopy on film. Dye solutions were prepared using directly the acid water solution of the natural extracts as well as furnished by Dc. Calogero, or diluting them in ethanol in ratio 1:10 = H_2O:Et-OH. The solutions were centrifuged in order to remove any solid residue. Compact layer of TiO_2 are created by spin coating using a $Ti(^iPrO)_4$ 0.2 M solution in ethanol. The layer was then sintered at 450°C for 20 minutes. $TiCl_4$ treatment was performed on TiO_2 surface by deposition of few drops of $TiCl_4$ 0.2 M water solution on TiO_2 surface for 12 hours. After that the glass was rinsed with water, dried and sintered at 450°C for 20 minutes.

5.1.2.2 Relay solution preparation: Electron transfer mediators solutions were prepared by the addition of Co(II) 0,15 M to a lithium triflate 0.5 M acetonitrile solution. Standard LiI/I_2 0.5/ 0.05 M in acetonitrile was prepared.

5.1.2.3 Counter electrodes preparation: Several kinds of counter electrodes were used in this work: Pt coated and Au coated FTO glasses. Platinum coated counter electrodes were obtained by spraying a $5*10^{-3}$ M H_2PtCl_6 solution in isopropanol. This procedure was repeated 5 times until the distribution of H_2PtCl_6 clusters was homogeneous. Then the electrodes were dried and treated in an oven at 380°C, during which metallic platinum clusters were formed. Gold electrodes were obtained by thermal evaporation. At first a Cr underlayer of 10 nm thickness was deposited in order to allow a better stability of Au deposite on FTO glasses. Successively a layer of 30 nm of Au was deposited.

5.1.2.4 Photoelectrochemical cell assembly: Parafilm sealed cells were built by pressing the sensitized photoanode against a counter electrode equipped with a parafilm frame used to confine the liquid electrolyte inside the cell. The thickness of liquid layer corresponds roughly to the thickness of the frame border (around 120 μm). In this configuration the cell is stable toward solvent evaporation and leaking for several hours even using volatile solvents like acetonitrile.

5.1.3 Photoelectrochemistry

Photoaction spectra were obtained from DSSCs in a two-electrode sandwich cell arrangement. Electrolyte solution was sandwiched between a TiO_2 photoanode and a counter

electrode (when the Co(II) mediator was used the counter electrode was gold, while when the electrolyte was LiI/I_2 0,5/ 0,05 platinum was used as counter). The cell was illuminated with a 150 W Xe lamp coupled with a Applied Photophysics monochromator. The irradiated area was 0,5 cm^2. Photocurrents were measured under short circuit conditions with an Agilent v34401A digital multimeter, incident irradiance was measured using a 1 cm^2 centronic OSD100-7G calibrated silicon photodiode.

IPCE% was calculated according to equation 2.18:

$$IPCE_{(\lambda)} = 1.24 \cdot 10^3 \ (eV \cdot nm) \cdot I_{sc} \ (\mu A \cdot cm^{-2}) \ / \ \lambda(nm) \ I \ (mW \cdot cm^{-2})$$

Current- voltage curves are collected under the white light illumination of a 150 W Xe lamp which was further attenuated using a 390 nm cutoff filter and defocused in order to achieve the light intensity equal to 100 mW/cm^2 determined using a Molectron PowerMax 500A power meter. The current output of each cell was recorded under solar illumination sweeping the potential between 0 and 0.6 V using PGSTAT30, an echo Chemie electrochemical workstation.

5.1.4 Transient spectroscopy

Nanosecond transient absorption spectroscopy was performed to study the kinetic of electron transfer between the sensitizer and the mediator. The II harmonic of Nd-YAG laser (FWHM = 10 ns) was used as excitation source. A $KMnO_4$ filter with 5% of trasmittance was used to attenuate the pulse power to 0,35 mJ/imp. The sample was a film of sensitized TiO_2 sinterized on a microscope glass that was oriented at 45° with respect to direction of the excitation beam. A second microscope glass was pressed onto the former one and few drops of mediator solution was introduced by capillarity from the edge.

An interference filter was placed in front of entrance slit of the monochromator to remove the light scattering at 532 nm. The evolution of oxidized dye was observed at 470 nm for the eggplant extract, at 500 nm for the red radicchio extract and at 500 nm for the red wines solutions using a Photophysics Monochromator coupled to an Hamamatsu R3896 Photomultiplier.

Transient absorption spectra were recorded to ethanol solutions of the natural extracts and the same instrumental setup was used. The transient photovoltage decay was acquired on a decroy 600 MHz oscilloscope transferred on a PC and converted to ΔA decays by of an

home built Labview Program. The signal/noise ratio was optimized summing and averaging 30 decays. The decays obtained for the measurements in solution were fitted by mono-exponential decay while the decays obtained from the measurements on TiO_2 film were fitted by bi-exponential fitting and the $t_{1/2}$ of the dye was calculated.

5.2 Photophysical characterization in solution and on TiO_2 film of the natural extracts of eggplants, red radicchio, Nero d'Avola and Giacché.

5.2.1 Stationary absorption spectroscopy.

While Ru(II) based dyes used in nanocrystalline solar cells to attain high photoconversion efficiencies are expensive and difficult to synthesize, natural dyes are low cost and readily available in nature from many plants, fruits and so on. Flavonoids are sugar bounds poliphenols founds in all plants; a class of flavonoids known as anthocyanins is responsible for the red and purple colours of many fruits and flowers. The most common anthocyanin dye is cyanin. Tennakone et al. have previously used cyanidin (cyanin without the sugar moiety) in dye sensitized solar cells, but cyanidin is hard to isolate and less photostable than cyanin[107].

In collaboration with Dc. Giuseppe Calogero of the CNR of Messina, several natural extracts, arising from eggplant peels, red radicchio leaves and red wine (grapes) as Nero d'Avola and Giacché have been studied as sensitizers in photoelectrochemical solar cells. Red orange juice, previously analyzed[108], was prepared by squeezing the fresh fruits (red Sicilian oranges) and filtering the resulting solution in order to remove any residual fragments, without any further purification or extraction procedure. Employing this solution as dye in DSSCs, a photocurrent of 3.84 mA/cm^2 and a total efficiency of 0.66% was obtained under AM 1.5 illumination. These results prompted us to start a study on the photophysics and photoelectrochemistry of these natural pigments to gain insights on the extract raw interaction with TiO_2 nanoparticles. Eggplant and red radicchio extracts were obtained by suspending eggplant peels and radicchio leaves in a pH = 1 aqueous solution. Red wines were

[107] Tennakone K.; Kumara G. R.; Kumarasinghe A.; Wijayantha, K.; Sirimanne P.; *Semicond. Sci. Technol.* **1995**, 10, 1689
[108] G.Calogero and G. Di Marco; *Solar Energy Materials & Solar Cells* 92 (**2008**) 1341-1346.

diluted in water and the pH was adjusted to 1 and used directly as sensitizers solutions. All measurements have been performed by using the raw extracts without further purifications.

As described in Chapter 2.4.2 the pigments responsible of TiO_2 anchoring in these natural extracts are delphinidine and cyanidin which belong to the anthocyanins family and differ by the presence of an hydroxylic group in R_2, and malvidine (the main component of red wines) which is characterized by the presence of 2 methoxy groups in R_1 and R_2 positions (Figure 74).

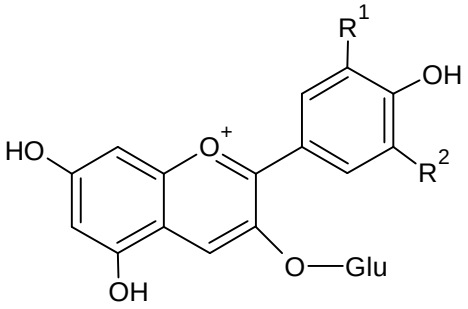

Figure 74 Chemical structure of anthocyanines.

In aqueous solution these species are in equilibrium between a protonated form (flavylium cation) and a quinonoidal form (figure 75). The extracts show a strong absorption band around 520 nm, typical of the anthocyanins family due to a $\pi-\pi*$ transition. Mixtures of natural dyes were stabilized in pH = 1 aqueous solution or in H_2O: EtOH the pH 1 aqueous solution 1:10 with ethanol.

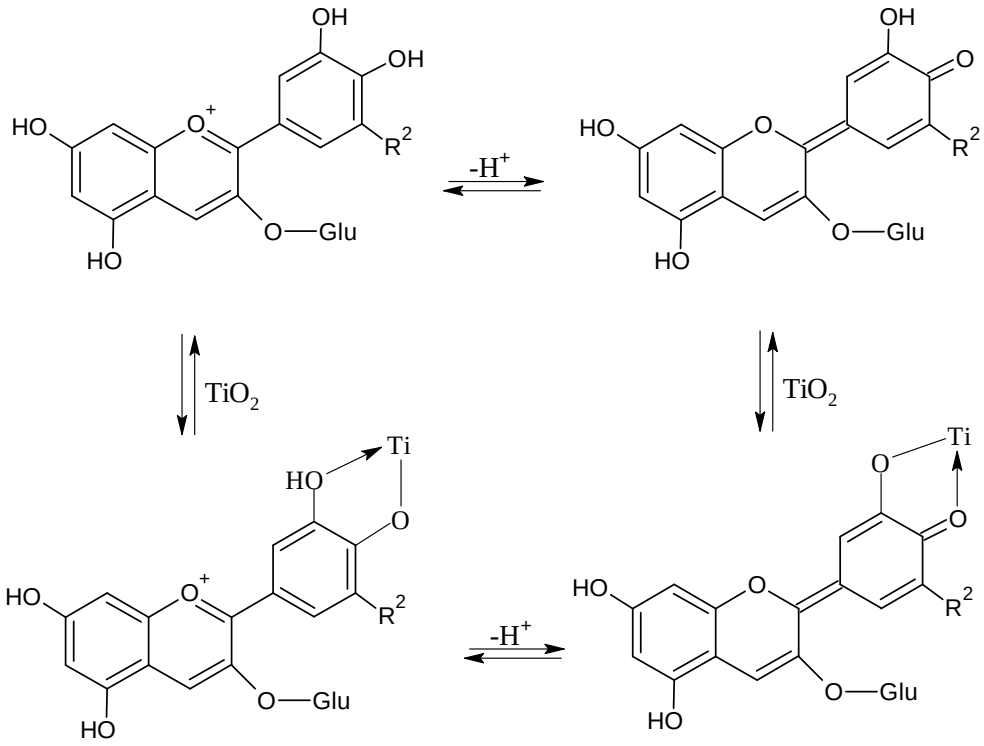

(a) Flavylium cation (b) Quinonoidal form

Figure.75 Equilibrium between flavylium and quinonoidal form in anthocyanins in solution and in presence of TiO_2 which is able to bind the anthocyanin.

The absorption spectra of these solutions (figure 76) show absorption maxima in the visible region which are sensitive to pH owing to the equilibrium reported in figure 75.

In table IX the absorption maxima of the investigated dyes solution are summarized

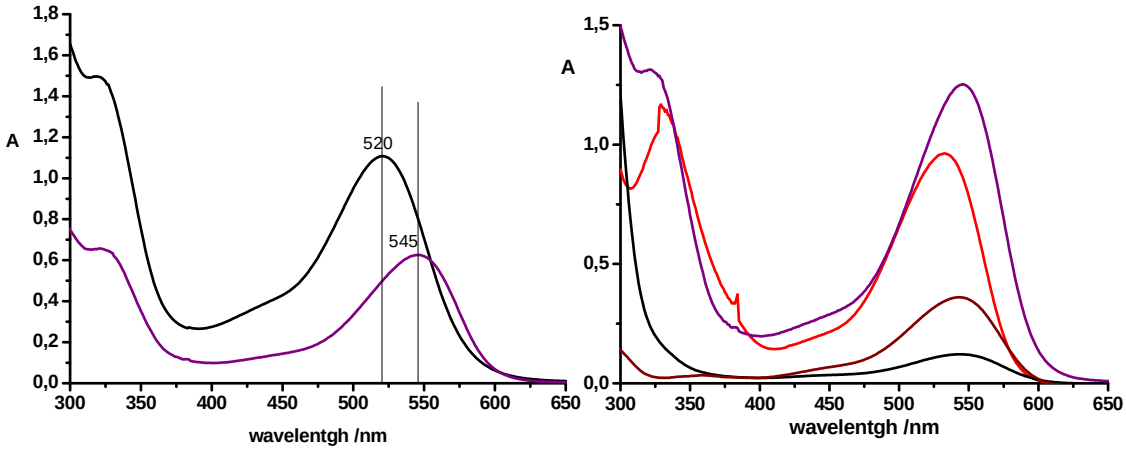

(a) (b)

Figure.76 (a) Absorption spectrum of eggplant extract in water solution at pH = 1 (black line) and in ethanol solution (violet line). (b) Absorption spectrum in ethanol solution of eggplant extract (violet line), red radicchio (red line), Nero d'Avola (wine line) and Giacchè (black line).

The visible absorption band also shifts to the red region upon complexation with metal ions. It's thought that the metal ions compete with the protons displacing them and shifting the flavylium-quinonoidal equilibrium toward the quinonoidal form.

The adsorption of these compounds on TiO_2 surface is very rapid and involves the quinonoidal form in equilibrium with a small amount of the flavylium form. The absorption spectra on TiO_2 show in fact an absorption band at 545 nm consistent with the quinonoidal form (Figure 77).

It should be noted (figure 77) that the absorption of the anthocyanins on the TiO_2 film is pH sensitive being higher in acidic solution where the flavylium form (protonated) predominates.

The binding geometry in figure 75 in agreement with DFT calculations indicate that HOMO is located on the chromophore end of the complex and LUMO electron density is located near the Ti end, showing that the LUMO is localized on the flavylium cation and on the quinonoidal form originated from the OH groups in orto position[109].

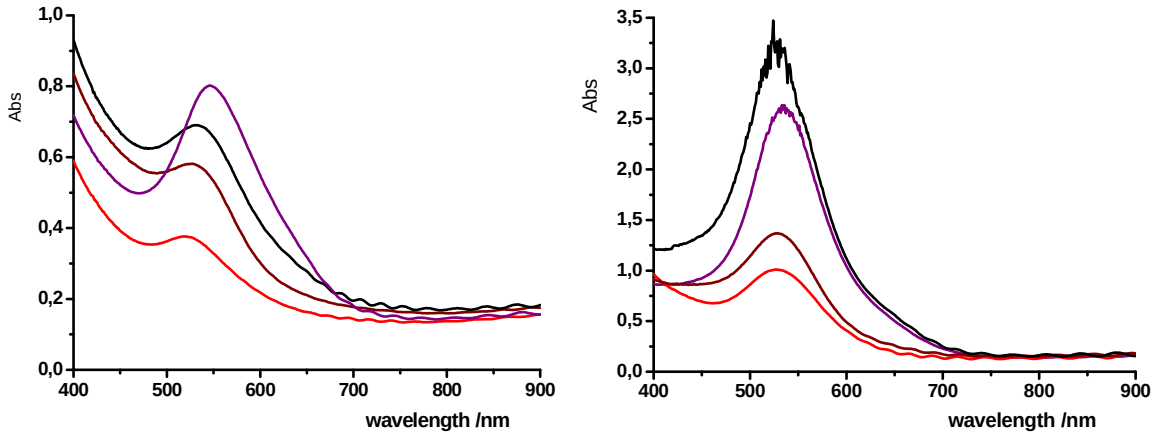

(a) (b)

Figure.77 Absorption spectra on TiO_2 film of eggplant extract (violet line), red radicchio (red line), Nero d'Avola (wine line) and Giacchè (black line).absorbed from (a) ethanol solution and (b) acid water solution.

[109] N. J. Cherepy, G. P. Smestad, M. Graetzel and J. Z. Zhang; *J. Phys. Chem.* B **1997**, 101, 9342-9351.

Table IX Photophysical properties of natural extracts arising from eggplant peels, red radicchio leaves and red wines grapes (in particular Nero d'Avola and Giacché).

	λ_{abs} (ethanol solution) /nm	λ_{abs} (water solution pH =1) /nm	τ (sol.) ($x10^{-7}$) /s*	τ (film) ($x10^{-7}$) /s*
Eggplant	546	520	0.686	0.99
Red Radicchio	533	510	0.368	1.84
Nero d'Avola	543	519	3.16	5.58
Giacchè	544	519	7.65	3.05

*They are obtained exciting the ethanol solution of the natural extracts at 532 nm and observing the decay at 450 nm. Measurements on TiO_2 film were observed at 500 nm.

5.2.2 Transient absorption spectroscopy.

Transient absorption spectra were recorded in ethanol solution of the different dyes and compared with the spectra of the same dyes absorbed on TiO_2 films. The spectra shown in figure 78 reveal a distinctive features of the excited dyes, positive absorption in the 400-480 nm region and 580-700 nm region accompanied by an intense bleaching from ca. 480 nm to ca 580 nm, with small shifts of the negative absorption depending by the dye. These spectral features are considerably different from those observed from the dye adsorbed on TiO_2. the transient absorption spectra of the adsorbed dyes are in fact lacking of the positive absorption in the 580-700 nm region and show an intense bleach which is red shifted with respect to the one observed for the dye solution. The lack of the positive absorption at 580-700 nm is most probably due to the excited charge injection to the conduction band of the TiO_2 leaving on the surface the radical cation of the quinonoidal species which is expected to adsorb at lower energy with respect to the neutral specie.

The lifetimes of the transient shown in figure 78 are summarized in table IX. It can be noted the both eggplants and red radicchio extracts are short living with respect to the red wines dyes and that the lifetime of the transient observed for the dyes on TiO_2 are remarkably longer. This is due to the fact that the charge recombination between conduction band electron and the radical cations is an interfacial process involving spatially separated redox sites, while excited state decay involves electron relaxation from $\pi*$ to π orbital localized on the same molecule.

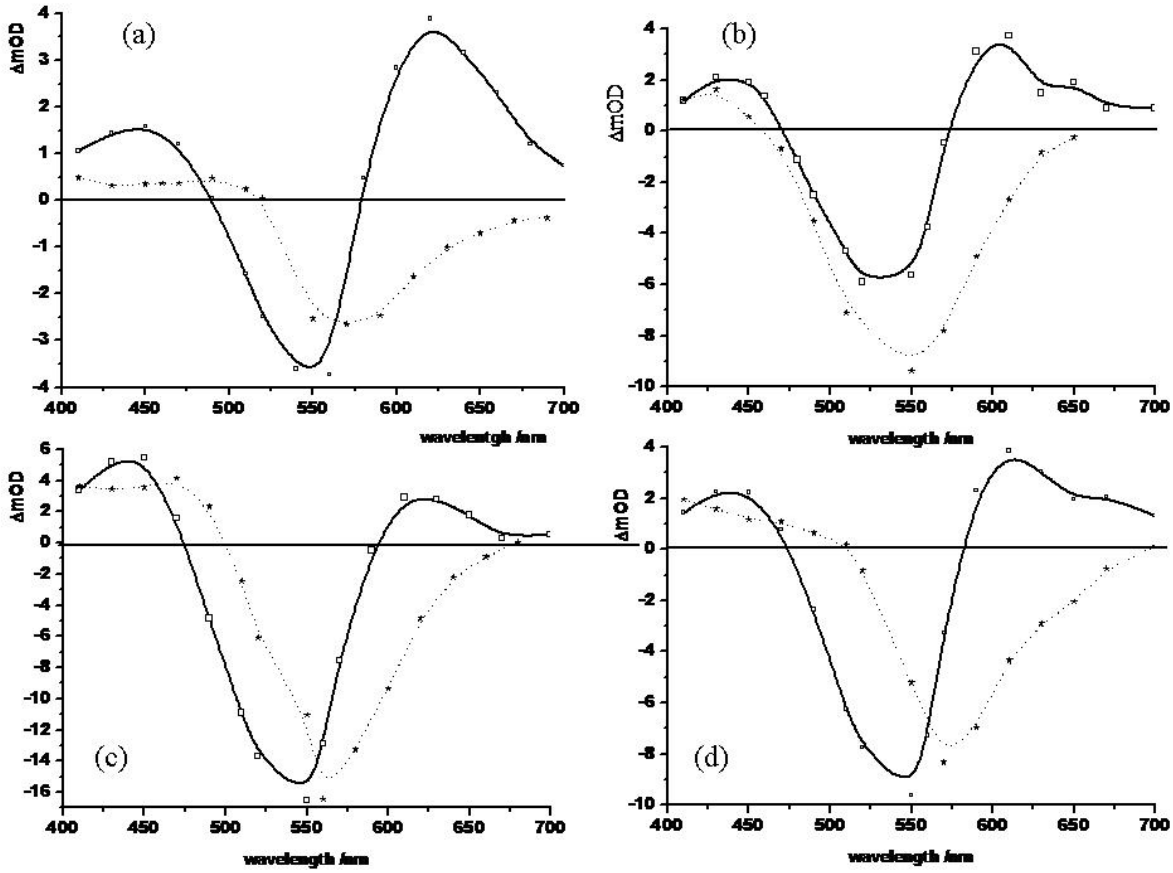

Figure.78 Transient absorption spectra in ethanol solution (solid line) and on TiO_2 film (dot line) of (a) eggplant extract (explored at 25 ns); (b) red radicchio (explored at 20 ns); (c) Nero d'Avola (explored at 80 ns) and (d) Giacchè (explored at 240 ns).

5.3 Photoelectrochemical characterization of natural extracts sensitized solar cells.

5.3.1 Sensitization of TiO_2 through absorption from an alcoholic dye solution.

The natural extracts of radicchio, eggplants and red wines in aqueous solution at pH 1 were diluted with ethanol (1:10) and used directly for absorption and sensitization of TiO_2 film in order to test their photoconversion efficiency in DSSCs. The IPCE% measurements shown in figure 79 point out the behaviour of this mixture when employed as sensitizers in DSSCs where Iodide / triiodide 0.5/ 0.05 M is used as electron transfer mediator and Pt/FTO as counter electrode material.

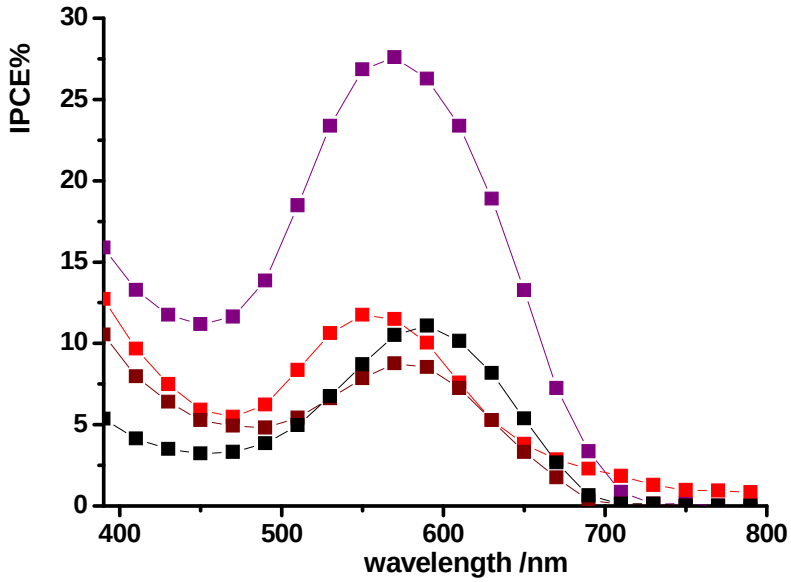

Figure.79 IPCE% measurements of DSSCs using LiI/ I_2 0.5/ 0.05 M in acetonitrile and sputtered Pt/FTO as counter electrode. TiO_2 film was sensitized with eggplant extract (violet line), red radicchio (red line), Nero d'Avola (wine line) and Giacchè (black line).

DSSCs sensitized with eggplant solution reach an IPCE% value of 27% at the maximum of the HOMO-LUMO transition, which is the best one obtained in these conditions. Nero d'Avola, Giacchè and red radicchio show in fact an IPCE% value around 10% . The low IPCE% values obtained with red wines may be explained by the fact that the main component of these natural extracts is malvidine which is characterized by the presence of methoxy groups in R_1 and R_2 position. This prevents a coordination with the TiO_2 by the side where LUMO is located inducing a loss in injection efficiency. So cyanidin and delphinidine, which bind the TiO_2 and ensure an efficient injection to the conduction band of the semiconductor, represent only a small fraction of the dye anchored to the TiO_2 nanoparticles. In the case of the dyes extracted from radicchio, the low IPCE% can be related to the weak absorption. The photoanodes show in fact a maximum optical density of 0.4 (figure 77) reducing LHE term which controlled IPCE% (see equation 2.17).

These experiments were performed by using a simple photoanode formed by the FTO glass and a thin film (a few micrometer thick) of TiO_2 colloidal paste.

The same measurements were repeated introducing an overlayer of $TiCl_4$ on TiO_2 film and as we can see from figure 80.a, a remarkable improvement of IPCE% was obtained.

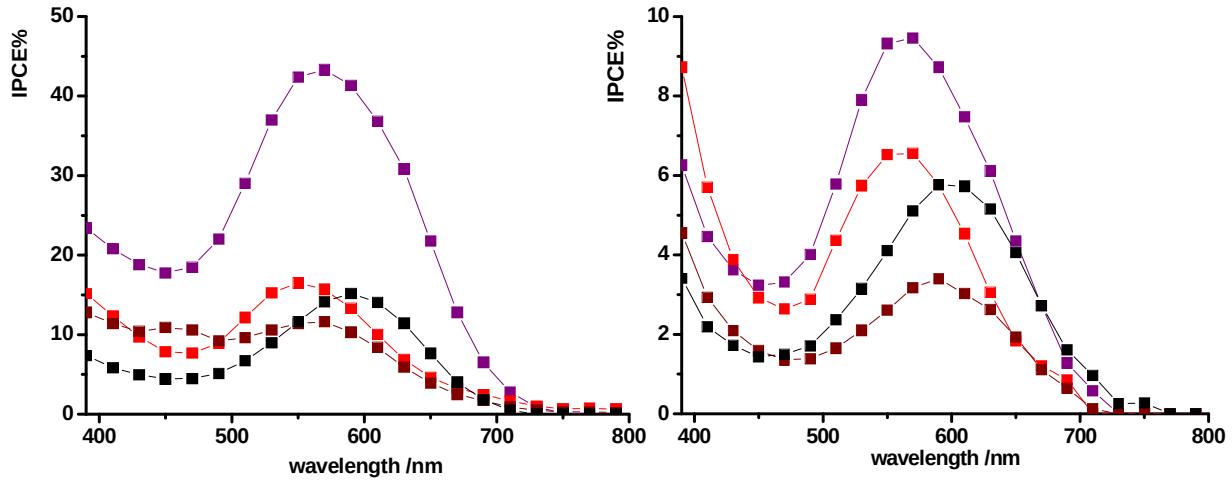

(a) (b)

Figure.80 IPCE% measurements of DSSCs using (a) LiI/ I_2 0.5/ 0.05 M in acetonitrile and sputtered Pt as counter electrode and (b) $Co(DTB)^{2+}$ 0.15 M and Li^+ 0.5 M with a gold counter electrode.
TiO_2 film was sensitized with eggplant extract (violet line), red radicchio (red line), Nero d'Avola (wine line) and Giacchè (black line). Photoanode are treated with $TiCl_4$ 0.2 m in ethanol before adsorbing natural dye.

In particular with the eggplant extract an IPCE% value of 45% was obtained. The improvement in device performance may be attributed either to increased film thickness or to a retardation of interfacial recombination process due to the interfacial blocking layer.

In analogous conditions, however, Co(II) mediators give very poor cell performances, most probably for the small driving force for the oxidized dye regeneration.

5.3.2 Sensitization of TiO_2 through absorption from an acid water dye solution.

TiO_2 films were also sensitized by using acidic aqueous solution of the natural extracts. This procedure allows to increase the optical density of the photoanode (figure 77.a and 77.b) and as a consequence the monochromatic photoconversion efficiency.

IPCE% values of 65% were obtained with TiO_2 photoanodes sensitized with eggplant extracts. This is a very promising result because there is no previous report on natural dyes giving a so high IPCE% value[110,111]. Murakami et al. have reported a maxima IPCE% of 20% obtained with the extract of Jaboticaba, a tropical fruit widely spread over the brazilian territory.

[110] D. Zhang, N. Yamamoto,T. Yoshida and H.Minoura; *Trans. MRS J.* 27 (**2002**) 811.
[111] A. S. Polo, N. Y. Murakami; *Solar Energy Materials and Solar Cells* 90 (**2002**) 1936.

Also the IPCE% trend of DSSC using Co(DTB) as mediators shows an enhancement in comparison with the previous measurements (Figure 80.b) probably because of the improvement in LHE factor. Nevertheless the $Co(DTB)^{2+}$ remains slow in the regeneration of the oxidized dye.

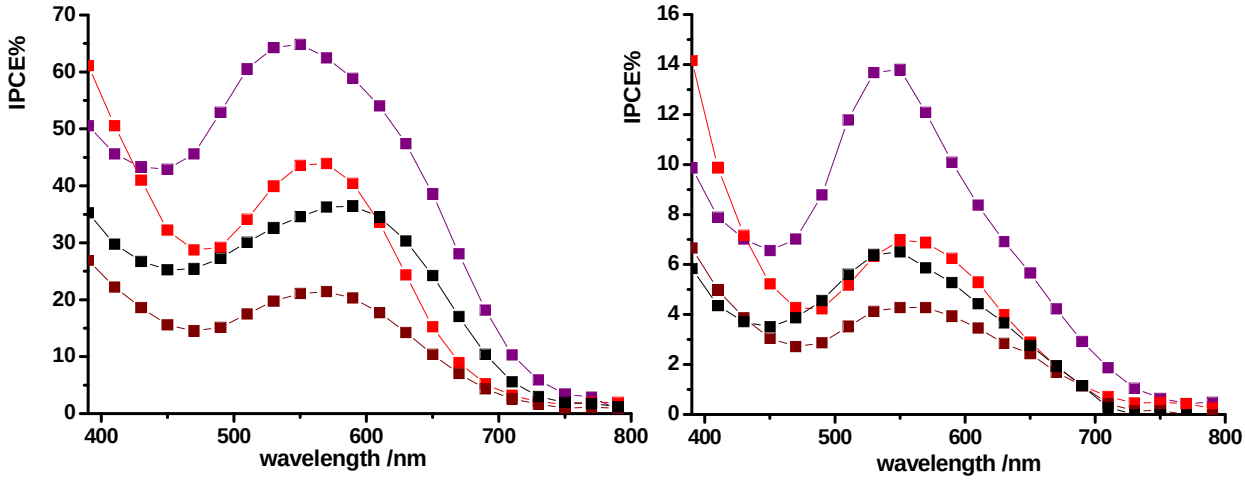

(a) (b)

Figure.81 IPCE% measurements of DSSCs using (a) LiI/ I_2 0.5/ 0.05 M in acetonitrile and sputtered Pt as counter electrode and (b) $Co(DTB)^{2+}$ 0.15 M and Li^+ 0.5 M with a gold counter electrode.
TiO_2 film was sensitized with eggplant extract (violet line), red radicchio (red line), Nero d'Avola (wine line) and Giacchè (black line). Photoanode are treated with $TiCl_4$ 0.2 m in ethanol before adsorbing natural dye.

5.4 Evaluation of the regeneration kinetics of the photoxidized dye by the electron transfer mediator through transient absorption spectroscopy.

In order to explain the ability of the natural extracts to inject electrons in the conduction band of the semiconductor and to be regenerated by the electron transfer mediator, transient absorption measurements of dye sensitized TiO_2 films were performed. The following processes are expected to occur upon photoexcitation of cyanin sensitized TiO_2 nanoparticles: electron injection to the conduction band, electron migration to the particle surface/ electron trapping and electron recombination to the dye cation. The absorption decay of the dye following the photoexcitation shows a bi-exponential kinetics. This fact is generally observed and can be related to a trapping-detrapping mechanism of the charge recombination process involving conduction band electrons. The biexponential nature of the process, however, is only apparent, in fact trapping-detrapping of the conduction band electrons would involve a multi exponential decay. It agreed, however, to give the complexity

of the charge recombination process, an average lifetime for the recombination of conduction band electrons and for the nascent form of the oxidized dye can be considered indicative for the evaluation of the time scale of process and for comparative purposes. The presence of the electron transfer mediator decrease the average lifetime of the nascent oxidized.

For the eggplant extract adsorbed on a TiO_2 film from an ethanol solution the results are shown in figure 82.

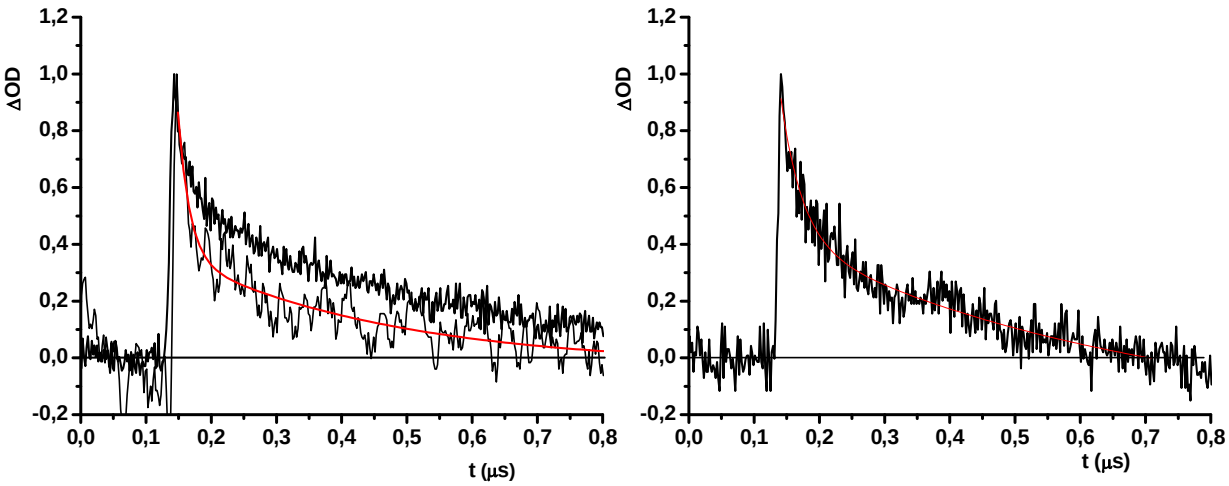

Figure.82 Normalized transient absorption spectra of eggplant extract adsorbed on TiO_2 film (a) with Li^+ 0.5 M in acetonitrile (black line) and with Li^+ 0.5 M and I^- 0.15 M in acetonitrile (red line); (b) with with Li^+ 0.5 M and $Co(DTB)^{2+}$ 0.15 M in acetonitrile. The samples have been excited at 532 nm and their absorption has been observed at 470 nm. Laser pulse of 0.35 mJ/pulse.

In presence of iodide the lifetime of the photoxidized anthocyanin is decreased with respect to the lifetime of the anthocyanin in presence of Li^+, meaning that iodide intercepts efficiently the oxidized dye before recombination with photoinjected electrons occurs. Table X shows that the lifetime of the eggplant extract adsorbed on TiO_2 decreases from 99 ns to 17 ns when iodide 0.15 M is added. $Co(DTB)^{2+}$ is also able to regenerate the photoxidized anthocyanin (Figure 82.b) but less efficiently than iodide. In presence of $Co(DTB)^{2+}$ a decrease of the lifetime to 66 ns is observed. With the exception of Nero d'Avola (Figure 84) the other natural extracts, red radicchio (Figure 83) and Giacchè (Figure 85) behave similarly (Table X). Table X resumes the lifetimes obtained in the different measurements.

Table X. Regeneration kinetics of the several photooxidized natural extract adsorbed on TiO_2 film. In Table II $t_{1/2}$ in nanosecond with Li^+ 0.5 M, I^- 0.15 M or Co(DTB) 0.15 M in acetonitrile are shown. Both Co(DTB) and Iodide solutions contain Li^+ 0.5 M. The samples have been observed at different wavelengths depending of the examined extract. Laser pulse of 0.35 mJ/pulse.

Extract	Li^+	I^-	Co(II)
Eggplant	99	17	61
Radicchio	184	16	26
Nero d'Avola	548	528	145
Giacchè	305	91	186

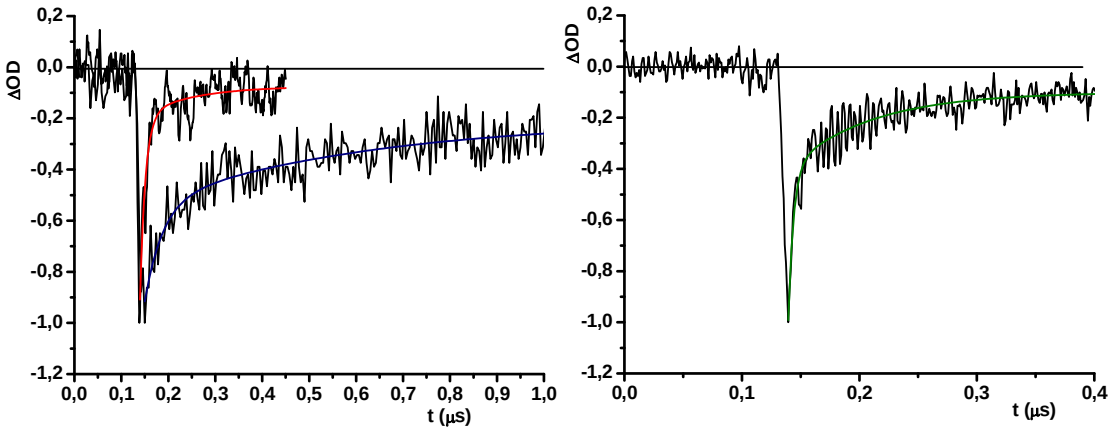

(a) (b)

Figure.83 Normalized transient absorption spectra of red radicchio extract adsorbed on TiO_2 film (a) with Li^+ 0.5 M in acetonitrile (black line) and with Li^+ 0.5 M and I^- 0.15 M in acetonitrile (red line); (b) with with Li^+ 0.5 M and $Co(DTB)^{2+}$ 0.15 M in acetonitrile. The samples have been excited at 532 nm and their absorption has been observed at 500 nm. Laser pulse of 0.35 mJ/pulse.

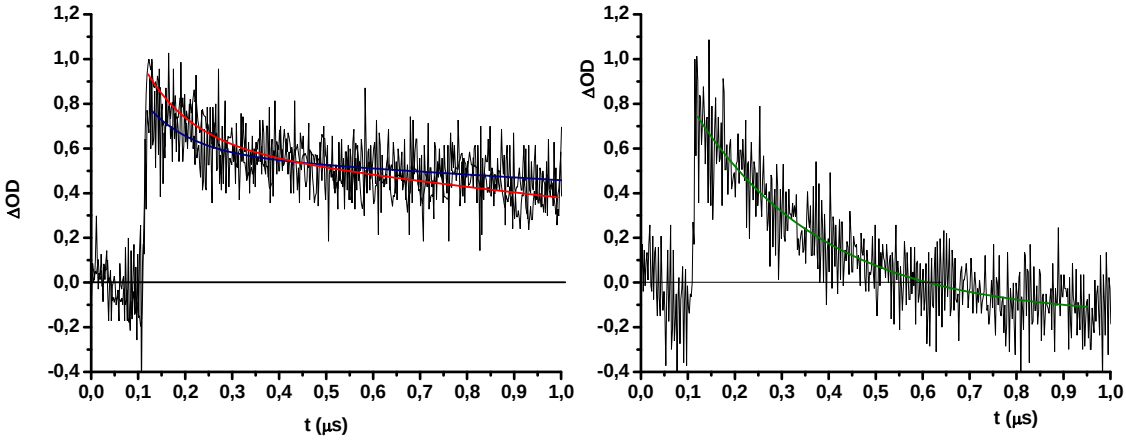

(a) (b)

Figure.84 Normalized transient absorption spectra of Nero d'Avola extract adsorbed on TiO_2 film (a) with Li^+ 0.5 M in acetonitrile (black line) and with Li^+ 0.5 M and I^- 0.15 M in acetonitrile (red line); (b) with with Li^+ 0.5 M and $Co(DTB)^{2+}$ 0.15 M in acetonitrile. The samples have been excited at 532 nm and their absorption has been observed at 450 nm. Laser pulse of 0.35 mJ/pulse.

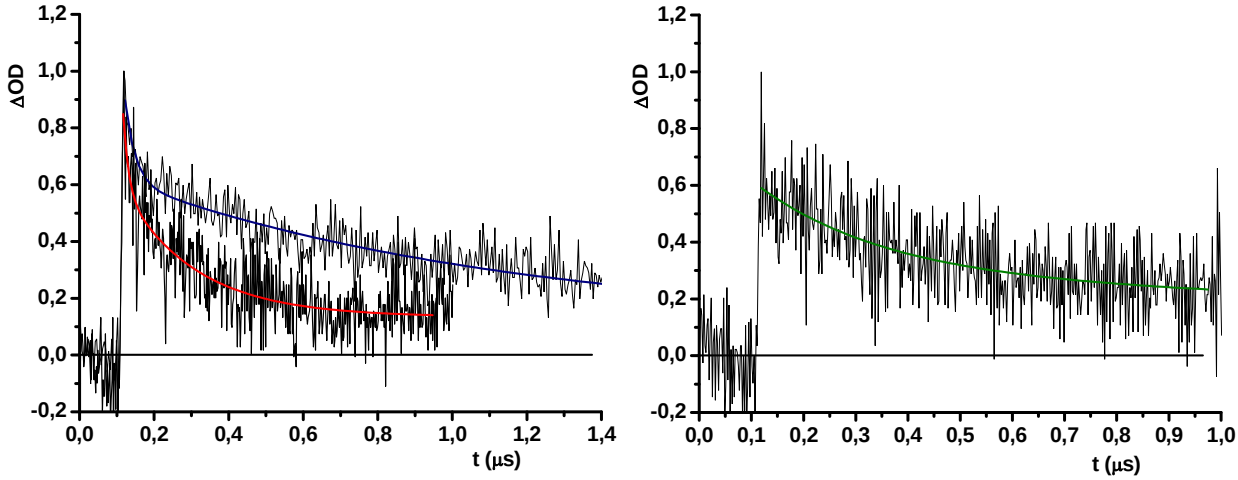

Figure.85 Normalized transient absorption spectra of Giacché extract adsorbed on TiO_2 film (a) with Li^+ 0.5 M in acetonitrile (black line) and with Li^+ 0.5 M and I^- 0.15 M in acetonitrile (red line); (b) with with Li^+ 0.5 M and $Co(DTB)^{2+}$ 0.15 M in acetonitrile. The samples have been excited at 532 nm and their absorption has been observed at 450 nm. Laser pulse of 0.35 mJ/pulse.

Going back to figure 82 it can be noted that the lifetime of the photoxidized anthocyanin is very short even if no redox couple able to intercept the oxidized dye is present. In an attempt to slow down the charge recombination process a TiO_2 blocking layer was introduced between the FTO glass and the TiO_2 film. J-V measurements with and without blocking layer have been carried out for the eggplant extract, which gives the best photoconversion efficiency. The results shown in figure 86 indicate that the presence of the blocking layer induces a remarkable improvement in J_{sc}, most probably due to the reduced rate of electron recapture from the oxidized dye.

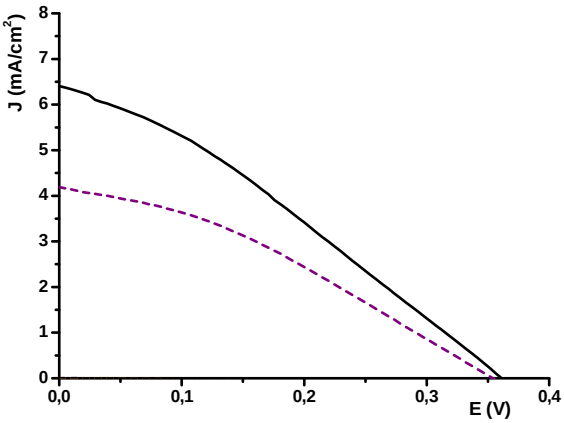

Figure 86. J-V curves of DSSC using eggplant extract as sensitizer, LiI/I_2 0.5/ 0.05 in acetonitrile as electron transfer mediator and Pt as counter electrode material. The photoanode is characterized by (violet line) TiO_2 and $TiCl_4$ overlayer; (black line) blocking layer, TiO_2 and $TiCl_4$ overlayer. Power intensity of 0.1 W/cm^2 of a Xe lamp is used as simulated solar source.

Table XI. Photoelectrochemical parameters related to J-V curves of DSSC using eggplant extract as sensitizer, LiI/I_2 0.5/ 0.05 in acetonitrile as electron transfer mediator and Pt as counter electrode material.

	J_{sc} (mA/cm^2)	V_{oc} (mV)	FF%	η%
Without blocking layer	4,18	350	33	0,49
With blocking layer	6,41	360	29	0,69

These results are of interest in the perspective of employing natural dyes as sensitizers in DSSCs. Their wide availability, non toxicity and possibility of improving the solar cells performances through the introduction of a blocking layer make the research in this field challenging and promote further studies towards other natural pigments.

5.5 Study of photoelectrochemical behaviour of DSSC containing raw red turnip extracts.

5.5.1 Methods and experimental procedures.

Photoanode preparation : Compact TiO_2 underlayers were obtained by spin coating (1000 rpm) of a 0.2 M solution of titanium isopropoxide (Fluka) in absolute ethanol (Aldrich) over a well cleaned TEC-8, (8 Ω/□) conductive glass (Fluorine-Tin Oxide (FTO, Hartford Glass, Stillwater Mn (USA)) at. The resulting transparent layer was baked in an oven at 450 C° for 30'. Mesoporous TiO_2 paste, prepared by hydrolysis of titanium isopropoxide in aqueous HNO_3 (Fluka) was cast onto the TiO_2 underlayer by the well known tape casting method , dried under a gentle warm air stream and fired at 450 C° for 45'. The sintered films were finally treated with an aqueous 0,2 M $TiCl_4$ solution for 12 hours, thoroughly rinsed with deionized water and cured in an oven at 450 C° for 30'. Adsorption of natural sensitizers was carried out in the dark and at ca. 4 C° by direct immersion of the TiO_2 electrodes in the raw extracts. After few hours (4-6) the adsorption was deemed complete.

Sandwich photoelectrochemical cell assembly: Parafilm® sealed cells (0,5 cm^2 active area) were built by pressing the sensitized photoanode against a counter electrode (platinum sputtered for I^-/I_2 electrolytes, gold coated for Co(II)/(III) electrolytes) equipped with a parafilm® frame used to confine the liquid electrolyte inside the cell. The thickness of liquid layer corresponded roughly to the thickness of the frame borders (≅120 μm). In this

configuration the cell was stable towards solvent evaporation and leaking for several hours/days even when using volatile solvents like ACN

IPCE spectra: the cell was illuminated with a water cooled Osram XBO 150 W Xe lamp coupled with an Applied Photophysics high radiance monochromator, using a spectral bandwidth of 10 nm. The irradiated area was 0.5 cm^2. Photocurrents were measured under short circuit conditions with an Agilent 34401A digital multimeter, incident irradiance was measured using a 1 cm^2 Centronic OSD100-7Q calibrated silicon photodiode.

IPCE % (Incident Photon to Current Conversion Efficiency) was calculated according to

$$\text{IPCE \%} = 1.24 \times 10^3 \text{ (V nm)} \frac{J(\mu A cm^{-2})}{\lambda(nm) P(W m^{-2})}$$

Where J is the monochromatic photocurrent density, P is the radiant power density and λ is the wavelength of the incident light.

J-V curves : Current-voltage curves were collected under the white light generated by an air cooled HDI (metal halogenide) lamp at about 0,1 W/cm^2 incident irradiance, measured with a Molectron PowerMax 500A power meter. The current output of each cell was recorded by linearly varying the potential from 0 to 0.7 V in a two-electrode configuration using a scan speed of 10 mV/s, employing an EcoChemie PGSTAT 30/2 electrochemical workstation interfaced with a personal computer. Photocurrent transients were collected at 0 constant potential by manually shutting the incident light.

5.5.2 Results and discussion.

In this paragraph the possibility of achieving a satisfactory TiO2 sensitization with raw indian fig and red turnip pigments have been explored. Whereas in a recent interesting report by Zhang et al. beet extracts obtained from a food company have been tested with moderate efficiencies (0.7 %)[112], here we have used aqueous dye solutions directly extracted from vegetables and fruits in our laboratories. Simply, red turnip (Detroit variety) (Beta Vulgaris Rubra, Kogel) slices have been immersed in an 0.1 M HCl solution and left under sonication for a few minutes. After filtration and centrifugation an intensely red coloured

[112] D. Zhang, S. M. Lanier, J. A. Downing, J. L. Avent, J. Lum, J. L. McHale*; J.Photochem. Photobio.* A **2008**, 195, 72-80.

solution was obtained and used directly for the adsorption stage. The same procedure was adopted with the indian fig (Opuntia Ficus-indica). Intentionally, any further purification of the extracts was avoided to check whether an efficient sensitization could be achieved with minimal chemical procedures. Red turnip and indian fig contain betalains, which in solution display an intense absorption band centered at about 530 nm. Upon adsorption on the TiO2 electrodes the visible absorption band shifts to higher energy, showing a broad maximum around 470-450 nm probably determined both by the interaction of the dyes with the surface and to the preferential binding of betaxanthin, one of the component of the betalains family. The acidic environment was essential for obtaining electrodes characterized by high optical densities, capable of an almost complete absorption of visible photons in the 400-600 nm range (Figure 87). The reason is ostensibly related to protonation of betalainic carboxylic groups which are otherwise unable, in their anionic form (they are probably dissociated under plant physiologic conditions), to interact strongly with the oxide surface.

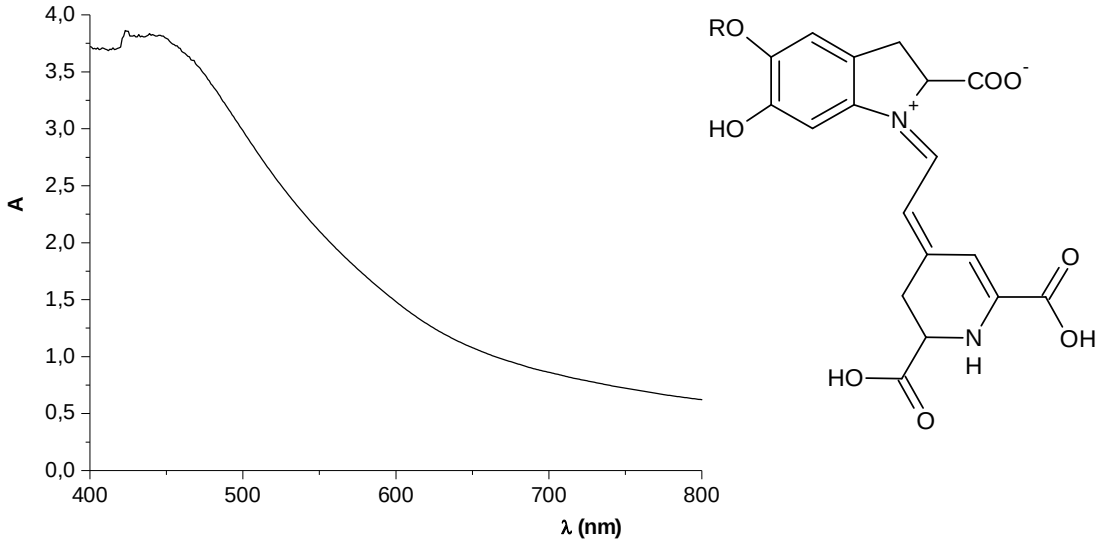

Figure 87. Absorption spectrum of a TiO2 film stained with red turinp extracts. Right: general structure of betalains.

Compared to red turnip, indian fig extracts were generally a poorer source of dyes, resulting in moderately coloured photoanodes with a modest light harvesting capability and photovoltaic performance, resulting in a J_{sc} = 1,77 mA/cm^2, V_{oc} = 0,4 V and η = 0.4 % under 0.1 W/cm^2 irradiation. On the other hand red turnip displayed promising results showing Jsc = 6 mA/cm2, Voc = 0.41 V, Fill Factor = 0.4 and η = 1% using an electrolyte composed of

0,5 M/0,05 M LiI/I_2 in acetonitrile (ACN). The application of a compact TiO2 underlayer was instrumental for enhancing the cell performance, increasing the short circuit photocurrent to about 10 mA/cm^2 and the photovoltage to 0,48 V (Figure 88). The employment of a less volatile electrolyte, more suitable for practical applications, composed of 0.6 M propyl-methyl imidazolium iodide (PMII), 0.1 M LiI and 0.2 M I_2 in methoxypropionitrile (MPN) left almost unchanged the J-V characteristic of the cell, allowing to obtain overall efficiencies of the order of 1,75 %, to our knowledge among the highest so far reported with natural dyes. The performance is thus relatively well comparable with an N719 sensitized cell which generated under identical conditions Jsc = 17.73 mA/cm^2, V_{oc} = 0,53 V, and η = 3,3 %. The presence of the compact underlayer seems to be essential for reducing the back recombination from the fluorine-tin oxide (FTO) electron collector. Indeed our findings agree with a recent paper by Burke et al(). in which it is pointed out that, compared to bulkier Ru(II) complexes, smaller and flat organic molecules like the sensitizers reported here may not be able to insulate well the underlying conductive oxide from the oxidized electrolyte (namely I_3^-) and that, for this reason, interface optimization is required to exploit the full potentialities of such dyes.

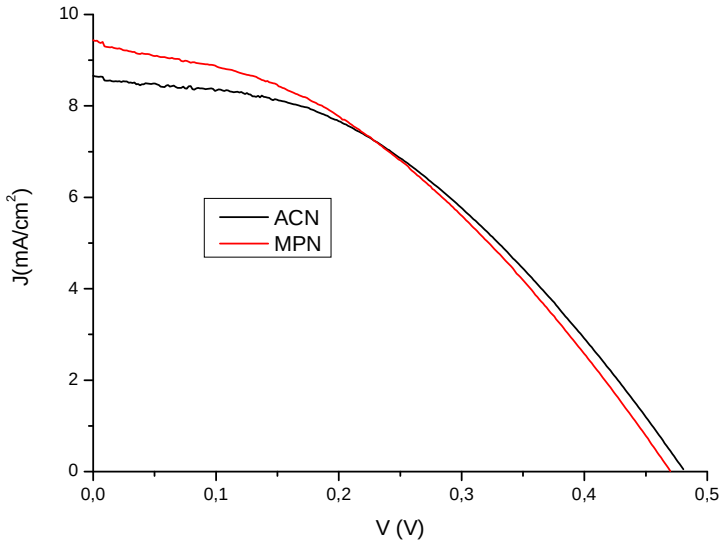

Figure 88. J-V curves of sandwich type DSSC sensitized with red turnip extracts in the presence of iodide based electrolytes in ACN and MPN

In our conditions the addition of 4-Tert-butyl pyridine had a detrimental effect on cell efficiency: to a modest gain in photovoltage and in Fill Factor (0,53 V and 0,53 respectively)

it corresponded a dramatic drop in photocurrent (1,53 mA/cm2). This phenomenon has been verified independently in our two laboratories and the reason is presently not well understood.

The IPCE spectra (Figure 89) were in good agreement with the absorption spectrum recorded on TiO_2 film, showing a maximum of 65 % at 450 nm, testifying the charge injection from the excited state of the sensitizers. Since the photon absorption at that wavelength is complete a value inferior to 100% can only be determined by an injection efficiency and/or by an electron collection efficiency smaller than unity. The excited state oxidation potential of betalains is very negative, in our case – 1,3 V vs SCE‡ and should allow for an activationless injection into the d band of the TiO2. Electronic coupling with empty TiO_2 states should also be good, as DFT calculations showed a localization of the LUMO on the dihydropyridine ring of the betalaine (see reference 112). Based on these indications, it is unlikely that charge injection is the IPCE limiting process. On the other hand recombination losses can reduce the electron collection efficiency. The importance of a blocking layer in controlling recombination with the electrolyte has been already pointed out, but also recombination with the oxidized dye can be important in the case of natural dyes. The ground state oxidation potential (0.75 V)‡ should ensure a good dye regeneration rate by iodide, however also electron recapture by dye cation is expected to be faster here compared to ruthenium sensitizers in which the hole is confined into a metal centred d orbital relatively decoupled from the semiconductor surface. Indeed the interaction between the dye and the electrolyte is crucial here and a change in electrolytic composition by switching from iodide to Co(II), a kinetically slower electron donor, results in an IPCE drop to less than 30 %.

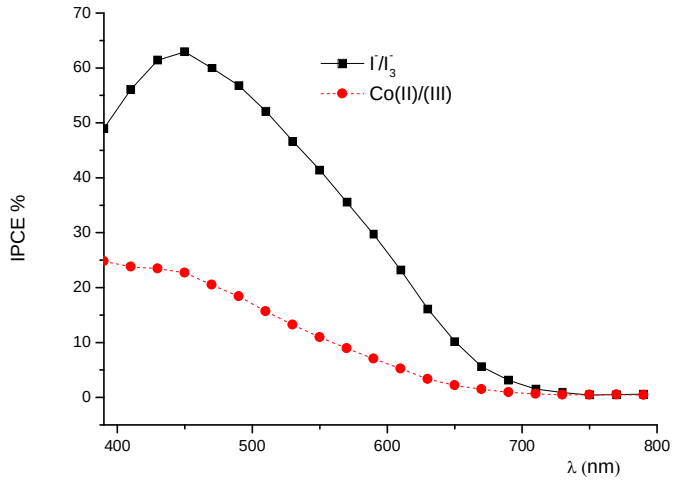

Figure 89. IPCE spectra of sandwich type DSSC sensitized with red turnip extracts in the presence of iodide/iodine (squares)and Co(II)/(III) (circles) electrolytes

To conclude, we have shown than in appropriate conditions natural pigments, without any purification or modification can serve as effective TiO2 sensitizers with promising efficiencies. It is also believed that the interaction with the electrolyte and recombination processes govern to a large extent cell efficiencies and a deeper study of these effects is currently underway

Chapter 6

Polipyridil Ru(II) complexes as photosensitizer for DSSCs.

6.4 Dye Sensitized Solar Cells based on PEDOP as a hole conductive medium.

6.4.1 Experimental section

6.4.1.1 Materials.
6.4.1.2 Photoanodes preparation.
6.4.1.3 PEDOP deposition.
6.4.1.4 Solar cell assembly.
6.4.1.5 Analytical instrumentation and measurements.

6.4.2 Study of the growth of the polymeric matrix on the photoanode through ossidative electrodeposition.

6.4.3 Photoelectrochemical characterization of quasi-solid state DSSCs.

6.4.4 Introduction of an Allumina overlayer.

6.4.5 Conclusions.

6.1 Tuning of Ru(II) complexes properties using pyrrole and pyrrolidine-containing polipyridine.

The design of polypyridine-complexes of ruthenium has been the focus of many research works for the elaboration of dye-sensitized solar cells (DSCs) or luminescent sensor [113]. The nature of the ligands around the metal has been found to dramatically affect the energy conversion process. Particularly, the introduction of electronic effects via electron-donor substituents on bpy and tpy ligands notably improved the absorption in the visible region which is required for efficient sunlight collection[114]. This effect is due to the propensity of the electron-donor substituents to destabilize the HOMO metal orbital (π t_{2g}) more than the LUMO ($\pi*$) orbital of the ligand.[114b] The consequence is a lower gap between the two orbital energy levels with respect to the parent complex leading to a red-shift of the MLCT (Metal Ligand Charge Transfer) absorption and decrease of the Ru(II)/Ru(III) oxidation potential. In this context, we have recently reported the positive effect of bipyridines (bpy), bearing pyrrole and pyrrolidine moieties bonded by their nitrogen, to the light harvesting property of $[Ru(bpy)_3]^{2+}$ and $[Ru(tpy)_2]^{2+}$type complexes[115]. High absorption maxima values and low oxidation potentials made the new ligands good candidates for the photovoltaic purpose. In DSCs, the sensitizing dye has to be chemisorbed at the surface of a nanocrystalline TiO_2 semiconductor usually via carboxylic acid groups[115b,116] or in a lesser extent via other bridging

[113] (a) Juris, A.; Balzani, V.; Barigelletti, F.; Campagna, S.; Belser, P.; von Zelewsky, A. *Coord. Chem. Rev.* **1988**, *84*, 85. (b) O'Regan, B., Grätzel, M. *Nature* **1991**, *353*, 737. (c) Hagfeldt A.; Grätzel, M. *Chem. Rev.* **1995**, *95*, 49. (d) Argazzi, R.; Bignozzi, C.A.; Hasselmann, G.M.; Meyer, G.J. *Inorg. Chem.* **1998**, *27*, 4533. (e) Schulze, X.; Serin, J.; Adronov, A.; Fréchet, J.M.J. *Chem. Commun.* **2001**, 1160. (f) Polson, M.I.J.; Taylor, N.J.; Hanan, G.S. *Chem. Commun.* **2002**, 1356. (g) Figgemeier, E.; Aranyos, V.; Constable, E.C.; Handel, R.W.; Housecroft, C.E.; Risinger, C.; Hagfeldt, A.; Mukhtar, E. *Inorg. Chem. Commun.* **2004**, *7*, 117. (h) Wang, P.; Klein, C.; Humphry-Baker, R.; Zakeeruddin, S.M.; Grätzel, M. *J. Am. Chem. Soc.* **2005**, *127*, 808. (i) Jiang, K.-J.; Masaki, N.; Xia, J.-b.; Noda, S.; Yanagida, S. *Chem. Commun.* **2006**, 2460. (j) Robertson, N. *Angew. Chem. Int. Ed.* **2006**, *45*, 2338.

[114] (a) Sullivan, B.P.;, Baumann, J.A.; Meyer, T.J.; Salmon, D.J.; Lehmann, H.; Ludi, A. *J. Am. Chem. Soc.*, **1977**, *99*, 7368. (b) Cook, M.J.; Lewis, A.P.; McAulife, G.S.; Skarda, V.; Thomson, A.J. *J. Chem. Soc. Perkin Trans. 2* **1984**, 1293. (c) Paw, W.; Connick, W.B.; Eisenberg, R. *Inorg. Chem.* **1998**, ***37***, 3919. (d) Fung, W.-H.; Yu, W.-Y.; Che, C.-M. *J. Org. Chem.* **1998**, *63*, 7715. (e) Ghaddar, T.H.; Castner, E.W.; Isied, S.S. *J. Am. Chem. Soc.*, **2000**, *122*, 1233. (f) Rau, S.; Büttner, T.; Temme, C.; Ruben, M.; Görls, H.; Walther, D.; Duati, M.; Fanni, S.; Vos, J.G. *Inorg. Chem.*, **2000**, *39*, 1621

[115] (a) Martineau, D.; Gros, P.C.; Beley, M.; Fort, Y. *Eur. J. Inorg. Chem.* **2004**, 3984. (b) Martineau, D.; Beley, M.; Gros, P.C. *J. Org. Chem.* **2006**, *71*, 566.

[116] (a) Nazeeruddin, M. K.; Kay, A.; Rodicio, I.; Humphry-Baker, R.; Müller, E.; Liska, P.;Vlachopoulos, N.; Grätzel, M. *J. Am. Chem. Soc.* **1993**, *115*, 6382. (b) Argazzi, R.; Bignozzi, C.A.; Heimer, T.A.; Castellano F.N.; Meyer, G. J. *Inorg. Chem.* **1994**, *33*, 5741.

units such as phosphonic acids[117]. Herein we report the preparation of heteroleptic complexes involving pyrrole or pyrrolidine-containing bipyridine ligands (L) and dicarboxy bipyridine (DCB), the characterization (UV-Vis, electrochemistry) and the evaluation of the photoelectrochemical performances of the new sensitizers (Figure 91) in nanocrystalline TiO_2 solar cells.

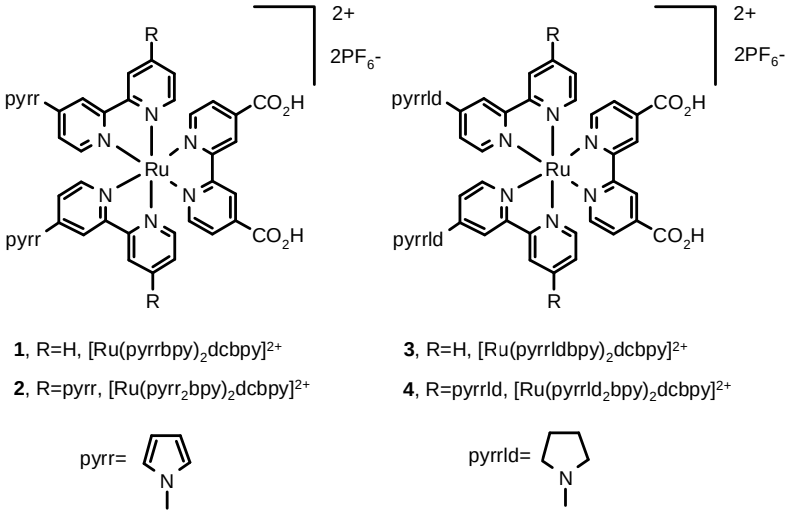

Figure 91 Structures of the new complexes **1**-**4** studied in this work

6.1.1 Experimental section.

6.1.1.1 Instrumental apparatus: ^{1}H and ^{13}C NMR have been recorded on AC200, AC250 or DRX400 Bruker spectrometers. GC experiments have been performed on a Shimadzu chromatograph fitted with a 15 m capillary column. Microwave experiments have been performed on a CEM Discover device fitted with infra-red probe temperature control. Absorption UV-Vis electronic spectra have been recorded on a Varian Cary E spectrometer and emission UV-Vis electronic spectra on a SLM Aminco-Bowman Series 2 apparatus using a (1 cm × 1 cm) quartz cell in deoxygenated solutions (OD < 0.05). Excited state lifetimes have been obtained by Nanosecond Transient Absorption in

[117] (a) Pechy, P.; Rotzinger, F.P.; Nazeerudin, M.K.; Kohle, O.; Zakeeruddin, S.M.; Humphry-Baker, R.; Grätzel, M. *Chem. Commun.* **1995**, 65. (a) Gillaizeau-Gauthier, I.; Odobel, F.; Alebbi, M.; Argazzi, R.; E. Costa, Bignozzi, C.A.; Qu P.; Meyer, G.J. *Inorg. Chem.* **2001**, *40*, 6073. (b) Zabri, H.; Gillaizeau, I.; Bignozzi, C.A.; Caramori, S.; Charlot, M.-F.; Cano-Boquera J.; Odobel, F. *Inorg. Chem.* **2003**, *42*, 6655.

acetonitrile as solvent by excitation at 355 nm of a laser Continuum Surelite II Q-switched Nd :YAG (FWHM = 7 ns, 8 Hz). Focalisation was realized by an Applied Photophysics monochromator. GC-MS (EI) spectra have been obtained on a HP 5971 analyzer. Electrospray mass spectra have been recorded on an Agilent MSD using CH_3CN as solvent. The electrochemical measurements were performed with a PGP 201 Radiometer/Tacussel potentiostat using a conventional single compartment three-electrode cell. The reference electrode was the potassium chloride calomel electrode (SCE), the working electrode was a 10 mm Pt wire and the counter-electrode a 1 cm^2 vitreous carbon disc. The supported electrolyte was $LiClO_4$ 0.1M in CH_3CN and the solutions were purged with argon before each measurement. A 0.5 mM solution of the studied compound was generally used. All potentials are quoted *versus* SCE, in these conditions the redox potential of Fc^+/Fc was found at 0.38 V. In all the experiments the scan rate was 100mV/s. IPCE measurements were performed by illumination of the cell using an Osram 150W Xenon lamp coupled to an Applied Photophysics monochromator. The irradiated surface was 0.5 cm^2. Photocurrents were measured under short circuit conditions by a digital Agilent 34410A multimeter. Incident irradiance was measured with a 1 cm^2 Centronic OSD100-7Q calibrated silicon photodiode.

The mediators (Fe- and Co-mediated) and DSCs were prepared according to published procedures.[117b,118] Chemical reagents and solvents were commercially available and used as such except ligands pyrrbpy, $pyrr_2bpy$, pyrrldbpy and $pyrrld_2bpy$ which were prepared according to our previous works.[119] DMF was degassed by several vacuum-argon cycles before use.

TiO_2 electrode preparation: TiO_2 colloidal paste was prepared by hydrolysis of Ti(IV) isopropoxide. The nanocrystalline TiO_2 photoelectrodes were prepared by depositing the paste onto transparent conducting FTO glass (either Delta Technologies or IBE, 7Ω/Square) according to the well known “scotch tape” method. The thin films were allowed to dry at room temperature for 20 min. and finally fired at 450°C for 40 minutes. The still hot electrodes were immersed in the dye solution and kept at 80°C for 5 hours, after which the absorption was deemed complete. The efficiency of absorption was evaluated by UV-Vis

[118] Sapp, S.A.; Elliott, C.M.; Contado, C.; Caramori, S.; Bignozzi, C.A. *J. Am. Chem. Soc.* **2002**, ***124***, 11215.

[119] (a) Sullivan, B.P.; Salmon D.J.; Meyer, T.J. *Inorg. Chem.* **1978**, *17*, 3334. (b) Hesek, D.; Inoue, Y.; Everitt, S.; Ishida, H.; Kumeda, M.; Drew, M. *Inorg. Chem.* **2000**, *39*, 308

spectroscopy: photoelectrodes characterized by an optical density ≥1 at the MLCT maximum of the sensitizer were commonly obtained. Dye solutions were prepared by dissolving a small amount of the Ru(II) complex in anhydrous ethanol (ca. 4 mg in 10 ml of solvent). The solutions were sonicated and filtered to remove suspended undissolved dye.

Counter electrodes preparation: Platinum coated counter electrodes were obtained by spraying a 5 x 10^{-3} M H_2PtCl_6 (Fluka) solution in isopropanol on the well cleaned surface of an FTO glass. This procedure was repeated from 5 to 10 times to obtain an homogeneous distribution of H_2PtCl_6 droplets. The electrodes were dried under a gentle air flow and treated in an oven at 380°C for 15 min obtaining the formation of stable platinum clusters.

Gold coated electrodes, used with cobalt-based mediators were obtained by thermal vapour deposition on FTO of a 5-7 nm thick chromium adhesion layer followed by a 30-35 nm thick gold layer. The average pressure of the vacuum chamber of the evaporator was about 9 ×10^{-6} torr.

Photoelectrochemical cell assembly:[120,121,122] Parafilm® sealed cells were built by pressing the sensitized photoanode against a counter electrode equipped with a parafilm® frame used to confine the liquid electrolyte inside the cell. The thickness of liquid layer corresponded roughly to the thickness of the frame borders (≅120 μm). In this configuration the cell was stable towards solvent evaporation and leaking for several days even using volatile solvents like acetonitrile. In both cases metallic clamps were used to hold firmly the two electrodes together. DMF was degassed by several vacuum-argon cycles before use.

6.1.1.2 Preparation of complexes: The complexes were prepared by a two-step procedure. The first step was the preparation of a dichlorinated complex[119] by reaction of $RuCl_3.xH_2O$ with an excess of pyrrole or pyrrolidine-containing bipyridine ligands synthesized according to our previous works.[123] In the second step, the chloro ligands were substituted by the dicarboxybipyridine ligand (DCB) used as its unprotected form.

[120] Sapp, S. A.; Elliott, C. M.; Contado, C.; Caramori, S.; Bignozzi, C. A., Substituted Polypyridine Complexes of Cobalt(II/III) as Efficient Electron-Transfer Mediators in Dye-Sensitized Solar Cells. *J. Am. Chem. Soc.* **2002,** 124, (37), 11215-11222.

[121] Cazzanti, S.; Caramori, S.; Argazzi, R.; Elliott, C. M.; Bignozzi, C. A., Efficient Non- corrosive Electron-Transfer Mediator Mixtures for Dye-Sensitized Solar Cells. *J. Am. Chem. Soc.* **2006,** 128, (31), 9996-9997.

[122] Gillaizeau-Gauthier, I.; Odobel, F.; Alebbi, M.; Argazzi, R.; Costa, E.; Bignozzi, C. A.; P., Q.; Meyer, G. J., *Inorg. Chem.* **2001,** 40, 6073.

[123] Martineau, D.; Gros, P.C.; Fort, Y. *J. Org. Chem.* **2004**, *69*, 7914.

The dichloro complexes were obtained quantitatively in a very short time (8 min.) under microwave irradiation in DMF (Scheme 1). The classical thermal heating in the same solvent was also efficient but extended reaction times were necessary (12 h). The obtained complexes were then reacted as such with a stoichiometric amount of dcbpy in refluxing acetic acid leading to **1-4** in good overall yields (two steps) and pure form after chromatography on Sephadex LH-20 column. The incorporation of DCB in pyrrolidine-containing complexes proceeded sluggishly since 3 days were needed to complete the reaction. An explanation could be the oxidation of the intermediate dichloro complex into its Ru^{III} form favoured by the electron-donor effect of pyrrolidine moieties.[3] The subsequent reaction with dcbpy was thus slowed down since a reduction step was needed before the coordination. The formation of Ru^{III} species was supported by the full solubility of the intermediate dichloro complex in water indicating the formation of a charged (cationic) species. This observation contrasted with those made with the pyrrole-based dichloro complexes which precipitated in water as expected for a neutral species.

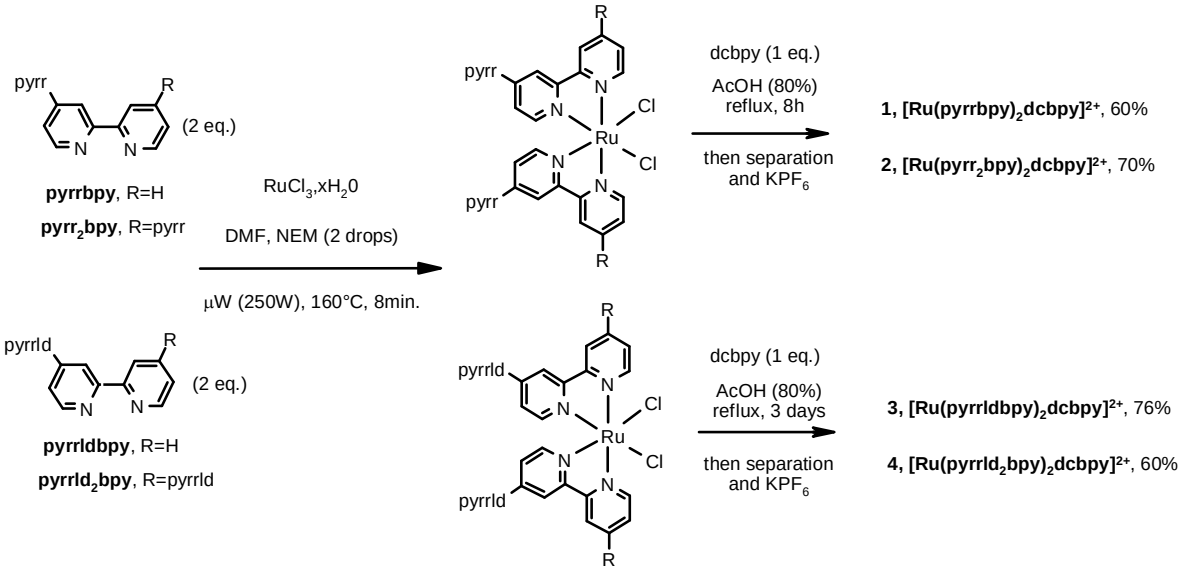

Scheme 1. Preparation of complexes **1-4**

Complexes **1-4** were then subjected to a range of photophysical and electrochemical analyses. The results are summarized in Table XIII. For comparison purpose and to evaluate the effect of the DCB ligand, the values obtained with the homoleptic analogues have also been added.

[Ru(pyrrbpy)$_2$(DCB)](PF$_6$)$_2$ (1). pyrrbpy (26.8 mg, 0.121 mmol) and $RuCl_3.xH_2O$ (15.7 mg; 0.06 mmol) were dissolved in DMF (5 mL) and N-ethylmorpholine (2 drops) was added. The solution was then irradiated in synthesis micro-wave oven (250 W; 160°C max; 10 min) leading to a dark pink mixture. After cooling, the solvent was evaporated and replaced by acetone (5 mL) and the mixture placed in a refrigerator for several hours until a precipitate formed. After filtration and successive washings with H_2O, acetone and Et_2O and drying under vacuum, Ru(pyrrbpy)$_2$Cl$_2$ (MS (ES) : m/z = 614.2142) was obtained as a dark green solid and used as such in the following step. dcbpy (14.6 mg; 0.06 mmol) and [Ru(pyrrbpy)$_2$Cl$_2$] previously obtained were suspended in 10 mL of acetic acid (80% in water). The mixture was refluxed and the reaction monitored by TLC. After 8 h an orange mixture was obtained. After cooling, filtration and evaporation of the solvents, the residue was treated with a small amount of methanol, filtered on glass wool and purified through a Sephadex LH-20 column by elution with methanol. The main fraction was collected and H_2O (5 mL) was added before methanol evaporation. The pH of the aqueous phase was then adjusted to 3 (diluted HCl) then 15 mL of a saturated aqueous KPF_6 solution were added. After 3 h in a refrigerator, the precipitate was filtered, washed with Et_2O and dried to give **1** as a red solid (38.8 mg ; 60%).

^{1}H NMR (DMSO-*d6*) : δH (ppm) = 9.18 (brs, 2H), 9.11 (d; *J* = 8 Hz, 2H), 8.97 (m, 2H), 8.73-8.88 (m, 2H), 8.16-8.26 (m, 2H), 7.71-8.01 (m, 10H), 7.47-7.67 (m, 6H), 6.46 (m, 4H). MS (ES): m/z = 394.0710 $[M - 2PF_6]^{2+}$. UV-vis (CH_3CN), λmax (ε) = 472 nm (19000 $M^{-1}cm^{-1}$).

[Ru(pyrr$_2$bpy)$_2$(DCB)](PF$_6$)$_2$ (2). The same procedure was repeated with pyrr$_2$bpy (34.7 mg, 0.121 mmol). After reaction with dcbpy and above described work-up, **2** was obtained as red powder (51 mg ; 70%).

^{1}H NMR (DMF-*d7*): δH (ppm) = 9.87 (brs, 2H), 9.40 (m, 4H), 8.61 (d, *J* = 5 Hz, 2H), 8.39 (d, 6 Hz, 2H), 8.18 (m, 2H), 8.13 (d, *J* = 6 Hz, 2H), 8.07 (m, 8H), 6.69 (m, 8H). MS (ES): m/z = 1063.1968 $[M - PF_6]^+$, 459.1146 $[M - 2PF_6]^{2+}$. UV-vis (CH_3CN): λmax (ε) = 483 nm (21000 $M^{-1}cm^{-1}$).

[Ru(pyrrldbpy)$_2$(DCB)](PF$_6$)$_2$ (3). pyrrldbpy (27.3 mg, 0.121 mmol) and $RuCl_3.xH_2O$ (15.7 mg; 0.06 mmol) were dissolved in DMF (5 mL) and N-ethylmorpholine (2 drops) was added. The solution was then irradiated in synthesis micro-wave oven (250 W; 160°C max; 10 min) leading to a dark pink mixture. After cooling, the solvent was evaporated and

replaced by acetone/Et_2O (1/1) (5mL) and the mixture placed in a refrigerator for several hours until a precipitate formed. After filtration and washings with Et_2O and drying under vacuum, $Ru(pyrrldbpy)_2Cl_2$ (MS (ES) : m/z = 622.1001) was obtained as a dark green solid and used as such in the following step. dcbpy (14.6 mg; 0.06 mmol) and $[Ru(pyrrldbpy)_2Cl_2]$ previously obtained were suspended in 10 mL of acetic acid (80% in water). The mixture was refluxed and the reaction monitored by TLC. After 3 days a red mixture was obtained that was then cooled. Filtration and evaporation of the solvents gave a residue which was treated with a small amount of methanol, filtered on glass wool and purified through a Sephadex LH-20 column by elution with methanol. The main fraction was collected and H_2O (5 mL) was added before methanol evaporation. The pH of the aqueous phase was then adjusted to 3 (diluted HCl) then 15 mL of a saturated aqueous KPF_6 solution were added. After 3 h in a refrigerator, the precipitate was filtered, washed with Et_2O and dried to give **3** as a red solid (49.5 mg, 76%).

^{1}H NMR (DMSO-*d6*) : δH (ppm) = 9.22 (brs, 2H), 8.86 (m, 2H), 7.99-8.18 (m, 2H), 7.64-7.99 (m, 7H), 7.52 (m, 1H), 7.40 (m, 1H), 7.11 (d, *J* = 6 Hz, 1H), 6.91-7.04 (m, 2H), 6.65 (m, 1H), 6.53 (m, 1H), 3.42 (m, 8H), 1.99 (m, 8H). MS (ES): m/z = 398.1006 $[M -2PF_6]^{2+}$. UV-vis (CH_3CN) : λmax (ε) = 492 nm (15240 $M^{-1}cm^{-}1$).

$[Ru(pyrrld_2bpy)_2(DCB)](PF_6)_2$ (4). The same procedure was repeated with $pyrrl_2dbpy$ (35.6 mg, 0.121 mmol) and $RuCl_3.xH_2O$ (15.7 mg; 0.06 mmol). After filtration the washings were realized with acetone/Et_2O (80/20) and Et_2O. After drying under vacuum, $Ru(pyrrld_2bpy)_2Cl_2$ (MS (ES) : m/z = 760.2062) was obtained as a dark blue solid and used as such in the following step with dcbpy (14.6 mg; 0.06 mmol). After above described treatment, **4** was obtained as a red solid (44.0 mg, 60%).

^{1}H NMR (DMSO-d6) : δH (ppm) = 9.12 (brs, 2H), 8.10 (brs, 2H), 7.85 (brs, 2H), 7.62 (s, 4H), 7.59 (s, 2H), 7.12 (d, *J* = 6 Hz, 2H), 6.90 (d, *J* = 6 Hz, 2H), 6.64 (d, *J* = 5 Hz, 2H), 6.45 (d, J = 5 Hz, 2H), 3.41 (m, 16H), 1.97 (m, 16H). MS (ESI) : m/z = 467.1603 $[M - 2PF_6]^{2+}$. UV-vis (CH_3CN) : λmax (ε) = 535 nm (11600 $M^{-1}cm^{-1}$).

6.1.2 Characterization of Ru(II) complexes

6.1.2.1 Electronic spectra: In the UV region, intense and sharp bands are observed corresponding to ligand centered transitions. The band near 300 nm is attributed to a π-π*

transition localized mostly on bipyridine. Near 250 nm are found π-π* transitions localized on pyrrole in **1** and **2**. n-π* transitions in the pyrrolidine-based complexes **3** and **4** are also found in the same region. The bands intensities grown as the number of pyrrole or pyrrolidine moities increased in the complexes.

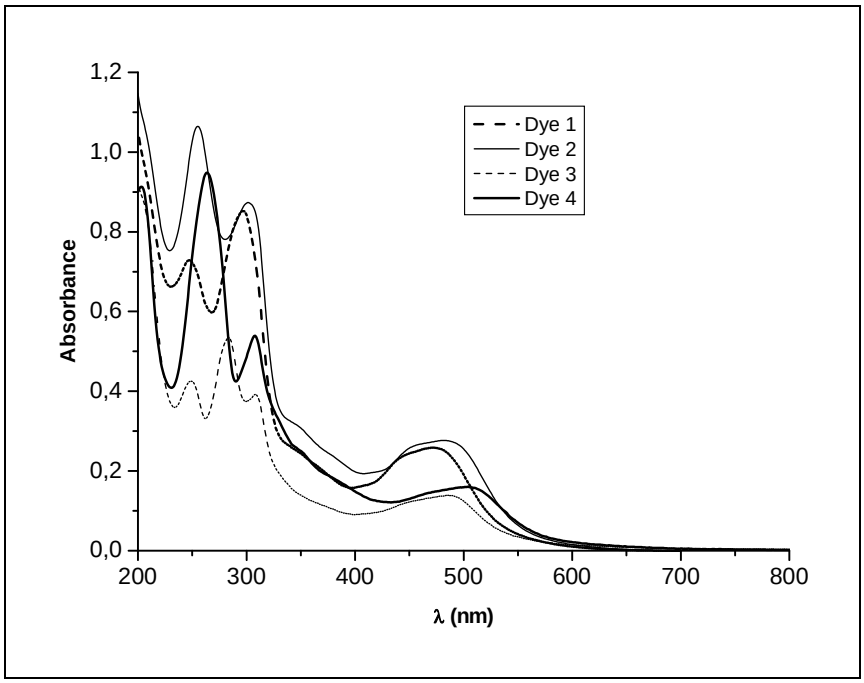

Figure.92 Absorption spectra of dyes **1-4** in acetonitrile

In the visible range, the heteroleptic complexes **1-4** exhibited red-shifted MLCT absorption bands compared to their homoleptic analogues. The highest absorption maximum value (535 nm) was obtained for complex **4** containing the pyrrld$_2$bpy ligands. This value is comparable to those observed with the known $[Ru(DCB)_2(NCS)_2]^{2+}$ (**N3**) dye.[124]

The pyrrole containing complexes **1** and **2** displayed the best molar extinction coefficients (ε) thanks to electron delocalization[125] which increases the electric dipole moment associated with the charge transfer transition. A weak additional effect was observed from one to two pyrrole groups on the ligand resulting in 19000 $M^{-1}cm^{-1}$ and 21000 $M^{-1}cm^{-1}$ ε values

[124] (a) Benko, G.; Kallioinen, J.; Korppi-Tommola, J.E.J; Yartsev, A.P.; Sundstrom, V. *J. Am. Chem. Soc.* **2002**, *124*, 489. (b) Nakade, S.; Kubo, W.; Saito, Y.; Kanzaki, T.; Kitamura, T.; Wada, Y.; Yanagida, S. *J. Phys.Chem.* B **2003**, *107*, 14244.

[125] For recent works on electronically delocalized structures see (a) Wang, P.; Klein, C.; Humphry-Baker, R.; Zakeeruddin, S.M., Grätzel, M. *J. Am. Chem. Soc.* **2005**, *127*, 808. (b) Jiang, K.-J.; Masaki, N.; Xia, J.-b.; Noda, S.; Yanagida, S. *Chem. Commun.* **2006**, 2460.

respectively. Interestingly, the absorption domain was found significantly extended for complexes **3** and **4** which showed two absorption maxima indicating the presence of two MLCT transitions. The highest absorption maximum value was attributed to the metal to ligand (π*DCB) transition and the lowest to the metal to ligand (π*L).

1-**4** also displayed higher emission maxima than the corresponding homoleptic $[RuL_3]^{2+}$ complexes. This increase of the $\lambda_{em\text{-}max}$ also implied a decrease of the radiative constant (k_r), of the excited-state lifetimes (τ) as well as the quantum yields (φ_{em}). This effect was notable in the pyrrolidine series in which electron delocalization is absent. Consequently, low τ values of 88 and 9 ns were measured for **3** and **4** respectively.

Table XIII Photophysical properties of complexes **1**-**4** and their homoleptic analogues.

Dyes	$\lambda_{abs\text{-}max}$ (nm)[a]	ε x 10^{-3} ($M^{-1}cm^{-1}$)	$\lambda_{em\text{-}max}$ (nm)[b]	φ_{em} (%)	τ (ns)	k_r (10^4 s^{-1})
Ru(pyrrbpy)$_3^{2+}$	465	8.6	630	0.022	635	12.3
Ru(pyrr$_2$bpy)$_3^{2+}$	480	22.2	650	0.044	357	8.9
Ru(pyrrldbpy)$_3^{2+}$	481	13.5	691	0.021	271	7.8
Ru(pyrrld$_2$bpy)$_3^{2+}$	520	13.2	710	-[c]	58	-
1	472	19.0	705	0.019	435	4.4
2	483	21.0	730	0.010	224	4.4
3	492 448	15.2 14.3	734	0.009	88	9.8
4	535 423	11.6 14.4	760	0.004	9	4.2

[a] Measured in CH_3CN at 25°C. [b] λexcit = 460 nm, OD<0.05 in the absence of O_2. [c] Photochemically instable.

6.1.2.2 Electrochemistry

Table XIV Electrochemical properties of complexes **1-4** and their homoleptic analogues.

Dyes	$E_{1/2}Ru^{III}/Ru^{II}(\Delta Ep)$ (V/SCE)[d]	Ligand processes (V/SCE)[e]	$E^*_{1/2}$ Ru^{III}/Ru^{II*} (V/SCE)[g]	E^{00} (eV)[h]
$Ru(pyrrbpy)_3^{2+}$	1.16 (90)	-1.21 (rev.)	-0.93	2.09
$Ru(pyrr_2bpy)_3^{2+}$	1.12 (90)	-1.20 (rev.)	-0.91	2.03
$Ru(pyrrldbpy)_3^{2+}$	0.55 (100)	-1.54 (rev.)	-1.58	2.13
$Ru(pyrrld_2bpy)_3^{2+}$	0.17 (100)	n.o.[f]	-1.80	1.97
1	1.19 (100)	-1.35 (irrev.)	-0.78	1.97
2	1.14 (100)	-1.18 (irrev.)	-0.81	1.95
3	0.72 (90)	-1.46 (irrev.)	-1.28	2.00
4	0.53 (70)	-1.00 (irrev.)	-1.46	1.99

[d] First oxidation potential standardized with Fc^+/Fc as internal standard and converted into SCE scale by adding 0.38V ($E_{1/2}Fc^+/Fc$), recorded at 100mV/s using $LiClO_4$ as supporting electrolyte. [e]First reduction potential. In case of reversibility, the value stands for $E_{1/2}$ (L/L^-). If irreversibility, the value stands for Epc (L/L^{-}). [f] not observed. [g] First oxidation potential at excited state. [h] Energy gap between vibrational levels ($\Delta=0$) at the ground and excited state.

The oxidation potentials of the Ru^{III}/Ru^{II} couple were reversible and found at lower values for the pyrrolidine series as a consequence of the expected electron-donor effect of the ligands. However, the potentials in **1-4** were higher than those of the corresponding homoleptic complexes indicating that the HOMO was at lower levels. This was a consequence of the electron-withdrawing effect of the dcbpy ligand favouring the HOMO stabilization. At first glance, the low potentials observed in the pyrrolidine series could be attributed to an oxidation of the pyrrolidine moiety itself. However, the variation of the potential values from homoleptics to heteroleptics and the observation of reversible monoelectronic waves led to discard such a hypothesis. The absence of the pyrrolidine oxidation was firmly demonstrated by performing an exhaustive oxidation of $[Ru(pyrrld_2bpy)_3]^{2+}$ at 0.5 V/SCE. After exchange of 1.2 $F.mol^{-1}$, the oxidized compound displayed the expected blue-green colour ($\lambda_{abs\text{-}max}$ = 763 nm) characteristic of a Ru(III)

complex. After reduction, identical electronic spectra were found for the corresponding reduced compound and starting $[Ru(pyrrld_2bpy)_3]^{2+}$.

Logically, a decrease of the HOMO level should induce a blue-shift of the absorption instead of the observed bathochromic effects. This discrepancy could be attributed to a concomitant decrease of the LUMO level allowing a smaller gap between the HOMO and the LUMO levels compared to homoleptic complexes. Such effect on the LUMO was the consequence of the position of the π*DCB orbital at a lower energetic value than the π*L. The comparison of electrochemical potentials of L/L^- couples between homoleptic complexes and **1-4** was made impossible due to the irreversibility of the L/L^- processes with the latter. It is worthy of note that the excited–state oxidation potential $E^*_{1/2}ox$ ($E^*_{1/2}ox = [E_{1/2}Ru^{III}/Ru^{II*}-E^{00}]$) for dyes **1-4** varied from -0.78 to -1.46 V/SCE indicating sufficient low reducing property to allow for the electron injection into the TiO_2 flat band potential which value is typically near 0.7 V/SCE.[126] From this series of measurements, the complexes **1-4** were found promising dyes with high ε values especially in the pyrrole series and extended absorption domains in the pyrrolidine series.

Dyes **1** and **2** could be seen as useful precursors for the preparation of polypyrrole films upon electrochemical oxidation. In a preliminary experiment, dye **1** was electrodeposited on an FTO electrode under potentiostatic conditions (1.2V vs SCE). The formation of a surface bound electroactive Ru^{II} species was clearly evidenced by cyclic voltammetry. Indeed after rinsing of the electrode with acetonitrile, the voltamograms showed a linear behavior of the peak current with the scan speed.[127]

Then we turned to the investigation of photoelectrochemical properties of the new dyes to evaluate their performance in a photovoltaic device.

[126] Grätzel, M. *Inorg. Chem.*, **2005**, *44*, 6841.
[127] This electropolymerization result will be published soonly.

6.1.3 IPCE% measurements.

The complexes **1**-**4** were chemisorbed on TiO_2 films and the semiconductor sensitization was first checked by UV-Vis analyses (Figure 93). The spectra were compared to those of known reference dyes $[Ru(DCB)_3]^{2+}$(**5**)[128] and **N3**[123].

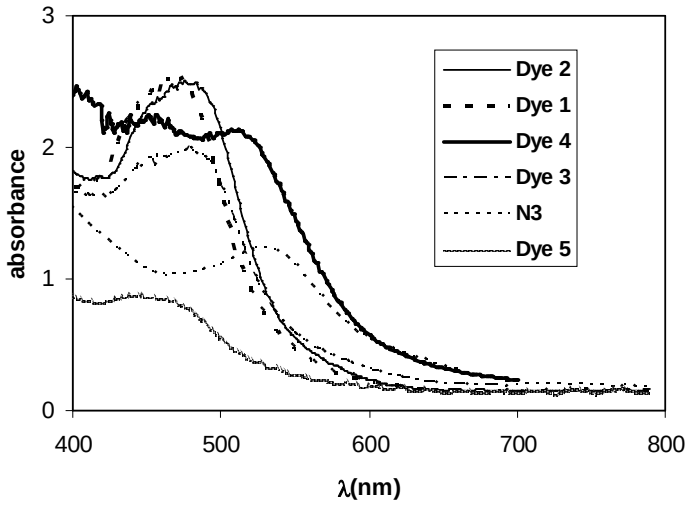

Figure.93 Overlay absorption spectra of $Ti0_2$ photoanodes modified with **1**-**4**, **N3**, and **5**.

All the electrodes modified with the new dyes exhibited higher absorbance than the reference complexes, the best scores being obtained for the pyrrole series (dyes **1** and **2**) just like in solution (see table XIV). In addition comparable absorption domains were observed for **4** and **N3**. This result was promising for the elaboration of "bpy only" dyes expected to prevent the known instability drawbacks of the NCS ligands.[129]

All the absorption maxima were lower than in solution. For example this value was decreased by 21 nm for **4**. Such blue shifts can be explained by the electron-acceptor character of the semi conductor that weakens the electronic charge on the dye. Additionally, the electronic delocalization through the titanates at the TiO_2-dye interface also contributed to HOMO level stabilization and thus to blue-shifts. Then we turned to the assembly of DSC using our new dyes and to IPCE measurements. The DSCs were assembled following

[128] Vlachopoulos, N.; Liska, P.; Augustynski, J.; Grätzel, M. *J. Am. Chem. Soc.* **1998**, *110*, 1216.

[129] For studies on the electrochemical stability of the NCS ligand see (a) Kohle, O.; Grätzel, M.; Meyer, A.F.; Meyer, T.B., *Adv. Mater.* **1997**, *9*, 904. (b) Cecchet, F.; Gioacchini, A.M.; Marcaccio, M.; Paolucci, F.; Roffia, S.; Alebbi, M.; Bignozzi, C.A. *J. Phys. Chem.* B **2002**, *106*, 3926.

reported methods.[120] The photoelectrochemical experiments were performed using various electron transfer mediators in the electrolyte including the most popular I_3^-/I^- couple (platinum cathode) and Co^{II}-based mediators[120,130] (gold cathode). The photo-anode was a film of nanocristalline TiO_2. The best performances were obtained in the pyrrole series (dyes **1** and **2**) attaining excellent IPCE values (near 80%) within the maximum absorption range (Figure. 93). The best results were recorded using a mixture of $[Fe(DMB)_3]^{2+}$ (DMB = 4,4'-dimethyl-bipyridine) and $[Co(DTB)_3]^{2+}$ (DTB = 4,4'-diterbutyl-bipyridine) as mediator[129] instead of I_3^-/I^-. While absorbing in the widest range with good absorbance, dyes **3** and **4** showed moderate IPCE results (near 40%). The best results were obtained with $[Co(DTB)_3]^{2+}$ as mediator (Figure. 95).

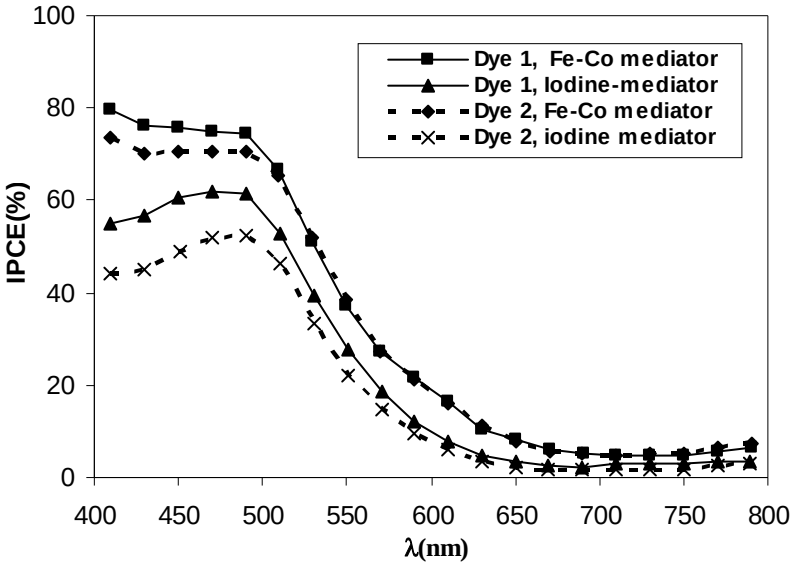

Figure.94 Photoaction spectra of dyes **1** and **2**. Fe-Co mediator : $[Fe(DMB)_3]$ $(PF_6)_2$ (0.015M) and $[Co(DTB)_3](PF_6)_2$ (0.15M) in CH_3CN. Iodine mediator: LiI (0.5M) and I_2 (0.05M) in CH_3CN.

[130] Cazzanti, S.; Caramori, S.; Argazzi, R.; Elliott, C.M.; Bignozzi, C.A. *J. Am. Chem. Soc.* **2006**, *128*, 9996.

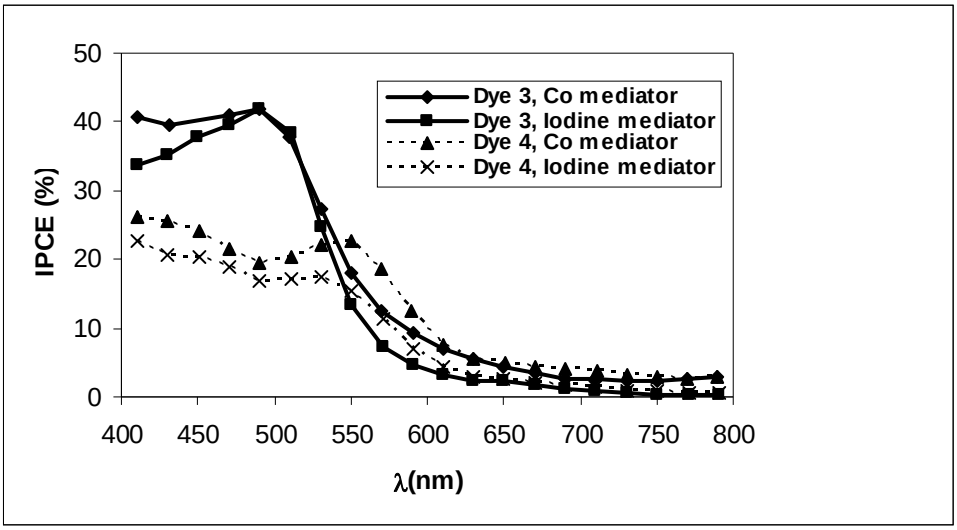

Figure.95 Photoaction spectra of dyes **3** and **4**. Co mediator: $[Co(DTB)_3](PF_6)_2$ (0.15M) in CH_3CN. Iodine mediator : LiI (0.5M) and I_2 (0.05M) in CH_3CN.

Interestingly, the best results were obtained with pyrrole-based dyes **1** and **2** which display the highest $E^*_{1/2}ox$ values and thus are not the best reductants. This indicated the probable involvement of other parameters such as the electron collection efficiency parameter ($\eta_{coll.}$) which reflects the charge recombination process and often determines the cell performances.[11]

Beside these promising performances of dyes **1** and **2,** some limitations have been pointed out probably resulting from a too slow regeneration of the oxidized dye after the injection step into the TiO_2 conduction band. As reported above (Table XIV), the pyrrole and pyrrolidine moieties induced a notable decrease of the Ru^{III}/Ru^{II} oxidation potentials especially with pyrrolidine (dyes **3** and **4**). Thus regeneration step was more efficient with the Co-based mediators (0.2 V/SCE) than with I_3^-/I^- (0.4 V/SCE).

6.1.4 Conclusion.

The electronic effect of pyrrole and pyrrolidine-containing ligands (L) on the properties of $[RuL_2DCB]^{2+}$ complexes has been demonstrated. The TiO_2 electrodes modified with the new dyes exhibited extended absorption domains and higher absorbances than the known **N3** dye. Good IPCE values (near 80%) have been obtained in the pyrrole series providing a Cobalt-based mediator instead of the usual I_3^-/I^- was used. The DSC efficiency depends strongly on both the dye properties (absorption domain, molar extinction, oxidation potentials) and

transfer mediator. Work is now progressing to design new dyes focusing on the optimization of the regeneration step. The electropolymerization of pyrrole-based dyes is also under active investigation for the elaboration of solid state solar cells.

6.2 Electron Donating Ligands and Electron Transport Mediators Effects on the Photovoltaic Performance of RuLdcbpy(NCS)$_2$ Dyes.

Chapter 6.1 reported new pyrrole and pyrrolidine-containing bipyridine ligands (**L^1-L^4**) which induced positive effects on light absorption of the corresponding $[RuL_3]^{2+}$ and $[RuL_2DCB]^{2+}$ complexes[131,132].

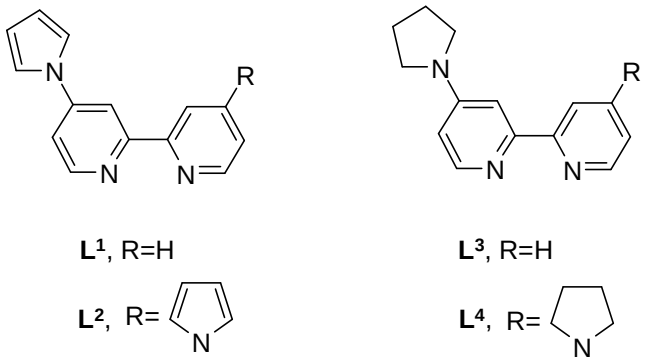

Figure. 96 Ligands used in the preparation of the new complexes **1-4.**

This was partly due to strong donor effects brought by the pyrrolidine moiety and charge delocalization into the pyrrole ring. The $[RuL_2DCB]^{2+}$ complex containing the pyrrole units reached good IPCE values (near 80%) when incorporated in a nanocrystalline TiO_2 solar cell. From these promising results we decided to investigate the effect of such ligands on the properties of trisheteroleptic Ru(L)(DCB)(NCS)$_2$ complexes. Herein we report the preparation and characterization of complexes **1-4** with L = L^1, L^2, L^3, L^4 respectively, their evaluation as sensitizers and the influence of various mediators on the photoaction spectra.

[131] Martineau, D.; Gros, P. C.; Fort, Y., *J. Org. Chem.* **2004,** 69, 7914.
[132] Martineau, D.; Beley, M.; Gros, P. C.; Cazzanti, S.; Caramori, S.; Bignozzi, C. A., *Inorg. Chem.* **2007,** in press.

6.2.1 Synthesis of bis-bipyridyl Ru(II) complexes.

Complexes **1-4** were prepared using an elegant and clean one-pot sequential synthesis from the dinuclear $[Ru(p\text{-}cym)Cl_2]_2$ complex.[133] Thus the ligands were successively coordinated to ruthenium by first adding **L**. DCB and finally NCS.

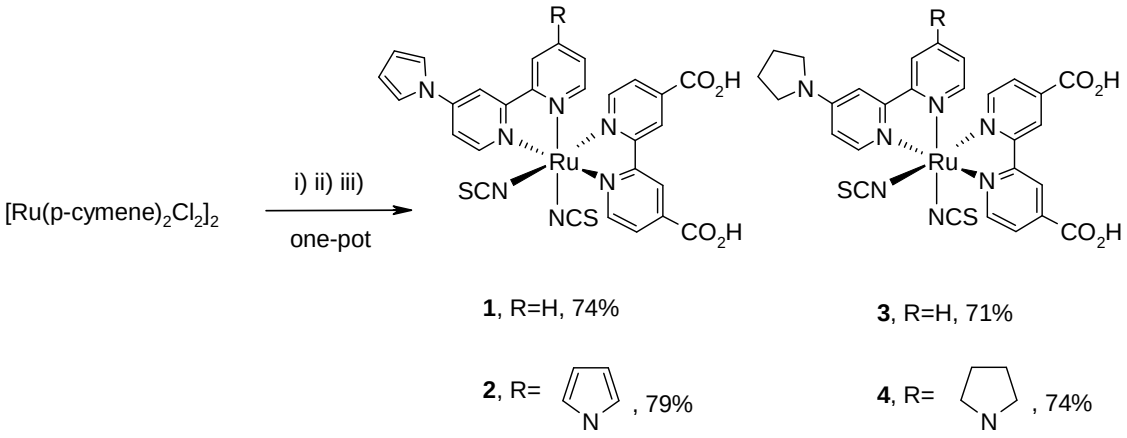

i) **L¹** or **L²** or **L³** or **L⁴** (1 eq.), DMF, reflux, 4 h. ii) dcbpy (1 eq.), DMF, reflux, 4 h.
iii) NH_4NCS (10 eq.) DMF, reflux, 4 h.

Scheme 1. Preparation of dyes **1-4.**

All the expected complexes were obtained in good yields after purification on a Sephadex LH20 column (size exclusion) and their characterization was performed by UV-Vis (absorption and emission electronic spectra) and electrochemistry (Table XV). The values were compared to those of the known reference dye $[Ru(DCB)_2(NCS)_2]$ (**N3)** in order to evaluate the influence of ligands **L^1-L^4 .**

Dye 1. L^1 (13.3 mg, 0.06 mmol) and $[Ru(p\text{-}cym)Cl_2]_2$ (18.4 mg; 0.03 mmol) were dissolved in DMF (5 mL) under Ar. The solution was then stirred for 4 h at 70°C, DCB (14.7 mg, 0.06 mmol) was then added as a solid and the mixture was refluxed for 4h. Finally, NH_4NCS (45.7 mg, 0.6 mmol) was added and the mixture stirred at the same temperature for an additional 4 h period. After cooling at room temperature, the solvent was evaporated, water was added and the suspension placed in a refrigerator for 4 h. The precipitate was filtered and dried under

[133] Wang, P.; Klein, C.; Humphry-Baker, R.; Zakeeruddin, S. M.; Grätzel, M., *J. Am. Chem. Soc.* **2005,** 127, 808-809.

vacuum. The dry solid was then treated with a solution of Bu_4NOH in methanol (1 mL of a 1M solution) filtered over glass wool and purified by elution with methanol through a Sephadex LH20 column. The violet coloured band was then collected and 5 mL of water were added before evaporation of methanol under reduced pressure. The aqueous phase was finally treated with dilute HNO_3 until pH 3. The solution was then placed in a refrigerator overnight . The obtained pink precipitate was then filtered, washed successively with water and diethylether and dried under vacuum yielding **1** (30.2 mg, 74%) as a pink powder.

^{1}H NMR (DMSO-*d6*) : δH (ppm) = 9.45 (d, J = 6Hz , 1H) , 9.42 (d, J = 6Hz , 1H) , 9.12 (m , 2H) , 9.07 (d : J = 5 Hz , 2H) , 8.96 (m , 2H) , 8.92 (m , 2H) , 8.52 (d, J = 6 Hz, 1H), 8.18-8.37 (m, 4H), 7.89-7.99 (m, 4H), 7.85 (t, J =7 Hz, 1H), 7.82 (d, J = 6 Hz, 1H), 7.77 (d, J = 6 Hz, 1H), 7.70 (m, 3H), 7.62 (m, 2H), 7.52-7.57 (m, 3H), 7.42 (d, J = 6 Hz, 1H), 7.16 (t, J = 7 Hz, 1H), 7.05 (dd, J^1 J = 6 and 2 Hz, 1H), 6.97 (m, 2H), 6.73 (m, 1H), 6.71 (m, 1H), 6.36 (td, , 1H). MS (ES): m/z = 681.99 ($[M-H]^-$), 638.00 ($[M-CO_2H]^-$), 594.01 ($[M-2CO_2H]^-$). UV-vis (CH_3CN), λmax (nm) (ε ($M^{-1}cm^{-1}$))= 532 (7300) and 385 (7200).

Dye 2. The same procedure was repeated with **L2** (17.2 mg, 0.06 mmol) and **2** was obtained as a pink powder (35.6 mg, 79%).

^{1}H NMR (DMSO-*d6*): δH (ppm) = 9.43 (d, J=5.8 Hz, 1H), 9.15 (d, J = 6.5 Hz, 1H), 9.13 (s, 1H), 9.02 (d, J = 1.7 Hz, 1H), 8.98 (s, 1H), 8.86 (d, J = 1.7 Hz, 1H), 8.36 (dd, J = 5.7 and 2 Hz, 1H), 8.28 (d, J = 5.5 Hz, 1H), 7.99 (t, J = 2 Hz, 1H), 7.91 (d, J = 5.7 Hz, 1H), 7.69 (t, J = 2 Hz, 2H), 7.61 (dd, J = 5.7 and 1 Hz, 1H), 7.52 (dd, J = 2 et 6.5 Hz, 1H), 7.40 (d, J = 6.5 Hz, 1H), 6.55 (t, J = 2 Hz, 2H), 6.41 (t, J = 2 Hz, 2H). MS (ES) : m/z = 747.0 ($[M-H]^-$), 703.0 ($[M-CO_2H]^-$), 659.0 ($[M-2CO_2-H]^-$). UV-vis (CH_3CN), λmax (nm) (ε ($M^{-1}cm^{-1}$))= 534 (8700) and 379 (10200).

Dye 3. The same procedure was repeated with **L3** (13.5 mg, 0.06 mmol) and **3** was obtained as a pink powder (29.3 mg, 71%).

^{1}H NMR (DMSO-*d6*) δH (ppm) = 9.43 (d, J = 5.8 Hz, 1H), 9.40 (d, J = 5.8 Hz, 0.7H), 9.24 (d, J = 4.9 Hz, 1H), 9.12-9.1 (m, 1.7H), 8.96 (s, 1.7H), 8.77 (d, J = 8 Hz, 1H), 8.61 (d, J = 6.6 Hz, 1H), 8.25-8.19 (m, 2.8H), 7.91 (d, J = 8 Hz, 0.7H), 7.89 (d, J = 6 Hz, 1H), 7.83 (t, J = 7.8 Hz, 1H), 7.78 (d, J = 6 Hz, 1H), 7.72 (s, 1H), 7.66 (d, J = 5.8 Hz, 1H), 7.60 (d, J = 5.6 Hz, 1H), 7.55 (s, 1H), 7.41 (d, J = 5.2 Hz, 0.7H), 7.15 (t, J = 6.5 Hz, 0.7H), 7.08 (d, J = 5.8 Hz, 0.7H), 6.72 (d, J = 6.5 Hz, 0.7H), 6.32 (d, J = 6.5 Hz, 0.7H), 3.59 (m, 2.8H), 3.33 (m, 4H),

2.08 (m, 2.8H), 1.92 (m, 4H). MS (ES) : m/z = 686.02 ($[M-H]^-$), 642.03 ($[M-CO_2H]^-$), 598.04 ($[M-2CO_2-H]^-$). UV-vis (CH_3CN), λmax (nm) (ε ($M^{-1}cm^{-1}$))= 538 (7600) and 385 (7200).

Dye 4. The same procedure was repeated with **L4** (17.7 mg, 0.06 mmol) and **4** was obtained as a pink powder (34 mg, 75 %).

^1H NMR (DMSO-*d6*) δH (ppm) = 9.45 (d, J = 6.2 Hz, 1H), 9.00 (s, 1H), 8.85 (s, 1H), 8.59 (d, J = 6.5 Hz, 1H), 8.20 (d, J = 6 Hz, 1H), 7.95 (d, J = 6 Hz, 1H), 7.65 (d, J = 6 Hz, 1H), 7.53 (s, 1H), 7.35 (s, 1H), 7.00 (d, J = 6.5 Hz), 6.63 (d, J = 6.6 Hz, 1H), 3.58 (m, 4H), 3.33 (m, 4H), 2.08 (m, 4H), 1.91 (m, 4H). SM (ES) : m/z = 755.08 ($[M-H]^-$), 711.09 ($[M-CO_2H]^-$), 667.11 ($[M-2CO_2-H]^-$). UV-vis (CH_3CN), λmax (nm) (ε ($M^{-1}cm^{-1}$))= 542 (6500) and 424 (7700).

6.2.2 Photophysical and photoelectrochemical characterization of Ru(II) complexes.

All complexes showed 2 MLCT transitions like did **N3**. For each complex the highest $\lambda_{abs\text{-}max}$ value was attributed to the metal to ligand (π*Ru-NCS) and the lowest to the metal to ligand (π*L). The Ru^{III}/Ru^{II} oxidation potentials were also notably decreased compared to those of **N3**. While **1** and **2** did not behave differently. significant changes were observed by increasing the number of pyrrolidine moieties in **3** and **4** as a consequence of the stronger electron donor effect.

Then we turned to the evaluation of the photovoltaic performances of the new dyes. The complexes were first chemisorbed on TiO_2 films and the sensitization checked by UV-Vis spectroscopy (Figure 97). Dyes **1-4** displayed a wide absorption range comparable to those of **N3**. The absorbances were optimal at 550 nm and decreased slowly until 700 nm. Dye **2** bearing two pyrrole units exhibited the best absorbance attributable to charge delocalization through the pyrrole and bipyridine. Pyrrolidine-containing complexes **3** and **4** showed lower absorbances which then decreased almost linearly. However, their absorbance and absorption domain were found comparable to those of **N3**.

The calculation of the excited-state oxidation potential ($E^*_{1/2ox}$(Ru^{III}/ Ru^{II*})) for sensitizers **1-4** (table XV**)** indicates that their excited states exhibit far sufficient reducting

abilities to allow the electron injection into the conduction band of TiO_2 which is estimated to lie at near -0.7V/SCE[134].

Then we examined the photoaction spectra (Figures 98-100). DSCs were assembled using the new dyes and IPCE measurements were performed using various mediators such as the popular I^-/I_3^- and the recently reported Co(II)-based ones. The incorporation of several redox co-mediators such as ferrocene and phenothiazine has also been investigated.

As shown in Figure 98 and Figure 100, while leading to good IPCE with **N3** the I^-/I_3^- couple gave poor performances with all the new dyes **1-4**. Despite extended absorption domains. **1** and **2** gave a 30% maximum value while negligible photocurrents were detected with **3** and **4**. We attributed these poor performances to the low regeneration of the dye by reduction of its oxidized form by the I^-/I^-_3 ($E°(I_2/I^-)$= 0.4V/SCE) couple due to the low driving force of this reaction.

Table XV. Photophysical and electrochemical properties of complexes **1**-**4**.

Dye	$\lambda_{abs\text{-}max}$ (nm)[a]	ε (10^3 $M^{-1}cm^{-1}$)	$\lambda_{em\text{-}max}$ (nm)[b]	φ_{em} (%)[c]	$E_{1/2}$ Ru^{III}/Ru^{II} (V/SCE)[d]	Ligand processes (V/SCE)[e]	$E^*_{1/2}$ Ru^{III}/Ru^{II*} (V/SCE)[f]	E^{00} (eV)[g]
1	532 385	7.3 7.2	798	0.034	0.62	-1.16	-1.30	1.92
2	534 379	8.7 10.2	805	0.22?	0.61	-1.17	-1.33	1.94
3	538 385	7.6 7.2	811	0.032	0.50	-1.12	-1.55	2.05
4	542 424	6.5 7.7	703	0.011	0.37	-1.15	-1.55	1.90

[a] Measured in CH_3CN at 25°C. [b] λ_{exc} = 460 nm. OD<0.05 in the absence of O_2. [c] Measured on the deprotonated form (TBAOH treatment). [d] First oxidation potential standardized with Fc^+/Fc as internal standard and converted into SCE scale by adding 0.38V ($E_{1/2}Fc^+/Fc$). recorded at 100mV/s using $LiClO_4$ as supporting electrolyte. [e]First reduction potential. All processes irreversible. the value stands for Epc ($L/L^{-\cdot}$). [f] First oxidation potential at excited state. [g] Energy gap between vibrational levels (ν=0) at the ground and excited state. Determined according to Adamson and Fleischauer[11] by taking the wavelength ($\lambda_{0.05}$) corresponding to 5% of the maximum intensity of the emission spectrum recorded at 298 K (E^{00}=1240/ $\lambda_{0.05}$).

[134] Gratzel, M., Solar Energy Conversion by Dye-Sensitized Photovoltaic Cells. *Inorg. Chem.* **2005,** 44, (20), 6841-6851.

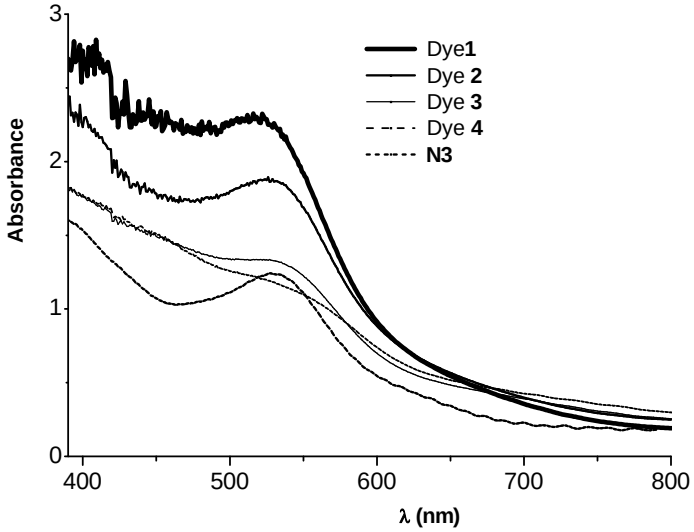

Figure. 97 Overlay absorption spectra of TiO_2 photoanodes modified with **1**-**4** and **N3**.

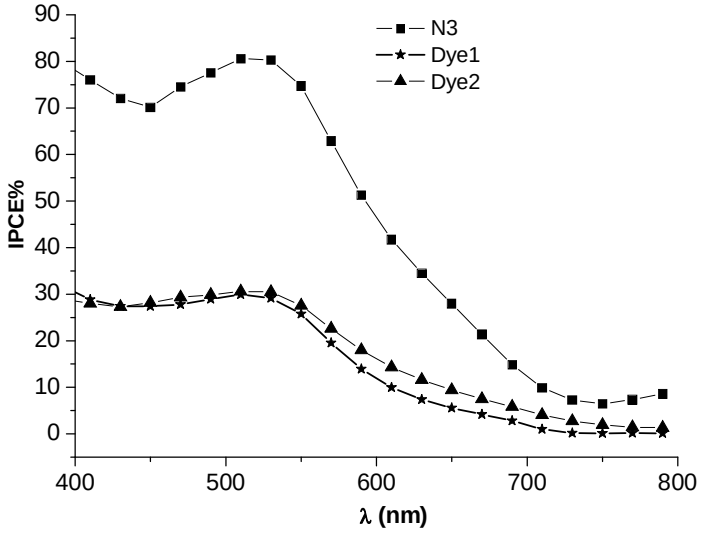

Figure.98 Photoaction spectra of **Dye 1**. **Dye 2** and **N3** with mediator LiI 0.5 M and I_2 0.05 M in acetonitrile. $LiClO_4$ (0.5 M) was present in every electrolyte solution.

In contrast, the photocurrents were notably enhanced with lower oxidation potential Co^{II}-based mediators. A 45 % IPCE value was attained near 550 nm using $[Co(DTB)_3]^{2+}$ / $[Co(DTB)_3]^{3+}$ for which ($E_{1/2}(Co^{III}/Co^{II})$= 0.2V/SCE).

An additive effect was observed with dye **2**. Indeed the presence of two pyrrole units induced a better performance (55% IPCE). This dye remained active until 700 nm where a 20% IPCE value could be measured. The introduction of phenothiazine or ferrocene as relays

did not improve the outcome. Interestingly. **N3** was less efficient than **1** and **2** using the cobalt-based mediator. Even using this mediator. low performances were obtained with the pyrrolidine-containing complexes **3** and **4** (Figure 100) . This could be due to the low oxidation potentials of these complexes making inefficient the regeneration step as well as by I^- or Co^{II} -based mediators. Particularly, no photocurrent was detected with **4** for which $E_{1/2}$ = 0.37 V/SCE.

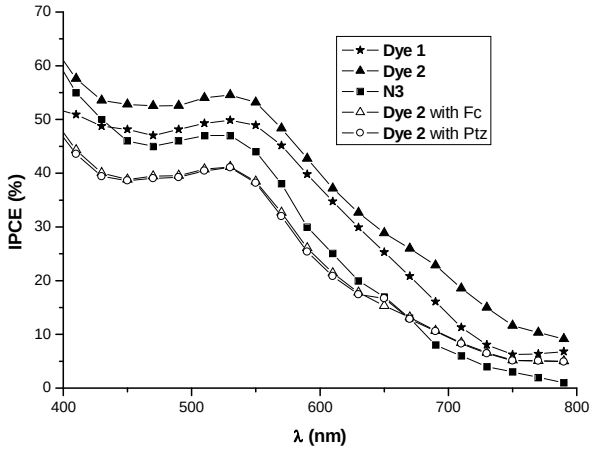

Figure.99 Photoaction spectra of **Dye 1**. **Dye 2** and **N3** with mediator $[Co(DTB)_3]^{2+}$ / $[Co(DTB)_3]^{3+}$ 0.15 / 0.015 M in acetonitrile. Fc = $[Co(DTB)_3]^{2+}$ 0.15 M / Ferrocene 0.015 M in acetonitrile. Ptz = $[Co(DTB_3]^{2+}$ 0.15 M / phenothiazine (0.015 M) in acetonitrile. $LiClO_4$ (0.5 M) was present in every electrolyte solution.

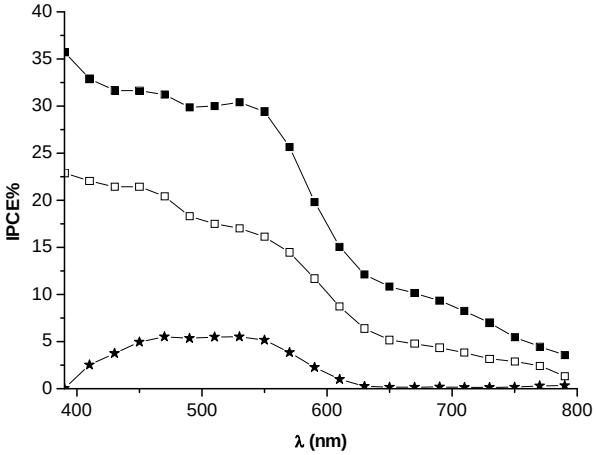

Figure.100. Photoaction spectra of Dye **3** with $[Co(DTB)_3]^{2+}$ / $[Co(DTB)_3]^{3+}$ 0.15 / 0.015 M in acetonitrile (black squares) and LiI 0.5 M and I_2 0.05 M in acetonitrile (stars). Photoaction spectrum of Dye **4** with $[Co(DTB)_3]^{2+}$ / $[Co(DTB)_3]^{3+}$ 0.15 / 0.015 M in acetonitrile (white squares). $LiClO_4$ (0.5 M) was present in the electrolyte solution. No photocurrent was detected with LiI 0.5 M and I_2 0.05 M in acetonitrile.

In summary, we have prepared new pyrrole and pyrrolidine-containing $RuL(DCB)(NCS)_2$ complexes using a one-pot sequence. Such substituents promoted red shifts of absorption and decrease of the metal oxidation potential. The best dye containing two pyrrole units exhibited high absorbance and extended absorption domain while offering a 55% IPCE value using a Cobalt-based mediator which ensured a faster regeneration of the dye than the I^-/I^-_3 couple. However, our best IPCE value reported here with dye **2** is about 70% of that given by **N3** with the I^-/I^-_3 couple. This limitation could be attributed to a slower Cobalt-complex diffusion in the electrolyte, due to its relatively weak mobility.

6.3 Ruthenium complexes bearing π-extended pyrrolo-stryryl-bipyridine ligand: electronic properties and evaluation as photosensitizers.

In this context, N-pyrrolo-bipyridine ligands (L) are promising and we have reported their effect on light harvesting ability of $[RuL_3]^{2+}$ and $[RuL_2(DCB)]^{2+}$ complexes[135]. Moreover, we have shown that the pyrrole moiety could be co-polymerized with EDOP (3,4-ethylenedioxy-pyrrole) molecules giving access to new solid state solar cells, the hole transporter being the polymer (PEDOP)[136]. In our continuing efforts to optimize the dye performance we have focused on complexes $[Ru(L1)_3]^{2+}$and **$Ru(L1)(DCB)(NCS)_2$** bearing an extended pyrrole-based ligand L1 (Figure 101). Herein we report the synthesis of the complexes as well as a comparison of their spectroscopic and electrochemical properties with those of complexes $[Ru(L2)_3]^{2+}$ and $Ru(L2)(DCB)(NCS)_2$ with the styryl group omitted in order to evaluate the effect of charge delocalization.

[135] D. Martineau, P. C. Gros, M. Beley and Y. Fort, Eur. J. Inorg. Chem. , 2004, 3984-3986. .
D. Martineau, M. Beley, P. C. Gros, S. Cazzanti, S. Caramori and C. A. Bignozzi, Inorg. Chem., 2007, 46, 2272-2277.
[136] S. Caramori, S. Cazzanti, L. Marchini, R. Argazzi, C. A. Bignozzi, D. Martineau, P. C. Gros and M. Beley, Inorganica Chimica Acta, 2008, 361, 627-634.

6.3.1 Experimental section.

6.3.1.1 Materials and instrumental apparatus.

Materials: 4-pyrrolobenzadehyde[137], L2[138] and $[Ru(L2)_3]^{2+}$[139] were prepared according to published procedures. Other chemical reagents were commercially available and used as such. DMF was degassed by several vacuum-argon cycles before use.

Analyses and Measurements: ^{1}H and ^{13}C NMR have been recorded on AC200, AC250 or DRX400 Bruker spectrometers. Microwave experiments have been performed on a CEM Discover device fitted with infra-red probe temperature control. Absorption UV-Vis electronic spectra have been recorded on a Varian Cary E spectrometer and emission UV-Vis electronic spectra on a SLM Aminco Bowman Series 2 apparatus using a (1 cm × 1 cm) quartz cell in deoxygenated solutions (OD<0.05). Excited state lifetimes were measured by time correlated single photon counting (TCSPC) using a Picoquant apparatus. 460 nm excitation of optically diluted (A460 ≈ 0.2) dye solutions in CH3CN was obtained with a PLS-8-2-271 nanoled (FWHM = 500 ps, repetition rate 5 MHz) driven by a PDL 800-B variable frequency pulsing unit. The same unit also provided the electric syncronization signal necessary to the Picoharp 300 TAC/ADC module for the photon arrival time measurement. Sample luminescence was filtered by a 610 nm cut-off filter and single photon emission events were detected by an Hamamatsu PMT-PMA-185-P phototube, preamplified and fed to the TAC/ADC unit. Emission decay histograms were automatically acquired on a PC and deconvoluted from the source profile using the Picoquant Fluofit® dedicated software. GC-MS (EI) spectra have been obtained on a HP 5971 analyzer. Electrospray mass spectra have been recorded on an Agilent MSD using CH_3CN as solvent. The electrochemical measurements were performed with a Voltalab PST006 Radiometer potentiostat using a conventional single compartment three-electrode cell. The reference electrode was the potassium chloride calomel electrode (SCE), the working electrode was a 10 mm Pt wire and the counter-electrode a 1 cm^2 vitreous carbon disc. The supported electrolyte was $Bu_4N^+BF_4^-$ 0.1M in CH_3CN and the solutions were purged with argon before each measurement. A 0.5 mM solution of the studied compound was generally used. All potentials are quoted versus

[137] J. Nakazaki, I. Chung, M. M. Matsushita, T. Sugawara, R. Watanabe, A. Izuoka and Y. Kawada, J. Mater. Chem, 2003, 13, 1011-1022.
[138] D. Martineau, P. Gros and Y. Fort, J. Org. Chem., 2004, 69, 7914-7918.
[139] D. Martineau, P. C. Gros, M. Beley and Y. Fort, Eur. J. Inorg. Chem. , 2004, 3984-3986. .

SCE, in these conditions the redox potential of Fc^{+}/Fc was found at 0.38 V. In all the experiments the scan rate was 100mV/s. IPCE measurements were performed by illumination of the cell using an Osram 150W Xenon lamp coupled to an Applied Photophysics monochromator. The irradiated surface was 0.5 cm2. Photocurrents were measured under short circuit conditions by a digital Agilent 34410A multimeter. Incident irradiance was measured with a 1 cm2 Centronic OSD100-7Q calibrated silicon photodiode.

Transient spectroscopy experiments were carried out by using a previously described transient absorption apparatus[140]. The 532 nm laser radiation was defocused with a plano-concave lens to obtain pulse energies of the order of 14 mJ/cm^2. No sample degradation was observed over several laser shots. To obtain a satisfactory S/N ratio, oscillographic traces were averaged over 10 laser shots. The sample consisted of a sensitized TiO2 film in contact with an appropriate electrolytic solution in acetonitrile.

6.3.1.2 Synthesis of ligands and related Ru(II) complexes.

L2 was obtained in 70% yield following our previous works by regioselective lithiation-chlorination of 4-pyrrolopyridine, and Ni-catalyzed homocoupling (Scheme 1) (ref.30). This methodology was not suitable for preparation of L1 since we knew from separate experiments that the styryl group was sensitive to nucleophilic additions by BuLi[141]. Thus, we turned to the direct functionalization of 4,4'-dimethylbipyridine using a Knoevenagel reaction with the appropriate 4-pyrrolo-benzaldehyde[142]. In the presence of t-BuOK in DMF at 100°C, L1 was obtained in acceptable 60% yield (Scheme 2).

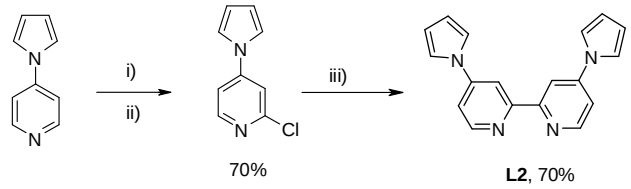

Scheme 1. Synthesis of ligand L2. Reagents and conditions: i) BuLi-Me2N(CH2)2OLi (2 eq.), toluene, -78°C, 1h. ii) C2Cl6 (2.5 eq.), toluene, -78°C to r.t. iii) NiCl2 (1.1 eq.), PPh3 (4.4 eq.), Zn (1.1 eq.), degassed DMF, 50°C, 1.5h.

[140] S. Cazzanti, S. Caramori, R. Argazzi, C. M. Elliott and C. A. Bignozzi, J. Am. Chem. Soc. , **2006**, 128, 9996-9997.
[141] T. Kaminski and P.C. Gros, unpublished results.
[142] J. Nakazaki, I. Chung, M. M. Matsushita, T. Sugawara, R. Watanabe, A. Izuoka and Y. Kawada, J. Mater. Chem, 2003, 13, 1011-1022.

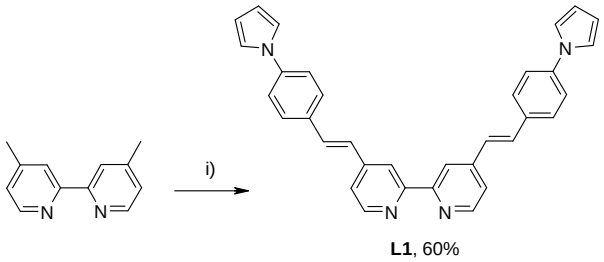

Scheme 2. Synthesis of ligand L1. Reagents and conditions: i) 4-pyrrolo-benzaldehyde (2.2 eq.), t-BuOK (4 eq.), DMF, 100°C, overnight.

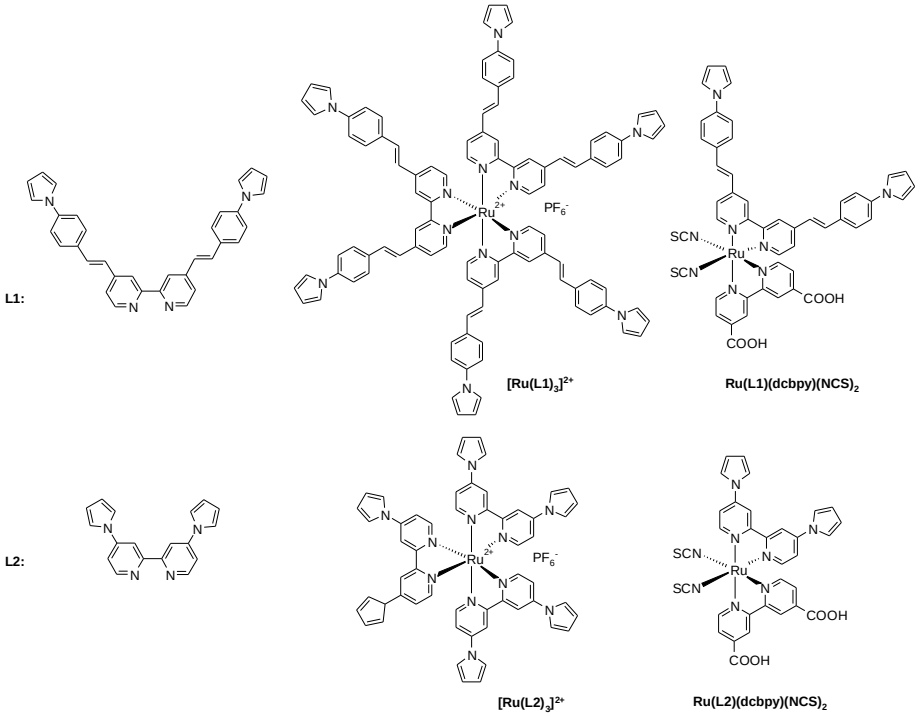

Figure.101 Ligands and complexes prepared and studied in this work

With ligands in hand, we investigated the preparation of symmetrically coordinated complexes $[Ru(L1)_3]^{2+}$ and $[Ru(L2)_3]^{2+}$ needed for evaluation of ligand effect on the complex properties in the absence of any electronic perturbation. The preparation of $[Ru(L2)_3]^{2+}$ was already reported by us.[143] We had found that when ligand L2 (3 eq.) was classically reacted overnight with $RuCl_3(H_2O)x$ in refluxing DMF, incomplete incorporation of ligands was obtained leading only to complex mixtures. A very practical and fast complexation under microwave irradiation was found to give $[Ru(L2)_3]^{2+}$ in good yield (85%) after 5 min at

[143] D. Martineau, P. C. Gros, M. Beley and Y. Fort, Eur. J. Inorg. Chem. , 2004, 3984-3986.

200°C in ethylene glycol. Our procedure was applied with success to the synthesis of the new complex $[Ru(L1)_3]^{2+}$ obtained as a a red solid in 60% yield from L1 (Scheme 2).

The heteroleptic complexes $Ru(L1)(DCB)(NCS)_2$ and $Ru(L2)(DCB)(NCS)_2$ were finally prepared using a one-pot synthesis from the dinuclear $[Ru(p\text{-cymene})Cl2]_2$ complex.8 The ligands were successively coordinated to ruthenium by first introducing L1 or L2 then 4,4'-dicarboxy-2,2'-bipyridine (DCB) and finally NCS anions (Scheme 3).

It is worthy of note that each step could be performed under microwave irradiation thus avoiding long periods of heating and possible degradation of ligands. The target complexes were obtained in acceptable to good yields after size exclusion separation on a Sephadex LH-20 column.

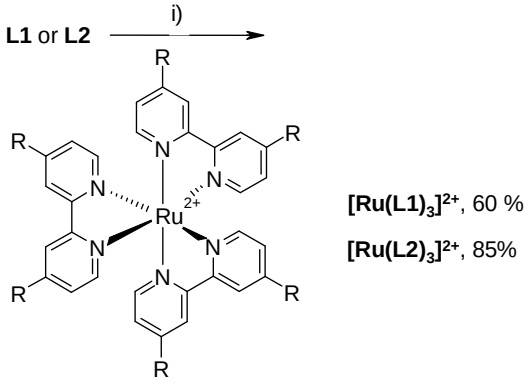

Scheme 2. Preparation of homoleptic complexes. Reagents and conditions. i) RuCl3(H2O)x (0.33 eq.), N-ethylmorpholine (2 drops), ethylene glycol, microwave irradiation, 250W, 200°C, 5 min.

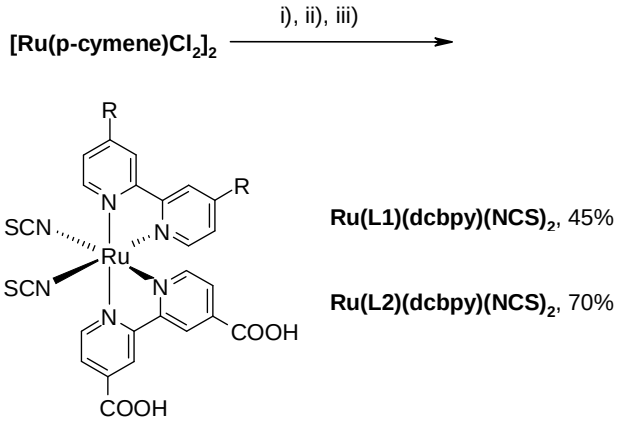

Scheme 3. Preparation of heteroleptic complexes. Reagents and conditions.All steps performed under microwave irradiation (250W). i) L1 or L2 (1 eq.) DMF, 70°C, 10min.. ii) dcbpy (1 eq.), DMF, 150°C, 10min. iii) NH4NCS (10 eq.), DMF, 150°C, 10 min.

L1. 4-pyrrolobenzaldehyde (257 mg, 1.5 mmol) and 4,4'-dimethyl-2,2'-bipyridine (92 mg, 0.5 mmol) were dissolved in 10 ml of deoxygenated anhydrous DMF. Solid potassium

tert-butoxyde (224 mg, 2.0 mmol) was then added rapidly. Immediately a yellow solid formed, which became darker. 3 drops of water were then added and the yellow suspension was stirred at 100 ºC overnight. The solid was filtered, washed with methanol and dissolved in boiling acetic acid (400-500 mL) giving a dark orange solution. After cooling, the liquid was concentrated and the solution left for several hours to precipitate. The bright yellow solid was filtered and washed with methanol. The solid was then suspended in methanolic KOH (approximately 1 M) and stirred for 48 hours at room temperature. Finally, the suspension was filtered and washed with methanol giving the product as a pale yellow powder (122 mg , 50%). Mp°C>200°C,

^{1}H NMR (400 MHz, dmso-d6), δ(ppm): 8.75 (m, 2H); 8.53 (m, 2H); 7.86 (m, 4H); 7.60-7.80 (m, 8H); 7.40-7.55 (m, 6H); 7.32 (m, 4H).

HRMS (ESI), [M+H], calcd(found) : 491.2230 (491.2198). UV-vis (CH3CN), λmax (nm) (ε (M^{-1} cm^{-1}))= 330 (44400).

[Ru(L1)$_3$]$^{2+}$ Ligand L1 (94.2 mg, 0.19 mmol), RuCl3•3H2O (15.7 mg, 0.06 mmol) and two drops of N-ethylmorpholine were suspended in 5 ml of ethyleneglycol. The mixture was irradiated in the microwave oven (5 minutes, 250 W, 200 ºC). Once cold, the dark red solution was poured into 25 ml of saturated aqueous solution of KPF_6 and left into the fridge for several hours. The red solid formed was filtered and washed with water, toluene and diethyl ether. The obtained solid was dissolved in the minimum amount of acetonitrile, poured into 25 ml of water and left precipitating into the fridge. After filtration and washing (water, toluene, diethyl ether) the product was obtained as a dark red solid (65 mg ,60 %).

^{1}H NMR- (400 MHz, CD3CN) δ(ppm): 8.79 (s, 6H); 7.82 (d, J = 16.0 Hz, 6H,); 7.80 (d, J = 6.8 Hz, 12H); 7.62 (d, J = 8.8 Hz, 12H); 7.54 (d, J = 5.2 Hz, 6H); 7.35 (d, J = 16.4 Hz, 6H); 7.29 (s, 18H); 6.37 (s, 12H).

MS (ESI): 1718.5 [M–PF_6]$^+$; 786.3 [M–2PF_6]$^{2+}$ UV-vis (CH3CN), λ_{max} (nm) (ε (M^{-1} cm^{-1}))= 490 (52000) and 374 (115000).

General procedure for preparation of heteroleptic complexes. L1 or L2 (0.06 mmol) and the ruthenium p-cymene dimer (18.4 mg, 0.03 mmol) were suspended in 5 ml of N,N-dimethylformamide. The mixture is irradiated in the microwave oven (10 minutes, 250 W, 70 ºC), resulting a clear yellow solution. Once cold, solid dcbpy ligand (14.7 mg, 0.06 mmol) was added and the mixture irradiated again (10 minutes, 250 W, 160 ºC). Once cold, NH_4NCS (45.7 mg, 0.6 mmol) was finally added to the dark green solution and irradiation was repeated

(10 minutes, 250 W, 160 ºC). Once cold, most of the solvent was evaporated and the flask filled with water and left in the fridge for several hours. The dark purple solid formed was filtered and washed with water. To purify the product, it was dissolved in a small amount of methanol (adding some drops of methanolic NBu4OH solution to help solubilization) and subjected to a Sephadex LH-20 column with methanol, the more coloured bands were collected together and mixed with 5 ml of water. The methanol was carefully evaporated and the aqueous solution treated with diluted HNO_3 until pH 3. Immediate precipitation was observed. The solid was filtered and washed with water and Et2O.

Ru(L1)(DCB)$(NCS)_2$. Yield: 45%.

δ(ppm) = ^{1}H NMR (DMSO-d6): 8.91 (d, J = 4.8 Hz, 2H), 8.85 (s, 2H), 7.91 (d, J = 4.2 Hz, 2H), 7.88-7.60 (m, 18H), 7.51 (brs, 2H), 7.48 (brs, 2H), 6.33 (brs, 2H), 6.30 (brs, 2H). MS (ESI): 1019.1 [M+3Na]+; 997.1 $[M–H+2Na]^+$; 975.1 $[M+Na]^+$; 916.1 [M–H–NCS+Na]+; 894.1 $[M–NCS]^+$. UV-vis (CH_3CN), λ_{max} (nm) (ε (M−1cm−1))= 540 (10300) and 357 (33200).

Ru(L2)(DCB)$(NCS)_2$. Yield : 70%.

^{1}H NMR (DMSO-d6): □ (ppm) = 9.43 (d, J=5.8 Hz, 1H), 9.15 (d, J = 6.5 Hz, 1H), 9.13 (s, 1H), 9.02 (d, J = 1.7 Hz, 1H), 8.98 (s, 1H), 8.86 (d, J = 1.7 Hz, 1H), 8.36 (dd, J = 5.7 and 2 Hz, 1H), 8.28 (d, J = 5.5 Hz, 1H), 7.99 (t, J = 2 Hz, 2H), 7.91 (d, J = 5.7 Hz, 1H), 7.69 (t, J = 2 Hz, 2H), 7.61 (dd, J = 5.7 and 1 Hz, 1H), 7.52 (dd, J = 2 et 6.5 Hz, 1H), 7.40 (d, J = 6.5 Hz, 1H), 6.55 (t, J = 2 Hz, 2H), 6.41 (t, J = 2 Hz, 2H).

MS (ESI) : m/z = 747.0 ($[M-H]^-$), 703.0 ($[M-CO_2H]^-$), 659.0 ($[M-2CO_2-H]^-$). UV-vis (CH_3CN), λ_{max}(nm) (ε (M−1cm−1))= 534 (8700) and 379 (10200).

$[Co(DTB)_3]^{2+}$ was prepared according to a published procedure[144]. $[Co(DTB)_3]^{3+}$ was obtained by addition of a slight excess of NOBF4 to an acetonitrile solution of $Co(DTB)_3^{2+}$. The solution was allowed to stir at room temp. for a couple of ours and evaporated (60 °C) to dryness, affording a yellow-orange solid. Unreacted NOBF4 quickly decomposed upon heating during evaporation.

[144] S. A. Sapp, C. M. Elliott, C. Contado, S. Caramori and C. A. Bignozzi, J. Am. Chem. Soc. , 2002, 124, 11215-11222.

6.3.2 Photophysical properties.

The absorption spectra of ligands have been measured in acetonitrile (Figure 102). Both ligands absorbed in the 220-320 nm region. In this domain, the extinction coefficient was much higher for L2 (124×10^3 $M^{-1}cm^{-1}$) instead of 36.1×10^3 $M^{-1}cm^{-1}$ for L1. The effect of delocalization in L1 was clearly evidenced by a band broadening and a red shift of the π-π* transition (λ_{max} = 330 nm, ε= 44.4×10^3 $M^{-1}cm^{-1}$).

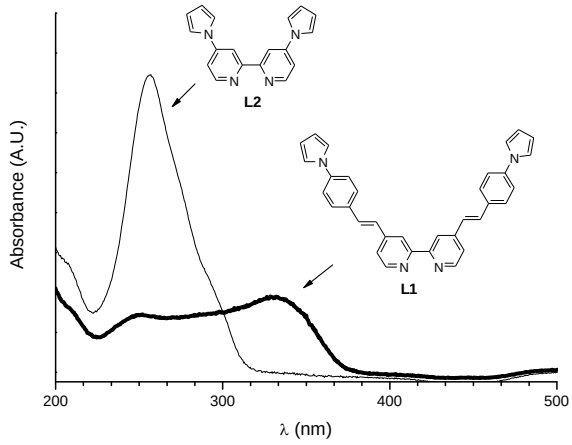

Figure.102 UV-Vis Absorption spectra of L1 and L2 in acetonitrile.

All the complexes were then next characterized by UV-vis spectroscopy and electrochemistry (Table XVI).

The absorption spectra of homoleptic complexes reported in Figure 103 clearly showed the influence of the π-conjugation. Indeed all the absorption maxima were slightly red shifted and molar extinction coefficients were considerably increased from $[Ru(L2)_3]^{2+}$ to $[Ru(L1)_3]^{2+}$. The latter complex exhibited two absorptions bands: the first at 374 nm with a very high ε value (115×10^3 $M^{-1}cm^{-1}$), the second at 490 nm (ε = 52×10^3 $M^{-1}cm^{-1}$) due to the MLCT transition. For comparison, the absorption of $[Ru(L2)_3]^{2+}$ was pointed out at 480 nm with a much lower molar extinction coefficients (22×10^3 M^{-1} cm^{-1}).

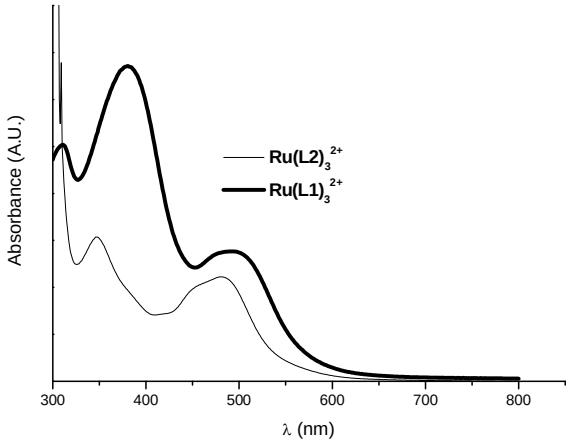

Figure. 103 UV-Vis Absorption spectra of homoleptic complexes in acetonitrile.

The red shift was also observed in emission spectra with λ = 650 and 689 nm for $[Ru(L2)_3]^{2+}$ and $[Ru(L1)_3]^{2+}$ respectively.

The cyclic voltammetry of both the complexes showed two oxidation waves, in addition to the reversible RuIII/RuII wave, pyrrole was found to be oxidized irreversibly at 1.2 V/SCE.

The extended ligand L1 had also a marked effect on the oxidation potential of the RuIII/RuII couple which was notably raised in $[Ru(L1)_3]^{2+}$ (1.30 versus 1.12 V/SCE for $[Ru(L2)_3]^{2+}$). The reason was a probable weakening of the donor effect of pyrrole through the stryryl group in L1 in contrast with L2 where the pyrrole was directly bonded to bipyridine. Thus it was clear that ligand L1 notably modified the electronic properties of the complex by increasing the molar exctinction coefficient and light harvesting, promising features for dye application.

The absorption spectra of the heteroleptic complexes (Figure 104) $Ru(L1)(DCB)(NCS)_2$ and $Ru(L2)(DCB)(NCS)_2$ showed a strong analogy with those of N3 (Table XVI) and of other $[Ru(L)(L')(NCS)_2]$ (where L is a bypiridine type ligand) complexes which have been deeply investigated. In the high energy region near 300 nm, sharp and intense bipyridine centered π-π* transitions were found. At lower energy (350-550 nm) two main broad MLCT transitions were observed, corresponding to the transfer from filled dπ metal orbitals to empty π* orbitals mainly localized on the bipyridine ligands.

The effect of L1 in $Ru(L1)(DCB)(NCS)_2$ was clearly shown by intense bands at 357 nm (ε= 33.2 x 10^3 M^{-1} cm^{-1}) and 540 nm (ε= 10.3 x 10^3 M^{-1} cm^{-1}). In the same region, the molar extinction coefficients of $Ru(L2)(DCB)(NCS)_2$ were much lower ($10.2x10^3$ and $8.7x10^3$ M^{-1} cm^{-1} at 379 and 534 nm respectively).

The lowest energy absorption tail up to 700 nm arised from transitions from non bonding NCS orbitals[145] to π^* bipyridine orbitals. The complexes were found to be emitting in fluid solution at room temperature in the 800-830 nm interval with an excited state (^{3}MLCT) lifetime near 30 ns (Table XVI). Upon deprotonation of the carboxylic moieties a blue shift of the emission maxima of about 20-50 nm, consistent with the destabilization of the dcbpy antibonding orbitals, was observed. The observed increase in emission intensity due to the augmented ground-excited state energy gap followed as a consequence. As already observed in homoleptic complexes, the reversible oxidation wave of pyrrole was clearly seen at 1.2 V/SCE. L1 was found to induce an increase of the oxidation potential of the RuIII/RuII couple compared to L2. This should make easier the regeneration by mediator after metal oxidation in the DSC.

Table 1. Photophysical and electrochemical properties of complexes.

Dyes	λabs-max (nm)[a]	ε (10^3 M^{-1} cm^{-1})	λem-max (nm)[b]	λem-max (nm)[c]	φem (%)[d]	τ (ns)[d]
$[Ru(L1)_3]^{2+}$	490	52.0	689	-	0.016	495
	374	115.0				
$[Ru(L2)_3]^{2+}$	480	22.2	650	-	0.044	357
	359	31.5				
N3	534	14.2	818	757	0.04	50
	396	14.0				
$Ru(L1)(dcbpy)(NCS)_2$	540	10.3	804	764	-	28
	357	33.2				
$Ru(L2)(dcbpy)(NCS)_2$	534	8.7	824	745	0.032	29
	379	10.2				

[a] Measured in CH_3CN at 25°C. [b] Photomultiplier corrected emission maxima for the complexes in acidic form in acetonitrile. [c] Photomultiplier corrected emission maxima for the complexes on the anionic form of the complexes in presence of Bu_4NOH. For b,c λ_{excit} = 460 nm, A<0.05 in the absence of O_2. [d] Emisson lifetimes and quantum yields were measured on the anionic form of the complexes in presence of Bu_4NOH in acetonitrile, λ_{excit} = 460 nm. A 460 ≈ 0.2 in the absence of O_2.

[145] H. Zabri, I. Gillaizeau, C. A. Bignozzi, S. Caramori, M.-F. Charlot, J. C. Cano Boquera and F. Odobel, Inorg Chem 2003, 42, 6656-6666.

Table XVII. Electrochemical properties of complexes.

Dyes	$E_{1/2}$ Ru^{III}/Ru^{II} (V/SCE)[e]	First ligand processes (V/SCE)[f]	$E^*_{1/2}$ Ru^{III}/Ru^{II*} (V/SCE)[g]	E^{00} (eV)[h]
$[Ru(L1)_3]^{2+}$	1.30	-0.80	-0.75	2.05
$[Ru(L2)_3]^{2+}$	1.12	-1.20 (rev.)	-0.91	2.03
N3	0.85[15]	-	-0.9	1.75
$Ru(L1)(dcbpy)(NCS)_2$	0.80	-1.00	-1.02	1.82
$Ru(L2)(dcbpy)(NCS)_2$	0.61	-1.17	-1.19	1.80

[e] First oxidation potential standardized with Fc^+/Fc as internal standard and converted into SCE scale by adding 0.38V ($E_{1/2}$ Fc^+/Fc). Recorded in CH_3CN using $Bu_4N^+BF_4^-$ as supporting electrolyte at 100mV/s. [f] First reduction potential. All processes irreversible. The value stands for E_{pc} (L/L^-.). g First oxidation potential at excited state for the complexes in acidic form. h Energy gap between vibrational levels (ν=0) at the ground and excited state for the complexes in acidic form. Determined by taking the wavelength (λ0.05) corresponding to 5% of the maximum intensity of the emission spectrum recorded at 298 K (E^{00}=1240/ λ0.05).[146]

In addition, the calculation of the excited-state oxidation potential for sensitizers $Ru(L1)(DCB)(NCS)_2$ and $Ru(L2)(DCB)(NCS)_2$ ($E^*_{1/2ox}$ (Ru(III)/Ru(II)*)) (Table XVII) indicated that their excited states exhibit far sufficient reducting abilities to allow the electron injection into the conduction band of TiO_2 which is estimated to lie at near -0.7V/SCE[147].
The dyes were then chemisorbed on TiO_2 films and the sensitization controlled by UV-Vis spectroscopy (Figure 105). As shown $Ru(L1)(DCB)(NCS)_2$ and $Ru(L2)(DCB)(NCS)_2$ displayed a wide absorption range comparable to those of N3. The absorbances were optimal at 550 nm and decreased slowly until 700 nm. Dye $Ru(L1)(DCB)(NCS)_2$ bearing L1 exhibited the best absorbance attributable to charge delocalization through the pyrrole styryl and bipyridine.

6.3.3 Photoelectrochemical characterization.

From these promising results, four DSCs were assembled using the new dyes and two different mediators such as the most popular I^-/I_3^- and the recently reported $[Co(DTB)_3]^{2+}$ [148]. IPCE measurements were performed and reported on Figure 106 and 107.

[146] A. W. Adamson and P. D. Fleischauer, Concepts of inorganic photochemistry, New York: Wiley edn., 1975.

[147] M. Gratzel, Inorg. Chem. , 2005, 44, 6841-6851.
[148] S. A. Sapp, C. M. Elliott, C. Contado, S. Caramori and C. A. Bignozzi, J. Am. Chem. Soc. , 2002, 124, 11215-11222.
32. S. Cazzanti, S. Caramori, R. Argazzi, C. M. Elliott and C. A. Bignozzi, J. Am. Chem. Soc. , 2006, 128, 9996-9997.

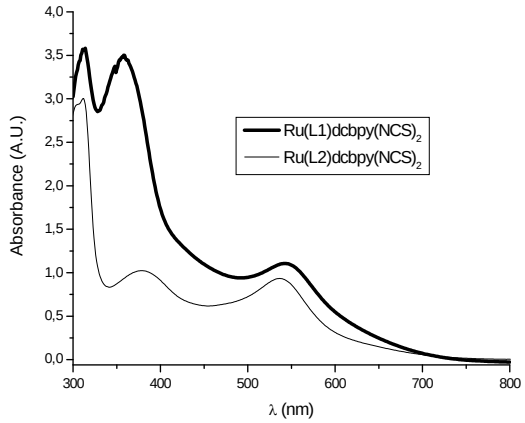

Figure 104. UV-Vis Absorption spectra of heteroleptic complexes.

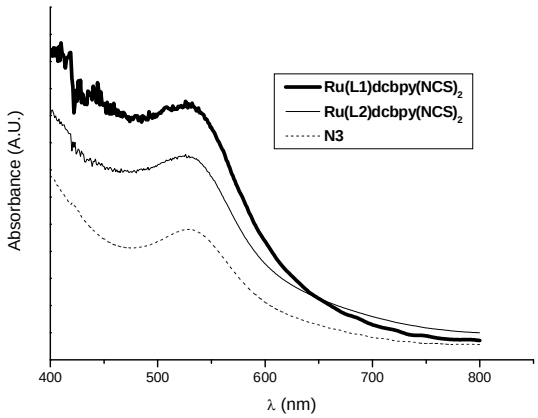

Figure 105. Overlay absorption spectra of TiO_2 photoanodes modified with the new heteroleptic complexes and N3.

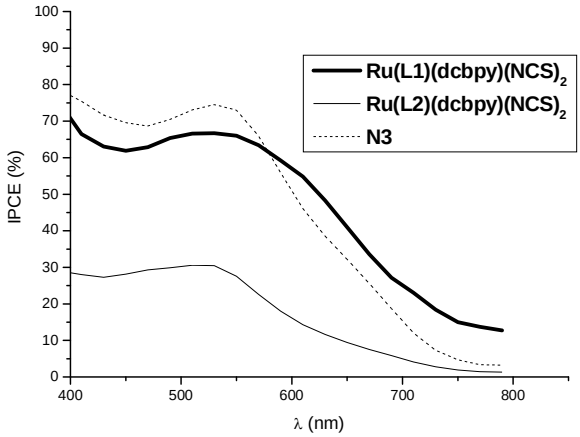

Figure 106. Photoaction spectra with mediator LiI 0.5 M and I_2 0.05 M in acetonitrile. $LiClO_4$ (0.5 M) was present in every electrolyte solution.

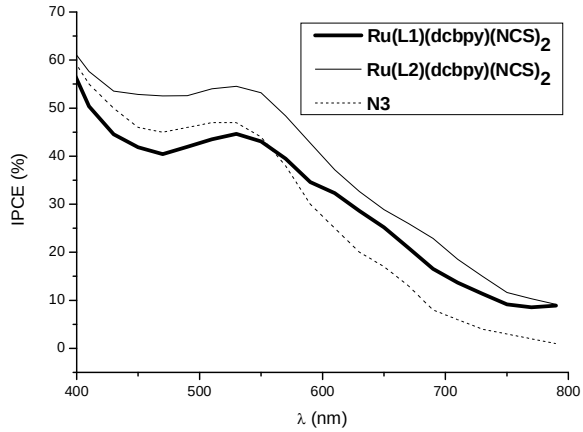

Figure 107. Photoaction spectra with mediator $[Co(DTB)_3]^{2+}$ /$[Co(DTB)_3]^{3+}$ 0.15 / 0.015 M in acetonitrile. $LiClO_4$ (0.5 M) was present in every electrolyte solution.

The effect of π-conjugation was very marked using I_3^-/I^- as mediator since the best performance was obtained with Ru(L1)(DCB)$(NCS)_2$ attaining a good IPCE value (near 70%) within the maximum absorption range (Figure 106). The results were found to be comparable to those of the standard N3 with wider absorption range. The IPCE at 700 nm was still of 25%. Ru(L2)(DCB)$(NCS)_2$ furnished a much lower photocurrent (30% IPCE) indicating a poorly efficient regeneration by the mediator.

With $[Co(DTB)_3]^{2+}$ as mediator (Figure 107), the IPCE were generally lower and a reverse order was observed. Ru(L2)(DCB)$(NCS)_2$ gave a better IPCE (55%) than did Ru(L1)(DCB)$(NCS)_2$ (45%). In any case the dyes showed a wider absorption domain than the standard N3.

The mediator effect on the IPCE could be partly explained by comparing the oxidation potentials of the RuIII/RuII couple in the dyes and those of the mediators couples. The oxidation of the RuIII/RuII couple for Ru(L1)(DCB)$(NCS)_2$ was 0.8 V/SCE and those of Ru(L2)(DCB)$(NCS)_2$ was 0.61V/SCE. Thus the I^-/I_3^- mediator (0.4V/SCE) regenerated much better Ru(L1)(DCB)$(NCS)_2$ giving the best IPCE.

6.3.4 Evaluation of regeneration and recombination kinetics through transient absorption spectroscopy.

To get a better understanding of the regeneration step, transient absorption spectroscopy have been performed using various mediators to get useful indications about the interaction between the dye and the electron mediators (Figure 108).

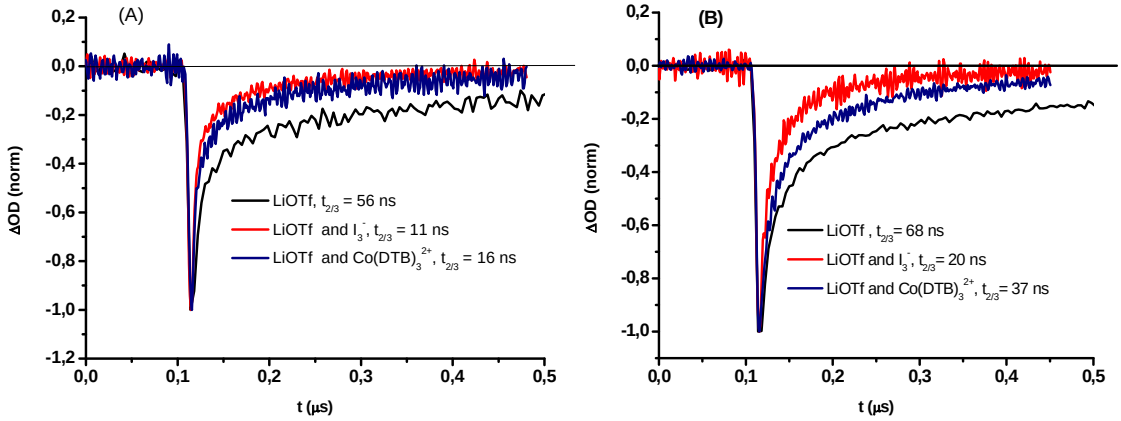

Figure 108. Transient absorption spectra of dye-sensitized TiO2 with Ru(L1)(dcbpy)$(NCS)_2$ (A) and Ru(L2)(dcbpy)$(NCS)_2$ (B) in the presence of various mediators LiOTf (0.5 M), I- (0.15M), $Co(DTB)^{2+}$ (0.15M) in acetonitrile (λ_{exc} = 532 nm, λ_{obs} = 500 nm; power intensity = 14 mJ/pulse).

From these experiments, it was evident that the Ru(L1)(DCB)$(NCS)_2$ dye was regenerated very efficiently, within a few nanoseconds, by both iodide and cobalt mediators, with iodide being slightly faster. The Ru(L2)(DCB)$(NCS)_2$ dye exhibited a very similar behaviour, although the dye recovery was slower than in the Ru(L1)(DCB)(NCS)2 case, due to a smaller driving force for the electron transfer. In general iodide displayed better reduction capabilities in both cases, despite a smaller driving force for the electron transfer reaction, due to its moderate reorganizational energy compared to the cobalt(II) complex. Thus, it was difficult to explain the different performances of the dyes in the presence of the two electron mediators only on the basis of dye regeneration, particularly in the case of Ru(L2)(DCB)$(NCS)_2$, which exhibited substantially better performances (on basis of IPCE) when associated to the cobalt couple.

Therefore, we have studied the recombination kinetics in the presence of identical concentrations of the oxidized mediators, respectively I3- and $Co(DTB)_3^{3+}$ [149]. In this way, in the absence of electron donating electrolytes, the only pathway of dye-cation recovery is recombination with photoinjected electrons.

In addition, to avoid interference from I_3^- absorption and photochemistry[150], we have monitored the decay of the dye cation absorption at 750 nm (Figure 109).

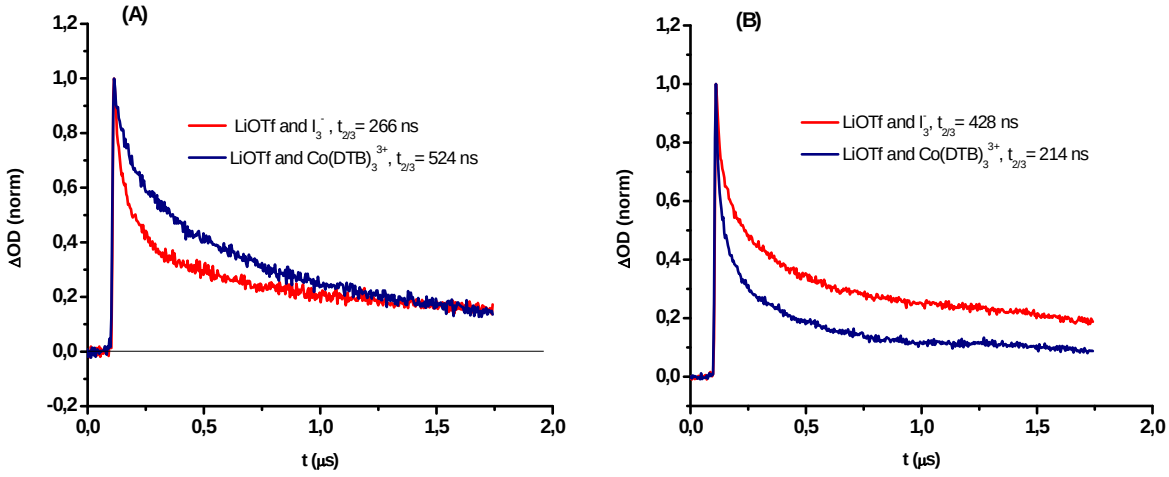

Figure 109. Recombination kinetics of photoinjected electrons in dye-sensitized TiO2 with Ru(L1)(dcbpy)(NCS)2 (A) and Ru(L2)(dcbpy)(NCS)2 (B) in the presence of LiOTf (0.5 M) and oxidized mediators I3- (0.1M) and Co(DTB)33+ (0.1M) in acetonitrile (λexc = 532 nm, λobs = 500 nm; power intensity = 14 mJ/pulse).

From Fig. 109A, it was clear that the dye cation recovery in Ru(L1)(DCB)(NCS)2 was faster in the presence of I_3^- was than in the presence of $[Co(DTB)_3]^{3+}$ meaning that the latter intercepted more efficiently the photoinjected electrons. The situation was reverted for $Ru(L2)(DCB)(NCS)_2$ where the dye recovery in the presence of I_3^- was significantly slower than in the presence of $[Co(DTB)_3]^{3+}$, meaning that, in these conditions, I_3^- was the best electron acceptor.

Thus, on the basis of the transient kinetics perfomed, the behavior of each dye in the presence of the two different mediators could be rationalized. Ru(L1)(DCB)(NCS)2 showed

[149] Comparisons between recombination rates in presence of oxidized mediators between different dyes should not be carried out essentially due to different dye loading, exposed TiO2 surface and different lithium content, all factors which can variably affect and alter the recombination rate. The only safe comparisons can be drawn relatively to the recombination rate of a single type of dye in the presence of different electron mediators.

[150] A transient positive absorption, with a lifetime of hundreds of nanoseconds, could be observed at 500 nm upon 532 nm laser excitation of an I_3^- solution in acetonitrile.

the best performances in association to the iodide/triodide mediator since it allowed for the fastest regeneration and the slowest electron recombination, while Ru(L2)(DCB)(NCS)2 was better with $[Co(DTB)_3]^{2+}$/ $[Co(DTB)_3]^{3+}$, essentially because of a less efficient electron recapture by $[Co(DTB)_3]^{3+}$ with respect to triiodide.

The sterically hindering styryl-pyrrolo groups in $Ru(L1)(DCB)(NCS)_2$ may be capable of forming a barrier even against access of small ions, like I_3^- to the TiO2 surface, therefore reducing electron recapture with respect to $[Co(DTB)_3]^{3+}$. The same protective effect was absent in the $Ru(L2)(DCB)(NCS)_2$ in which the pyrrole groups could passivate the surface against the bulky cobalt complex, but were unable to prevent, with the same effectiveness, the back recombination with the smaller triiodide.

6.3.5 Conclusions.

In summary, we have prepared new pyrrole-based valuable ruthenium dyes for solar cells. Ru(L1)(DCB)(NCS)2 bearing the pyrrole-based π-extended ligand L1 showed very good light harvesting ability with near 70% IPCE in the visible region. The π-conjugation in L1 contributed to a dramatic improvement compared to complex Ru(L2)(DCB)(NCS)2 bearing ligand L2 with pyrrole directly bonded to bipyridine when used in the presence of the I^-/I_3^- mediator. This difference could be explained by a better protective effect of the hindering styryl-pyrrolo groups against photoinjected electrons recapture by the mediator.

The new Ru(L1)(DCB)(NCS)2 performance is very close to those of the standard N3 with a wider absorption range. Another advantage is the availability of the pyrrole group for further polymerizations and access to solid state devices.

6.4 Dye-Sensitized Solar Cells based on PEDOP as a Hole Conductive Medium

Very few electron mediators have proved to be effective: notably only the classical iodide/iodine couple and certain Co(II) complexes display reasonable efficiencies, low cost and ease of handling for possible practical applications[151]. The reason for such a low number of candidates resides in at least three strict thermodynamic and kinetic requirements that have to be satisfied by the mediator: (1) its redox potential must be located at a value such as to allow for an efficient reduction of the majority of sensitizers, without being too negative, otherwise a penalty in terms of photovoltage is paid, (2) recombination between photoinjected electrons and oxidized mediators has to be as slow as possible, (3) reduction of its oxidized form at the counter electrode has to be fast. Summarizing the last two points, in order to avoid a significant electronic recombination, the mediator should exhibit an electrochemical asymmetry, resulting almost electrochemically inert on semiconductor oxides like SnO_2, TiO_2 , In_2O_3:SnO_2 which constitute the photoanode, whereas should undergo an efficient heterogeneous electron transfer at the counter electrode, at least in presence of suitable catalytic materials.

The presence of an electron mediating redox couple dissolved in a solvent yields to obvious long term instability problems for operating DSSCs, mainly related to cell sealing and leaking; for this reason the realization of a fully solid state device, free of corrosive and volatile couples like the I^-/I^-_3 system, would be an important step for further development and implementation of these photoelectrochemical systems.

Conductive polymers based on polythiophenes and polypyrroles could be interesting candidates for replacing the liquid electrolyte in DSSC, due to their low cost, thermal stability and good conductivity[152]. Thanks to these properties, these systems have already found application in the OLED technology as charge transporting matrices[153].

---

[151] [(a)]S. Cazzanti, S. Caramori, R. Argazzi, C.M. Elliott, C.A. Bignozzi, J. Am. Chem. Soc 128 (2006) 9996.
[(b)]S.A. Sapp, C.M. Elliott, C. Contado, S. Caramori, C.A. Bignozzi, J. Am. Chem. Soc. 124 (2002) 11215.
[(c)]H. Nusbaumer, J.-E. Moser, S.M. Zakeeruddin, M.K. Nazeeruddin, M. Graetzel, J. Phys. Chem. B 105 (2001) 10461.

[152] K. Murakoshi, R. Kogure, Y. Wada, S. Yanagida, Chem. Lett. (1997) 471.
K. Murakoshi, R. Kogure, Y. Wada, S. Yanagida, Solar Energy Mat. Solar Cells 55 (1998) 113.

[153] H.-K. Shim, J. Jung-Il, Advances in Polymer Science, vol. 158, Springer Verlag, Berlin, Heidelberg, 2002, pp. 193–243.
M. Gross, D.C. Muller, H.-G. Nothorfer, U. Scherf, D. Neher, C. Brauchle, K. Meerholz, Nature 405 (2000) 661.

In this paragraph we discuss the photoelectrochemical properties of PEDOP (poly-ethylene-dioxy-pyrrole) based DSSCs in which the conductive polymer is deposisted on a sensitized TiO_2 photoanode via a photoassisted electropolymerization initiated by a purpose built ruthenium complex[154], $Ru(DCB)(pyrr\text{-}bpy)_2^{2+}$ [155]: this approach should ensure, at least in principle, an intimate contact between the sensitizer and the polymeric chains facilitating charge transfer processes.

During the course of our studies it has been found that the presence of lithium ions dramatically improves and stabilizes cell performances, therefore our experiments have been usually conducted in presence of Li^+ 0.3 M in γ-butyrolactone. This finding is not surprising after all : it is well known that, like H^+, Li^+ is a potential determining ion for TiO_2 and its adsorption/intercalation on the semiconductor surface induces a Fermi Level stabilization to values more suited for charge injection from the sensitizer. Besides possibly facilitating charge injection, mobile lithium cations also provide charge compensation and are believed to contribute to electron transport through the nanoparticle network according to an ambipolar diffusion mechanism[156].

The presence of an electrolytic solution obviously nullifies the advantages of having a solid electron conductive matrix and solvent-free means of intercalating Li^+ at the TiO_2 surface have to be sorted out before obtaining real solid state devices. Nevertheless, as a first attempt, we consider interesting to investigate and report on iodide/iodine free photoelectrochemical cells where the *electronic conduction* takes place within a PEDOP matrix selectively grown on the photoactive surface of the semiconductor.

6.4.1 Experimental Section

6.4.1.1 Materials:

EDOP solution 2% in THF and $LiClO_4$ were purchased from Aldrich. Spectroscopic grade γ-butyrolactone, acetonitrile , absolute ethanol, obtained from Fluka, were used without further purification. Tetraisopropyl-orthotitanate (Titanium (IV) tetra-isopropoxide,

[154] S. Saito, T. Azechi, T. Kitamura, Y. Hasegawa, Y. Wada, S. Yanagida, Coord. Chem. Rev. 248 (2004) 1469. A.J. Mozer, Y. Wada, K.J. Jiang, N. Masaki, S. Yanagida, N.S. Mori, Appl. Phys. Lett. 89 (2006) 043509.
[155] D. Martineau, M. Beley, P.C. Gros, S. Cazzanti, S. Caramori, C. A. Bignozzi, Inorg. Chem. 46 (6) (2007) 2272.
[156] S. Nakade, S. Kambe, T. Kitamura, Y. Wada, S. Yanagida, J. Phys. Chem. B 105 (2001) 9150.

$Ti(ip)_4$) 98% and 98% $TiCl_4$ were bought from Fluka and used as received. Gold (ca. 50 nm) or carbon (ca. 20 nm) coated counter electrodes were obtained by deposition of gold (ISTA) or graphite (ISTA) vapours onto well cleaned conductive FTO (Fluorine-Tin-Oxide) glasses (Pilkington, 8 Ω/cm^2, ca. 2 x 2.5 cm) using a custom built thermal evaporator. The average pressure in the vacuum chamber during the evaporation was of the order of 7×10^{-6} Torr. Indium-Tin-Oxide (ITO) coated glasses, 4-8 Ω/ cm^2, were purchased from Delta Technology. Both FTO and ITO substrates were carefully cleaned by sonication in an Alconox®/water solution and generously washed with acetone, ethanol and acetonitrile in order to insure removal of surface contaminants, grease and oil traces.

The synthesis of ligands and related Ru(II) complex is previously described (chapter 6.1….)

6.4.1.2 Photoanode preparation:

In order to avoid incidental electronic recombination from the FTO back contact, a compact TiO_2 underlayer was created prior to porous TiO_2 deposition: typically ≈ 200 µl of freshly prepared precursor solution, (0.2 M $Ti(ip)_4$ in absolute ethanol), was spin coated onto cleaned FTO substrates (2 x 2.5 cm) at 2000 rpm for about 30 seconds. The resulting transparent layer was baked at 450 C° in an oven for 30 minutes, yielding to a perfectly transparent compact 2 cm^2 TiO_2 film .

Mesoporous TiO_2 films were obtained by casting over the compact TiO_2 underlayer a colloidal TiO_2 paste using the well known scotch tape method[157]. The resulting membrane was sintered in an oven at 450 C° for 40-45 minutes. Finally, the last step involved the application of an aqueous 2 M $TiCl_4$ solution onto the mesoporous TiO_2 substrate, as it has been generally recognized that such treatment improves the photoelectrochemical properties of the semiconductor.

Sensitization was carried out by immersion of the TiO_2 photoelectrodes in a ca. 10^{-5} M sensitizer solution in acetonitrile. This procedure was carried out in the dark either at refluxing temperature for 3-4 hours or at room temperature for approximately 12 hours. After this time dye adsorption on TiO_2 was complete, leading to coloured photoelectrodes characterized by an almost unitary absorbance in the visible region corresponding to the maximum of the MLCT transition of the Ru(II) complex.

6.4.1.3 PEDOP deposition:

[157] M.K. Nazeeruddin, A. Kay, I. Rodicio, R. Humphry-Baker, E. Mueller, P. Liska, N. Vlachopoulos, M. Graetzel, J. Am. Chem. Soc. 115 (1993) 6382.

Photoassisted PEDOP deposition was obtained by exposing the sensitized photoanode, in presence of 10^{-3} M EDOP / 0.1 M $LiClO_4$ in acetonitrile, to the output (0.2 W/cm^2) of a 385 nm filtered Xe lamp. Usually irradiation was carried out under potentiostatic conditions, applying a + 0.2 V Vs Ag potential bias in a three electrode configuration with a platinum wire as a counter electrode. Both the reference and the counter electrodes were separated from the working photoelectrode compartment by glass frits. Photocurrent transients were recorded by manually shutting the light source.

6.4.1.4 Solar Cell assembly:

The photoactive electrode, functionalized with PEDOP was pressed and firmly clamped over the counter electrode. Gold coated counter electrodes gave better performances with respect to carbon coated ones. $LiClO_4$ 0.3 M in γ-butyrolactone was eventually drawn inside the cell by capillarity. The cell geometrical active surface was 1 cm^2.

6.4.1.5 Analytical instrumentation and measurements:

Uv-Vis spectra were collected using a Perkin Elmer Lambda 40 spectrophotometer equipped with a photodiode detector. Electrochemical and photoelectrochemical measurements were carried out using either an Ecochemie Autolab PGSTAT 30 electrochemical workstation or an Amel model 562 Potentiostat-Galvanostat. Polychromatic light irradiation was obtained using a 385 nm filtered Xe lamp (Cermax, air cooled, 175 W) and incident irradiance, measured with a Molectron Power Max 500A power meter, was adjusted at the desired value by varying the distance between the sample and the light source.

Typically, photocurrent density-voltage characteristics of PEDOP based solar cells were collected under white light illumination at an incident irradiance of about 0.1 W/cm^2 using a two-electrode arrangement, sweeping the potential from 0.5 to - 0.5 V with a scan speed of 5 mV/s. The same potential program was employed to record the dark current.

Photoaction spectra were obtained with a custom made apparatus comprising a water cooled Xe lamp (Osram XBO, 150 W) coupled to an Applied Photophysics monochromator, adopting a 5 nm band pass. Photocurrents, sampled at 20 nm intervals under monochromatic light irradiation, were recorded under short circuit conditions using an Agilent 34401A digital multimeter. Incident irradiances were measured by means of an Centronic OSD 100-7Q calibrated silicon photodiode and the IPCE (Incident Photon-to-electron Conversion Efficiency) calculated according to:

$$\text{IPCE \%} = 1240\ \frac{J}{\lambda W}$$

where J is the photocurrent density expressed in μA, λ is the wavelength of incident monochromated light in nm and W is the power of the incident photon flux in W/m^2.

6.4.2 Study of the growth of the polymeric matrix on the photoanode through ossidative electrodeposition.

It is well known that upon chemical or electrochemical oxidation pyrrole and its derivatives, like EDOP, undergo a cationic polymerization with the formation of a conductive polymer[158]. As an example the cyclic voltammetry (CV) of a 10^{-3} M EDOP at an ITO working electrode in acetonitrile is reported in figure 110 :

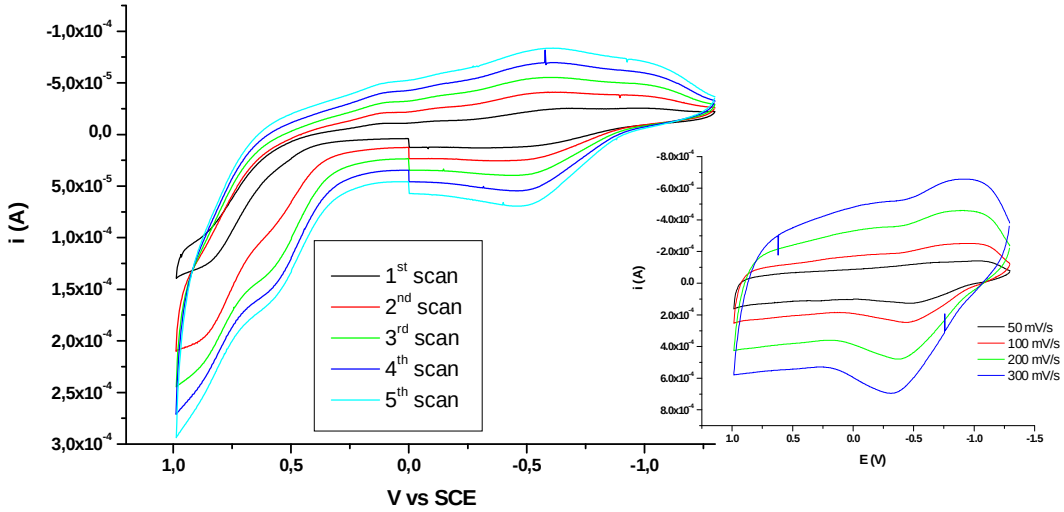

Figure 110. Cyclic voltammetry of 10^{-3} EDOP in ACN/ $LiClO_4$ 0.1 M. ITO/Pt/SCE 50 mV/s. Inset : CV of the PEDOP coated ITO electrode in neat ACN/$LiClO_4$ 0.1 M as a function of the scan speed.

The CV of an EDOP solution showed two distinct processes: the irreversible peak at 0.7 V Vs SCE was determined by EDOP oxidation which resulted in the concomitant formation of PEDOP, evidenced by the broad reversible process centred at -0.5 V Vs SCE

158 [a]P. Schottland, Z. Kenz, L.C. Gaupp, B.C. Thompson, C.A. Thomas, I. Giurgiu, R. Hickman, A.K. Abboud, R.J. Reynolds, Macromolecules 33 (2000) 7051.
[b]E. Desimoni, B. Brunetti, P. Ugo, R. Cazzaniga, Synth. Met. 130 (2002) 135.
[c]A. Deronzier, J.-C. Moutet, Coord. Chem. Rev. 147 (1996) 339.

determined by polymer electroactivty (i.e. polymer reduction and reoxidation). The rise in wave intensity upon subsequent scans was due to the increase of the active electrodic surface consequent to PEDOP growth at the ITO/solution interface.

After potentiodynamic deposition the functionalized electrode was studied in a fresh supporting electrolyte solution: in absence of free oxidazable monomer, the irreversible peak at positive potentials disappeared, while the electroactivity of the surface bound polymer was retained, showing the linear dependence of the peak current from the scan speed expected in case of surface adsorbed species. When the polymer is in its oxidized form exhibit a reasonable conductivity[159], being characterized by the presence of mobile holes. Since charge compensation within the polymeric matrix is provided by counter ions of the supporting electrolyte, in this case ClO_4^- anions, the oxidized polymer is referred to as perchlorate doped PEDOP.

A process analogous to the electrochemical deposition showed above is responsible for the photo-induced PEDOP deposition on the sensitized TiO_2 surface: the oxidized dye, $[Ru(III)(DCB)(pyrr\text{-}bpy)_2]^{3+}$, created after the charge injection into TiO_2, is indeed a sufficiently strong oxidizer, with a potential of about 1,19 V vs SCE[47], to oxidize EDOP monomers and induce cationic polymerization. It is also reasonable that, due to a favourable electronic communication, are the pyrrole moieties directly linked to the chromophoric ligands of the sensitizer which undergo a first electron transfer and are oxidized by Ru(III); these radical cations can then react with EDOP molecules in solution leading, at least in principle, to the growth of polymeric chains chemically attached to the dye. This would be an obvious advantage in term of electronic coupling and charge transfer rate between electron donor (PEDOP) and acceptor (oxidized dye).

The photo-induced electropolymerization was demonstrated by the sudden charge flow recorded under illumination, which quickly dropped to zero in the darkness (Figure 111).

[159] C.S.C. Bose, S. Basak, K. Rajeshwar, J. Electrochem. Soc. 96 (1992) 9899.
J. Simon, J.-J. Andre`, Molecular Semiconductors, Springer Verlag, Berlin, 1985.

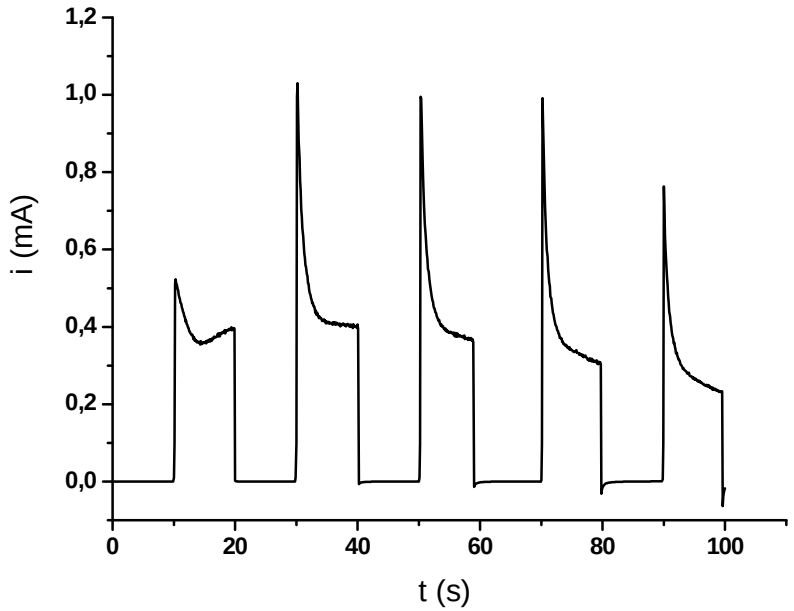

Figure 111. Photocurrent transients recorded during photo-electropolymerization in presence of EDOP 10^{-3} M / $LiClO_4$ 0.1 M in ACN. Applied bias : + 200 mV Vs Ag .

The shape of the photocurrent transients was qualitatively influenced by at least two factors : first, despite a positive bias, a strong electronic recombination, probably involving both oxidized dyes and electron acceptors in the electrolyte (i.e. EDOP radical cations, PEDOP oligomers etc.), was evident as a fast relaxation ($t_{1/2} \approx 1s$) from the initial spike of about 1 mA, to a value of about 0.4 mA; second, as polymerization progressed the thickness of the polymer film increased leading both to a rise in electrical resistance and to competitive light absorption with the dye, thus limiting the amount of current that could be produced by the system, evidenced by a second slower decay component and by the general decrease of photocurrent magnitude evident when comparing, for example, the first transients with the last one.

PEDOP growth was also confirmed by visual inspection and by absorption spectra, showing, with the advance of polymerization , an absorbance increase in the whole visible region, consistent with the green/black coloration of oxidized/doped PEDOP.

It would be interesting to ascertain whether the polymer chains were really linked to the sensitizer or simply physically adsorbed at the electrodic surface in analogy to a more conventional electropolymerization. Photo-electrochemical polymerization experiments carried out with an heteroleptic ruthenium dye lacking pyrrole groups

($[Ru(DCB)_2(dnbpy)]^{2+}$)[160] proved that PEDOP deposition could be obtained with similar efficiency (i.e. similar magnitude and shape of the photocurrent transients recorded during polymerization), however, despite nearly coincidental electrochemical and spectroscopic properties of the two sensitizers, cells based on PEDOP/$[Ru(pyrr\text{-}bpy)_2(DCB)]^{2+}$ generated, in the same conditions, nearly twice the photocurrent delivered by the analogous PEDOP/$[Ru(DCB)_2(dnbpy)]^{2+}$ system. This fact seems to suggest, at least indirectly , that a certain degree of specific interaction between the polymer and the dye could be obtained by using a pyrrole-functionalized sensitizer.

6.4.3 Photoelectrochemical characterization of quasi-solid state DSSCs.

PEDOP based DSSCs, obtained at different polymerization times, were assembled and characterized through J-V curves. The results are summarized in Table XVIII.

Table XVIII. Photoelectrochemical parameters of PEDOP based solar cells under 0.1 W/cm^2 Xe lamp irradiation.

Polymerization Time (s)	J_{sc} (μA)	V_{oc} (mV)	FF	η %
2	164	438	0.16	0.0117
5	187	450	0.18	0.0125
10	110	414	0.31	0.0141
30	78	396	0.25	0.0071
50	14.6	285	0.25	0.0010

Our results showed very low efficiencies mostly due to small Jsc , < 200 μA, and a poor fill factors, ≤ 0.31 . In general, the highest efficiencies were obtained for relatively short polymerization times, from 2 to 10 s, indicating that the increase in resistance of thicker polymeric films, deposited at irradiation times longer than 10 s, was a performance limiting factor. There are at least two different contribution to cell resistance: one is due to the bulk polymer resistance, the other is due to the interfacial resistance at the counter-electrode/polymer contact. The bulk polymer resistance obviously rises as its thickness

[160] S. Cazzanti, S. Caramori, R. Argazzi, C.M. Elliott, C.A. Bignozzi, J. Am. Chem. Soc 128 (**2006**) 9996.

increases, but the interfacial resistance is expected to decrease since, using thicker films, it will be easier to establish an electrical contact with a larger number of longer polymer chains grown on different nanoparticles. Since these two effects are opposite, it is expected to find a compromise allowing to maximize cell performances. In our experiments we found the best results adopting a 10 s irradiation time, however, these results have to be taken cautiously, since global efficiency differences between, say, 5 and 10 seconds were really small. An example of a J-V curve obtained with such cells is reported in Figure 112.

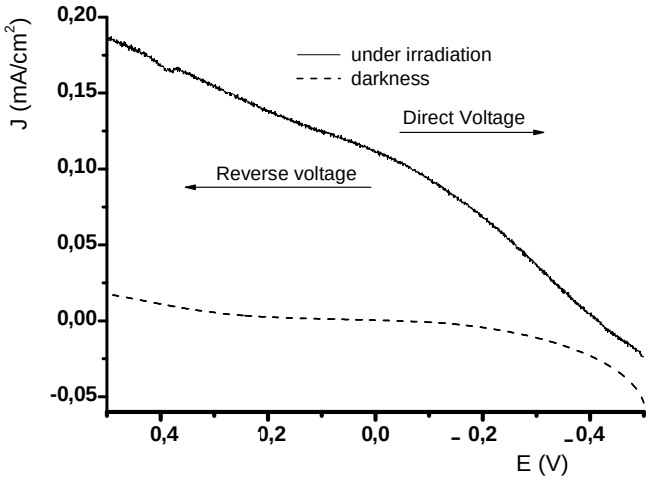

Figure 112: J-V characteristic obtained on PEDOP based DSSC in presence of Li^+ 0.3 M. 10 seconds polymerization time.

The J-V characteristics seemed to indicate a strong recombination and an high serial resistance, affecting the fill factor. The dark current corroborated the indication of an efficient recombination showing a marked increase in its magnitude as the direct bias approached -0.4 V, probably reaching the onset of PEDOP reduction (see Fig.110), suggesting that, as the potential increased towards negative values, higher lying states of the TiO_2 were filled from which recombination with PEDOP holes occurred without a significant activation energy. The fact that oxidized/doped PEDOP was directly photo-electrochemically deposited onto TiO_2 probably enhanced the electron/hole recombination pathways, since photoinjected electrons diffusing to the back contact had a certain probability of reaching the surface of the nanoparticles in close proximity of PEDOP acceptor states. While the dark current suggested a possible photocurrent loss mechanism through PEDOP reduction, a relevant recombination with the oxidized dye could not be ruled out. Dark current simply could not provide

informations on the latter process since, in the dark, after equilibrium was attained, no oxidized Ru(III) centers should be present at the TiO_2/Dye/polymer interface.

Indications of efficient recombination could also be obtained from cell photocurrent transients under short circuit conditions (Figure 113).

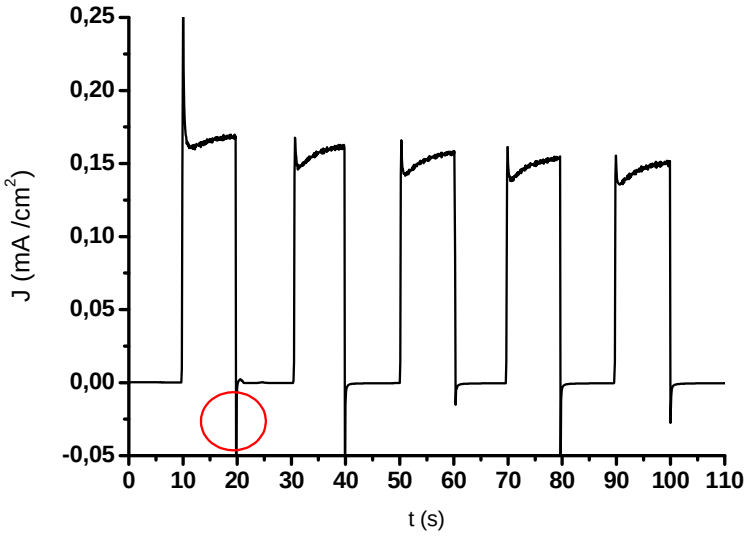

Figure 113. Cell photocurrent transients recorded under short circuit conditions in presence of Li^+ 0.3 M. The red circle evidences the cathodic current.

Figure 113 shows a fast photo-response of the cell with an almost instantaneous rise of the photocurrent as soon as it was exposed to light. However both the relaxation from the initial photoanodic spike to a lower steady value and the presence of a cathodic peak when light was switched off provided evidence of the presence of recombination processes[161]. The cathodic spike was probably due to recombination of photoinjected electrons with acceptor states at the TiO_2 surface, namely PEDOP holes and oxidized Ru(III) centers. The fact that the cathodic current dropped to zero on a very short time scale also suggested that recombination was kinetically fast, at least for the time scale of our experiments.

In order to gain additional insights on the behaviour of this type of PEDOP based photoelectrochemical cells, IPCE measurements were undertaken (Figure 114).

[161] A. Hagfeldt, H. Lindstroem, S. Soedergren, S.-E. Lindquist, J. Electroanal. Chem. 381 (1995) 39.

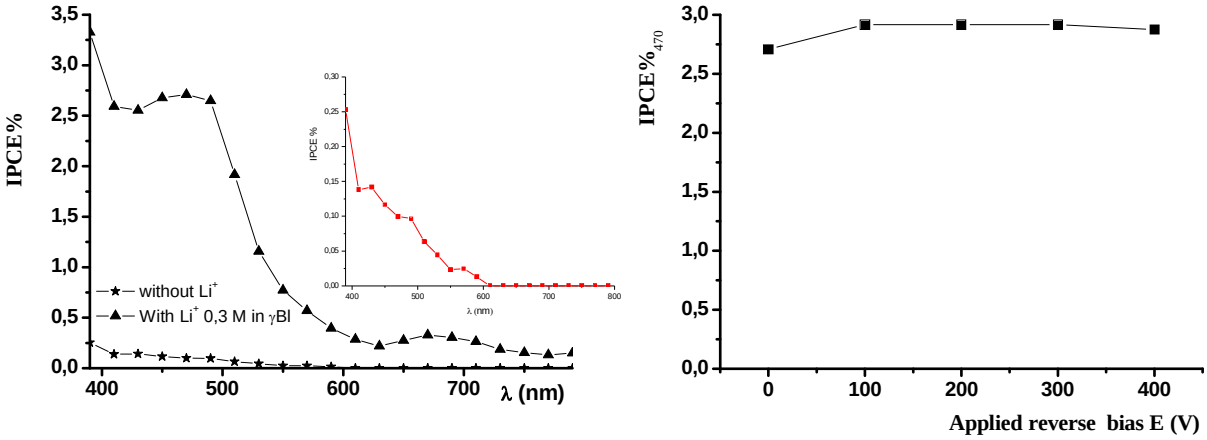

(A) (B)

Figure 114. (A) IPCE % spectra recorded on sandwich PEDOP based DDSC with (triangles) and without (stars) Li^+ 0.3 M; inset figure 5 (A) : magnification of the IPCE spectrum obtained in absence of Li^+. (B) : dependence of maximum IPCE % from applied reverse bias.

IPCE % spectra were in good agreement with the absorption spectrum of the sensitizer adsorbed on nanocrystalline TiO_2 providing further evidence of photoinduced charge injection from the excited state of the dye. It was also evident the profound influence of Li^+ cations on cell performances leading , in presence of $LiClO_4$ 0.3 M in γ-butyrolactone, to conversion efficiencies almost ten times higher than the ones obtained with the fully solid state device. Besides influencing the flat band potential of the semiconductor, many authors have pointed out the role of the electrolyte in assisting the transport of electrons through the interconnected TiO_2 particles[162], suggesting that, in order to preserve electroneutrality, the movement of photoinjected electrons must be counterbalanced by a reorganization of oppositely charged counter ions. Hence it can be expected that, in presence of an highly conductive electrolyte, the electrons traversing the film are more easily charge compensated, leading to a general decrease of their transit time, thus diminishing the probability of trapping and recombination.

Photoaction spectra allowed for the calculation of the electron collection efficiency of our devices, since IPCE is given by the product of three terms according to

$$IPCE(\lambda) = \varphi_{inj}\eta(1\text{-}10^{-A(\lambda)})$$

[162] A. Solbrand, H. Lindstroem, H. Rensmo, A. Hagfeldt, S.-E. Lindquist, J. Phys. Chem. B 101 (1997) 2514.

where φ_{inj} is the charge injection quantum yield of the sensitizer, η is the charge collection efficiency and $1\text{-}10^{-A(\lambda)}$ express the light harvesting efficiency of the sensitized film.

Our films were characterized by a nearly unitary maximum absorbance, hence an LHE term of the order of 0.9 could be obtained, while a φ_{inj} close to unity could be reasonably hypothesized, since the same dye gave rise to very high IPCE ($\approx$ 80 %)[47] using suitable electrolytic mediators; in addition, quantum yields of charge injection have been generally found independent from external factors like chemical environment, temperature etc.. As a consequence, an η of about 3 % in presence of Li^+ could be easily calculated, indicating that only 3 % of the photogenerated electrons escaped from recombination flowing out of the cell as a photocurrent. Quite surprisingly IPCE % was found to be nearly independent from the presence of a reverse bias of up to 400 mV: while no band bending is expected in case of nanocrystalline substrates, the presence of a positive polarization should in any case influence charge transfer kinetics across the TiO_2 surface, emptying higher lying TiO_2 states from which recombination could more easily occur. Based on its electrochemistry, PEDOP reduction should not take place from TiO_2 states lower than -0.3/-0.4 V vs SCE which are unlikely to be still fully populated in presence of an applied voltage of + 400 mV. Therefore, the IPCE % constancy over the reverse potential interval chosen for the this study could be determined by an efficient charge recombination with Ru(III) centers, which lying at about +1 V Vs SCE, could still undergo a recapture with electrons occupying relatively low lying TiO_2 states. Probably, under low monochromatic light intensities (the conditions in which IPCE spectra are usually measured), the majority of photoinjected electrons relax to low lying states from which recombination with PEDOP is not very probable, being recombination with oxidized dye the major photocurrent loss mechanism. Under stronger irradiation however, due to higher electronic population, the situation could be different, and higher lying states, from which PEDOP reduction might occur, could be occupied, as it is suggested by the photocurrent rise in Figure 112 as the potential was scanned towards positive values.

An efficient electron-oxidized dye recombination could take place only if dye-holes were not efficiently scavenged by the mediator. While transient spectroscopic measurements would be needed to ascertain this point, it is possible that this is indeed the situation : since PEDOP is in its oxidized form, only a limited number of electrons could be available for direct dye reduction. Therefore, in order to restore the reduced form of the dye,

photogenerated electrons would need to flow out of the cell and reduce the polymer at the counter electrode before being transported across the polymeric matrix in proximity of the dye, leaving a longer time for recombination processes to take place.

6.4.4 Introduction of an Allumina overlayer.

Indications of efficient recombination was also gained from cell photocurrent transients under short circuit conditions, showing cathodic spikes due to recombination of photoinjected electrons with acceptor states at the TiO_2 surface, namely PEDOP holes and oxidized Ru(III) centres. The cathodic current dropped to zero on a very short time scale suggesting that recombination was kinetically fast, at least for the time scale (0.1 s sampling time) of the experiment. Passivation of the TiO_2 surface via the application of a nanometric insulating Al_2O_3 overlayer[163] was instrumental in reducing the electronic recapture, allowing for an IPCE % doubling (from 3 to 6%) (Figure 115). Cell Jsc and Voc measured under 0.05 W/cm^2 white light irradiation were also significantly improved (from 50 to 100 μA/cm^2 and from 0.4 to 0.7 V respectively).

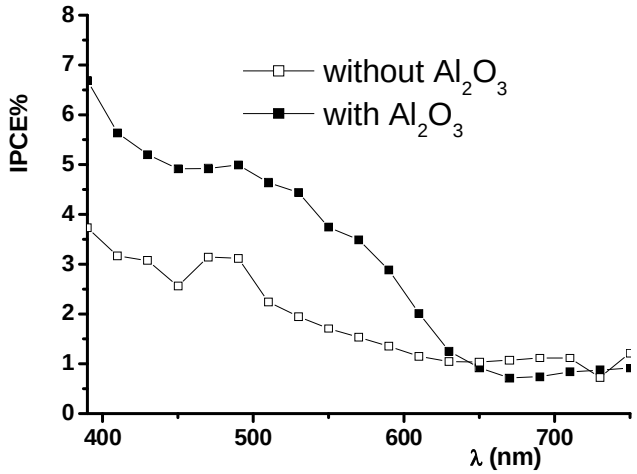

Figure.115 Photoaction spectra of a TiO_2/Dye/PEDOP/Au cell (white squares) compared to a TiO_2/Al_2O_3/Dye/PEDOP/Au system (black squares).

Besides strong back recombination and despite the intimate contact between the dye and the hole transporting layer, the low efficiencies could be explained also by a non optimal

[163] E. Palomares, J. N. Clifford, S. A. Haque, T. Lutz, J. R. Durrant, *Chem. Commun.* **2002**, 1464.

hole injection into the PEDOP matrix, as evidenced by the slow oxidized dye recovery observed at 450 nm (Figure 116).

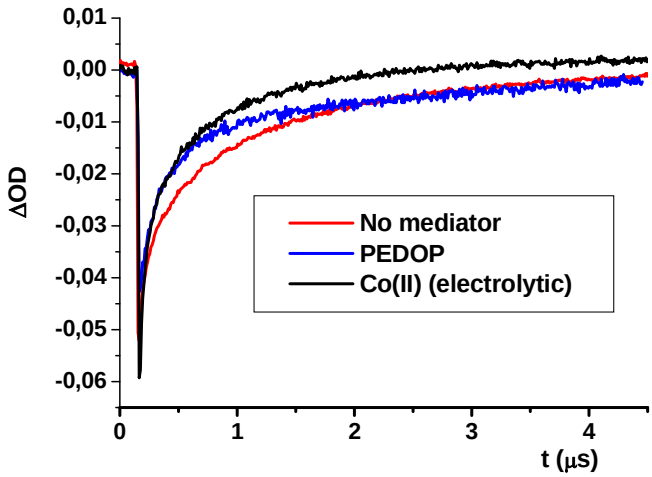

Figure 116 Ru(III) recovery in the presence of: no mediator (red line); photoelectropolymerized PEDOP (blue line); electrolytic 0.1 M Co(II)$(DTB)_3^{2+}$ (black line). Differential absorbance changes observed at 450 nm. Pulse energy ≈ 10 mJ/cm^2, 532 nm excitation wavelength.

6.4.5 Conclusions

Photoelectrochemical cells based on a PEDOP conductive polymer directly deposited onto the sensitized TiO_2 surface by photo-assisted polymerization were assembled and characterized . While these type of cells generated reasonable photovoltages suffered from very low J_{sc} and FF, generating low efficiencies explainable by efficient electronic recombination processes. Nevertheless these systems revealed quite interesting properties that are worth to be further investigated, with particular regard to charge separation events at the sensitized TiO_2/polymer interface. Improvements of counter electrode material, polymer doping and cell design may lead in the future to an increase of cell performances, allowing to approach efficiencies of more direct interest for practical purposes.

Chapter 7

Catalytic Materials for Cathodes of DSSCs.

7.1 Catalytic Materials for Cathodes of DSSCs

A kinetically fast reduction of the oxidized redox mediator at the cathodic compartment of the cell is required to maintain a sufficiently high concentration of electron donor for ensuring an efficient dye regeneration. With the I^-/I_3^- couple the use of a catalytic platinum coating is almost mandatory to achieve a satisfactory electrochemical kinetics, but the use of redox mediators alternative to the I^-/I_3^- couple opens the way to the search for new, less expensive, more flexible and available catalytic materials and to their application in new cell configurations. Many electrode materials (carbon, gold, platinum) function adequately in the case of Co(II)/(III) mediators, but are generally opaque. In contrast, optically transparent conductive oxide (TCO) are very poor cathodes for the $Co(DTB)_3^{2+/3+}$ couple, unless they are chemically modified by surface chemisorption of certain metal complexes. This allows to obtain optically transparent cathodes with a good electrochemical response which can be employed to build stacked cells either serially or in parallel connected in which, for example, two spectrally complimentary dye can work in their optimal absorption region, improving the spectral responsivity of the modules.

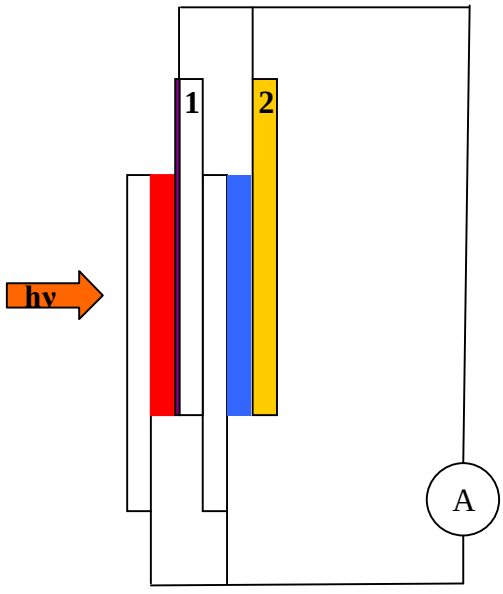

Figure 117. In parallel connected stacked cell based on the Co(II)/(III) couple. **1** Is a transparent FTO cathode modified via chemisorption of an electro-active molecule. **2** is a conventional gold cathode. The red and the blue dyes, absorbing in complimentary spectral regions, result in a panchromatic sensitization.

In a first study [170] it was demonstrated that ITO and FTO electrodes modified by irreversibly adsorbing a monolayer of $Fe(DCB)_3^{2+}$ electrocatalyze efficiently the $Co(DTB)_3^{2+}$ oxidation via an EC' mechanism. However, while electrogenerated Fe(III) has an ample driving force for oxidizing Co(II), Fe(II) is a thermodynamically too weak reductant for catalyzing Co(III) reduction, and the Fe(II)/(III) couple is of no value for building transparent cathodes. Nevertheless it was found that the electrocatalysis of the Co(II)/(III) redox chemistry promoted by surface bound electroactive species is a relatively general phenomenon and a number of molecular species with appropriate potential can promote the desired catalytic effect. For example, the osmium complex $Os(DCB)_2Cl_2$ can be strongly adsorbed on FTO and, with its potential (-310 mV Vs Ferrocene) slightly negative of the Co(II)/(III) couple, proved to efficiently catalyze both the oxidation and reduction of $Co(DTB)_3^{2+/3+}$. Indeed, the cyclic voltammetry of Co(II)/(III) (Figure 118) recorded at osmium modified electrodes showed well defined quasi reversible waves ($\Delta E_p \approx 140$ mV), nearly identical to those obtained on gold, whereas on the unmodified FTO or ITO it was almost impossible to observe the analogous charge transfer process. Cyclic voltammetry results were substantially confirmed by thin layer photoelectrochemical experiments which demonstrated that the osmium modified transparent cathodes gave rise to a very small overpotential (ca. 12 mV under cell short circuit conditions) for Co(III) reduction, indicative of a facile heterogeneous electron transfer[171].

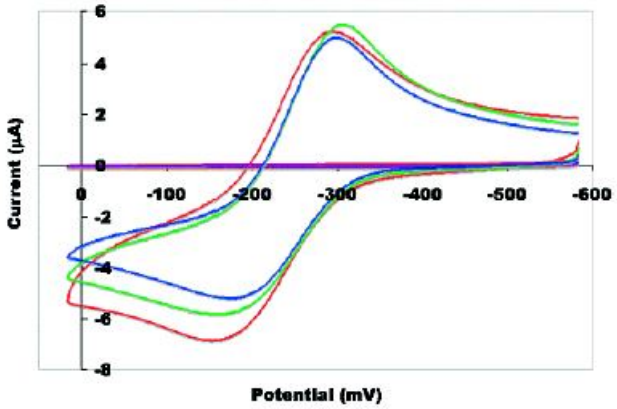

Figure 118 CV on gold (red)), FTO (brown), ITO (violet) and osmium modified FTO (green) and ITO (blue) working electrodes in the presence of ca. 0.1 mM $Co(DTB)_3ClO_4$. Potential referred to ferrocene.

[170] C. M. Elliott, S. Caramori, C. A. Bignozzi, *Langmuir* **2005**, *21*, 3022
[171] M. J. Scott, J. J. Nelson, S. Caramori, C. A. Bignozzi, C. M. Elliott, *Inorg.Chem.* **2007**, *46*, 10071.

The stacked cell configuration, employing N3 and a red absorbing cyanine dye which absorbs photons in a region where N3 does not, showed a J_{sc} improvement of about 15 % over a single N3 cell. It must be considered that the blue dye is a relatively inefficient dye, generating very modest IPCE % (ca. 5-8%) due to less than ideal redox properties and electronic coupling with the TiO_2. Nevertheless the results confirmed the principle and with a better performing dye substantial performance improvements are expected.

Conductive polymers like PEDOP an PEDOT were also found effective in promoting the Co(II)/(III) electrochemical response Figure 119. Both PEDOP and PEDOT can electrodeposited on a transparent conductive substrate by an anodic potentiostatic (ca. + 1.3 V vs SCE) or potentiodynamic electrolysis of the appropriate precursor solution in the presence of a perchlorate containing supporting electrolyte. Co(II)/(III) appeared to have a clearly diffusion limited electrochemical behaviour on both PEDOP and PEDOT functionalized cathodes. PEDOT gave rise to a more ideal behaviour associated to a smaller separation of the catalytic waves, with a peak separation of the order of 200 mV, substantially independent from Co(II) concentration, the slight peak shift at higher cobalt concentration being essentially determined by uncompensated cell resistance.

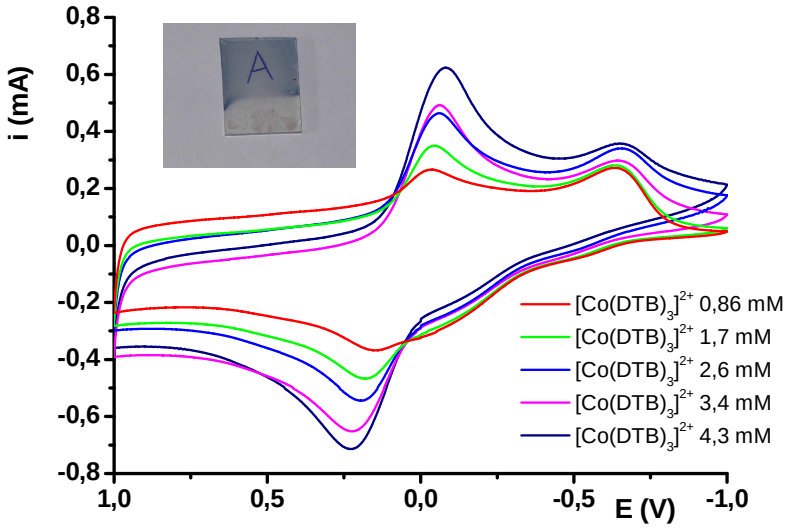

Figure 119 Cyclic voltammery of $Co(DTB)_3^{2+}$ at a transparent PEDOT modified FTO. Scan speed 100 mV/s, potential referred to SCE. The smaller peak centred at about -650 mV is determined by the intrinsic polymer electroactivity. PEDOT was grown by multiple scan deposition (3 scans), cycling the potential between -0.7 and +1.5 V Vs SCE with a scan speed of 20 mV/s.

The electrodeposition offer the advantage of a fine control of the thickness of the catalytic layer, thus optimizing the electro-active area and the transparency of the cathode. A cathode which possesses both a remarkable catalytic activity and a partially porous structure with a large active area is important for limiting the concentration overpotential which may develop at the counter electrode of the cell under strong illumination, allowing for the consequent reduction of the photocell series resistance. An improvement in cell fill factor and global efficiency is therefore expected and found (Figure.120).

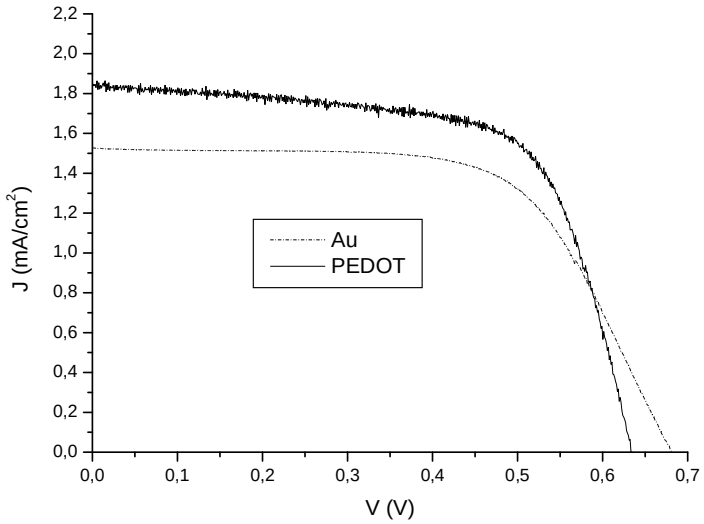

Figure 120 J-V curves of Co(II)/(III) mediated cell employing a gold (dashed line) and a PEDOT counter electrode (solid line). Electrolyte composition 0.15 M Co(II)/0.5 M Li^+/0.1 M Tbpy in acetonitrile. Cell equipped with a 120 μm spacer. Photosensitizer : Z907.

Conclusions

DSSCs are photoelectrochemical solar devices, currently subject of intense research in the framework of renewable energies as a low-cost photovoltaic device. Their functioning is based on the interlacing of subsystems working in tandem: the photoanode on which the dye sensitizer is adsorbed, the electron mediator and the counter electrode. In this chapter we have tried to give an overview on the recent advances in the design of these solar cell components.

Research on dye sensitizers are mainly focused on transition metal complexes, but a considerable of work is now directed towards the optimization of organic sensitizers and of natural sensitizers extracted from fruits.

Concerning the electron mediators, iodide/iodine has been so far the most efficient and commonly used redox system, due to the fact that I^- allows for a fast regeneration of the oxidized dye. The use of alternative redox couples as electron mediators has been addressed, so far, by a limited number of research groups but the results are promising. The research has been triggered by the fact that the electrochemical properties of coordination compounds can be easily tuned through a rational choice of the metal and an appropriate design of the coordination sphere and their electrochemical response is sensitive to the electrodic material. The choice and design of the redox couples has been done by considering inexpensive and available metals like the elements of the first transition row and easily synthesizable ligands. To date, the most successful attempts have been based on octahedral cobalt(II) complexes and the best results obtained in combination with specific heteroleptic complexes. The performances of such mediators have been improved by using kinetically fast couples in conjunction with Co(II) complexes. It has been in addition observed that copper complexes with a distorted tetragonal geometry show promise for developing alternative low cost mediators for photoelectrochemical cells.

The transport of the electroactive ions is expected to play a significant role in determining DSSC efficiency: this is particularly true under strong illumination when a large number of photooxidized dye molecules are simultaneously generated at the photoanode ad an efficient turnover of electron donating species is required to sustain the photocurrent. Cell and TiO_2 engineering are therefore required to avoid or reduce the mass transport limitations in DSSCs based on coordination compounds as redox mediators: minimizing the spacing between the electrodes, choosing low viscosity solvents and changing the morphology of the

TiO_2 substrate with ordered nanostructures with large pore size or with TiO_2 nanotubes and nanorods, expected to enhance mediator transport and cell efficiency.

The search for suitable solid materials that can replace the liquid electrolyte is an additional interesting and active area of research. In a solid state DSSC the solid hole conducting material captures the holes and closes the circuit with the counter electrode. Solid hole conductors include conducting polymers, organic hole conductors and inorganic semiconductors such as CuI and CuSCN. Organic hole conductors like spiro-compounds and conductive polymers based on polythiophenes and polypyrroles have demonstrated some promise for application in dye sensitized solar cells. In particular it has been reported that the presence of ionic liquids may improve the charge transporting capabilities of the heterointerface through screening of space charge effects.

In the last part of the chapter we have described some efforts towards the modification of the counter electrode with inexpensive and transparent materials. The interest being also related to the possible realization of stacked cells, either serially or in parallel connected, in which two spectrally complementary dyes can work in their optimal absorption region, improving the spectral responsivity of the modules. In these studies it has been found that osmium complexes as well as electrodeposited conductive polymers like PEDOP an PEDOT are effective in promoting the electrochemical response of Co(II) electron mediators.

The development of efficient and non corrosive electron mediators is considered of particular relevance since it may allow the building large area modules where the different components are in parallel interconnected, increasing the single module short circuit photocurrent and allowing for a more flexible and solar panel production.

Publications

- **Cazzanti, S.; Caramori, S.; Argazzi, R.; Elliott, C. M.; Bignozzi, C. A.,** Efficient Non-corrosive Electron-Transfer Mediator Mixtures for Dye-Sensitized Solar Cells, ***J. Am. Chem. Soc.;*** (Communication); 2006**;** ***128*****(31); 9996-9997.**

- **Martineau, D.; Beley, M.; Gros, P. C.; Cazzanti, S.; Caramori, S.; Bignozzi, C. A.**Tuning of Ruthenium Complex Properties Using Pyrrole- and Pyrrolidine-Containing Polypyridine Ligands ***Inorg. Chem.;*** (Article); ***46*****(6); 2272-2277**; 2007

- **Stefano Caramori, Silvia Cazzanti, Luca Marchini, Roberto Argazzi, Carlo Alberto Bignozzi, David Martineau, Philippe Gros and Marc Beley**, Dye sensitized Solar cells based on PEDOP as a Hole Conductive Medium**,** ***Inorganica Chimica Acta , Volume 361, Issue 3, 15 February 2008, Pages 627-635.***

- **Michele Brugnati, Stefano Caramori, Silvia Cazzanti, Luca Marchini, Roberto Argazzi and Carlo A. Bignozzi,** Electron Transfer Mediators for Photoelectrochemical Cells based on Cu(I) Metal Complexes. *International Journal of Photoenergy,* ***Volume 2007 (2007), Article ID 80756, 10 pages.***

- **A. Grabulosa, D. Martineau, M. Beley, P. C. Gros, S.Cazzanti, S. Caramori, C. A. Bignozzi,** Ruthenium complexes bearing p-extended pyrrolo-styryl bipyridine ligand: electronic properties and evaluation as photosensitizer, Dalton Transactions (accepted).

- **Silvia Cazzanti, Stefano Caramori, Giuseppe Calogero, Roberto Argazzi and Carlo A. Bignozzi,** Natural dye raw extracts as promising DSSCs photosensitizer, Chem. Comm. (submitted).

Acknowledgements

Ringrazio il Professor Bignozzi per avermi dato la possibilità di sviluppare questo progetto all'interno di un gruppo di lavoro stimolante e costruttivo, per avermi permesso di svolgere all'interno del percorso di dottorato molte esperienze all'estero per congressi e stages permettendomi di venir a contatto con persone di diverse lingue e culture, e per avermi sempre trasmesso un notevole entusiasmo per lo studio ed il lavoro di ricerca svolto.

Ringrazio Stefano Caramori per avermi seguito costantemente e diligentemente in questi 3 anni permettendomi di acquisire indipendenza e propositività nel progetto di ricerca affidatomi.

I'm indebeted to Prof. C. M. Elliott for the electrochemical contribution. I would thank Dr. Philippe Gros and Dr. David Martineau for the synthesis of ligands and related Ru(II) complexes and Dr. Giuseppe Calogero for his contribution in the study of organic dyes as photosensitizers.

Ringrazio tutto il gruppo in cui ho lavorato: Roberto Argazzi, Valeria Dissette (il cui aiuto organizzativo e l'immancabile sostegno in qualsiasi momento di crisi e di gioia si è rivelato fondamentale) e Vito Cristino.

Ringrazio i miei genitori, ovviamente, per avermi sopportato e supportato (è la classica frase, ma racchiude veramente mille significati!!!!!!!!) in questi 3 anni.

Ringrazio dei ragazzi, il cui supporto è stato e lo ritengo tuttora indispensabile e che, per mille motivi, mi hanno aiutato a superare quest'anno permettendomi di non perdermi e di portare a completamento questo mio percorso: Diego, Mik, Iarno, Flower, Luca, Nic, Jerry, Zott, Sara, Chiara, Laura, Tebo, Rita.

Ultimi ma primi per importanza sono i ringraziamenti che voglio dedicare a mia sorella Sara: non ho veramente parole per descrivere quanto mi abbia aiutato, e a Marco…Ghiro! a cui dedico questo lavoro e tutti questi tre anni di dottorato che abbiamo vissuto insieme.